UNIVERSITY OF SOUTHAMPTON

FACULTY OF ENGINEERING AND THE ENVIRONMENT

Institute of Sound and Vibration Research

Piezo-actuated structural waves for delaminating surface accretions

by

Michał K. Kalkowski

Thesis for the degree of Doctor of Philosophy

January 2015

UNIVERSITY OF SOUTHAMPTON

ABSTRACT

FACULTY OF ENGINEERING AND THE ENVIRONMENT
Institute of Sound and Vibration Research

Doctor of Philosophy

PIEZO-ACTUATED STRUCTURAL WAVES FOR DELAMINATING SURFACE ACCRETIONS

by Michał K. Kalkowski

In recent years substantial attention has been given to the problem of unwanted accretions on structures of which the foremost example is aircraft icing. A potentially promising alternative to the traditional thermal methods for tackling ice build-ups is a mechanical approach in which the accreted layer is removed with the aid of structural waves induced by piezoelectric actuators. This thesis originates from research questions regarding this concept with a twofold motivation: assessment of the feasibility of the method and development of a wave-based modelling strategy applicable to a waveguide that contains layers made of a material with electromechanical coupling.

The thesis starts with a broad theoretical study on free plane wave propagation in structures with accretions. The dispersion curves of a weakly coupled bilayer are analysed highlighting the aspects important from the viewpoint of the application. Conditions promoting high interface shear stress are identified and supported with a discussion on energy distribution patterns and their importance if a lossy accretion is considered. This part is concluded with a parametric study where accretions of different Young's moduli and different thicknesses are analysed with respect to the achievable interface shear stress yielding some implications for practical application. In the next part the mechanical forcing is introduced in the analysis. Two different approaches, namely analytical and semi-analytical, are compared and the latter is validated with an experiment. In the light of injected power partitioning between the propagating waves, a similar parametric study is conducted aimed at broadening the insight gained from free wave analysis. Then, as a practical excitation strategy piezoelectric actuators are introduced. The common approaches for modelling piezoelectric excitation are reviewed and their strengths and limitations discussed.

The background application requires high induced strain, therefore the actuators are expected to work near their resonances which violates the applicability conditions of the well-established models. In order to circumvent these limitations and avoid expensive conventional finite element model, a new methodology is developed in this thesis. The approach consists of the development of a piezoelectric semi-analytical finite element that enables wave-based modelling of piezoelectric materials and calculation of the response to a distributed voltage excitation. The coupling of a finite length actuator to a mechanical waveguide is done with the aid of the analytical wave approach. A validation experiment on a beam with anechoic terminations is conducted showing very good agreement with the numerical results. The presented approach is very general and can be used for many 'smart structure' applications.

The wave model is then used to investigate power and energy propagation in waveguides including the electrical system driving the actuator. The efficiency of the piezoelectric excitation is assessed with respect to the consumed electrical power and power loss in the driving system transmission line. The parametric study shows the dependence of power transmission coefficients on the dimensions of the actuator and the thickness of the bonding layer.

In the last part the methodology is applied to predict the interface shear stress generated by the piezoelectric excitation. The stress recovery routine is explained and validated with the conventional finite element method. The final parametric study is conducted showing the interface shear stress achievable for a structure with different accretions excited by a piezoelectric actuator and yielding the electrical power requirements. The concept of delaminating surface accretions with piezo-actuated structural waves is demonstrated in an experiment on a waveguide with emulated anechoic terminations. The corresponding numerical predictions for power requirements are found to be in a good agreement with experimental observations. The thesis is concluded with recommendations on the applicability of the wave-based concept and the design of the system that enables exploiting the described physical phenomena.

Contents

List of Figures

List of Tables

Declaration of Authorship

I, Michał K. Kalkowski , declare that the thesis entitled *Piezo-actuated structural waves for delaminating surface accretions* and the work presented in the thesis are both my own, and have been generated by me as the result of my own original research. I confirm that:

- this work was done wholly or mainly while in candidature for a research degree at this University;
- where any part of this thesis has previously been submitted for a degree or any other qualification at this University or any other institution, this has been clearly stated;
- where I have consulted the published work of others, this is always clearly attributed;
- where I have quoted from the work of others, the source is always given. With the exception of such quotations, this thesis is entirely my own work;
- I have acknowledged all main sources of help;
- where the thesis is based on work done by myself jointly with others, I have made clear exactly what was done by others and what I have contributed myself;
- none of this work has been published before submission

Signed:.....

Date:.....

Acknowledgements

I would like to thank my supervisors, Dr. Emiliano Rustighi and Dr. Timothy Waters, for their guidance, technical insight and encouragement. Above all, however, I am grateful for their friendship which helped me to grow as a researcher and supported in various aspects of life. I would also like to express my deepest gratitude to my examiners, Prof. Stephen Elliott and Prof. Svante Finnveden, as well as my internal reviewer, Dr. Neil Ferguson, for challenging questions and helpful advice during viva examination and milestone reviews.

For assistance, advice and wonderful atmosphere I thank all friends and colleagues from ISVR, in particular from the Dynamics Group, and all students and academics from the University of Southampton that I had a chance to meet during my PhD project. All your contributions are invaluable for me.

My gratitude goes also to Prof. Romana Śliwa from the Rzeszów University of Technology (Poland) for motivating discussions and ongoing friendly encouragement.

I would like to acknowledge funding bodies that made my research possible. I gratefully appreciate financial support from Structural Funds in the Operational Programme - Innovative Economy (IE OP) financed from the European Regional Development Fund - Project "Modern material technologies in aerospace industry", Nr POIG.01.01.02-00-015/08-00 and the University of Southampton Postgraduate Studentship programme.

Last but not least, I would like to thank my family and numerous friends both in Southampton and all over the world for their ongoing support and companionship. Above all, I thank my wife Ewa – my best friend, inspiration and often a lifesaver – for her love and patience. To her and to our wonderful daughter, Róża, I dedicate this work.

Nomenclature and constants

In order to facilitate comprehending the equations and simulations in the thesis, common material properties and the most important symbols and notation conventions are listed below. Units are given if appropriate. The entries are grouped in subject related areas for convenience.

Material properties used throughout the thesis

Table 1: Noliac NCE40 PZT ceramics properties (material used in the experiments)

Property	value
ρ, $\mathrm{kg\,m^{-3}}$	7850
η	0.007
$c^E_{xx} = c^E_{zz}$, GPa	126.35
$c^E_{xy} = c^E_{yz}$, GPa	58.68
c^E_{yy}, GPa	99.88
c^E_{xz}, GPa	62.93
c^E_{xz}, GPa	31.71
$c^E_{yz} = c^E_{xy}$, GPa	36.77
$\varepsilon^\epsilon_{xx} = \varepsilon^\epsilon_{zz}$, $\mathrm{F\,m^{-1}}$	5.5e-09
$\varepsilon^\epsilon_{yy}$, $\mathrm{F\,m^{-1}}$	5.196e-09
$e_{yxx} = e_{yzz}$, $\mathrm{N\,V^{-1}\,m^{-1}}$	-3.239
$e_{zyz} = e_{xyx}$, $\mathrm{N\,V^{-1}\,m^{-1}}$	13.075
e_{yyy}, $\mathrm{N\,V^{-1}\,m^{-1}}$	16.335

Table 2: Isotropic material properties. The properties for ice are chosen within the typical range reported in the literature – see e.g. [1] (esp. Fig 2.8), [2], [3] – except the loss factor which is assumed.

material	E, GPa	ν	ρ, kg m^{-3}	η
Aluminium	70	0.3	2700	0.002
Steel	163	0.3	8000	0.0001
Silvered epoxy	15	0.4	1000	0.0001
Glaze ice	8.2	0.351	900	0.01
Rime ice	1.5	0.282	600	0.01

Time, frequency and wavenumber quantities

$\lambda^{\sim}$	wavelength (spatial period), m
ω	circular frequency, rad s^{-1}
φ	nodal potential, V
$\mathbf{N}(x, y)$	displacement shape function matrix
$\mathbf{N}_{\varphi}$	potential shape function matrix
k	propagating wavenumber, rad m^{-1}

Wave field quantities

ϵ	strain
σ	stress, Pa
ϱ	surface charge, C m^{-1}
$\mathbf{D}$	electric displacement vector, C m^{-1}
$\mathbf{E}$	electric field vector, V m^{-1}
u	displacement, m

Analytical wave model - global matrix method and excitability

$\alpha_{L,S}$	longitudinal and shear bulk wave attenuation, Np m^{-1}
δ	strain energy originating from the longitudinal waves
γ	strain energy originating from the shear vertical waves
γ_{SH}	strain energy originating from the shear horizontal waves
$\langle P \rangle$	total power flow along the propagation direction
DC	elastic bilayer decoupling coefficient
ENR	fraction of the total strain energy enclosed in the accreted layer
$\mathbf{a}$	vector of partial waves amplitudes
$\mathbf{D}_{(i)}$	field matrix for the i^{th} layer

$\mathbf{G}$	global matrix
ζ	guided wave attenuation
$A_i^{(n)}$	wave mode receptance, n-mode, i- excitation direction
e_s	peak strain energy per unit volume (at a point)
k_{PZT}	static stiffness of the piezoelectric actuator
P_d	average dissipated power in a volume (total)
p_d	average dissipated power per unit volume (at a point)
$u_{\text{PZT, free}}$	voltage induced displacement of a free piezoelectric actuator

SAFE

Γ	boundary of the element
$\hat{\mathbf{\Phi}}_i$	matrix of right eigenvectors of the linearised SAFE QEP
$\hat{\boldsymbol{\phi}}_i$	right eigenvector of the linearised SAFE QEP associated with mode i
$\hat{\mathbf{\Psi}}_i$	matrix of left eigenvectors of the linearised SAFE QEP
$\hat{\boldsymbol{\psi}}_i$	left eigenvector of the linearised SAFE QEP associated with mode i
Ω	cross-sectional domain of the element
$\tilde{\cdot}$	matrices accounting for condensed potentials
$\mathbf{\Phi}$	matrix of displacement wave mode shapes
$\boldsymbol{\phi}_i$	displacement wave mode shape associated with mode i
$\mathbf{\Theta}$	matrix of force wave mode shapes
$\boldsymbol{\theta}_i$	force wave mode shape associated with mode i
$\mathbf{a}$	wave amplitudes vector
$\mathbf{A}$, $\mathbf{B}$	linearised SAFE 'stiffness' and 'mass' matrices, respectively
$\mathbf{f}_i$	nodal forces vector
$\mathbf{K}_0$, $\mathbf{K}_1$, $\mathbf{K}_2$	SAFE stiffness matrices; the index denotes the power of the multiplying wavenumber exponent
$\mathbf{K}_f$	SAFE stiffness-related matrix used in the calculation of internal forces
$\mathbf{M}$	SAFE mass matrix
$\mathbf{N}(x, y)$	displacement shape function matrix
$\mathbf{p}$	SAFE external traction vector
$\mathbf{q}$	nodal displacement vector
$\mathbf{R}$	reflection matrix
$\mathbf{T}$	scattering matrix
$\mathbf{t}_i$	nodal traction vector
$c_g^{(i)}$	group velocity associated with mode i
$e_k^{(i)}$	time-average of the kinetic rain energy associated with mode i

$e_u^{(i)}$	time-average of the strain energy associated with mode i
$p^{(i)}$	time-average of the power flow associated with mode i
$v_e^{(i)}$	energy velocity associated with mode i

Electrical quantities

C_0	static capacitance of a piezoelectric actuator, F
$P(t)$	instantaneous electrical power, W
P_{app}	apparent power (power rating) of the actuator, V A
P_{capab}	required power capability (power rating) of the source, V A
P_I	peak reactive electrical power, W
P_R	time-average of active electrical power, W
Z	electrical impedance, Ω
Z_L	electrical impedance of the load, Ω
Z_S	electrical impedance of the source, Ω

Material properties, geometry and dimensions

λ, μ	Lame constants, GPa
λ_v, μ_v	complex Lame constants for the viscoelastic layer, GPa
ρ	mass density, $\mathrm{kg\,m^{-3}}$
$\boldsymbol{\varepsilon}^{\epsilon}$	dielectric constant matrix measured under zero strain (clamped) condition
$\mathbf{C}$	stiffness matrix for an elastic material
$\mathbf{C}^{\mathrm{E}}$	stiffness matrix for a piezoelectric material measured under zero-electric field (short-circuit) condition
$\mathbf{e}$	piezoelectric stress coefficient matrix
c_L	longitudinal bulk wave velocity, $\mathrm{km\,s^{-1}}$
c_S	shear (transverse) bulk wave velocity, $\mathrm{km\,s^{-1}}$

Operators and notation conventions

$\bar{\cdot}$	spatial Fourier transform of a quantity, $\bar{\mathbf{q}} = \int_{-\infty}^{\infty} \mathbf{q} \exp[jkz]\,\mathrm{d}z$
$\cdot^*$	complex conjugate
$\cdot^\top$	transpose
$\nabla \cdot \{\ \}$	divergence operator: $\nabla \cdot \{\ \} = \frac{\partial}{\partial x}\{\ \}\hat{\mathbf{x}} + \frac{\partial}{\partial y}\{\ \}\hat{\mathbf{y}} + \frac{\partial}{\partial z}\{\ \}\hat{\mathbf{z}}$

Abbreviations

DOF	degree of freedom
EMI	electro-mechanical impedance
GEP	Generalised eigenvalue problem
GMM	Global matrix method
PZT	Lead zirconium titanate - most common piezoelectric ceramic; abbv. often used to represent piezoelectric ceramic in general
QEP	Quadratic eigenvalue problem
SAFE	Semi-analytical finite element method
SFEM	Spectral finite element method
WFE	Wave and finite element method

Chapter 1

Introduction

1.1 Motivation

An unwanted material built-up on various types of structures is a common engineering problem in machinery maintenance which seriously affects performance and safety of operation. A type of a potential accretion is defined by the working conditions of a particular object, e.g.:

- for aircraft the main problem is the ice accumulation during the flight which seriously deteriorates the aerodynamic properties of the profile;
- a similar phenomenon causes the wind turbines to experience a drop in efficiency and potentially severely hurt people or damage objects around due to a self-induced ice shedding. Furthermore, uneven ice loading promotes various damage mechanisms. In general, any machinery that works in the cold climate regions is often subject to icing issues (e.g. suspension railway, chairlifts);
- machines that operate with different types of sedimentary rocks (e.g. industrial handling systems) often suffer from the transported material accretion (e.g. gypsum) on its components;
- depositions on the internal walls of pipelines especially in the food or pharmaceutical industry degrade their flow parameters and possibly influence the quality of a transported medium; since those surfaces cannot be reached and cleaned easily, systematic chemical cleaning is necessary for proper operation;
- ships suffer from the undesirable accumulation of various types of organisms: algae, plants, microorganisms. The degradation of the properties of the surface is associated with an increase of fuel consumption and requires a systematic cleaning and refurbishment of the hull, which is a very expensive operation.

From the aforementioned issues the one that gets the greatest attention from engineers and researchers is the aircraft icing. Ice accretion on the aircraft significantly changes the aerodynamic properties of the airfoil and disturbs the operation of avionics and induction system. Since the 1920s, when the problem was first noticed, the physics of ice accretion as well as methods of tackling icing have received considerable attention from scientists resulting in many anti-/de-icing methods based on various phenomena, starting from pneumatic boots first implemented during the Second World War (B-29, DC-3). Many of them (e.g. anti-icing fluids, electro-thermal systems, bleed air) are currently in common use. However, the increase of use of composites in modern aircrafts introduced new complications for incorporating standard (especially thermal) methods. Therefore, their drawbacks and limitations are still a challenge to overcome and an inspiration for looking for new ways of neutralising the danger caused by ice accretion.

1.2 Review of the state of the art

1.2.1 Delaminating surface accretions with structural waves

Structural waves have been widely studied and successfully exploited in many areas of industry (aircraft, railway, space, etc.) throughout recent decades (see e.g. [4–6]). Notably advantageous applications have been developed in the non-destructive testing (NDT) field, including bond inspection, structural health monitoring (SHM), elastic constants determination, and many others. Although the most common approach is to use waves to gather information about the structure (elastic properties, flaws, defects), they have the potential to interact with the carrier actively by invoking delamination at ultrasonic frequencies. A potentially promising alternative to the traditional methods for tackling build-ups is a mechanical approach in which the accreted layer is removed with the aid of structural waves induced by piezoelectric actuators. An unwanted build-up is treated as a layer of a multi-layered waveguide. Propagating waves are associated with a frequency dependent stress distribution. Since the bonds created by accretions are usually weaker in shear then in tension, if a high enough shear stress is generated at the interface by a propagating wave the accreted material is debonded.

Although aircraft icing is the most common background for the research on the topic, a more general discussion on invoking delamination in stratified structures is of interest in this thesis. The literature on guided waves in layered structures is formidably extensive, however, there is a relatively small amount of references addressing particularly the problem of inducing debonding, of which almost all are motivated by aircraft icing.

Mechanics of ice accretion have been extensively studied since 1940s [7]. Two main types of icing have been distinguished – *glaze ice* and *rime ice*. *Glaze ice* creates a smooth, transparent and dense layer. It is formed by supercooled water droplets impinging the surface at high freezing temperatures (relatively close to 0°C) in clouds with high liquid water content. If not treated on time, glaze ice accretion forms characteristic 'horns' that significantly change the aerodynamic profile. It adheres more strongly to the substrate than the *rime ice* – opaque, porous and less dense accretion. It forms at low freezing temperatures (typically less than 10°C) in clouds with small droplets and low liquid water content. Given the variability of the environmental condition a mixture of the two aforementioned ice types can be observed. Typical mechanical properties of the two types of ice are gathered in Tab. 2.

Ice properties and particularly the shear strength of the bond it creates with various substrates are very difficult to quantify and many results reported in the literature are significantly different from each other. For instance, for aluminium substrates they vary from 0.026 to 1.42 MPa [7–10], whereas for steel substrates from 0.77 to 1.96 MPa [11, 12]. These refer only to a limited number of references but indicate large variability in the ice bond strength related to various environmental condition and chosen test procedure.

An idea of tackling the problem of ice accretion by means of ultrasonic waves was first proposed by Adachi et al. [13], who noticed that the ultrasonic vibration reduces the frost accumulation on a plate excited at a frequency of about 37 kHz (under frosting conditions). The possibility of using guided waves for de-icing has since been spotted and developed in Pennsylvania State University (PSU). Ramanathan has published a few papers, e.g. [14] summarised in his PhD thesis [15] which brings up the concept of applying shear horizontal waves as a way of provoking delamination in an iced aluminium plate. Although delamination has been observed during the experiments, the thermal processes seem to have played a crucial role in achieving this effect since the debonding was not immediate. Moreover, the wave model adopted in [15] was rather simple and not capable of representing wave propagation at considered frequencies accurately and providing reliable predictions.

Seppings [16] employed ultrasonic transverse vibration for removing ice and frozen sucrose build-up from pipes. With the aid of a finite element model and an experiment his analysis was focused on the intrinsic material effects associated with build-up cracking and determining the mechanisms responsible for the failure.

Palacios (PSU) implemented a multi-layered plate wave model for the preliminary design of the de-icing system and paid a particular attention to providing impedance matching

for excitation, which lead to very promising experimental results [2, 17–23]. Instantaneous delamination was observed for both freezer and impact ice, proving the feasibility of the method. Palacios' extensive experimental work provided some recommendations for actuator configuration and various conditions associated with ice shedding that can facilitate or impede the effect. The follow-up work by Overmeyer et al. [24]addresed important design issues such as the actuators' optimal bonding conditions and techniques to avoid actuator cracking. A successful experimental verification with a few actuators attached to a helicopter blade was also performed.

Zhu (PSU) [25] extended the theoretical wave analysis for the two-layered plate. Combining the results from finite element and wave models she drew a rather tentative conclusion that the transient state stress is the same as the steady-state vibration response. Furthermore, she introduced one of the possible ways of optimising structural design which has been named the 'tailored waveguide'. The idea is to make use of the local stress concentration points that occur near the discontinuities within the plate. An appropriate distribution of those points determined by the design of the structure (or one of its layers) enhances the capability of invoking delamination (ca. 40% less input power required for effective operation [25]). Zhu also performed an actuator survey indicating that the radial PZT-4 disc transducer used both in former and the discussed work does not seem to be an optimal choice for de-icing applications and proposed shear actuators. Finally, ultrasonic de-icing tests were performed on a composite coupon which confirmed the feasibility of the method for such materials and indicated that their integrity is not jeopardised.

A recent work by DiPlacido et al. [26] (PSU), supported by modelling and experiments, shows that the transient effects associated with piezoelectric actuation provide much higher stress than the steady-state response (contradictory to [25]). They also indicate that it is not possible to excite the system continuously at resonance, since the delamination and shedding is very rapid and alters the frequency response of the system during actuation. Despite that, the transient effects are claimed to be associated with higher interface stress than the one achieved in the steady state vibration and hence are concluded to be the main mechanism responsible for ice shedding.

Ultrasonic vibration of a plate with frozen water droplets has been recently analysed by Li and Chen [27]. They shown that the droplets can be successfully removed if 60 watts are supplied to an ultrasonic transducer.

The results briefly recalled above are very interesting and promising, however there are still some aspects to be developed and investigated. First of all, although aircraft icing is a primary motivation, it is informative to generalise the discussion on invoking delamination to include a wider range of configurations and backgrounds. Most of

the references recalled above are supported with finite element modelling which, unless certain conditions are met, is not the most reliable tool for stress prediction (and these conditions seem often not to have been met). Therefore, resulting stress predictions might be biased. Moreover, the implemented FE models are usually representing steady-state ultrasonic vibration strongly dependent on factors of secondary interest such as dimensions of the plate and boundary conditions. Although the aforementioned authors refer to wave models of various origin and complexity and point out waves as fundamental effects responsible for high interface shear stress, they leave a gap between the theory of waves and FE models used to validate the experimental campaigns. Therefore, the nature of the interaction of structural waves with unwanted accretions is still not clear and the influence of the boundary conditions cannot be separated from the results achieved. It is believed that an entirely wave-based approach can attempt to provide more understanding of the conditions promoting delamination associated with propagating waves and insight into power requirements that make this action effective.

At the beginning of the work reported in this thesis, the author conducted preliminary experiments on invoking delamination using ultrasonic actuation. The experimental setup was very similar to the one used in [2], however building plaster was used to emulate brittle, ice-like build-ups. The plaster patches were successfully debonded, which demonstrated the potential of the approach. Some issues related to driving a complex load with high power and with actuator cracks were also encountered and shortly discussed. The measurement, results and following observations supported parts of the thesis (especially Chapter 6 and Chapter 7) and therefore are attached in Appendix A.

1.2.2 Modelling structural wave propagation

The physics of wave propagation has been widely studied and is nowadays very well understood. Waves are often defined as phenomena that propagate energy or pressure without the net transport of the medium [28]. Their complex character is usually simplified and studied at single frequencies separately assuming a linear behaviour of the medium. An unbounded isotropic solid allows only the fundamental wave types to travel as a solution of the Navier's displacement equation [29–31]. In the presence of the boundaries fundamental waves are reflected and undergo wave conversion when incident on boundaries following certain physical laws such as the Snell's Law [28, 30]. A new wave pattern emerges and the energy propagation seems to be 'guided' by the boundaries in a certain direction(s) – this is the origin of the term *guided waves* originates from. The pioneering works on guided waves include the famous paper by Rayleigh on the propagation of waves along a surface of a semi-infinite solid [32] and the mathematical

description of waves in an infinite plate immersed in a vacuum by Lamb [33] from whom the widely used term *Lamb* or *Rayleigh-Lamb* waves comes from.

Vibration of structures is effectively a superposition of waves reflecting between its boundaries. In the event that the reflected waves share the phase with the incident waves, so-called *standing waves* (vibrational modes) are formed. Wave attenuation limits the response and the amplitudes of subsequent standing waves. Vibration is a very powerful way of looking at structures that enables analysing various practically useful effects accompanying standing waves (such as natural frequencies, mode shapes, acoustic radiation, etc.) without a need for tedious wave analysis. However, certain problems (e.g. non-destructive evaluation, scattering of waves at joint of multi-component waveguides) require a deeper insight in the fundamental physics of wave propagation in order to understand intrinsic effects of the wave motion or draw practical conclusions from a relatively simple model as opposed to large models of complex vibratory systems.

As it has been mentioned in the previous section, publications on invoking delamination with piezoelectric actuators discuss mainly high frequency vibration with some theoretical reference to waves. It is expected that a deepened wave analysis can bring better understanding of the feasibility of the concept and provide insight into physical phenomena that promote generating high interface stress as an effect of a propagating wave. Furthermore, the observations drawn will also be valid for a bounded vibrating structure (since its response is a composition of standing waves).

A fundamental introduction to wave propagation concepts *per se* is not given in this thesis as it can be found in numerous textbooks, e.g. [28–31, 34]. However, a brief review of the most common modelling methods is presented below. The implemented methodologies are described in more detail in due course for the sake of consistency and reference.

The analysis of waveguides with an unwanted build-up with a particular interest in the interface shear stress at high frequencies introduces certain requirements for the method to be used. Firstly, the method needs to facilitate multi-layered waveguide modelling and enable extracting a reasonably precise through-thickness stress distribution. Secondly, it is expected to be valid in the high-frequency regime.

1.2.2.1 Analytical methods based on approximate theories

Simple structures like beams or rods can be analysed with the aid of the approximate theories such as Euler-Bernoulli, Timoshenko, Love, Mindlin-Hermann or others [35, 36]. The resulting partial differential equations are written under the time and space harmonic assumption yielding solutions that can be obtained analytically. The propagation

phenomenon and free wave solutions are often further exploited to calculate wave reflection and transmission at boundaries and discontinuities [36–38], analyse dynamics of finite waveguides (via the phase closure principle) or solve relatively simple forced wave problems via a generalised wave approach [39]. An alternative way to use various analytical structural theories for vibration analysis is known as the frequency domain spectral element method [40, 41]. The structure is subdivided into substructures that can be represented by an analytical structural theory and then coupled together in a manner similar to the finite element formulation (yet not involving any of the FE approximation). It has found numerous applications and implementations thanks to its relatively straightforward implementation and versatility. The name given by the authors can be confused since spectral methods have been known in the literature before [42] and they represent a completely different methodological approach but no other name was reported. The limitations of the analytical methods lie in the limited frequency range within which the solution is valid and the fact that they can be directly applied only to simple waveguides (i.e. single-layer beams). The analytical formulation for waveguides with a finite number of Euler-Bernoulli or Timoshenko beam layers can also be found in the literature [43–45] but these are expected not to fulfil the requirements outlined above since the beam theories make assumptions regarding the stress distribution.

1.2.2.2 Analytical methods based on bulk waves in solids

Originating from the fact that guided waves are composed of fundamental bulk wave types that undergo a particular reflection/mode conversion pattern at the boundaries, the partial waves approach has been proposed. It has been very well described in [46] but has been used prior to that publication in various works on wave propagation in stratified media. Two main approaches for the assembly of system equations based on partial waves are known in the literature – transfer matrix method (TMM) as proposed by [47, 48] and global matrix method (GMM) described by Lowe in [49, 50] but used long before. The two conditions outlined in the previous section are met for these methods as they provide an accurate through-thickness wave field distribution an can be used at high frequencies. However, GMM has some advantages over TMM related to the stability of the solution at low wavelength limit and therefore GMM has been implemented for the purpose of the thesis. Note that although these methods have an analytical origin, they can only be solved numerically. This is not a trivial tasks since it requires relatively complicated root tracing routines that are sensitive to initial guess and prone to fail for complex structures if the frequency step is not very small. GMM can be used only for plane wave calculations, i.e. two-dimensional plain strain formulation.

1.2.2.3 Semi-analytical methods

Semi-analytical methods couple finite element approximation with some analytical technique that facilitates calculation of the wave characteristics of the structure. Two main methods are recalled here: wave and finite element (WFE) method and semi-analytical finite element (SAFE) method.

The key idea of the WFE [51, 52] is to consider an infinite waveguide as a periodic structure composed of identical cells. The cell (short section of the waveguide) is modelled using a conventional FE and periodicity conditions are imposed on the extracted dynamic stiffness matrices of the cell. Applications of WFE and usage examples including the response to general excitation and wave reflection/transmission can be found in [39, 53–55]. Since the section is discretised in the propagation direction, some numerical problems can arise and need to be accounted for properly as discussed in [56].

The SAFE method is known in the literature under different names, depending on the area or application for which the method was established. The base concept common to all of them is to use finite element approximation to the wave field over the cross section allowing an additional degree of freedom (DOF) in the direction of propagation. The equations of motion are derived using variational principles and solved using the spatial Fourier transform (SFT) or, equivalently, assuming a space-harmonic variation of the displacement in the propagation direction. The framework dates back at least to the 1970s [57, 58] and was further developed and expanded in recent years by many researchers. In vibroacoustics it is known as the waveguide finite element method [59–63], in ultrasonics the name SAFE is used [64–68], and finally in railway vibration field it is called the wavenumber finite element method [69, 70] following from [71, 72]. The wave solutions in uniform waveguides of indefinite length formed a basis for the development of computational methods for finite and build-up structures, such as the spectral finite element method [73–75]. In this work the name semi-analytical finite element method is preferred as its use is least ambiguous. In this thesis the understanding of the scope of this method is extended to include wave scattering and reflection calculation and the assembly of multicomponent waveguides, making it analogous to WFE but with a different approach to obtaining dispersion curves and wave mode shapes.

1.2.2.4 Numerical methods

Wave propagation can be analysed using conventional finite element method if the mesh is sufficiently fine. Details on the performance of different strategies can be found in [76]. The main limitations of FE analysis are the large computational load as a result

of fine mesh and the need for absorbing boundaries to enable wave calculation, which can be a cumbersome task [76, 77]

The alternative approach is to use time-domain spectral element method, sometimes called spectral finite element method (SFEM) as presented in [78]. SFEM originates from spectral methods used for solving partial differential equations numerically assuming the solution to be of the form of a Fourier series or polynomials of a high order (Chebyshev, Lobatto) over non-uniformly spaced nodes. The spectral approach combined with the FE paradigm of system assembly and element-wise formulation was first proposed for fluid dynamics in [42] and over the following years has been successfully applied to structural wave propagation problems. Details of the methodology and exemplary applications can be found in [78].

1.2.3 Piezoelectric excitation in structural waveguides

Over the past decades many excitation strategies for structural waves have been developed originating from various phenomena [6]. One of the approaches is to use conventional ultrasonic probes – wedge, comb or Herzian contact – which require a silicon/-grease coupling or air-coupled electromagnetic acoustic transducers (EMATs). They can be precisely tuned to match the desired excited wavelength but due to the couplant they are not able to excite waves very efficiently. One of the alternatives is laser-based ultrasonics which provides a non-contact method for activating structural waves especially at uneven or rough surfaces. However, the obvious drawbacks such as high cost and bulkiness of the equipment limit its possible applications to research laboratory environments.

The other group consists of active elements that can be permanently attached or embedded in the structure where the piezoelectric effect is employed to convert the electrical driving signal into mechanical deformation. Their main advantages over the aforementioned techniques are low cost, non-intrusive character (small size) and relatively simple operational principle. The electromechanical coupling in the piezoelectric material enables an active interaction with the structure providing the means of excitation and sensing its dynamic response. There are many types and configurations of piezoelectric materials available on the market (e.g. Macro Fibre Composites,polymer based interdigital transducers), but in this thesis only monolithic ceramic elements are discussed.

A piezoelectric monolithic actuator is essentially a single layer of piezoelectric ceramic coated with silvered electrodes on two surfaces normal to the poling direction. The most popular group of piezoelectric ceramics consists of solutions of Lead Zirconate and Lead Titanate with some additives and is widely known as PZT materials [79]. From the

elasticity point of view PZT ceramics are transversely isotropic and the electromechanical coupling originates from the piezoelectric property. The direct piezoelectric effect is responsible for generating an electric charge upon a mechanical stress applied (sensing). The inverse piezoelectric effect enables exciting a structure, i.e. the piezoelement deforms when voltage (or charge) is applied and induces strain in the medium to which it is bonded. The interaction between the piezoelement and a structure is mutual, i.e. the actuator deforms and induces strain in the substrate as a response to the driving voltage but at the same time generates charge since its motion is constrained.

1.2.3.1 Modelling approaches

The interface to piezoelements is electrical – they are activated by means of electric driving signal and their response to structural deformation is read as an electric output. Therefore, since one piezoelement can act both as an actuator and as a sensor measuring its electrical response enables obtaining useful information about structural dynamics of the substrate. This configuration is widely used in NDT as a tool for structural health monitoring and known as impedance (EMI) testing [80].

From an electrical static viewpoint a piezoelement behaves as a capacitor (two electrodes separated by a dielectric) with resistance corresponding to dielectric loss and leakage. The electromechanical coupling reflects vibrations of the actuator in the electrical response, therefore the mechanical properties of the actuator can also be represented using lumped electrical elements [81] in a so-called electrical equivalent circuit (Fig. 1.1). Far below its first resonance, the mechanical equivalent components can be neglected and the

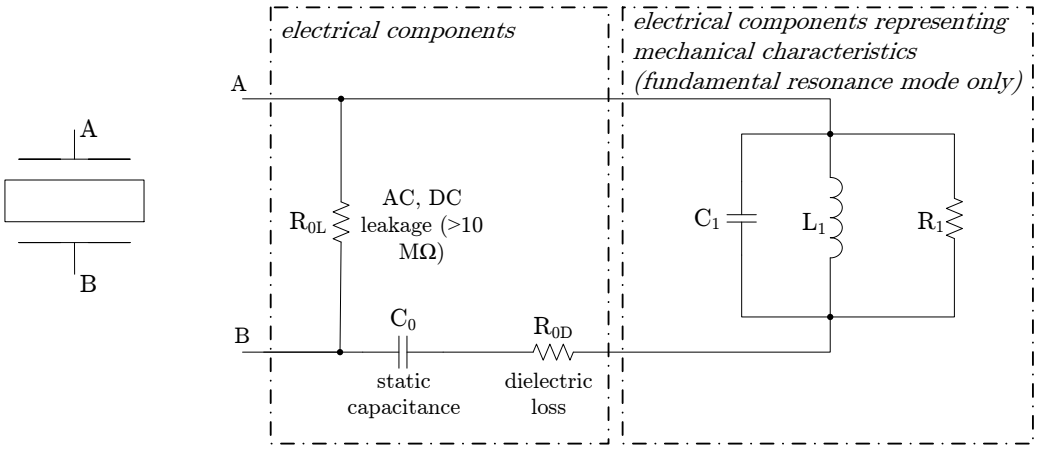

Figure 1.1: PZT transducer equivalent electrical ciruit.

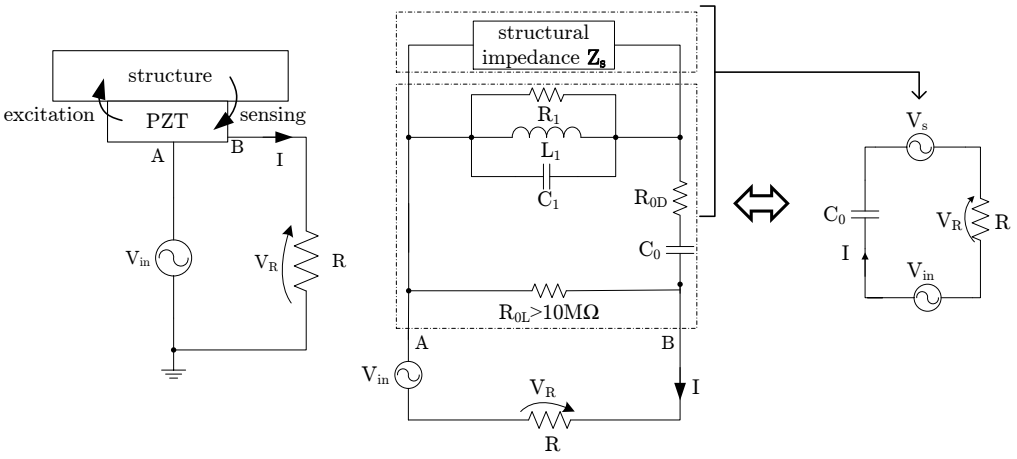

Figure 1.2: Principle of impedance monitoring and loaded PZT transducer equivalent circuit.

impedance of a PZT element is approximated as an electrical impedance of a capacitor ($Z_{\text{PZT}} \approx \frac{1}{\jmath\omega C_0}$).

When attached to a structure, a piezoelectric element's behaviour is changed since it is constrained by a structural stiffness. In this case, applying voltage to the transducer invokes both inverse and direct piezoelectric effects [82]. Firstly, the element deforms and induces strain in the host structure (inverse effect), which is represented by an impedance Z_s loading the transducer in the equivalent circuit (Fig. 1.2). However, as its motion is constrained it generates a 'back-charge' (direct effect), forming a voltage source V_s whose voltage is a function of mechanical mass, stiffness and damping (see Fig. 1.2). This sensing action of a piezoelement 'inserts' information about the host structure's dynamics that forms the basis of the powerfulness of the impedance monitoring technique.

1.2.3.2 Modelling piezoelectric excitation in waveguides

The ability to describe the interaction between the piezo patch and the host structure accurately is an essential aspect of both the design and operational stages of piezo equipped dynamic systems. Over the past decades this problem has been widely studied bringing a considerable number of modelling approaches. A review of these can be found in a recent paper by Huang *et al.* [83]. Among research published to date, two general approaches to the described problem can be distinguished [84]. The first group considers the dynamics of the structure and piezo actuation separately assuming that they are fully decoupled - a set of equivalent forces is applied to the substrate model by means of some coupling strategy. The second group of models accounts for the dynamic

interaction between the actuator and the structure and is based on the solution to some kind of boundary problem.

One of the earliest attempts to provide a mathematical description of the piezoelectric excitation was the shear-lag Euler-Bernoulli beam model presented by Crawley and de Luis [85]. The main contribution of this work was the formulation of the quasi-static assumption stating that the actuator behaves quasi-statically provided that it operates at frequencies far below its own resonances and is thin and light compared to the host structure. This also implies that the dynamics of the actuator are neglected and that for thin bonding layers the shear load transfer is confined at the ends of the actuator (pin-force assumption). The bonding layer is accounted for in [85] via a *shear lag parameter* describing the effectiveness of the shear load transfer. The *shear lag parameter* depends on the thickness and stiffness of the bonding layer and was developed under the assumption of uniform strain.

The pin-force and quasi-static assumptions have been widely used by researchers since then. The model of Crawley and de Luis has been further developed in [86] by allowing linear strain both in the structure and the actuator and considering the contribution of the flexural stiffness of the actuator, and further in [87] where Timoshenko beam theory was incorporated. An analogous methodology was also applied to plates and shells [88–90]. These purely analytical approaches were limited in application to a single beam/-plate system with little flexibility. Therefore, some researchers employed the frequency-domain spectral element method (SEM) to model coupled flexural-longitudinal-shear vibrations of homogeneous [45] or composite [44, 45, 91, 92] beams based on Timoshenko and Mindlin-Hermann theories. Although using the same approximate analytical theories SEM provides versatility in structure configuration and ability to couple together elements of different types. Moreover, although the model allowed only a uni-axial deformation of the piezoelectric and employed the pin-force assumption, the mechanical dynamic contribution of the piezo layer was incorporated and its effect was present in piezoelectric equivalent forces.

Piezo elements have become a standard for high-frequency wave-based NDT [93]. The high frequency regime is associated with more complex through-thickness field variation therefore the limitations of approximate theories enabling only linear distribution of strain needed to be overcome. Thick elastic plates with thick piezo actuators in a sandwich configuration have been studied by Yang [94]. Lin and Yuan [95] investigated Lamb wave excitation with piezo elements both theoretically and experimentally. They provided a model based on Mindlin plate theory and classical lamination theory for the A_0 Lamb mode, which was validated with an experiment. Moulin et al. [77] proposed

a hybrid technique employing finite element analysis to obtain the excited wave amplitudes and normal modes expansion to account for the propagation. Giurgiutiu [96] solved the problem of Lamb wave excitation with a single PZT wafer as a boundary problem, presenting a methodology incorporating full Lamb wave equations solved for external piezo-induced traction excitation. He assessed the performance of the Euler-Bernoulli beam based shear lag parameter for Lamb wave-like displacement fields. The problem of the bonding layer has been further developed in [97–99] leading to the exact shear lag solution for any number of wave modes derived from normal mode expansion. Raghavan and Cesnik [100] presented an interesting work in which the Lamb wave displacement fields excited by rectangular and disk piezo actuators bonded to plates were obtained. The model was derived by an integral transform solution to the full 3-D elasticity equations with the external forcing approximated using a pin-force assumption.

From the aforementioned references it is clear that researchers treated the bonding conditions as the essential factor for understanding and representing accurately the energy transfer between the actuator and the substrate. However, most of the above models do not take into account the dynamics of the piezo layer and the mutual interaction between the patch and the structure. Some studies attempting to account for these issues have been presented in [101–103]. In these papers the authors study wave propagation induced by piezoelectric elements attached to an elastic half-spaces highlighting the dependencies on the geometry, material configuration and phase distribution. An integral equation based methodology for modelling piezo-structure interaction that accounts for the dynamic contribution of the piezo actuator and can be applied both to a plate and an elastic half-space has been published by Glushkov *et al.*[104]. With the aid of the Fourier transform they solve the Navier displacement equation and a uniaxial piezo-patch equation as a coupled boundary-value problem.

Apart from analytical solutions, many researchers investigated piezo-excited waves using conventional FE. Being versatile and easily applicable to complex structures, this technique has important drawbacks in high frequency applications such as a very large computational cost and a limited insight into wave propagation phenomenon. However, in other numerical methods, some of these can be circumvented, e.g. by using the spectral finite element method as proposed in [78, 105, 106] where the number of degrees of freedom required is largely reduced. Recent advances in computational engineering resulted in an interesting work by Paćko et al.[107] where a hybrid Local Interaction Simulation Approach (LISA)-FE method has been implemented using parallel computing and graphical card processing offering significant time savings when compared to FE.

The wide range of models briefly discussed above serves many purposes well in NDE/SHM (structural health monitoring) applications, but has certain limitations both from the viewpoint of assumptions made and the model development. Since the actuators quite often work at quasi-static frequencies (with reference to their dynamics) the interaction with the structure is modelled as quasi-static. The bonding conditions that seem to largely affect transferred traction are often accounted for by means of an additional parameter which also has limited validity. Since large strains are expected to be required for invoking delamination, a suitable modelling method is thought to be able to include the dynamics of the actuator (so far available only in FE) and at the same time take advantage of a wave based formulation. Removing the pin-force and quasi-static assumptions is needed for analyses of structures with thick actuators, or structures operating near resonance frequencies of the piezo elements in power ultrasonics applications. Finally, it is desirable to create a methodology that enables modelling of wave propagation in multi-component waveguides without the need to employ full FE.

1.3 Aims of the thesis

The review of the state of the art given above led to the following research tasks which are identified as the aims of this thesis:

1. To understand the conditions that promote high interface shear stress in a waveguide with an undesired accretion.
2. To build a wave-based model that is able to predict the interface stress as response to a piezoelectric actuation without the need of employing conventional FE.
3. Obtain realistic, quantitative power requirements for structural waves-based invoking delamination system for different types of accretion and support them with the experiment.

1.4 Contributions of the thesis

The results of the investigation presented in this thesis form the following contributions:

1. Structures with an undesired accretion have been described in general sense as elastic bilayers. Wave motion features including stress distribution, energy propagation, attenuation, excitability and power partitioning have been discussed leading to optimal mode selection criteria.

2. The influence of mechanical properties of the accreted layer on the wave induced stress have been investigated in the light of the above.

3. A new methodology for modelling piezoelectric excitation in waveguides originating from the coupling between the semi-analytical finite element method and analytical wave approach has been proposed. The semi-analytical formulation for a piezoelectric element has been developed and the solution to a distributed voltage excitation problem has been presented.

4. The new coupled-field wave model has been successfully validated on a beam-like waveguide with emulated anechoic terminations.

5. Power transfer between the actuator and the structural waves has been modelled including the bonding layer effect. The influence of the actuator's dimensions and the bonding layer's thickness on the power transfer efficiency has been discussed

6. Piezo-actuated structural waves' capability of invoking delamination has been assessed using the developed methodology. Electrical power requirements for removal of unwanted build-ups have been specified for various build-up properties.

7. Piezo-actuated structural waves' effectiveness for removing surface accretions has been demonstrated experimentally. The model plaster patches have been successfully debonded from the beam-like waveguide with anechoic terminations. Corresponding numerical analysis was conducted and a good agreement with the recorded power requirements was observed.

1.5 Outline of the thesis

The thesis is organised into eight chapters. The order of the chapters follows the complexity of the modelling tools and a direct correspondence to a practical case. The numerical tools developed or employed during the investigation were implemented in Python with NumPy, SciPy, IPython and matplotlib packages (among others). Some computations benefited from the time savings offered by the IRIDIS High Performance Computing Facility at the University of Southampton. Finite element models were build and run in ABAQUS.

The current introductory chapter opens the thesis, providing the motivation and the state of the art for the topic of interest. The qualitative study on the aspects of wave propagation relevant to removing surface accretions is presented in Chapter 2. In this chapter an analytical model for an infinite multilayered plate is adopted from the literature. Waveguides with unwanted build-ups are treated as elastic bilayers. Associated

dispersion curves and the nature of wave mode shapes is discussed. As many of the real world accretions are expected to be lossy, the issue of wave attenuation is addressed using an approximate model based on the modal energy distribution. Based on the analysis, optimal wave mode selection criteria are specified. The influence of the properties of the accretion on the generated interface shear stress with the fundamental waves is analysed is the concluding parametric study.

In Chapter 3 the modelling approach is extended to include the forced response calculation. It is investigated how the injected mechanical power is partitioned between the propagating modes. Using this formulation, a simple pin-force model is implemented to approximate the piezoelectric excitation. The effect of the excitation on the generated interface shear stress is illustrated in the parametric study for different types of accretions. Limitations of the approach are discussed.

In Chapter 4 the semi-analytical finite element (SAFE) method is introduced. It is expected that this methodology will enable overcoming the constraints of the fully analytical models and bring the simulations closer to a practically implementable cases. The mechanical SAFE model is validated in an experiment on a beam-like waveguide with anechoic terminations. The wave selection criteria from Chapter 2 are verified.

In order to implement the piezoelectric actuation in the wave domain but without the need for assumptions on the dynamic character of the interaction, a new piezoelectric SAFE element is derived in Chapter 5. The mathematical background is presented together with the methodology for calculating the response to a distributed voltage excitation. The piezoelectric SAFE element is coupled with the elastic SAFE elements using wave scattering/reflection relationships to represent a waveguide with a finite piezoelectric actuator attached. The model is validated in an experiment for both the mechanical response and the electromechanical impedance of the actuator-structure system.

The newly presented methodology is employed to analyse the power conversion in piezoelectrically excited waveguides in Chapter 6. The issues related to driving a complex load and the impedance mismatch are discussed. The influence of the dimensions of the actuator and the properties of the bonding layer on the effectiveness of power transfer is investigated in a parametric study.

Finally, in Chapter 7 the proposed approach is applied to interface shear stress prediction in waveguides covered with accretions. The stress recovery routine is validated with commercial FE simulations. Transfer functions for interface stress as a response to driving voltage are presented together with the decomposition of the total stress into particular waves' contributions. The power transfer aspects addressed in Chapter 6 are employed to obtain realistic power requirements for surface accretion removal for

both ice and accretions with properties falling into wide range of stiffensses considered. The benefit of residual reflections which are expected to occur in real world cases is briefly discussed. Finally, the concept of removing accretions with structural waves is demonstrated in an experiment. The piezo-actuated wave successfully removed plaster patches representing the build-up. Corresponding numerical simulations and the analysis of the observations are also presented showing that the model predictions represent well the observed electrical power requirements.

A set of final conclusions and recommendations for future work are presented in Chapter 8.

Chapter 2

Qualitative study on invoking delamination with structural waves

In the first chapter invoking delamination with structural waves is looked at from a theoretical perspective. The fundamental insight into effects associated with wave motion can be gained using free wave analysis. Although it is sometimes difficult to be related to real cases directly, it provides useful qualitative information. The analysis is performed with the aid of a plane strain multilayered plate model based on the global matrix method (GMM). The accretion that covers waveguides is usually of much lower stiffness. A two-layered plate with layers of very different properties is commonly referred to as an elastic bilayer. Particular characteristics of elastic bilayers, typical for weakly coupled systems, are analysed first. The influence of the coupling between the layers on wave propagation is discussed aiming at understanding the physical phenomena that promote high interface shear stress. Since real accretions are often lossy, the importance of energy propagation patterns is highlighted with reference to an approximate method for calculating guided wave attenuation in plates with viscoelastic coating. Based on the insight gained, a few observations on the interface shear stress associated with propagating waves are given. The chapter is concluded with a parametric study that addresses the aforementioned issues for build-ups of different stiffnesses and thicknesses yielding approximate mechanical power requirements and practical implications for the method.

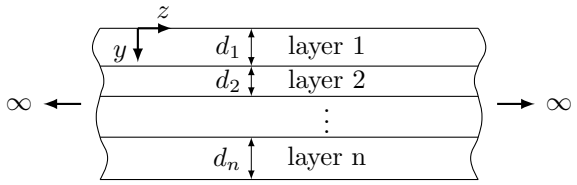

Figure 2.1: Multi-layered plate - geometry and labelling system.

2.1 Modelling free wave propagation in structures with an undesired accretion

The global matrix method (GMM) together with partial wave technique provide an analytical description of wave propagation in a generally multi-layered one-dimensional waveguide. It provides an exact distribution through the thickness of the waveguide, however is limited to plain-strain problems with simple geometries (infinite plates, cylinders). The implementation used for this thesis is based on [50, 108]. A short summary of this approach is presented below for reference purposes. More details on partial waves and the global matrix method can be found in [30, 46, 109] and [49, 50, 108], respectively.

The geometry of a multilayered plate together with the labelling system is shown in Fig. 2.1. Only plane waves are considered i.e. waves whose wavefront is an infinite plane perpendicular to the direction of propagation z. The external boundary conditions can be arbitrary, however it is assumed here that the plate is immersed in a vacuum which implies that the external surfaces are traction-free:

$$\sigma_{yz}(0) = \sigma_{xy}(0) = \sigma_{yy}(0) = \sigma_{yz}\left(\sum d_n\right) = \sigma_{xy}\left(\sum d_n\right) = \sigma_{yy}\left(\sum d_n\right) = 0 \qquad (2.1)$$

At the interfaces between the layers the displacements and tractions are continuous. The traction is understood as a force between the two layers that acts across the interface divided by the area of the interface.

2.1.1 Partial waves in a layer

The motion of each layer is expressed in terms of partial waves (see Fig.2.2), which are understood as waves that travel along a waveguide reflecting back and forth between the boundaries (to which they are often oblique) [46]. There are six partial waves propagating in each layer and for isotropic materials they are pure fundamental bulk wave types (longitudinal, shear vertical and shear horizontal). Because of the coupling at the interfaces and boundaries, at angular frequency ω, the partial waves share the

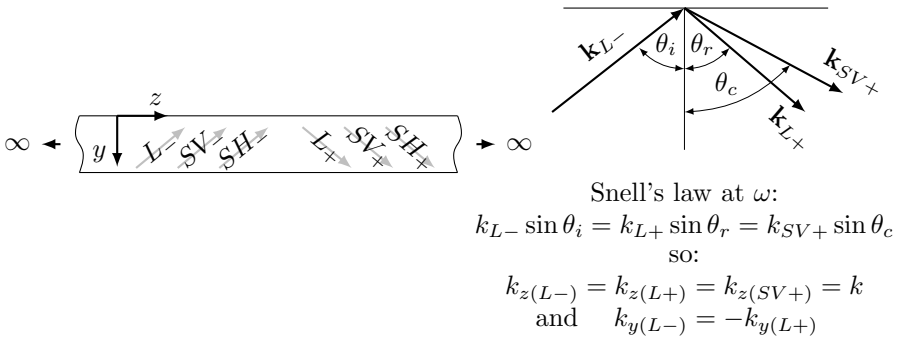

Figure 2.2: Partial waves in a layer.

same wavenumber component in the direction of propagation, according to Snell's law [30]. The transverse (y-direction) wavenumber component k_y is different for each wave type. The displacement field within an isotropic layer satisfies the Navier's equations of motion:

$$(\lambda+\mu)u_{k,ik}+\mu u_{i,jj}=\rho\ddot{u}_i \qquad (i,j,k=x,y,z) \tag{2.2}$$

where λ, μ are the Lame constants, the summation is performed over repeated subscripts, the dot stands for time-derivative and subscripts after the comma represent space derivatives, e.g.:

$$(\lambda+\mu)\frac{\partial}{\partial x}\left(\frac{\partial u}{\partial x}+\frac{\partial u}{\partial y}+\frac{\partial u}{\partial z}\right)+\mu u_x\left(\frac{\partial^2}{\partial x^2}+\frac{\partial^2}{\partial y^2}+\frac{\partial^2}{\partial z^2}\right)=\rho\ddot{u}_x \tag{2.3}$$

In case of an anisotropic layer pure wave types do not exist except the cases when the propagation direction matches crystal symmetry axes. The dynamics of each layer are then governed by a more general Christoffel equation [30, 46]. In this thesis anisotropic materials are not considered, thus the Christoffel equation is not discussed in detail.

Eq. (2.2) can only be solved using a trial solution. Here, since the layers are assumed to be isotropic a convenient Helmholtz method of potentials can be used [50] following which the longitudinal partial waves are described using a scalar function L and shear partial waves using vector potentials $\mathbf{S}_V$, $\mathbf{S}_H$ for shear vertical and shear horizontal partial waves, respectively [50]:

$$\begin{aligned} L &= A_L \exp\left[\jmath(\mathbf{k}\cdot\mathbf{z}-\omega t)\right] \\ |\mathbf{S}_V| &= A_{SV} \exp\left[\jmath(\mathbf{k}\cdot\mathbf{z}-\omega t)\right] \\ |\mathbf{S}_H| &= A_{SH} \exp\left[\jmath(\mathbf{k}\cdot\mathbf{z}-\omega t)\right] \end{aligned} \tag{2.4}$$

where vector $\mathbf{z}=[x \quad y \quad z]^\top$.

The physical displacement resulting from the longitudinal and shear partial waves can be calculated from the potentials as:

$$\begin{aligned}\mathbf{u}_L =& \nabla L = \left\{0 \quad k_{y(L)} \quad k_z\right\} A_L \exp\left[\jmath(\mathbf{k}\cdot\mathbf{z} - \omega t)\right] \\ \mathbf{u}_{SV} =& \nabla \times \mathbf{S}_V = \left\{0 \quad -k_z \quad k_{y(SV)}\right\} A_{SV} \exp\left[\jmath(\mathbf{k}\cdot\mathbf{z} - \omega t)\right] \\ \mathbf{u}_{SH} =& \nabla \times \mathbf{S}_H = \left\{-k_{y(SH)} \quad 0 \quad 0\right\} A_{SH} \exp\left[\jmath(\mathbf{k}\cdot\mathbf{z} - \omega t)\right]\end{aligned} \tag{2.5}$$

where the arbitrary (and unknown) amplitudes are rescaled to account for multiplication by the imaginary unit $\jmath$ resulting from the differentiation. For the sake of consistency it is noted that the physical displacements are given by the real parts of the above equations.

Substituting displacements from Eq. (2.5) into Eq. (2.2) leads to bulk wave velocities:

$$c_L = \sqrt{\frac{\lambda + 2\mu}{\rho}} \qquad c_S = \sqrt{\frac{\mu}{\rho}} \tag{2.6}$$

As it has already been said all the partial waves share the same wavenumber component in the propagation direction, hence for simplicity k stands for the wavenumber component along the propagation direction or plate wavenumber, i.e. $k = k_z$. The transverse wavenumber k_y for each type of partial waves can be calculated as:

$$\begin{aligned} k_{y(L\pm)} &= \pm\sqrt{\omega^2/c_L^2 - k^2} \\ k_{y(S\pm)} = k_{y(SV\pm)} = k_{y(SH\pm)} &= \pm\sqrt{\omega^2/c_S^2 - k^2}\end{aligned} \tag{2.7}$$

Note that this is for positive-going waves. The positive transverse wavenumber implies that the partial wave is travelling 'downwards' (referring to Fig. 2.2), whereas negative k_y denotes a partial wave propagating 'upwards'. Depending on the ratio between the bulk wavenumber and the plate wavenumber partial waves are either propagating ($\omega^2 \big/ c_{L,S}^2 \geq k^2$) or evanescent ($\omega^2 \big/ c_{L,S}^2 < k^2$).

The total displacement or stress field is a linear combination of components associated with particular partial waves. Therefore, from the relationships derived above and Hooke's law defined as:

$$\sigma_{ij} = \lambda\delta_{ij}\Delta + 2\mu\epsilon_{ij} \qquad i, j = x,\, y,\, z \tag{2.8}$$

where:

$$\epsilon_{ij} = \frac{1}{2}\left(\frac{\partial u_i}{\partial j} + \frac{\partial u_j}{\partial i}\right) \qquad i, j = x,\, y,\, z \tag{2.9}$$

one can write a matrix relationship describing displacements and tractions within the layer. The remaining stress components can be calculated using the same procedure.

$$\begin{Bmatrix} u_x \\ u_y \\ u_z \\ \sigma_{yy} \\ \sigma_{yz} \\ \sigma_{yx} \end{Bmatrix}_{(i)} = \begin{bmatrix} 0 & 0 & 0 & 0 & D_{25} & D_{26} \\ D_{31} & D_{32} & D_{33} & D_{34} & 0 & 0 \\ D_{11} & D_{12} & D_{13} & D_{14} & 0 & 0 \\ D_{41} & D_{42} & D_{43} & D_{44} & 0 & 0 \\ D_{51} & D_{52} & D_{53} & D_{54} & 0 & 0 \\ 0 & 0 & 0 & 0 & D_{65} & D_{66} \end{bmatrix}_{(i)} \begin{Bmatrix} A_{(L+)} \\ A_{(L-)} \\ A_{(SV+)} \\ A_{(SV-)} \\ A_{(SH+)} \\ A_{(SH-)} \end{Bmatrix}_{(i)} \tag{2.10}$$

where:

$$\begin{aligned} D_{11} &= km_{(L+)} & D_{12} &= km_{(L-)} & D_{13} &= k_{y(S)}m_{(S+)} \\ D_{14} &= -k_{y(S)}m_{(S-)} & D_{25} &= k_{y(S)}m_{(S+)} & D_{26} &= k_{y(S)}m_{(S-)} \\ D_{31} &= k_{y(L)}m_{(L+)} & D_{32} &= -k_{y(L)}m_{(L-)} & D_{33} &= -km_{(S+)} \\ D_{34} &= -km_{(S-)} & D_{41} &= \jmath\rho Bm_{(L+)} & D_{42} &= \jmath\rho Bm_{(L-)} \\ D_{43} &= -2\jmath\mu k k_{y(S)}m_{(S+)} & D_{44} &= 2\jmath\mu k k_{y(S)}m_{(S-)} & D_{51} &= 2\jmath\mu k k_{y(L)}m_{(L+)} \\ D_{52} &= -2\jmath\mu k k_{y(L)}m_{(L-)} & D_{53} &= \jmath\rho Bm_{(S+)} & D_{54} &= \jmath\rho Bm_{(S-)} \\ D_{65} &= -\jmath\mu k^2_{y(S)}m_{(S+)} & D_{66} &= \jmath\mu k^2_{y(S)}m_{(S-)} & & \\ m_{(\pm L)} &= \exp\left[\pm\jmath k_{y(L)}y\right] & m_{(\pm S)} &= \exp\left[\pm\jmath k_{y(S)}y\right] & B &= (\omega^2 - 2k^2_{y(S)}k^2) \end{aligned} \tag{2.11}$$

Since matrix **D** contains exponential terms of the $\exp[\pm\jmath ky]$ form, it may be prone to ill-conditioning for very thin or very thick layers in particular.

2.1.2 Assembly of a multi-layered plate using the global matrix method

The global matrix assembly is briefly shown for the simplest two-layered case. We consider only isotropic layers here, hence partial waves are the fundamental bulk wave

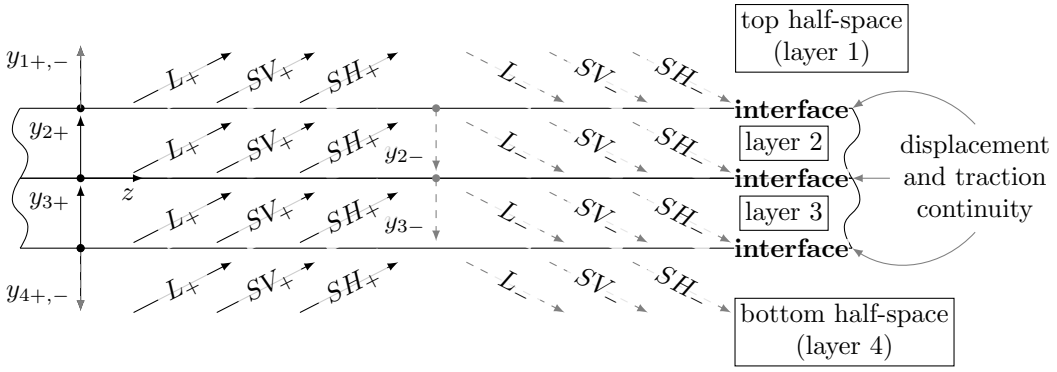

Figure 2.3: Multilayered plate assembly using the global matrix method.

types and Lamb and SH waves are decoupled. A detailed schematic view of the plate together with partial waves, boundary and continuity conditions and labelling system is depicted in Fig.2.3. All layers (including half-spaces) are numbered starting from the top. The main modification with respect to the partial wave scheme outlined above is that the y origin for each partial wave in every finite layer is set independently at its entry to the layer. This simplifies the field matrices assembly [50] and provides numerical stability. Alternatively, the layer matrices can be appropriately scaled to ensure numerical stability as done in [73]. For the half-spaces the y origin is defined to be at the outer surfaces of the plate in order to avoid placing it at $\pm\infty$ [50]. Following from this amendment, the i$^{\text{th}}$ layer field matrices can be written separately at its top and bottom as a product of the $\tilde{\mathbf{D}}$ matrix and the appropriate rotation matrix:

$$\begin{aligned}\mathbf{D}_{t,(i)} &= \tilde{\mathbf{D}}_{(i)} \circ \mathbf{R}_{t,(i)} \\ \mathbf{D}_{b,(i)} &= \tilde{\mathbf{D}}_{(i)} \circ \mathbf{R}_{b,(i)}\end{aligned} \tag{2.12}$$

where $\circ$ stands for element-wise multiplication, and:

$$\tilde{\mathbf{D}}_{(i)} = \begin{bmatrix} 0 & 0 & 0 & 0 & k_{y(S)} & k_{y(S)} \\ k_{y(L)} & -k_{y(L)} & -k & -k & 0 & 0 \\ k & k & k_{y(S)} & -k_{y(S)} & 0 & 0 \\ \jmath\rho B & \jmath\rho B & -2\jmath\mu k k_{y(S)} & 2\jmath\mu k k_{y(S)} & 0 & 0 \\ 2\jmath\mu k k_{y(L)} & -2\jmath\mu k k_{y(L)} & \jmath\rho B & \jmath\rho B & 0 & 0 \\ 0 & 0 & 0 & 0 & -\jmath\mu k_{y(S)}^2 & \jmath\mu k_{y(S)}^2 \end{bmatrix}_{(i)}$$

$$\mathbf{R}_{t,(i)} = \begin{bmatrix} 1 & 1 & 1 & 1 & 1 & g_{(S)} \\ 1 & g_{(L)} & 1 & g_{(S)} & 1 & 1 \\ 1 & g_{(L)} & 1 & g_{(S)} & 1 & 1 \\ 1 & g_{(L)} & 1 & g_{(S)} & 1 & 1 \\ 1 & g_{(L)} & & g_{(S)} & 1 & 1 \\ 1 & 1 & 1 & 1 & 1 & g_{(S)} \end{bmatrix}_{(i)}, \qquad \mathbf{R}_{b,(i)} = \begin{bmatrix} 1 & 1 & 1 & 1 & g_{(S)} & 1 \\ g_{(L)} & 1 & g_{(S)} & 1 & 1 & 1 \\ g_{(L)} & 1 & g_{(S)} & 1 & 1 & 1 \\ g_{(L)} & 1 & g_{(S)} & 1 & 1 & 1 \\ g_{(L)} & 1 & g_{(S)} & 1 & 1 & 1 \\ 1 & 1 & 1 & 1 & g_{(S)} & 1 \end{bmatrix}_{(i)}$$

$$g_{(L)} = \exp\left[\jmath k_{y(L)} d_i\right], \qquad g_{(S)} = \exp\left[\jmath k_{y(S)} d_i\right] \tag{2.13}$$

The continuity condition between the layers can be written in terms of the above matrices as:

$$\begin{bmatrix} \mathbf{D}_{b,(2)} & -\mathbf{D}_{t,(3)} \end{bmatrix} \begin{Bmatrix} \mathbf{a}_2 \\ \mathbf{a}_3 \end{Bmatrix} = \mathbf{0} \tag{2.14}$$

where $\mathbf{a}_2$, $\mathbf{a}_3$ are the vectors of partial wave amplitudes in layers 2 and 3, respectively. Following this pattern the global matrix representing the continuity conditions between

the layers of the multilayer can be assembled:

$$\begin{bmatrix} \mathbf{D}_{(1)b} & -\mathbf{D}_{(2)t} & & & & & \\ & \mathbf{D}_{(2)b} & -\mathbf{D}_{(3)t} & & & & \\ & & \mathbf{D}_{(3)b} & \ddots & & & \\ & & & \ddots & -\mathbf{D}_{(n-1)t} & & \\ & & & & \mathbf{D}_{(n-1)b} & -\mathbf{D}_{(n)t} \end{bmatrix} \begin{Bmatrix} \mathbf{a}_1 \\ \mathbf{a}_2 \\ \mathbf{a}_3 \\ \vdots \\ \mathbf{a}_n \end{Bmatrix} = \mathbf{0} \tag{2.15}$$

The partial waves incident on the multilayer from the half-spaces represent external excitation. However, this formulation is not very useful for practical application (it is not straightforward to link the exciting partial wave amplitudes to e.g. mechanical forces) and therefore in this thesis they are set to zero what restricts the functionality of the model to free wave analysis only. The half-space field matrices $\mathbf{D}_{(1)b}$, $\mathbf{D}_{(n)t}$ are appropriately trimmed accounting for the deletion of the waves incoming from the half-spaces. After all above manipulations the multilayered system equation takes the following form:

$$\mathbf{G}\mathbf{a} = \mathbf{0} \tag{2.16}$$

where $\mathbf{G}$ is the final assembled global matrix and $\mathbf{a}$ is the vector of partial waves amplitudes.

2.1.3 Free wave solution

Free waves can be found by solving the non-trivial solution condition, i.e. $|\mathbf{G}| = 0$, which can be done only numerically. The solution algorithm used in the implementation in this thesis is based on those presented in [50, 108]. Since $\mathbf{G}$ depends both on wavenumber and angular frequency, the solver fixes one of the variables and looks for roots of the resultant characteristic functions. In this work the wavenumber is fixed as this facilitates tracing the solution curves with changing direction of energy transport. The details of the routine can be found in the literature.

Having found the dispersion curves one can extract from the global system equation the through-thickness distribution of the wave fields often called the wave mode shape or the wave structure for a given frequency-wavenumber pair. In order to do this, the amplitude of one of the partial waves is arbitrarily set to 1 (in this work it is the positive longitudinal wave in the first finite layer) and the corresponding column of the global system matrix $\mathbf{G}$ is shifted to the right hand side. The resulting overdetermined set of simultaneous equations is solved using singular value decomposition (SVD) of the

trimmed matrix $\tilde{\mathbf{G}}$, defined as:

$$\text{SVD}\left(\tilde{\mathbf{G}}\right) = \mathbf{USV}^{*} \tag{2.17}$$

from which the unknown wave amplitudes vector is obtained:

$$\tilde{\mathbf{a}} = \mathbf{V}^{\top}\mathbf{S}^{-1}\mathbf{U}^{\top *}(-\mathbf{G}_{1,L+}) \tag{2.18}$$

where $\tilde{\mathbf{a}}$ is the eigenvector corresponding to the trimmed global matrix $\tilde{\mathbf{G}}$ and $\mathbf{G}_{1,L+}$ is the column of the global matrix corresponding to the positive longitudinal partial wave in the first finite layer.

The final eigenvector $\mathbf{a}$ is reconstructed from $\tilde{\mathbf{a}}$ by appropriately inserting the fixed amplitude. Wave field (displacements, strains, stresses) at the chosen frequency and wavenumber is obtained via multiplication of the field matrix from Eq. (2.10) by $\mathbf{a}$.

$$\begin{bmatrix}\mathbf{u}\\ \boldsymbol{\sigma}\end{bmatrix} = \mathbf{D}_{(i)}\mathbf{a} \tag{2.19}$$

where the appropriate columns of $\mathbf{D}_{(i)}$ need to be modified to account for the phase shift resulting from translation of the origin of the upward travelling waves in the global matrix method.

It is also advantageous to compute the energy and power mode shapes which provide an interesting insight into the physics of wave propagation. Energy and power are cyclic quantities so their time-averages are of most interest. They are calculated as follows:

- strain energy density - represents stored (potential) energy per unit volume and is given by a product of stress and strain components:

$$e_u = \frac{1}{4}\left(\sigma_{xx}\epsilon_{xx} + \sigma_{yy}\epsilon_{yy} + \sigma_{zz}\epsilon_{zz} + \sigma_{yz}\epsilon_{yz} + \sigma_{xz}\epsilon_{xz} + \sigma_{xy}\epsilon_{xy}\right) \tag{2.20}$$

- kinetic energy density - represents energy possessed due to wave motion per unit volume and is given by a quarter of the sum of mass-velocity squared products. Velocity is obtained from displacement after multiplication by $\jmath\omega$:

$$e_k = \frac{\rho}{4}\left[\left(\frac{\partial u_x}{\partial t}\right)^2 + \left(\frac{\partial u_y}{\partial t}\right)^2 + \left(\frac{\partial u_z}{\partial t}\right)^2\right] \tag{2.21}$$

- power flow density - given by the complex acoustic Poynting vector $\mathbf{P}$ [109] represents the rate at which the waves propagates energy along a particular direction. The acoustic Poynting vector is defined as the product of the complex conjugate

of particle velocity and the stress tensor:

$$\mathbf{P} = \mathrm{Re}\left\{\frac{-\mathbf{v}^*\boldsymbol{\sigma}}{2}\right\} = \mathrm{Re}\left\{-\frac{1}{2}\begin{bmatrix}\frac{\partial u_x}{\partial t}^* & \frac{\partial u_y}{\partial t}^* & \frac{\partial u_z}{\partial t}^*\end{bmatrix}\begin{bmatrix}\sigma_{xx} & \sigma_{xy} & \sigma_{xz}\\ \sigma_{yx} & \sigma_{yy} & \sigma_{yz}\\ \sigma_{zx} & \sigma_{zy} & \sigma_{zz}\end{bmatrix}\right\} \tag{2.22}$$

The displacements and stresses obtained from Eq. (2.19) are modal hence their actual amplitudes are arbitrarily scaled and not physically meaningful. The power-based normalisation approach which is adopted in this thesis enables a consistent way of presenting and comparing different mode shapes. Normalised wave structure plots indicate amplitudes of displacements, stresses and energy densities as they would be if a mode at a chosen frequency had a unit power flow - see e.g. [108] for details. Note that the structure extends to infinity along the x direction and that the wave field is constant along x. The adopted normalisation assumes unit power flow in a strip of width 1 m along x. The scaling factor a_{norm} is calculated from the square root of the power flow density along z (z-component of the Poynting vector) integrated across the thickness of the structure:

$$a_{\mathrm{norm}} = \frac{1}{\sqrt{\int_{-0.5}^{0.5}\int_{\mathrm{thk}} P_z \,\mathrm{d}y\,\mathrm{d}x}} = \frac{1}{\sqrt{\langle P\rangle}} \tag{2.23}$$

After multiplying the displacements, strains and stresses by a_{norm} the normalised energy densities are computed, and of course $\langle P\rangle = 1$.

Throughout this thesis the wave mode shapes presented are normalised with respect to the unit power flow unless otherwise explicitly stated. Therefore, the dimension of all modal field quantities hereafter is of the form: $\frac{\mathrm{m}}{\sqrt{\mathrm{Wm}^{-1}}}$, $\frac{\mathrm{Pa}}{\sqrt{\mathrm{Wm}^{-1}}}$ and for clarity the power related part $\sqrt{\mathrm{Wm}^{-1}}$ is omitted hereafter.

2.2 Wave propagation in infinite plates

2.2.1 Dispersion curves and wave mode shapes

In this short section Lamb wave dispersion curves, associated wave mode shapes and energy and power structures are presented for the case of an infinite elastic plate. The particular features of the plate dispersion curves are widely known and well discussed in many textbooks [30, 35, 93, 109] so only some general comments regarding the wave solutions are presented.

The relationship between the frequency and the wavenumber of free wave modes is usually presented on a dispersion curves plot. Elastic waves are usually dispersive,

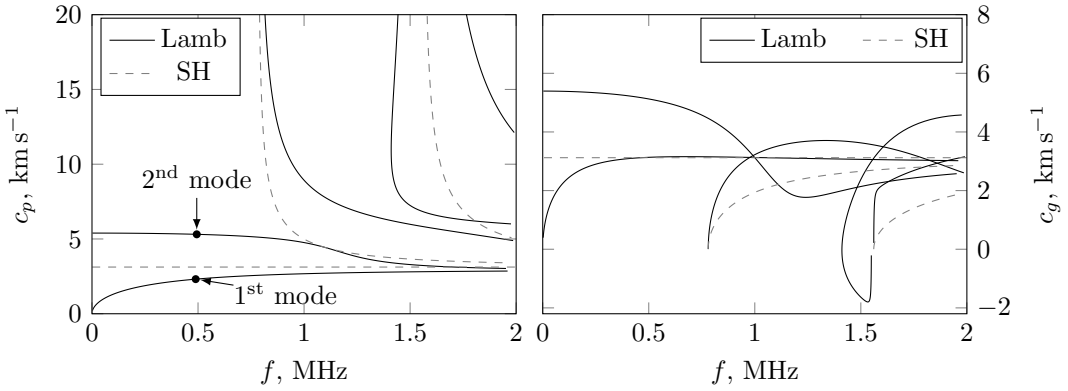

Figure 2.4: Phase and group velocity dispersion curves for a 2 mm aluminium plate.

i. e. spatial frequency (wavenumber) is not linearly related to temporal frequency, except particular configurations. Dispersion curves illustrate this relationship, hence they provide the most informative basic information on wave characteristics. Dispersion curves can be plotted using any wave-related quantity: wavenumber, phase velocity, or group velocity. The term 'dispersion curves' is used interchangeably with wave spectrum in this thesis. In most applications only propagating waves are of interest therefore dispersion curve plots present only the real part of the wavenumber of positive-going waves (or corresponding phase or group velocity).

Phase and group velocity dispersion curves for a 2 mm aluminium plate with both surfaces traction-free (called free-free hereafter) are shown in Fig. 2.4. For Lamb waves there are two fundamental waves, i.e. waves propagating from zero frequency onwards. The one starting at zero phase velocity is predominantly flexural in the low frequency limit and commonly referred to as A_0 (antisymmetric distribution of the in-plane displacement) and the other one starting at phase velocity close to the bulk longitudinal wavespeed of the material is predominantly compressional in the low frequency limit and commonly known as S_0 (symmetric distribution of the in-plane displacement). Wave mode shapes for the two fundamental waves at frequencies marked in Fig. 2.4 are presented in Fig. 2.5 for reference.

At higher frequencies new waves cut-off (i.e. start to propagate). Cut-off frequencies are related to either shear– or longitudinal–dominated resonances of the cross-section. At the cut-off frequency the whole waveguide vibrates uniformly as the wavenumber k is zero (hence the wavelength $\lambda^{\sim}$ is infinite). Higher-order waves in plates are usually labelled using the letter specifying whether the associated mode shape is symmetric or antisymmetric with respect to the neutral plane and with order number, e.g. S_1, A_1, S_2, etc.

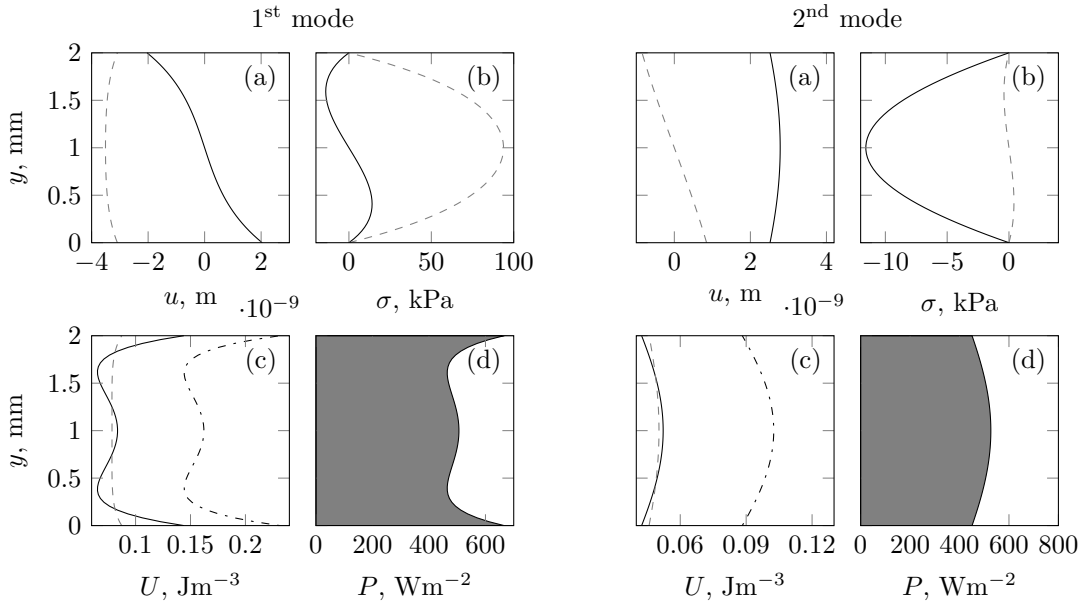

Figure 2.5: Wave mode shape, energy structure and power flow distribution for the first (commonly A_0) and second (commonly S_0) wave modes of the 2 mm aluminium free-free plate at around 490 kHz; (a) displacement: u_y (- - -), u_z (——); (b) stress: σ_{yy} (——), σ_{yz} (- - -);(c) energy density: e_u (——), e_k (- - -), e_{tot} (· - · -); ; (d) power flow density P_z.

Although the plotting and naming conventions presented above are practical and simple, they might invoke some misunderstandings related to the physics of the phenomenon. The GMM model's output has the form of frequency-wavenumber pairs which satisfy the characteristic equation. When plotted on a frequency-wavenumber plane, these points seem to form a set of continuous curves. Therefore, the points along one 'solution curve' are often connected and treated as one wave, commonly referred to as 'mode'. It is noted that associating points to one solution curve without a more detailed information about the energy velocity and complex modes and dense enough frequency resolution may yield non-physical results and bias the interpretation.

The term 'mode' can be slightly misleading since when used in vibration analysis it refers to vibration of the structure that has a particular shape, i.e. the deflected shape is what identifies the mode. Along any wave dispersion curve, however, the associated mode shape changes with frequency, e.g. the 'longitudinal' motion associated with the S_0 wave becomes 'flexural' at some frequency.

Given the intricacy of the topology of the dispersion curves and the fact that the wave structure changes with frequency for each curve, the naming conventions for the waves originating from the deflection shape at a particular frequency can be misleading even for a single layer. Therefore, in this thesis the numerical convention is preferred (wave 1, wave 2, wave 3, ...), with the exception of the fundamental waves A_0, S_0, SH_0 which

are used interchangeably with the numerical ones to keep the link with the common terminology.

It is also worth mentioning that as the usual way of presenting dispersion curves is confined to positive and propagating (according to some arbitrary criterion) waves, the curves can be 'connected' and interpreted incorrectly [110]. In fact, even for a lossless waveguide the full wavenumber spectrum contains an infinite number of imaginary and complex wavenumbers. If one plots wavenumber dispersion curves in the complex domain, the actual shape of the dispersion curves reveals itself more clearly giving more insight into such phenomena as zero group velocity, energy velocity direction and others. The dispersion curves in the complex wavenumber domain can be computed using any of the methods presented in this thesis. For reference purposes, they can be found in e.g. [35].

2.3 Elastic bilayers

Structures covered with an undesired accretion represent a particular configuration commonly referred to as an elastic bilayer. In the literature this term is usually used for analysis of metallic components with a low-stiffness (e.g. polymer) coating [111], however in this work it can be extended to a class of waveguides that can be subdivided into two components having significantly different stiffnesses. This approach reflects a typical unwanted build-up scenario, where the host structure is much stiffer than the build-up. For instance, an aluminium host structure's Young's modulus (70.3 GPa) is almost ten times higher than that of a glaze ice build-up (8.2 GPa). The analysis of the physical aspects of wave propagation in such structures brings an interesting insight into the understanding of potential effect that waves may have on the integrity of the structure.

A schematic view of the elastic bilayer and the terminology used hereafter is depicted in Fig.2.6. The metallic substrate is denoted as the 'host layer' (HL), whereas the unwanted build-up as the 'accreted layer' (AL). The two components of the waveguide have significantly different material properties, i.e. HL is usually of much higher stiffness than AL. The acoustic character of the components is represented by the characteristic acoustic impedance, therefore a quantitative measure of this difference can be obtained

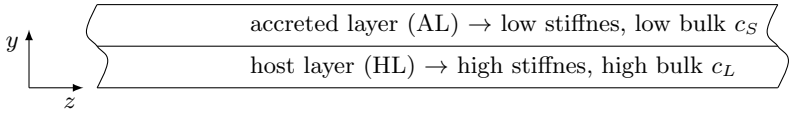

Figure 2.6: Schematic view of a bilayer together with labelling system shown.

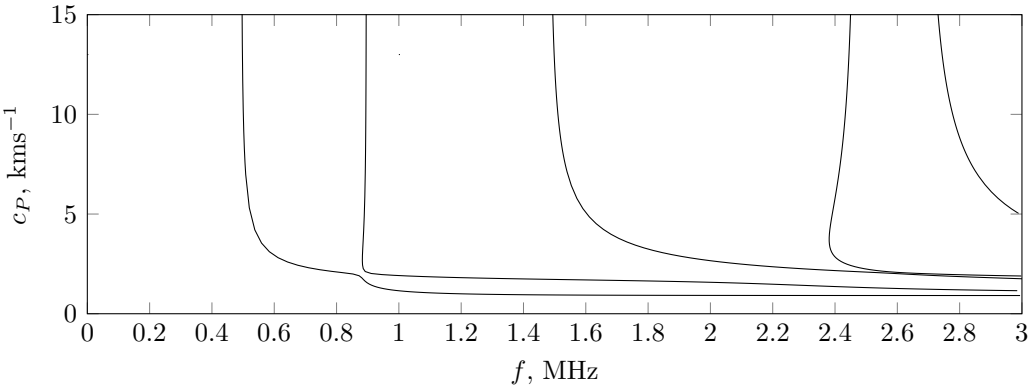

Figure 2.7: Lamb waves dispersion curves for a clamped-free plate. $E = 1.5$ GPa, $\rho = 600$ kg m^{-3}, $\nu = 0.282$, $h = 0.5$ mm.

from the ratio of the characteristic acoustic impedances, which is hereafter denoted as the decoupling coefficient DC. Similarly to the elastic bilayer case [111] the characteristic impedance of HL is much larger that the characteristic impedance of AL:

$$\mathrm{DC} = \frac{(\rho c_L)_{\mathrm{HL}}}{(\rho c_L)_{\mathrm{AL}}} >> 1 \tag{2.24}$$

For instance, in case of rime ice accretion on aluminium (material properties listed in Section 2), the impedance ratio is 14.5. This observation has important implications on how the partial waves are transmitted between the layers. The impedance ratio can be thought of as a measure of how strongly the two layers, or components, are coupled. Large values indicate weak coupling. In this case, from the viewpoint of the AL the HL almost rigidly constrains its free surface. Hence, the partial waves encountering the interface from AL are almost totally reflected. On the other hand, HL having a much higher impedance is not affected by AL and behaves like a free-free plate. Having said that, if one assumes an infinite impedance ratio, the bilayer modes are fully decoupled into two asymptotic families - one associated with the free-free host and the other with the clamped-free build-up [111]. This can also be shown using the global matrix formulation of the bilayer by setting the stiffness and density of the HL to be infinite as done in [112].

The clamped-free plate dispersion curves can be obtained using the partial wave methodology with the matrices appropriately amended to account for the boundary conditions. Since only a single plate is considered the plate field matrix can be deducted from Eq. (2.13). The free-surface is traction-free, therefore the traction related rows provide the boundary condition for the top surface (top sub-matrix), whereas at the clamped surface the displacements are zero, therefore the bottom sub-matrix is formed by the

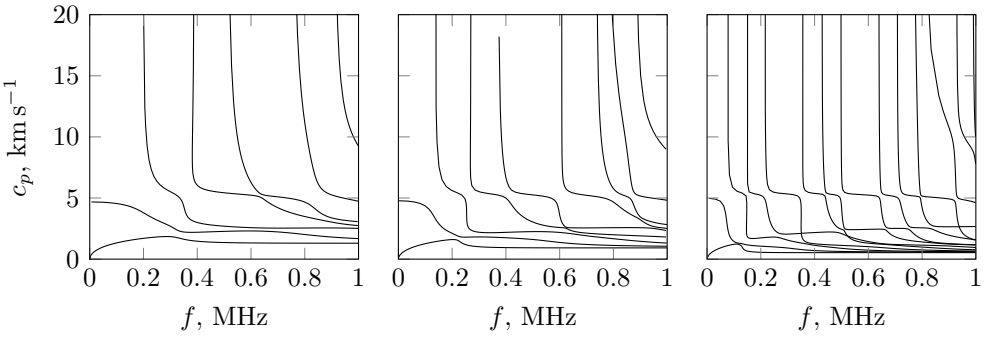

Figure 2.8: Evolution of the Lamb waves dispersion curves with the increase of the decoupling coefficient DC; from the left: DC = 5, DC = 10, DC = 30.

displacement corresponding rows. Surrounding half-spaces are not modelled. The dispersion curve tracing and wave structure extraction procedures are not changed. The typical appearance of the clamped-free plate dispersion curves is presented in Fig. 2.7. As expected, there are no fundamental modes present.

The evolution of the bilayer dispersion curves with the increase of the impedance ratio is illustrated in Fig. 2.8, where a 2 mm thick aluminium plate is covered by accretion of the same thickness and Poisson ratio with other properties computed from the impedance ratio (e. g. $c_{L2} = c_{L1}\mathrm{DC}^{-0.5}$). Hence the increase of DC refers here to the diminishing stiffness of AL. When DC grows, the number of waves in the frequency range increases and, more importantly, mode curves become less smooth and exhibit frequent rapid jumps. In the next section the bilayer dispersion curves is analysed in more detail with particular attention to how the aforementioned asymptotic solutions emerge in the bilayer wave spectrum.

2.4 Topology of the dispersion curves and wave curve veering

The dynamic behaviour of an elastic bilayer is inherently associated with the aforementioned asymptotic solutions (free-free HL and clamped-free AL). Note that the decoupling coefficient DC was defined in a way that high value of DC refers to a very low coupling between the layers. Therefore, most of the elastic bilayers can be thought of as weakly coupled continuous systems, which has many properties in common with a weakly coupled two degree-of-freedom vibratory system [111]. In order to gain more insight into the physics of waves in bilayers an illustrative example is analysed.

The dispersion curves for a 1 mm aluminium plate with 0.5 mm rime ice accretion are shown in Fig. 2.9 (Lamb waves) and Fig. 2.10 (SH waves). The bilayer solution is

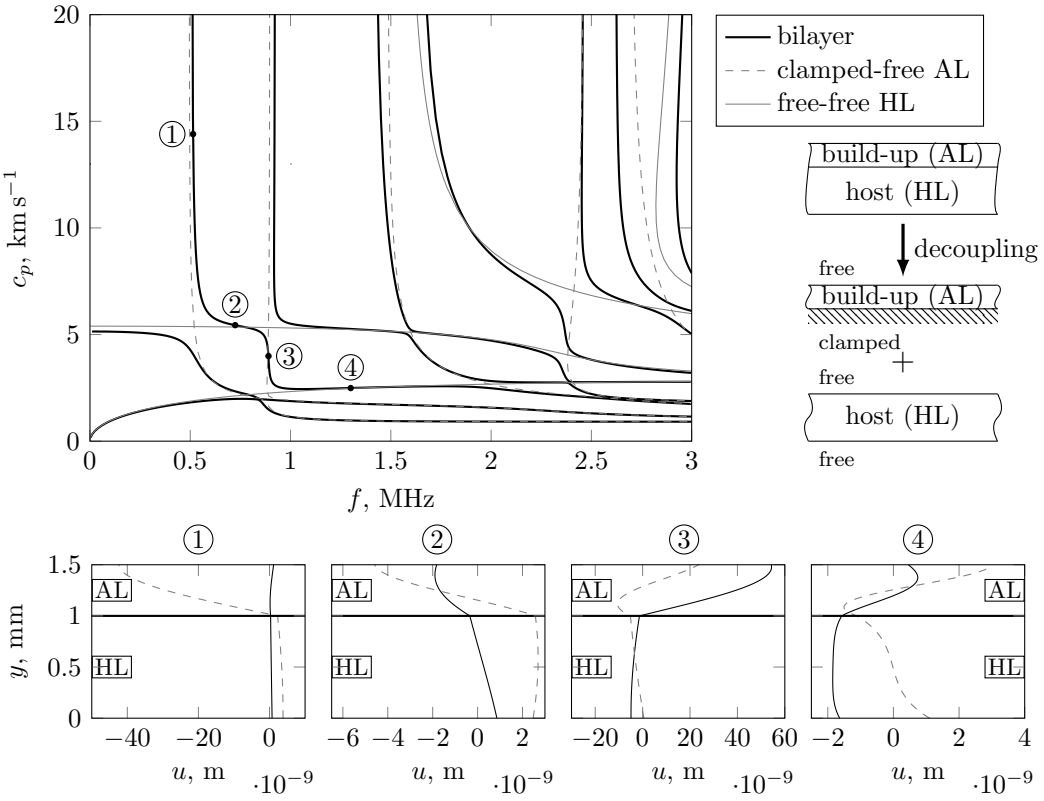

Figure 2.9: Bilayer Lamb waves dispersion curves with asymptotic solutions and wave mode shape evolution along one of the modal curves. Wave mode shape graphs are labelled with respect to the points along the dispersion curve; transverse displacement u_y (——) , in-plane displacement u_z (- - -).

marked with bold black lines and the asymptotic solutions - with thin grey lines. For both classes of solutions the dispersion curves behave in a similar way.

The contribution of the asymptotic solutions is apparent. Before accretion appears the host structure's dynamics are described by the free-free HL asymptotes (solid grey lines). When the accretion covers HL, a bilayer is formed and its dispersion curves (solid black lines) deviate from the original HL trajectories. From the viewpoint of the 'clean structure' the accreted material imposes the dispersion curves of the clamped-free AL (dashed grey lines) on the wave spectrum of the free-free HL. This causes a significant aberration of the original shape of the curves. At some regions the bilayer curves align with the HL asymptote, whereas at the others with the AL asymptote. In fact, the bilayer wave curves seem to be guided by the paths given by the asymptotic solutions, which create a sort of a grid. When approaching the intersection of the two asymptotic solutions, the bilayer curve exhibits a sudden change of path (see Fig. 2.9 at e.g. 0.5 MHz). This phenomenon is called dispersion curve veering here but is also known as mode jumping, mode veering or mode repulsion [112, 113]. It originates from the weak coupling between the layers. The components of a weakly coupled system behave as if

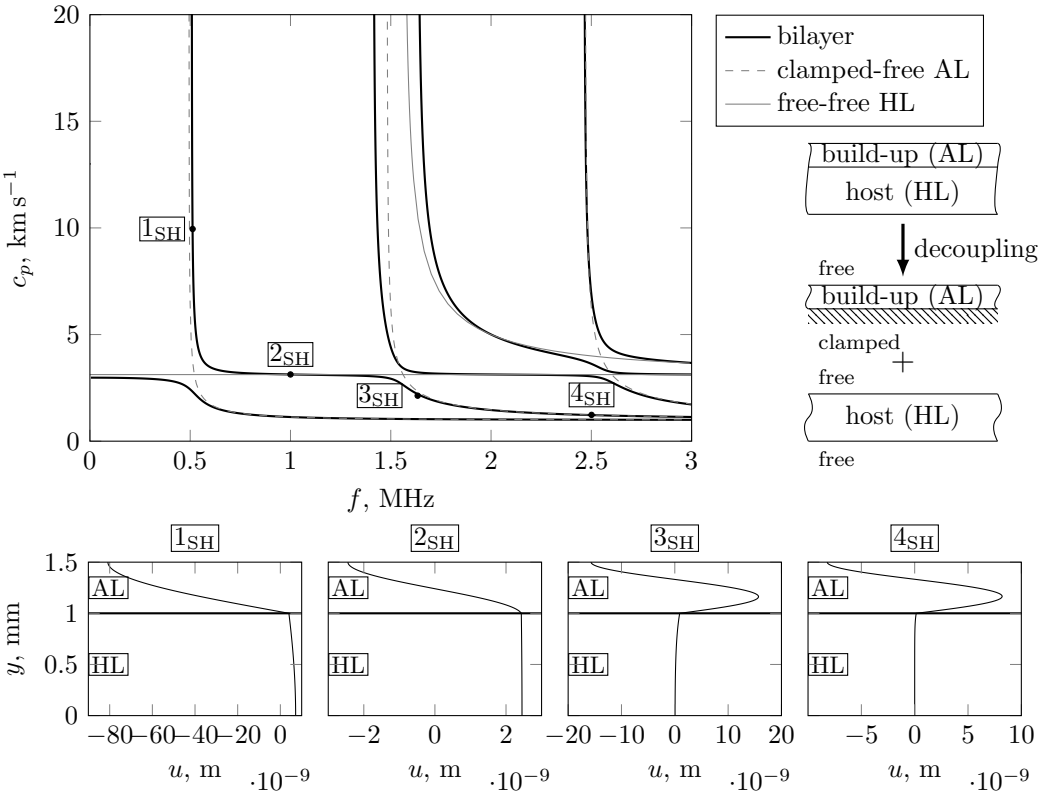

Figure 2.10: Bilayer SH waves dispersion curves with asymptotic solutions and wave mode shape evolution along one of the modal curves. Wave mode shape graphs are labelled with respect to the points along the dispersion curve; perpendicular in-plane displacement u_x (——).

they were uncoupled, unless the uncoupled solutions are close to crossing each other. Since at a given frequency-wavenumber point only one wave is present (i.e. two waves with different mode shapes cannot exist at the same point of a wave spectrum), the coupled system dispersion curves veer, aligning with the approached asymptote. On a dispersion curve plot it looks like a jump.

Following from that, each wave curve can be subdivided into regions in which the system behaves almost as uncoupled and is dominated by either of the two components and the regions where the coupling effect is very strong, i.e. the dispersion curves do not clearly follow any of the asymptotes and the associated mode shape is a combination of the two uncoupled mode shapes. The latter is associated with veering of the curves.

In fact, a similar phenomenon occurs in simple one-layer plates. The partial waves (fundamental wave types: L, SV) are initially uncoupled but the boundaries of the plate, where reflection and mode conversion occur, introduce the coupling. Using boundary conditions that do not involve partial wave conversion (such as mixed boundary conditions) leads to the wave solution consisting of completely decoupled either longitudinal or shear waves (see [35] for details). Therefore, for a traction-free plate one can observe

that plate dispersion curves originate from vibration of the cross section associated with only one partial wave and then veer when a node of the grid of asymptotes ([35]) is encountered. The repulsion of the dispersion curves for plates has been analysed with the aid of perturbation theory by Überall et al. [114], who also drew an analogy to atomic physics.

The bilayer is the simplest multilayer configuration, hence the coupling effects are clearly noticeable. The dispersion curve is veering from one asymptotic path towards the other when it approaches subsequent 'repulsive points' (the intersections between two different asymptotic solutions). In the low frequency limit, the bilayer dispersion curves tend to those of a single HL, as there are no fundamental modes in a clamped-free plate (see Fig. 2.9). The displacement field is then predominantly in the host structure, and the field distribution is defined by the mode shape of a free-free HL. Most of the higher-order modes tend to the modes of the clamped-free AL in the low wavenumber limit (near their cut-off frequencies), since the mode count increases when stiffness gets lower and the stiffness of AL is relatively low. Each wave starts propagating close to one of the asymptotes. While moving up with frequency along the asymptotic path, it meets subsequent repulsive points and in their close neighbourhood more or less smoothly veers towards a new path given by the asymptote approached.

The stronger the coupling (in this case the more the properties of the layers are similar), the less evident dispersion curve veering is. For high stiffness accretions such as e.g. glaze ice wave motion of the bilayer has a strongly coupled character along large sections of the dispersion curves (see Fig. 2.8).

In order to illustrate how the mode shapes evolve with the dispersion curve veering, four points along the 3$^{\text{rd}}$ bilayer dispersion curve were picked and their associated field distributions were plotted in Fig. 2.9. Near the cut-off frequency the motion is dominated by a clamped-free mode of the accreted layer (point 1). While approaching the first repulsive point it veers towards the free-free HL 2$^{\text{nd}}$ asymptote. When aligned with this line the bilayer adopts a characteristic, symmetric u_z displacement pattern - typical of the fundamental compressional wave (called S_0) (point 2). The curve veers again around 900 kHz and aligns with the AL 2$^{\text{nd}}$ decoupled solution. The wave mode shape shows a clear prevalence of the build-up mode (point 3). At point 4 the tracked curve is following the fundamental flexural HL wave (called A_0) showing the well-known antisymmetric u_z displacement pattern.

An analogous analysis can be performed for SH waves in the bilayer. The dispersion curves and the wave mode shape evolution along the second bilayer curve are presented in Fig. 2.10. Note that the HL has only one fundamental SH wave.

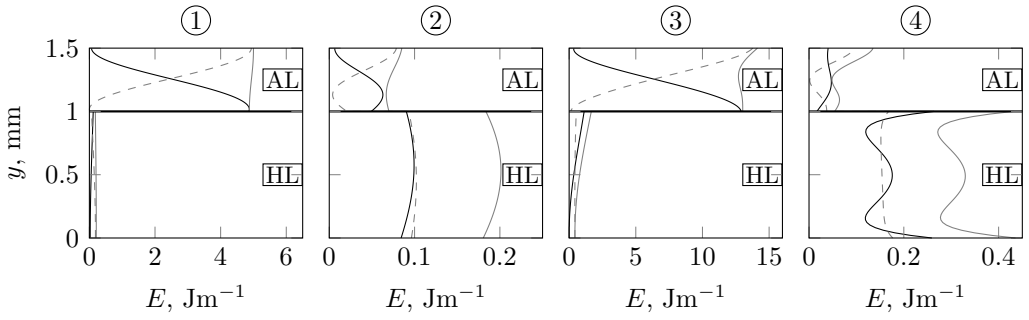

Figure 2.11: Energy wave mode shapes at points along the bilayer dispersion curve as chosen in Fig. 2.9; strain energy density (——), kinetic energy density (- - -), total energy density (——).

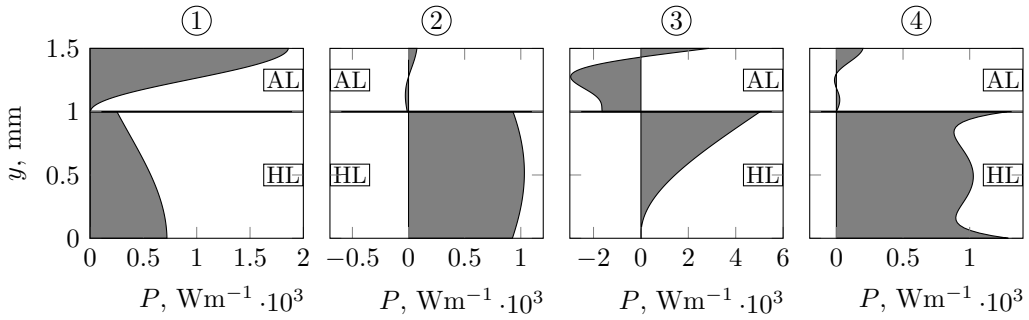

Figure 2.12: Power flow density distribution at points along a bilayer dispersion curve as chosen in Fig. 2.9.

2.5 Energy propagation

The field distributions related to the points along the HL asymptotes in Fig. 2.9 and Fig. 2.10 show some significant displacement in the build-up which can be misleading. However, this apparent ambiguity is related to the fact that the traction is continuous across the interface of a multilayered plate (Section 2.1). Recalling that the AL is of a relatively low stiffness one can conclude that along the HL asymptotes, the displacement in the AL can be significant. The complete picture of the topology of the bilayer dispersion curves can be seen when wave energy is taken into account.

The energy propagation in weakly coupled systems is closely related to the asymptotic solutions. The distribution of strain energy and power flow density in the direction of propagation for Lamb wave modes as chosen in Fig. 2.9 are presented in Fig. 2.11 and Fig. 2.12, respectively. For modes close to the AL asymptotes, most of the wave energy is trapped in the accreted layer and the strain energy density has its maximum at the interface. This effect is not so apparent if power flow density is considered (Fig. 2.12). It is interesting that a large section of the power flow density distribution in AL at point 3 in Fig. 2.12 is negative. It originates from the fact that the AL asymptote which is followed by the bilayer wave curve at this point has a negative energy velocity. Therefore

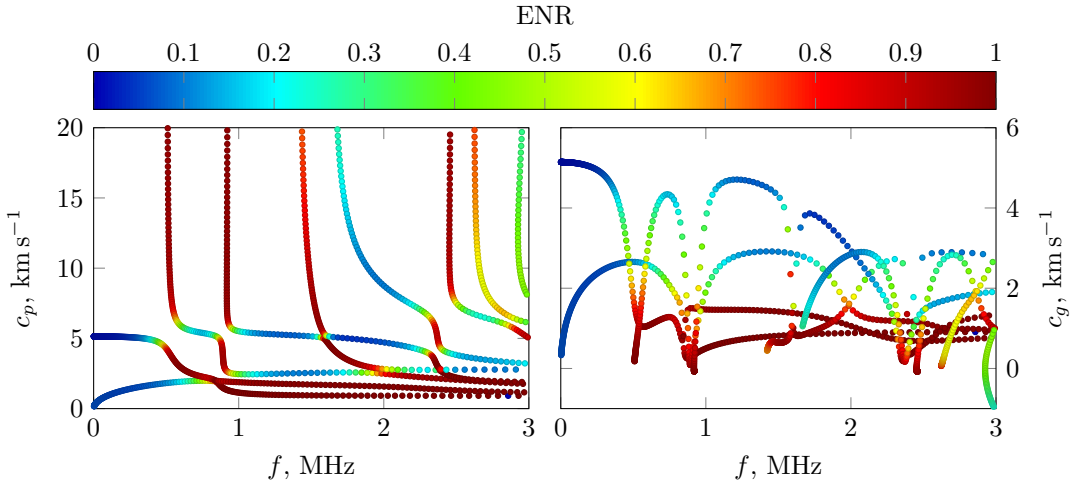

Figure 2.13: Fraction of the strain energy ENR enclosed in the accreted layer imposed on the Lamb waves dispersion curves for a 1 mm aluminium plate with 0.5 mm rime ice accretion.

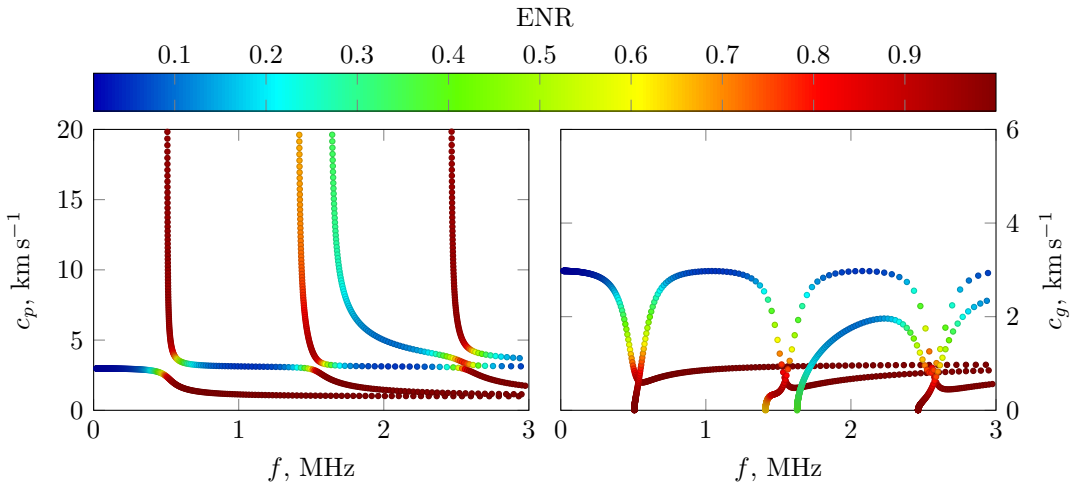

Figure 2.14: Fraction of the total peak strain energy ENR enclosed in the accreted layer imposed on the SH waves dispersion curves for a 1 mm aluminium plate with 0.5 mm rime ice accretion.

at this point part of the total wave power is propagated in the positive direction along the HL and the other part in the negative direction along the AL.

From a viewpoint of invoking delamination with waves when the energy is confined mainly in the AL the cracks can be expected to be mainly cohesive, and because of the loss of integrity of the layer, the energy might not propagate over a long distance. On the other hand when close to the HL asymptotes the bilayer modes seem to be more likely to induce adhesive breaks and the build-up shedding should not affect the energy flow.

An interesting way of analysing the energy propagation in bilayers is to look at how

much of the overall wave energy is contained in one of the layers. In order to do this the strain energy ratio ENR is defined here as a fraction of the total strain energy which is enclosed in the accreted layer. The strain energy contained in a layer is given by the integral of e_u across its thickness. The ENR is calculated as:

$$\mathrm{ENR} = \frac{\int_{\mathrm{AL}} e_\epsilon \, \mathrm{d}y}{\int_{\mathrm{AL+HL}} e_\epsilon \, \mathrm{d}y} \tag{2.25}$$

where 'AL' and 'AL+HL' denote integration across the build-up and across the total thickness, respectively. In order to illustrate which layer is the predominant energy carrier for different modes, the value for ENR has been imposed on the dispersion curves of the sample bilayer in Fig. 2.13 for Lamb waves and in Fig. 2.14 for SH waves.

In the ENR graphs the energy trapping is most evident. It can be easily spotted that the sections corresponding to AL asymptotes are characterised by ENR close to 1, whereas along the host free-free wave curves ENR is much lower than 0.5. Hence AL-dominated modes are not able to propagate energy over a long distance and possibly induce internal cracks in the build-up. While looking at the group velocity plots on the right hand side of Fig. 2.13 and Fig. 2.14 it is also clear that ENR is very large when the group velocity is low. The velocity of energy transport (which for lossless waveguides is the same a s the group velocity) seems to be closely related to the strain energy distribution. Except the cut-off frequencies (for which c_g is always 0), the energy propagates slowly when it is confined in the accreted layer.

The energy distribution has another important implication on wave propagation which is introduced and explained in the next paragraphs.

2.6 Wave attenuation in structures covered with lossy accretions

Most of the accreting materials that are within the potential scope of applicability of the wave-based cleaning concept are lossy. An exact quantification of damping in unwanted build-ups is very complicated because of the nature of the accretion process and is outside of the scope of this thesis. However, since wave attenuation seems to be an important aspect of wave propagation in structures with accretions a qualitative discussion is presented below which aims to on draw some practical conclusions.

Ice material properties (including viscosity) are highly dependent on particular conditions (including atmospheric) and vary significantly among researchers. It has been

observed that ice as formed in an icing wind tunnel is highly damped. Thus, the attenuation of guided waves needs to be carefully considered in order to ensure that the excited wave mode expected to invoke delamination will propagate over a sufficient distance and be effective.

The GMM wave model introduced in Section 2.1 and implemented for this thesis is capable of predicting the dispersion curves for lossless waveguides only. Incorporating damping in the routine is feasible but undesirable since it involves the need for complicated three-dimensional tracing of the roots of the determinant of the global matrix. However, even with a lossless waveguide model the attenuation analysis is possible.

Following the work of Simonetti [112] a simple approximate approach has been employed here enabling the calculation of guided wave attenuation based on so-called energy factors of an equivalent elastic bilayer (with no damping). This means that wave attenuation can be found using the implemented GMM model from the strain energy distributions for an undamped structure. The methodology is briefly recalled below.

For viscoelastic materials the Lamé constants λ_v, μ_v are complex and can be derived from the relaxation curves. The imaginary parts of λ_v, μ_v are related to the loss modulus of the material.

The guided wave attenuation ζ (equivalent to the imaginary part of the propagating wavenumber k) is related to the dissipated power in a unit volume averaged over one cycle P_d as:

$$\zeta = \frac{\mathrm{d}P_d/\mathrm{d}z}{2\langle P\rangle} \tag{2.26}$$

where $\langle P\rangle$ is the integral of the component of the Poynting vector in the direction of propagation across the thickness, which denotes total power flow along the waveguide (it is recalled that all the wave mode field and energy quantities are normalised with respect to the unit power flow in this thesis, hence $\langle P\rangle = 1$).

The average dissipated power per unit volume at a point p_d can be derived from the peak strain energy per unit volume e_s for a viscoelastic medium [112]. For Lamb waves, one writes:

$$\begin{aligned} e_s &= \frac{1}{2}(\mathrm{Re}\{\lambda_v\} + 2\mathrm{Re}\{\mu_v\})\epsilon_0\epsilon_0^* + 2\mathrm{Re}\{\mu_v\}(\epsilon_{yz}\epsilon_{yz}^* - \epsilon_{zz}\epsilon_{yy}^*) = \delta + \gamma \\ p_d &= \frac{1}{2}\omega(\mathrm{Im}\{\lambda_v\} + 2\mathrm{Im}\{\mu_v\})\epsilon_0\epsilon_0^* + 2\omega\mathrm{Im}\{\mu_v\}(\epsilon_{yz}\epsilon_{yz}^* - \epsilon_{zz}\epsilon_{yy}^*) = \\ &\omega\left(\frac{\mathrm{Im}\{\lambda_v + 2\mu_v\}}{\mathrm{Re}\{\lambda_v + 2\mu_v\}}\delta + \frac{\mathrm{Im}\{\mu_v\}}{\mathrm{Re}\{\mu_v\}}\gamma\right) \end{aligned} \tag{2.27}$$

For SH waves the above quantities are calculated from:

$$\begin{aligned} e_s &= 2\mathrm{Re}\{\mu_v\}(\epsilon_{xz}\epsilon_{xz}^* + \epsilon_{xy}\epsilon_{xy}^*) = \gamma_{\mathrm{SH}} \\ p_d &= 2\omega\mathrm{Im}\{\mu_v\}(\epsilon_{xz}\epsilon_{xz}^* + \epsilon_{xy}\epsilon_{xy}^*) \end{aligned} \tag{2.28}$$

In the above equations subscript v indicates that the quantity is related to the viscoelastic layer, and δ, γ and γ_{SH} denote contributions to the strain energy originating from longitudinal, shear vertical and shear horizontal partial waves, respectively.

Following the plane wave assumption the field quantities are constant along the x direction, hence the total dissipated power in a volume can be written as:

$$P_d = \int_L \int_{d_v} p_d \,\mathrm{d}y \,\mathrm{d}z \tag{2.29}$$

hence

$$\frac{\mathrm{d}P_d}{\mathrm{d}z} = \int_{d_v} p_d \,\mathrm{d}y \tag{2.30}$$

Combining Eq. (2.26), Eq. (2.27), Eq. (2.28) and Eq. (2.30) one gets the following expressions for the guided wave attenuation:

$$\begin{aligned} \zeta_{\mathrm{Lamb}} &= \frac{\omega}{2\langle P\rangle}\left(\frac{\mathrm{Im}\{\lambda_v+2\mu_v\}}{\mathrm{Re}\{\lambda_v+2\mu_v\}}\int_{d_v}\delta\,\mathrm{d}y + \frac{\mathrm{Im}\{\mu_v\}}{\mathrm{Re}\{\mu_v\}}\int_{d_v}\gamma\,\mathrm{d}y\right) \\ \zeta_{\mathrm{SH}} &= \frac{\omega}{2\langle P\rangle}\frac{\mathrm{Im}\{\mu_v\}}{\mathrm{Re}\{\mu_v\}}\int_{d_v}\gamma_{\mathrm{SH}}\,\mathrm{d}y \end{aligned} \tag{2.31}$$

Eq. (2.31) shows how guided wave attenuation can be expressed as a linear combination of the longitudinal and shear strain energies contained in the viscoelastic layer. Simonetti showed that in the case of low attenuation one can employ a Maclaurin expansion up to the first order term to enable calculation of the wave attenuation for the lossy bilayer from the strain energy in the equivalent elastic bilayer (e.g. such that $\mathrm{Im}\{\lambda_v\} = \mathrm{Im}\{\mu_v\} = 0$) [112]:

$$\begin{aligned} \zeta_{\mathrm{Lamb}} &\simeq \left.\frac{\alpha_L f\int_{d_v}\delta\,\mathrm{d}y + \alpha_S f\int_{d_v}\gamma\,\mathrm{d}y}{\langle P\rangle}\right|_{\mathrm{Im}\{\lambda_v+2\mu_v\}=\mathrm{Im}\{\mu_v\}=0} \\ \zeta_{\mathrm{SH}} &\simeq \left.\frac{\alpha_S f\int_{d_v}\gamma_{\mathrm{SH}}\,\mathrm{d}y}{\langle P\rangle}\right|_{\mathrm{Im}\{\mu_v\}=0} \end{aligned} \tag{2.32}$$

where $\alpha_{L,S}$ are the bulk wave attenuations in nepers per meter corresponding to the longitudinal and shear waves and the normalisation of the modal energy with respect to unit power flow is assumed. In [112] $\int_{d_v}\delta\,\mathrm{d}y$, $\int_{d_v}\gamma\,\mathrm{d}y$ and $\int_{d_v}\gamma_{\mathrm{SH}}\,\mathrm{d}y$ are referred to as the energy factors Q_Δ, Q_Γ and Q_E, respectively.

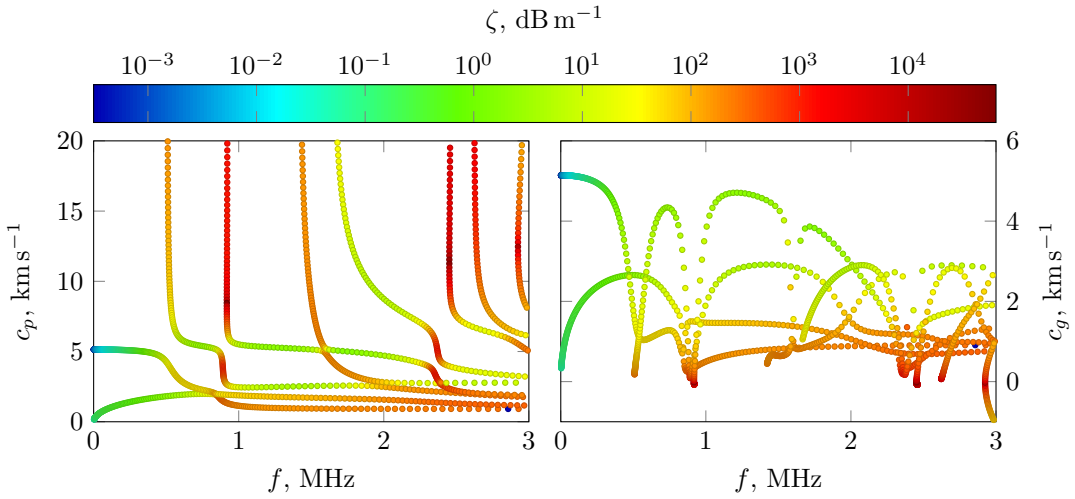

Figure 2.15: Guided wave attenuation imposed on the Lamb waves dispersion curves (phase velocity: on the left; group velocity: on the right) for a 1 mm aluminium plate with 0.5 mm rime ice accretion with bulk attenuation in rime ice assumed to be $\alpha_L = \alpha_S = 0.01$ Np m^{-1}.

Eq. (2.32) provides a straightforward way to obtain the wave attenuation directly from the elastic model assuming that the damping is low. It also shows how the wave attenuation is influenced by the longitudinal and shear effects. The analysis of the dispersion of the energy factors gives a clear indication of the wave attenuation in the viscoelastic bilayer given the bulk attenuations $\alpha_{L,S}$.

As an indicative example a case of a 0.5 mm rime ice accretion on a 1 mm aluminium plate is considered with both longitudinal and shear bulk attenuations of ice set to 0.01 Np m^{-1}. This is an arbitrarily chosen value, corresponding to the low attenuation regime but is expected to provide an informative outcome on how waves are attenuated in a lightly damped bilayer. The results for Lamb and SH waves are presented in Fig. 2.15 and Fig. 2.16, respectively. Waves in a lossy bilayer are considerably more attenuated when close to AL asymptotes, while the 'green' (low attenuation) sections align with the free-free HL curves. The energy is dissipated within the accreted layer and the loss is considerably greater whenever the bilayer waves are dominated by the AL influence. This observation is enforced with the fact that expressions Eq. (2.31), Eq. (2.32) indicate a direct link between the attenuation of guided waves and the energy distribution described via the ENR parameter.

Thus, energy distribution becomes an important criterion while looking at the possibility of wave-invoked delamination. From this viewpoint the optimal wave candidate propagates most of the energy along the host structure, facilitating a longer range effect and preventing cohesive breaks.

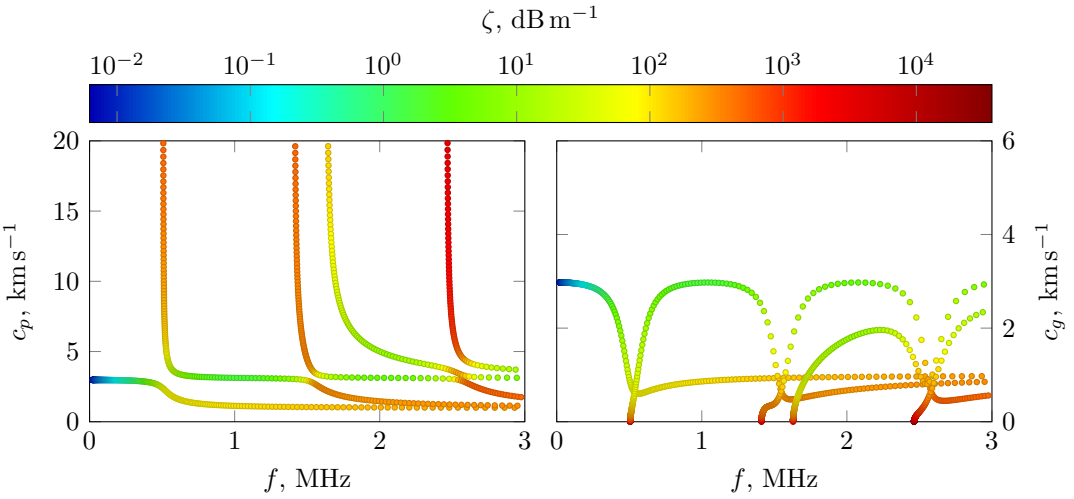

Figure 2.16: Guided wave attenuation imposed on the SH waves dispersion curves (phase velocity: on the left; group velocity: on the right) for a 1 mm aluminium plate with 0.5 mm rime ice accretion with bulk attenuation in rime ice assumed to be $\alpha_L = \alpha_S = 0.01$ Np m^{-1}.

2.7 Interface shear stress

Finally, the main criterion for discussing the possibility of wave-induced delamination is the stress generated at the interface and the question of whether it is capable of breaking the bond. Firstly, it is important to state clearly which stress components are of interest. For most practical cases (including ice accretion) the bond created by the build-up is weaker in shear than in tension, hence the aim is to overcome the shear adhesion strength of the added layer. Two stress fields may be induced by plane wave propagation, i.e. shear stress σ_{xz} (exclusively for SH waves) and transverse shear stresses σ_{yz}, σ_{xy} which are generated by Lamb and SH waves, respectively [2].

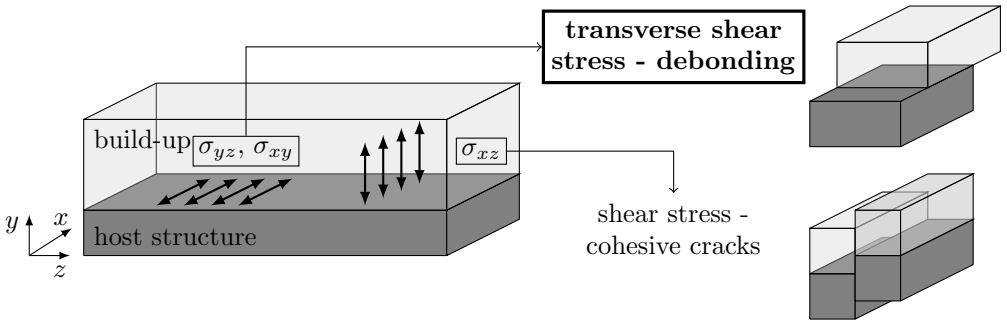

Figure 2.17: Interface shear stress components in a plate with an accreted layer.

As it can be seen in Fig. 2.17, σ_{xz} causes shearing of the vertical cross-sections of the plate and thus, is expected to contribute to cohesive breaks and cracks within the

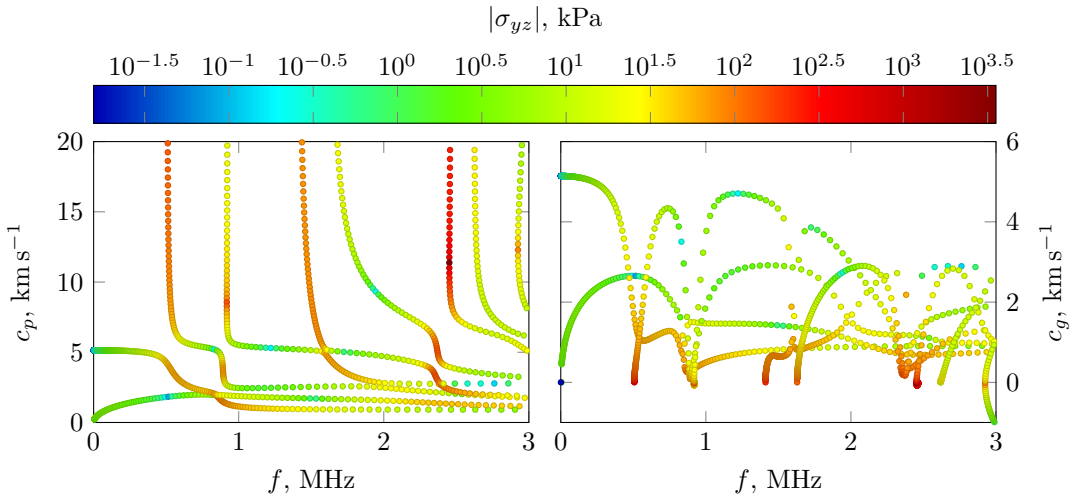

Figure 2.18: Interface shear stress magnitude imposed on the Lamb waves dispersion curves (phase velocity: on the left; group velocity: on the right) for a 1 mm aluminium plate with 0.5 mm rime ice.

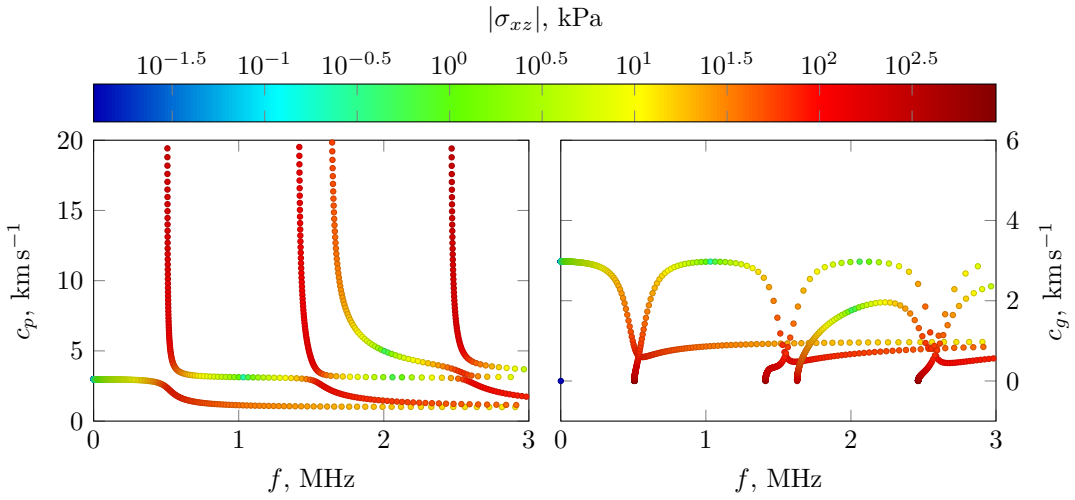

Figure 2.19: Interface shear stress magnitude imposed on the SH waves dispersion curves (phase velocity: on the left; group velocity: on the right) for a 1 mm aluminium plate with 0.5 mm rime ice accretion.

accreted layer . The transverse shear stresses σ_{yz}, σ_{xy} at the interface may be good candidates for detaching the layer, as shearing occurs in the horizontal plane in these cases. Therefore, the interest is focused on these components.

The through-thickness distribution of stress associated with a propagating wave can be obtained from the displacement wave mode shape after appropriate transformation as explained in Section 2.1. The stress obtained with the global matrix method is continuous and represent accurate values. Modal stress as presented here is normalised with respect to the unit power flow, i. e. as if each mode propagated 1 W in the strip of unit width in the x direction (see Eq. (2.23)).

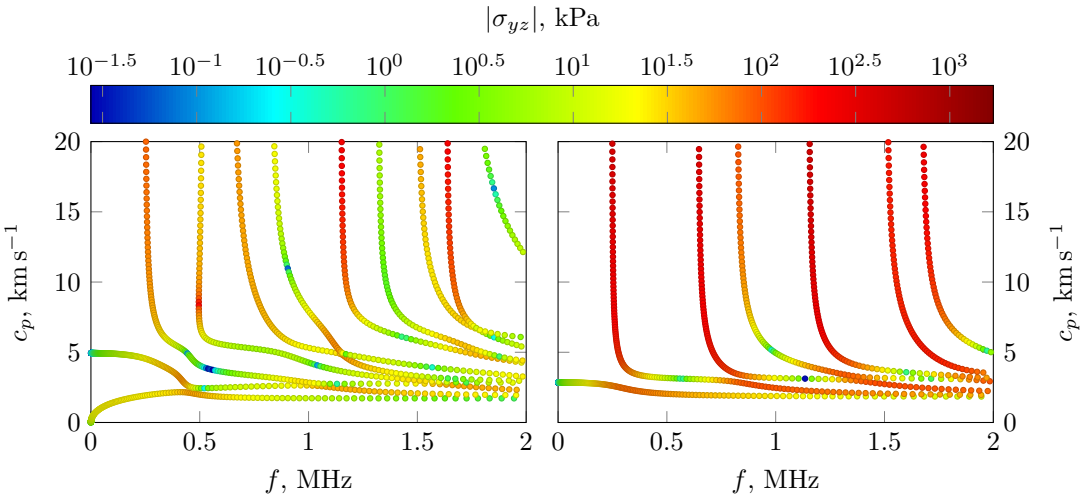

Figure 2.20: Interface shear stress magnitude imposed on the Lamb (on the left) and SH (on the right) waves dispersion curves (phase velocity) for a 2 mm aluminium plate with 2 mm glaze ice accretion.

In order to analyse the stress generation capability of different modes, the modal interface shear stress values were imposed on the dispersion curves for a sample structure in Fig. 2.18 and Fig. 2.19. It is apparent that large interface stress occurs in regions where mode curves follow the AL asymptote. The decoupled wave structure of the clamped-free accreted layer is characterised by very large strain near the rigid surface. When coupling is taken into account, the predominant contribution of the AL decoupled mode shape is responsible for generating high stress at the interface. HL dominated sections of the bilayer spectrum are usually associated with much lower stress, since they originate from the decoupled free-free plate waves which obey the traction-free boundary condition. Therefore, in Fig. 2.18 the vertical sections of the mode curves (which usually refer to the AL-dominated cut-off frequencies) are usually dark which means high stress at the interface, while sections that approach the HL asymptote are light-coloured. The highest modal interface shear stress occurs at so-called zero group velocity points [115] corresponding to the through-thickness localised resonances. They are characterised by very large local deformation of the cross-section that are not accompanied by energy transport (energy velocity is zero) so are expected to occur only at the excitation location. Zero group velocity points occur only for Lamb waves.

There is no significant difference in stress magnitude generated by Lamb and SH waves. The maxima of group velocity correspond to the smallest interface shear stress and, conversely, the minima of the group velocity dispersion curves are associated with very large interface stress in Fig. 2.18 and Fig. 2.19. One can notice that along the HL asymptotes there are regions where the interface shear stress drops significantly and those should be avoided.

In Fig. 2.20 the interface shear stress is plotted for a 2 mm aluminium plate with 2 mm glaze ice accretion, i.e. for a structure with stronger coupling between the layers. Veering of the dispersion curves is now less rapid and hence large sections of the dispersion curves represent waves whose mode shapes show a coupled character with larger interface shear stress.

2.8 Invoking delamination using guided waves

2.8.1 Optimal wave mode selection criteria

The discussion presented in the previous section indicates that for a particular mode there are two main factors that influence its debonding potential: (i) high modal interface shear stress; (ii) desirable energy distribution across the thickness that enables the wave to propagate over long distances and makes it insensitive to partial removal of the accreted layer. However, these two criteria are contradictory and so a trade-off exists between them. Waves that have a desirable energy distribution generate relatively low interface shear stresses and vice versa.

Based on the above analysis it is concluded that from a modal point of view there is no substantial difference between the plausibility of invoking delamination by waves in different frequency regimes. Distinguishable peaks of interface shear stress are linked with zero group velocity points and/or cut-off frequencies but in the light of the criteria outlined in the previous paragraph they might not be effectively excited. Apart from those, the interface shear stress along the HL asymptotes seems to be of a similar order of magnitude at low, medium or high frequencies. Therefore, the following analysis is confined to frequencies up to 200 kHz as it is expected to give representative results qualitatively valid at higher frequencies.

2.8.2 Influence of the properties of the accreted layer on the generated interface stress

In the subsequent paragraphs the influence of the thickness and stiffness of the accreted layer on generated interface shear stress is analysed. The influence of thickness represents the effect of 'growing' accretion, whereas the comparison with respect to the stiffness brings a qualitative insight to the limits of the applicability of the method. Note that all comparisons below are based on the power-normalisation of the wave mode shapes. Regardless of the thickness or stiffness of the accretion the values plotted below represent stress as if 1 $\mathrm{W\,m^{-1}}$ of mechanical power is carried by the mode considered. This

enables a qualitative comparison between different waves and structural configurations. However, when scaling the results it should be borne in mind that the unit of stress including the normalisation is $\mathrm{Pa}/\sqrt{\frac{\mathrm{W}}{\mathrm{m}}}$ so the given stress value must be multiplied by the square root of mechanical power injected to the waveguide.

2.8.2.1 Influence of thickness

The evolution of the dispersion curves with the increase of the accreted layer thickness for a sample structure is presented in Fig. 2.21. One can recall that a common way to represent the dispersion curves of elastic homogeneous plates is to plot them as a function of the frequency-thickness product [30]. For a bilayer with growing AL the frequency-thickness product representation is valid for the build-up only, therefore the effect of the imprint of the AL decoupled dispersion curves is shifted to the left with the thickness of the AL increasing. AL-dominated modes cut off at lower frequencies and the HL wave curves are altered sooner in frequency.

More indicative conclusions can be drawn from examining the transverse shear stress field for different build-up thicknesses. In Fig. 2.22 and Fig. 2.23 the through-thickness transverse shear stress distributions for different thicknesses of build-up are plotted for Lamb (first two) and SH waves, respectively, at 100 kHz. Among the three fundamental waves the 1$^{\mathrm{st}}$ Lamb mode (flexural) generates the highest stress, however the stress at the interface is not the maximum of the whole distribution. The interface shear stress for the 1$^{\mathrm{st}}$ Lamb wave grows with the thickness of the build-up up to some critical thickness (here: 4 mm when it starts decreasing again. The interface stress value is lower than the maximum stress achieved in the neutral plane of the host layer.

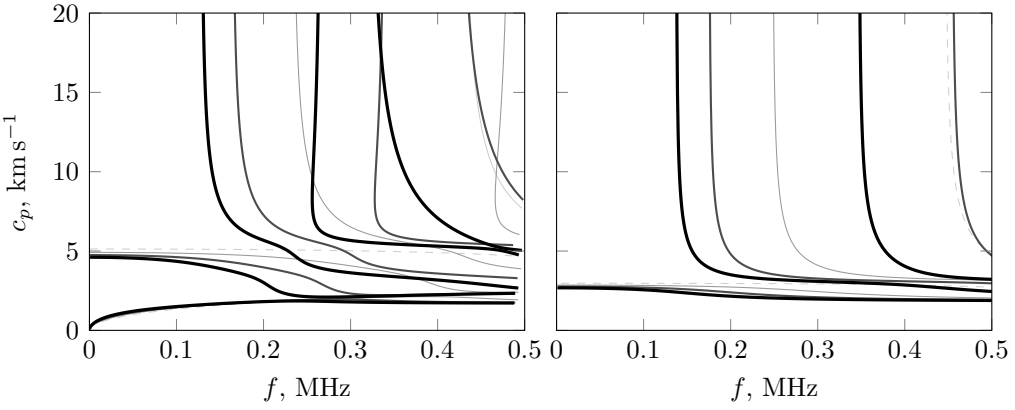

Figure 2.21: Lamb (left) and SH (right) dispersion curves changing with accretion thickness growth for a 2 mm aluminium plate with growing glaze ice accretion: 1 mm (- - -), 2 mm (——), 3 mm (——), 4 mm (——).

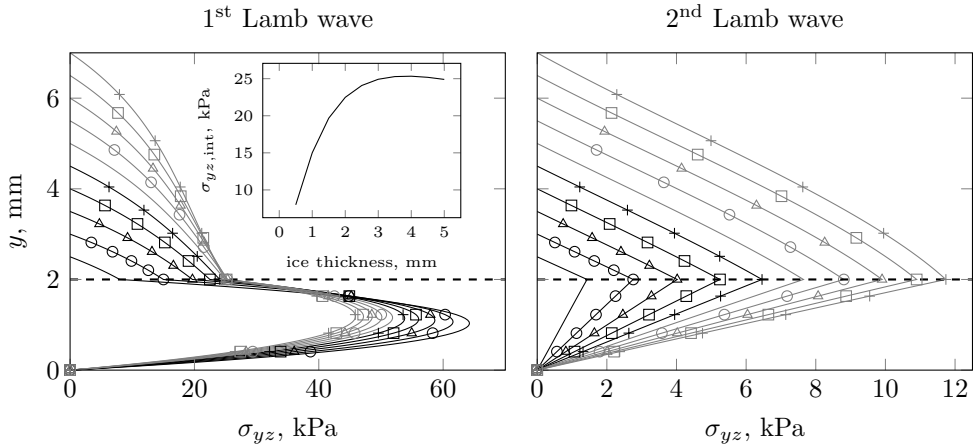

Figure 2.22: Through-thickness distribution of the transverse shear stress at 100 kHz resulting from the propagation of the first two Lamb wave modes for a 2 mm aluminium plate with growing glaze ice accretion: 0.5 mm (——), 1 mm (—○—), 1.5 mm (—△—), 2 mm (—□—), 2.5 mm (—+—), 3 mm (——), 3.5 mm (—○—), 4 mm (—△—), 4.5 mm (—□—), 5 mm (—+—).

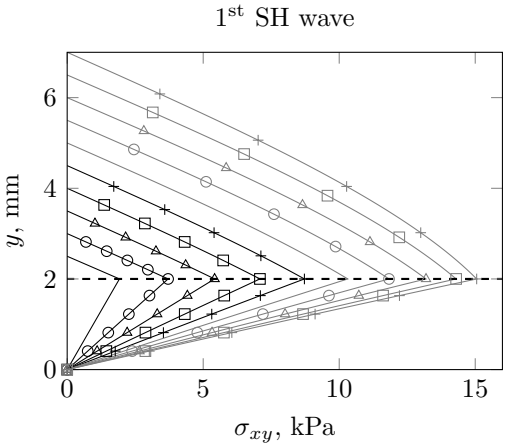

Figure 2.23: Through-thickness distribution of the transverse shear stress at 100 kHz resulting from the propagation of the first SH wave mode for a 2 mm aluminium plate with growing glaze ice accretion: 0.5 mm (——), 1 mm (—○—), 1.5 mm (—△—), 2 mm (—□—), 2.5 mm (—+—), 3 mm (——), 3.5 mm (—○—), 4 mm (—△—), 4.5 mm (—□—), 5 mm (—+—).

The shape of the distribution associated with the 2nd Lamb wave (compressional)and the SH wave are very similar. Corresponding stress components at the interface are increasing with the accretion growth (nonlinearly). The values for the SH wave are around $\approx 25\%$ higher than the values for S_0 wave. For both modes the maximum of the through-thickness stress distribution is at the interface.

Based on the above results, one can conclude that wave-invoked delamination is facilitated if the accretion is moderately thick (up to twice the HL thickness), however the flexural wave effectiveness drops over some critical thickness.

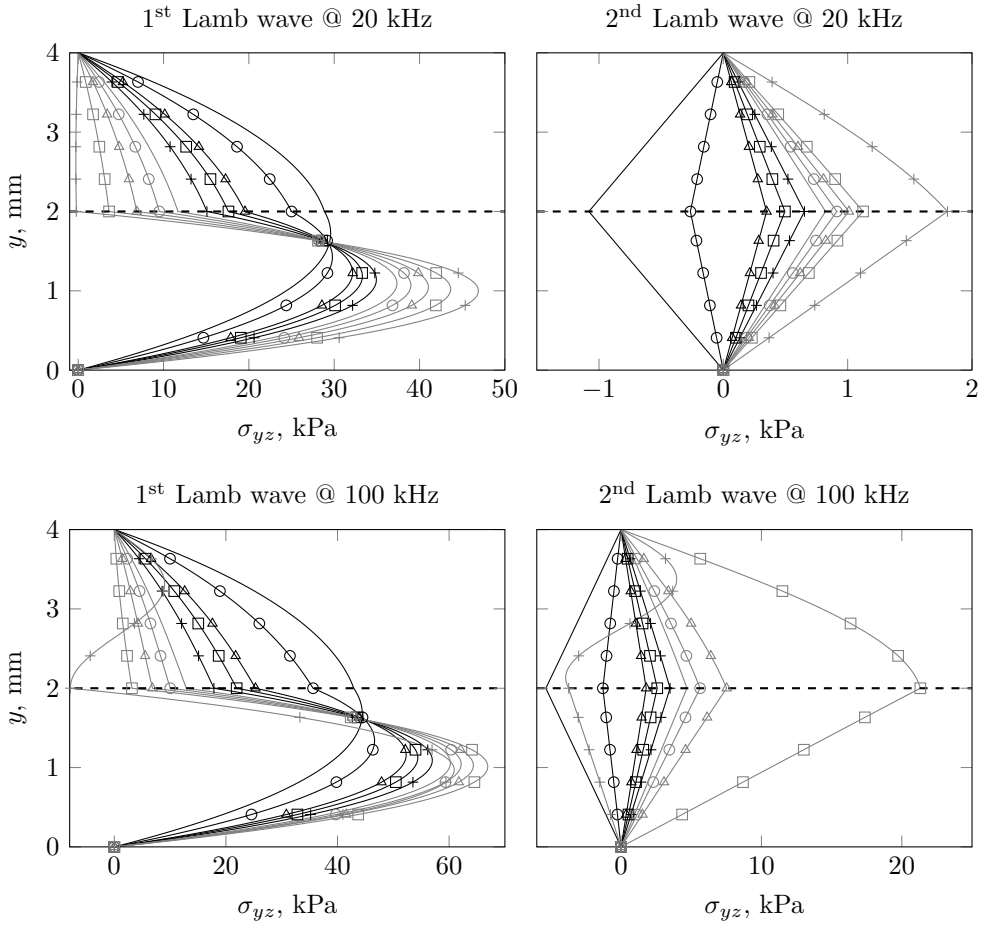

Figure 2.24: Through-thickness distribution of the transverse shear stress at 20 and 100 kHz resulting from the propagation of the first two Lamb wave modes for a 2 mm aluminium plate a 2 mm accretion ($\rho_{\mathrm{AL}} = 600\ \mathrm{kg\,m^{-3}}$, $\nu_{\mathrm{AL}} = 0.351$) and stiffness: 40 GPa (——), 20 GPa (—○—), 10 GPa (—△—), 8 GPa (—□—), 6 GPa (—+—), 4 GPa (——), 3 GPa (—○—), 2 GPa (—△—), 1 GPa (—□—), 0.1 GPa (—+—).

2.8.2.2 Influence of stiffness

The fundamental question related to the effectiveness of propagating waves in inducing delamination is how the stiffness of the build-up affects the generated stress. Analogously to the above paragraphs the through-thickness transverse shear stress distributions for accretions of different Young's moduli are compared here. The comparison is done at two different frequencies: 20 kHz, where the effect of higher-order AL-originating modes is not expected to play any role and 100 kHz where the higher-order AL-originating modes influence can be observed for low stiffnesses.

The interface shear stress generated by the first two Lamb waves at 20 kHz and 100 kHz is presented in Fig. 2.24. The distribution associated with the SH wave is shown in Fig. 2.25 – at 20 kHz on the left and at 100 kHz on the right.

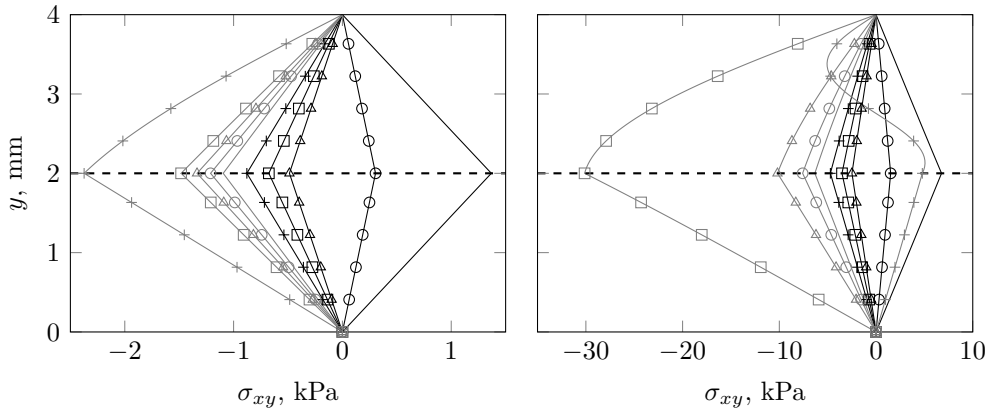

Figure 2.25: Through-thickness distribution of the transverse shear stress at 20 kHz (left) and 100 kHz (right) resulting from the propagation of the first SH wave mode for a 2 mm aluminium plate a 2 mm accretion ($\rho_{\mathrm{AL}} = 600\ \mathrm{kg\,m^{-3}}$, $\nu_{\mathrm{AL}} = 0.351$) and stiffness: 40 GPa (——), 20 GPa (—○—), 10 GPa (—△—), 8 GPa (—□—), 6 GPa (—+—), 4 GPa (——), 3 GPa (—○—), 2 GPa (—△—), 1 GPa (—□—), 0.1 GPa (—+—).

The flexural wave (1st Lamb mode) is discussed first. If the characteristic impedances of both layers are comparable the bilayer behaves very similarly to a single plate with a symmetric σ_{yz} distribution that has a peak in the mid-plane (see 40 GPa curve in Fig. 2.24). Along with the stiffness decreasing, the distribution tends to represent decoupled wave propagation, i.e. σ_{yz} is symmetrical only with respect to the mid-plane of the HL and goes to zero at the boundaries of HL. For instance at 20 kHz the interface shear stress for a 0.1 GPa build-up is almost zero (Fig. 2.24). This implies that if one follows exactly the HL asymptotes for a flexural wave, accretions of a very low stiffness behave as almost uncoupled and cannot be removed.

At 100 kHz the values of interface shear stress are slightly higher (by ca. 20 %), preserving the same distribution with the exception of the lowest E curve (0.1 GPa). In this configuration the first AL-originating asymptote starts to affect the bilayer motion. The interface shear stress benefits from the coupling and has a non zero value.

Both in-plane waves (S_0 and SH_0) have almost identical distributions, however as observed in the previous subsection the SH wave generated approximately 25% higher transverse shear stress at the interface. Contrary to the flexural wave, the in-plane bilayer modes when following the HL asymptote do not behave as decoupled and the stress distribution is not similar to the one of a clean single-layer plate. For the configurations considered in this section the interface transverse shear stress crosses zero for E between 10 and 20 GPa. When E is smaller than 10 GPa the interface shear stress grows with the stiffness of the build-up decreasing. One should however notice that S_0 and SH_0

provide interface transverse shear stress of more than one order of magnitude lower than the flexural mode at 20 kHz.

The interface shear stress grows significantly (around an order of magnitude) for S_0 and SH_0 waves when the frequency is increased from 20 kHz to 100 kHz as can be seen in Fig. 2.24 and Fig. 2.25. This is related to the fact that with growing frequency more AL-dominated modes cut-off. Whenever the bilayer curve is close to the AL asymptote, the interface shear stress increases rapidly.

The effectiveness of the in-plane wave modes is enhanced if they are excited in the region where the asymptotic solutions are strongly coupled. They seem to be suitable for removing low stiffness accretions ($E < 2$ GPa), especially if the above conditions are met. The flexural wave appears to be more effective for high-stiffness build-ups.

2.8.2.3 Parametric study

In order to examine potential of the guided waves for invoking delamination in the light of the mode selection criteria outlined above, a parametric study was performed. The numerical routine developed was used to compute wave characteristics for a range of different build-ups. The host structure properties were kept constant (2 mm aluminium layer), whereas the stiffness of the build-up was varied from $E_{\mathrm{AL}} = 0.1$ GPa to $E_{\mathrm{AL}} = 10$ GPa, with fixed $\rho_{\mathrm{AL}} = 900$ kg/m^3, $\nu_{\mathrm{AL}} = 0.351$ and $h_{\mathrm{AL}} = 2$ mm.

It has already been emphasised that the first two criteria are in conflict, hence a choice is connected with a trade-off between them. Therefore, the following procedure was

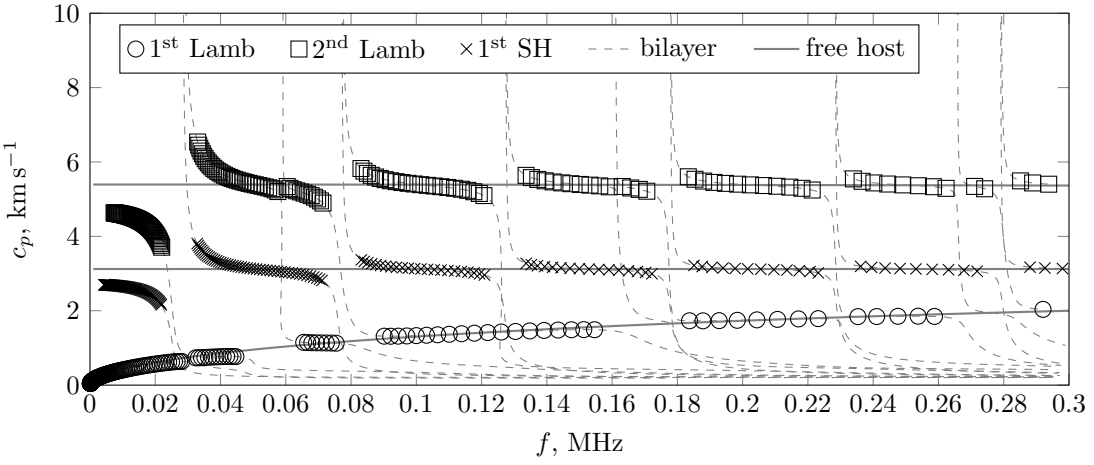

Figure 2.26: Illustration of how the frequency points are picked according to strain energy ratio criterion.

chosen in order to take into account all factors. Firstly the dispersion curves and power-normalised mode shapes are computed. Then they are interpolated over a common frequency vector (the GMM routine implemented provides results with fixed wavenumber increments). Finally, in order to account for energy propagation issues, only the waves on the ω–k plane for which no more than 60% of the total strain energy propagates along the build-up (ENR < 0.6) were chosen for the stress comparison. Although it is an arbitrarily chosen fraction, it enables one to exclude modes which do not seem to be useful as a consequence of their contribution to cohesive cracking and possibly high wave attenuation (if lossy build-up is considered). A sample result of this 'picking' procedure is shown in Fig.2.26. The mode labelling convention is such that a point on the bilayer mode curve is labelled as belonging to '1$^{\text{st}}$ Lamb' if it is aligned with the free-free HL 1$^{\text{st}}$ Lamb wave. The whole frequency range considered (0–200 kHz) was divided into four sub-ranges: 0–50, 50–100, 100–150 and 150–200 kHz. Higher frequencies are not discussed here. In each frequency range the maximum interface shear stress for each wave is shown on Fig. 2.27.

As it can be seen from Fig. 2.27 the stress generation capability of the 1$^{\text{st}}$ Lamb wave is the best for a higher stiffness build-up (here $E_{\text{AL}} = 8$ and 10 GPa). For the three highest values of E_{AL} shown here the 1$^{\text{st}}$ Lamb wave maximum stress values for a given frequency grow with the accretion stiffness, however for a given accretion they are very similar for all frequency ranges ($\approx$ 12 kPa for $E = 4$ GPa; $\approx$ 18 kPa for $E = 6$ GPa; $\approx$ 21.5 kPa for $E = 8$ GPa and $\approx$ 25 kPa for $E = 10$ GPa. In fact, stiff build-ups provide a strong coupling between the layers, hence the stress distribution associated with the bilayer flexural wave tends to the one related to the flexural wave in an homogeneous layer which has a peak in the mid-plane. The closer the build-up stiffness to the host stiffness is, the higher the peak. Over the frequency range considered the height of the peaks does not change significantly.

For low stiffness build-ups the stress generation capability of the 1$^{\text{st}}$ Lamb wave is lower. The first reason is that the HL does not see the constraint on one of its surfaces if the coupling is weak. Thus, the bilayer dynamics follow that of the free host, i.e. the shear stress at the boundaries of the HL goes to zero. This effect is disturbed by the AL-dominated modes which promote high stress (e.g. for $E_{\text{AL}} = 2$ GPa in the fourth frequency range). At high frequencies the effect of the ENR criterion is more dominant – many waves are not taken into account in the analysis which results in very low stress values for low stiffnesses.

The in-plane waves (2$^{\text{nd}}$ Lamb and 1$^{\text{st}}$ SH) show much better performance for low values of E_{AL}, where they are largely affected by the AL asymptotes. Similarly to the flexural wave case, one can look at the stress results in the light of the topology of the bilayer

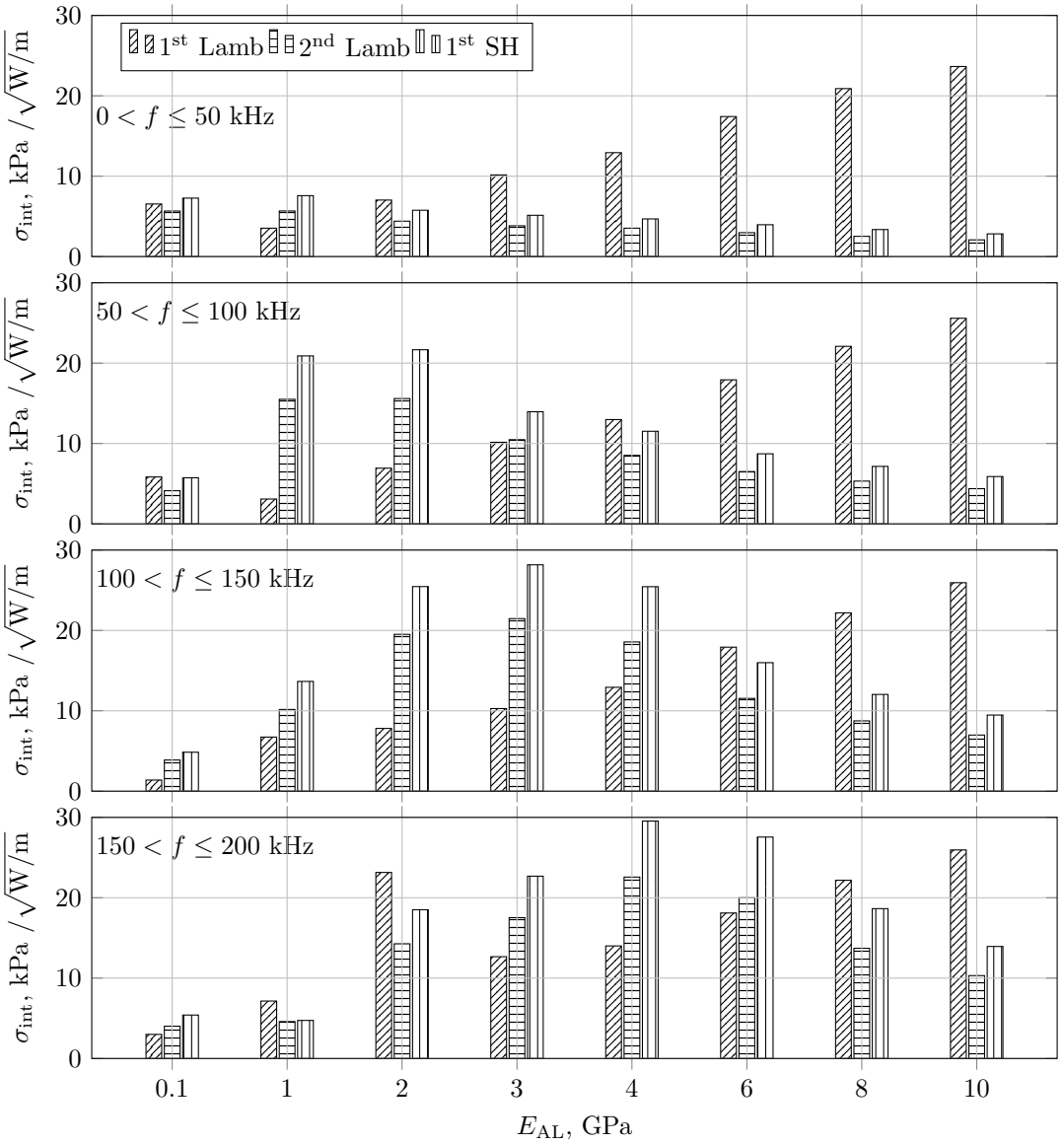

Figure 2.27: Maximum transverse interface shear stress that can be obtained in the stated frequency ranges. The stress is normalised with respect to unit power flow.

wave spectrum. In a single elastic layer the in-plane waves generate very low transverse shear stress until they are in the vicinity of another mode. Therefore a strongly coupled bilayer (high stiffness) follows this pattern providing very small interface stress which grow slowly with frequency. It is interesting to notice that the coupling between the wave in the layers is stronger for in-plane waves than for the flexural wave. For example, it can be seen in Fig. 2.26 that starting from zero frequency the 2$^{\text{nd}}$ Lamb wave mode does not follow the HL asymptote as precisely as the 1$^{\text{st}}$ Lamb wave mode does. Therefore even for a high stiffness build-up the bilayer stress distribution does not tend to the one related to the free-free plate but the presence of the coupling is clearly visible. For these reasons, the in-plane waves in a weakly coupled bilayer can accommodate very

large interface shear stress only when close to the AL asymptote. The crucial role here is played by the critical energy ratio (here ENR = 0.6) that restricts the AL-dominated modes in the comparison. In most configurations, the SH wave provides ca. 25% higher stress than the in-plane Lamb wave.

2.8.3 Implications for practical application

The results obtained using a plane strain wave model employed in this chapter cannot be directly compared to any benchmark figures, however they still provide a basis upon which some conclusions and recommendations for application of the method can be drawn. Firstly, it should be stated that to the author's best knowledge only the ice adhesion studies can be found in the literature. No results are available for any other accretions. Furthermore, the results for the strength of the ice to aluminium bond found in the literature are substantially different from each other and vary from 0.1 to 1.6 MPa depending on the type of ice, growing conditions and test procedure. Therefore, the scope for the reference to practical cases is rather limited.

Fig. 2.27 indicates that high stiffness accretions such as glaze ice can be the most easily removed with the flexural wave (1$^{\text{st}}$ Lamb wave). Assuming ice bond strength to be $\sigma_b = 1.5$ MPa the excitation should be able to inject between 5.15 and 4.58 kW m^{-1} of mechanical power into the waveguide in order to instantaneously remove ice over the whole frequency range considered (this refers to the range 103–91 W applied over a 20 mm wide line). The in-plane waves (2$^{\text{nd}}$ Lamb and 1$^{\text{st}}$ SH) would require 11.97 kW m^{-1} and 6.48 kW m^{-1}, respectively if excited in the highest frequency range considered (this refers to 239 W and 130 W, respectively applied to a 20 mm width).

For very low stiffness build-ups ($E_{\text{AL}} = 0.1$ GPa) the achievable interface stress is 0.327 MPa for the flexural wave, 0.283 MPa for the compressional wave and 0.363 MPa for the 1$^{\text{st}}$ SH wave, if 50 W is applied over a 20 mm wide line, which seems to be still promising for dealing with accretions that create weaker bonds. In order to formulate a more precise indication for a particular application (apart from icing), the adhesion strength values for other accretion-like bonds would have to be known.

The crucially important problem is whether a specified amount of power can be injected to a structure using available actuators. Although this needs to be studied in future, it should be emphasised that if a finite structure is considered subsequent reflections from the boundaries at the resonance would increase the stress level, and thus less power would be needed to induce debonding. Furthermore, the performance of the method can be improved by applying appropriate structural modifications of which some have been studied in detail in [25].

2.9 Conclusions

The feasibility of the wave-based method for invoking delamination was analysed from a theoretical perspective in this chapter with the aid of the GMM wave model. Fundamental wave characteristics of structures covered with unwanted accretions were specified and linked to the behaviour of weakly coupled systems. The topology of the bilayer dispersion curves was explained with the aid of the uncoupled asymptotic solutions. The importance of the energy distribution was highlighted and related to the attenuation of guided waves for lossy build-ups. The insight into the physical phenomena associated with wave propagation in bilayers enabled identifying conditions under which the interface stress associated with a propagating wave is high and likely to invoke delamination.

Based on the above, the influence of the thickness and the stiffness of the accreted layer was addressed in the parametric study. Achievable interface stress for a wide range of build-up Young's moduli gave on overview of the potential scope of application of the approach. The parametric study was concluded with a set of implications for application outlining theoretical power requirements for ultrasonic de-icing.

The free wave analysis which the current chapter originates from is informative and helps to understand the mechanisms behind wave-induced stress, but is difficult to be directly linked to a real world case. The modelling approach and physical analysis is extended in the next chapter by incorporating the possibility of calculating forced response and introducing a simple technique to represent a typical piezoelectric actuator.

Chapter 3

Wave excitation in structures with an undesired accretion - analytical approach

Free wave propagation analysis presented in Chapter 2 brings useful and interesting insight into the physics of structural waves in waveguides with accretions, but the resulting indications regarding the feasibility of invoking delamination or power requirements can only be treated as qualitative. Aiming at enhancing them with a reference to practical cases, mechanical excitation is introduced in this chapter. The approach is based on the analytical excitability functions originating from the elastodynamic complex reciprocity principle [109], which enables the partitioning of the injected power among propagating modes to be determined. The following sections facilitate understanding of how different modes contribute to the overall stress distribution in the light of the efficiency with which they are excited.

In the second part of the chapter an approximate piezoelectric excitation model (pin-force) is briefly outlined and employed for the analysis of a structure with accretion yielding approximate electrical power requirements. The limitations of the approximate approach and conformity with the assumptions in place are critically assessed. Both parts describing different excitation sources, namely mechanical forcing and piezoelectric actuation under pin-force assumption, are supported with a parametric study analogous to that in Section 2.8.2 in which the maximum achievable interface shear stress for accretions of various stiffnesses is computed with reference to input power.

3.1 Excitation of structural waves by mechanical forces and tractions

3.1.1 Analytical excitability for infinite plate-like structures

The far-field motion of a plate excited by a harmonic force is a sum of the contributions of all available modes at a given frequency. It is a weighted sum since some modes are strongly and others weakly excited under particular conditions. Wilcox [116] has proposed the term 'excitability' to describe the weighting coefficients of the superposition. From a physical viewpoint, excitability is defined as the surface displacement of a mode induced by a unit force per unit length (in the case of plane strain) or unit point force (3D case)[116]. The partial waves technique and global matrix method for model assembly are developed under the plane strain assumption [50], therefore it is assumed that the force is uniformly distributed along an infinite line parallel to the wavefront. The forced response model implemented here is based on [116–118]. This approach is commonly known as the normal mode expansion (NME) method and is derived from the acoustic complex reciprocity relation known from [109]. It should be stated here that it is only valid for propagating modes in lossless waveguides. Generalised excitability which is also applicable to damped waveguides can be straightforwardly derived from the real reciprocity relation as recently shown in [119].

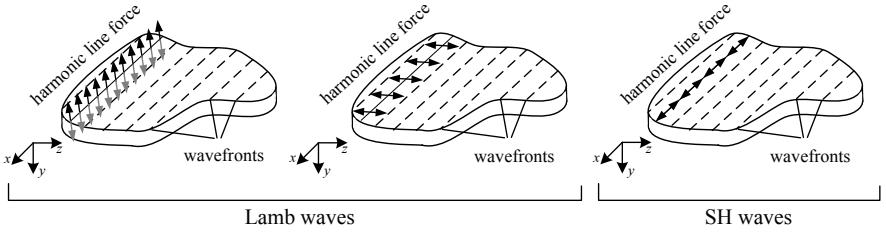

Figure 3.1: 2D excitability concept: a) Lamb waves, out-of-plane forcing; b) Lamb waves, in-plane forcing; c) SH waves, in-plane forcing.

Fig. 3.1 schematically presents the 2D excitability concept for Lamb and SH waves (as they are decoupled under the plane strain assumption) together with the labelling and coordinate system. The force may act in one of the three directions: (i) y: out-of-plane, exciting Lamb waves only; (ii) z: in-plane, parallel to the direction of propagation, exciting Lamb waves only; (iii) x: in-plane, perpendicular to the direction of propagation, exciting SH waves exclusively.

The derivation of guided wave excitability starts from recalling the acoustic complex reciprocity principle, which relates two wave fields, namely $\mathbf{v}^{(m)}$, $\boldsymbol{\sigma}^{(m)}$ and $\mathbf{v}^{(n)}$, $\boldsymbol{\sigma}^{(n)}$ driven by sources $\mathbf{F}^{n}$ and $\mathbf{F}^{(n)}$, respectively, to each other. The subscripts m, n distinguishing the solutions correspond to two propagating waves. The reciprocity relation is derived by adding the two aforementioned wave solutions to each other (see [109] for details), which yields:

$$\nabla \cdot \left(-\mathbf{v}^{(n)*} \cdot \boldsymbol{\sigma}^{(m)} - \mathbf{v}^{(m)} \cdot \boldsymbol{\sigma}^{(n)*}\right) = \mathbf{v}^{(n)*} \cdot \mathbf{F}^{(m)} + \mathbf{v}^{(m)*} \cdot \mathbf{F}^{(n)*} \tag{3.1}$$

where $\nabla \cdot \{\ \}$ is the divergence operator.

It is recalled that the wave field does not change along the x direction as a consequence of the plane wave assumption and that:

$$\mathbf{v}^{(m)}(y,z) = \mathbf{v}^{m}(y) \exp\left[-\jmath k^{(m)} z\right] \tag{3.2}$$

If the source terms on the RHS are set to zero, after appropriate transformations and integration across the waveguide one gets:

$$\begin{aligned} \jmath\left(k^{(m)} - k^{(n)*}\right) \int_{\Omega} \left(-\mathbf{v}^{(n)*} \cdot \boldsymbol{\sigma}^{(m)} - \mathbf{v}^{(m)} \cdot \boldsymbol{\sigma}^{(n)*}\right) \cdot \hat{\mathbf{z}}\, \mathrm{d}y = \\ \left(-\mathbf{v}^{(n)*} \cdot \boldsymbol{\sigma}^{(m)} - \mathbf{v}^{(m)} \cdot \boldsymbol{\sigma}^{(n)*}\right) \Big|_{y=0}^{y=d} \end{aligned} \tag{3.3}$$

where $\hat{\mathbf{z}}$ is the unit vector in the z direction and Ω is the cross-section domain.

The boundaries of the waveguide are traction-free, therefore the RHS of Eq. (3.3) is zero, which yields the wave mode orthogonality relation:

$$\jmath\left(k^{(m)} - k^{(n)*}\right) \int_{\Omega} \left(-\mathbf{v}^{(n)*} \cdot \boldsymbol{\sigma}^{(m)} - \mathbf{v}^{(m)} \cdot \boldsymbol{\sigma}^{(n)*}\right) \cdot \hat{\mathbf{z}}\, \mathrm{d}y = 0 \tag{3.4}$$

where the integral on the LHS is commonly written as:

$$P^{(mn)} = \frac{1}{4} \int_{\Omega} \left(-\mathbf{v}^{(n)*} \cdot \boldsymbol{\sigma}^{(m)} - \mathbf{v}^{(m)} \cdot \boldsymbol{\sigma}^{(n)*}\right) \cdot \hat{\mathbf{z}}\, \mathrm{d}y \tag{3.5}$$

so that the wave mode orthogonality relation becomes:

$$\jmath\left(k^{(m)} - k^{(n)*}\right) 4P^{(mn)} = 0 \tag{3.6}$$

Eq. (3.5) is very similar in appearance to the definition of power flow (Poynting vector) from Eq. (2.22). In fact if $m = n$, Eq. (3.5) becomes:

$$P^{(mm)} = \frac{1}{2} \int_{\Omega} -\mathbf{v}^{(m)*} \cdot \boldsymbol{\sigma}^{(m)} \cdot \hat{\mathbf{z}} \, \mathrm{d}y \tag{3.7}$$

and the real part of $P^{(mm)}$ gives the average power flow associated with the wave mode m.

Since only propagating modes are considered here, k_m, k_n are real and Eq. (3.6) states that if $k_m \neq k_n$, then no power flows, i.e. $P^{(mn)} = 0$. Auld [109] presents an in depth discussion on the meaning of wave orthogonality relation in different regimes, i. e. when wavenumbers are imaginary or complex. A similar procedure can be applied to Eq. (3.1) yielding the excitability of the guided wave by a surface load. The reciprocity relation is written for two wave fields – the excited wave field $\mathbf{v}$, $\boldsymbol{\sigma}$ and the modal wave field $\mathbf{v}^{(n)}$, $\boldsymbol{\sigma}^{(n)}$. The excited wave field is assumed to be a weighted sum of modal contributions, with weights corresponding to particular waves amplitudes:

$$\begin{aligned} \mathbf{v} &= \sum_m a^{(m)}(z)\mathbf{v}^{(m)}(y) \\ \mathbf{u} &= \sum_m a^{(m)}(z)\mathbf{u}^{(m)}(y) \\ \boldsymbol{\sigma} &= \sum_m a^{(m)}(z)\boldsymbol{\sigma}^{(m)}(y) \\ &\text{etc.} \end{aligned} \tag{3.8}$$

The traction force source is assumed to act on the upper boundary of the waveguide $y = d$ and the body forces are neglected, so that Eq. (3.1) becomes:

$$\frac{\partial}{\partial z}\left(-\mathbf{v}^{(n)*} \cdot \boldsymbol{\sigma} - \mathbf{v} \cdot \boldsymbol{\sigma}^{(n)*}\right) \cdot \hat{\mathbf{z}} = \frac{\partial}{\partial y}\left(\mathbf{v}^{(n)*} \cdot \boldsymbol{\sigma} + \mathbf{v} \cdot \boldsymbol{\sigma}^{(n)*}\right) \cdot \hat{\mathbf{y}} \tag{3.9}$$

where $\hat{\mathbf{y}}$ is the unit vector in the y direction. After integration across the waveguide, and recalling Eq. (3.4), Eq. (3.5) one gets:

$$\frac{\partial}{\partial z} \sum_m 4a^{(m)} P^{(mn)} \exp\left[\jmath k^{(n)*} z\right] = \left(\mathbf{v}^{(n)*} \cdot \boldsymbol{\sigma} + \mathbf{v} \cdot \boldsymbol{\sigma}^{(n)*}\right) \exp\left[\jmath k^{(n)*} z\right] \cdot \hat{\mathbf{y}} \Big|_{y=h} \tag{3.10}$$

Note that for a traction-free plate $\boldsymbol{\sigma}^{(n)} \cdot \hat{\mathbf{y}} = 0$. The LHS is non-zero only if $m = n$, so:

$$4P^{(nn)}\left(\frac{\partial}{\partial z} + \jmath k^{(n)}\right) a^{(n)}(z) = \left(\mathbf{v}^{(n)*} \cdot \boldsymbol{\sigma}\right) \cdot \hat{\mathbf{y}} \Big|_{y=h} \tag{3.11}$$

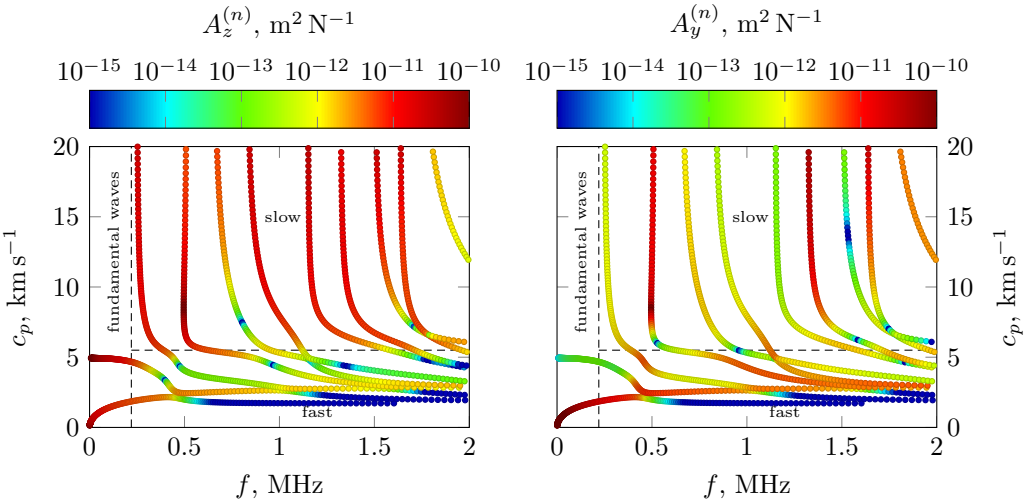

Figure 3.2: $A_z^{(n)}$ and $A_y^{(n)}$ excitability imposed on the Lamb wave dispersion curves for a 2 mm aluminium plate covered with a 2 mm glaze ice accretion. Graphs are divided in regions which at frequencies higher than the first cut-off frequency correspond to the low or high group velocity.

Solving the above equation for $a^{(n)}(z)$ brings to the expression for modal excitability:

$$a_i^{(n)}(z) = \frac{v_i^{(n)*}(h)\exp\left[-\jmath k^{(n)}z\right]}{4P^{(nn)}} \int_{-L/2}^{L/2} \exp\left[\jmath k_n \gamma\right]\sigma_i(\gamma)\,\mathrm{d}\gamma \tag{3.12}$$

where σ_i is the external traction applied over length L of the upper surface of the plate, and the subscript i refers to the direction.

If the surface excitation is a line traction resulting from line force F_i understood as a force per unit width acting in the direction i the equation reduces to:

$$a_i^{(n)}(z) = \frac{v_i^{(n)*}(h)\exp\left[-\jmath k^{(n)}z\right]}{4P^{(nn)}} F_i \tag{3.13}$$

Eq. (3.13) provides an expression for the excited wave amplitude of mode n if a surface force F is applied in the direction i. Note, that the modal field quantities are normalised with respect to the unit power flow ($P^{(nn)} = 1$) what simplifies the above equations.

The wave mode excitability as discussed e.g. in [117] can be thought of as the wave mode receptance, i. e. the transfer function between the induced surface displacement associated with a chosen wave mode and the applied force. With the aid of Eq. (3.8) and Eq. (3.13), one writes (omitting the time harmonic terms):

$$A_i^{(n)} = \frac{a_i^{(n)}u_i^{(n)}}{F_i} = \frac{v_i^{(n)*}(h)}{4}u_i^{(n)}(h) = \frac{-\jmath\omega u_i^{(n)*}(h)}{4}u_i^{(n)}(h) \tag{3.14}$$

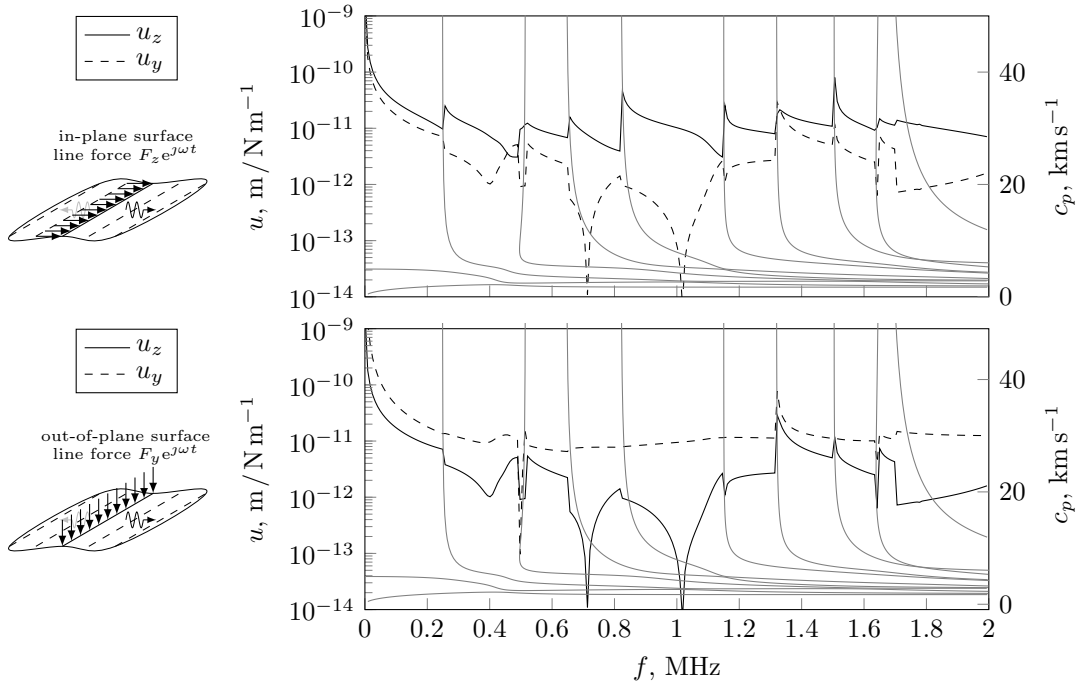

Figure 3.3: The total displacement (sum of all modes) associated with Lamb waves excited with a surface line force on a 2 mm aluminium plate covered with a 2 mm glaze ice accretion. Corresponding phase velocity dispersion curves are shown in grey.

where $A_i^{(n)}$ is the induced displacement in direction i associated with mode n and resulting from a force acting in direction i.

It is also possible to calculate cross-excitability (or transfer wave mode receptance) when the direction of the induced displacement of interest is different from the direction of the applied force:

$$A_{i,j}^{(n)} = \frac{a_i^{(n)} u_j^{(n)}}{F_i} = \frac{v_i^{(n)*}(h)}{4} u_j^{(n)}(h) = \frac{-\jmath\omega u_i^{(n)*}(h)}{4} u_j^{(n)}(h) \tag{3.15}$$

Excitability of guided waves by line forces acting along the z and y directions computed for a sample case are shown in Fig. 3.2. The response of the structure is rather complex, but some general observations can be made. In order to do so, the f–c_p plane is divided into three regions – fundamental waves region which is the low frequency part where only the fundamental modes propagate, 'slow region' encapsulating the dispersion curves above the first cut-on frequency and up to the first host layer HL asymptote (see Section 2.3 for details), i.e. the vertical sections of the dispersion curves, and the 'fast region' that includes the waves that fit below the first HL asymptote (in Fig. 3.2,

5 $\mathrm{km\,s^{-1}}$).The regions' descriptors 'slow' and 'fast' correspond to the associated group velocity.

At low frequencies the in-plane forcing excites both the flexural and the compressional Lamb waves very well, whereas for the out-of-plane force the flexural wave is strongly predominant. Waves in the 'slow' region (including the build-up dominated waves) are better excited with the in-plane loading since most of the high frequency structural waves originate from so called thickness-shear modes when they cut off. Thickness-shear modes are associated with a predominant in-plane surface particle displacement as opposed to the thickness-stretch modes for which the out-of-plane component is prevalent. In the 'fast' region the out-of-plane forcing performs better which is related to the fact that at high frequency (short wavelength) the waves tend to follow the flexural-shear behaviour in order to finally evolve into a surface wave. The blue spots in the 'fast region' correspond to the waves that propagate along the surface of the build-up which is why they cannot be excited by a force that acts on the host surface.

3.1.2 Power partitioning

In principle, it might be beneficial if the input force excites all possible modes at a given frequency since they would all contribute to overcoming the shear adhesion strength of the build-up. It is safe to assume that their superposition will increase the interface stress for they do not share the same phase in space and in time and they propagate with different group velocities. However, modes are not excited with the same efficiency. The guided waves' excitability as introduced in the preceding section provides information on how well a wave is excited but only from a viewpoint of a particle displacement at a surface of the plate. A more indicative measure, namely power flow, can be employed as it captures the behaviour of the whole structure. Excitability enables to determine how the power produced by the excitation is partitioned between the waves.

Any loading injects power to the structure. Field and energy distributions across the thickness are normalised with respect to the total power flow trough the unit-width cross-section of the plate in the direction of propagation, according to the Poynting Theorem. The time-averaged complex Poynting vector describing the power flow associated with a free wave is defined in Eq. (2.22). Recalling that the excited wave field is written as an expansion of normal modes (see Eq. (3.8)), Eq. (2.22) is rewritten to represent the power flow associated with a forced wave as:

$$P^{(n)}_{\text{forced}} = \mathrm{Re}\left\{ \frac{1}{2} \int_{\Omega} - \left(a^{(n)} \mathbf{v}^{(n)} \right)^{*} \cdot \left(a^{(n)} \boldsymbol{\sigma}^{(n)} \right) \cdot \hat{\mathbf{z}} \, \mathrm{d}y \right\} \tag{3.16}$$

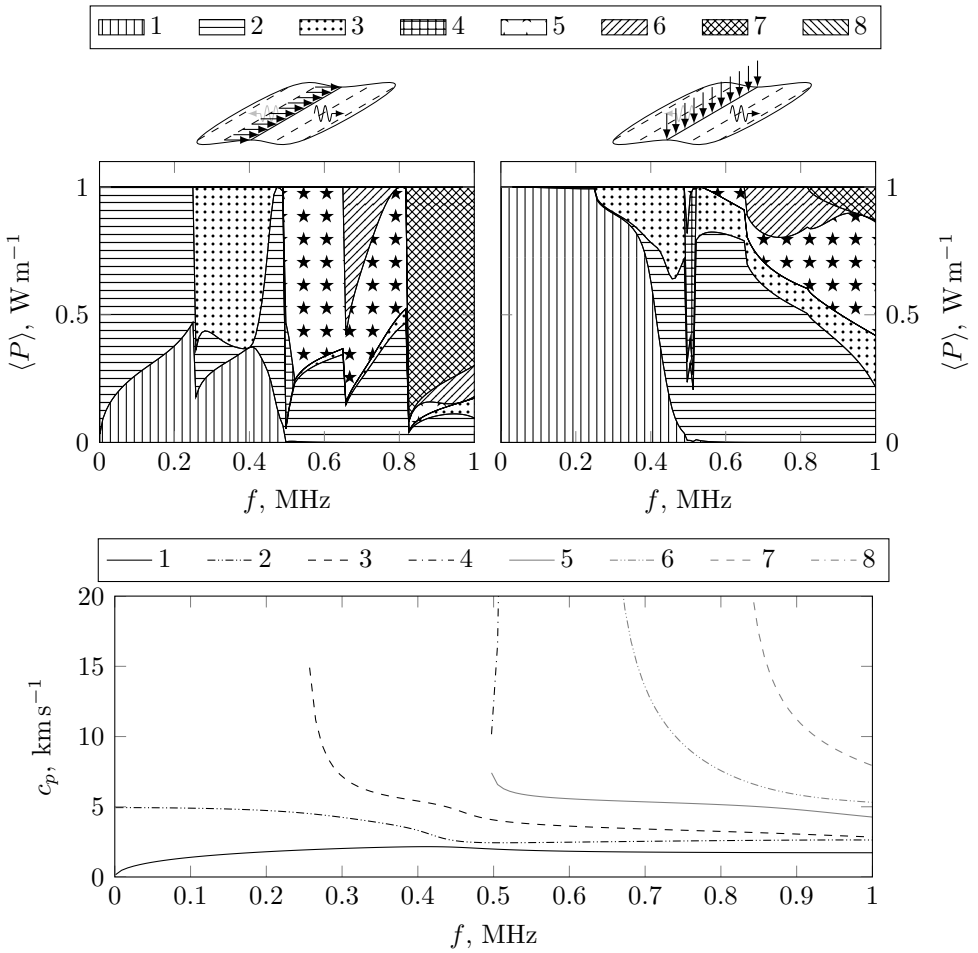

Figure 3.4: Power partitioning between the propagating Lamb wave modes in a 2 mm aluminium plate covered with a 2 mm glaze ice accretion given a 1 W m^{-1} line source exciting the structure in different directions. The dispersion curves are presented in the bottom figure for mode labelling reference.

Denoting free power flow as $\left\langle P^{(n)} \right\rangle$ for clarity, one writes:

$$P^{(n)}_{\text{forced}} = a^{(n)*} a^{(n)} \left\langle P^{(n)} \right\rangle \tag{3.17}$$

If one assumes that 1 W m^{-1} is supplied by a line force acting in direction i, the power injected to each mode can be calculated from the excited wave amplitudes as given in Eq. (3.13). Since the mode shapes are power-normalised, the power flow associated with a mode as a response to a given excitation becomes:

$$P^{(n)}_{\text{forced}} = a^{(n)*} a^{(n)} \tag{3.18}$$

In order to evaluate power partitioning, one needs first to compute the forced power flow associated with each propagating wave as a response to force excitation. The results are then rescaled with respect to the sum of all forced power flows. The approach presented

above does not deal with power transfer between the actuator and the structure, but gives a useful insight as to how well a mode is driven for a particular direction of excitation. A power partitioning pattern for a sample structure is shown in Fig.3.4.

Although relative phase relationships between respective displacement and stress components are fixed, the phase of the mode shape is arbitrary. Therefore, in order to enable power delivery to the structure in the model (so that $\frac{v^{(n)}_{i,\,\mathrm{modal}(h)}}{4} F^i$ is real), one needs to ensure that the power-normalised surface modal displacement component in direction i is purely imaginary by appropriate scaling. This comment does not refer to some physical phenomenon, but only to the attention that needs to be given while implementing the excitability model that supports interpretable outcome.

3.1.3 Parametric study

The partitioning of the injected power between propagating modes is now included in the parametric study on interface shear stress achievable for accretions with certain Young's moduli – analogous to that presented in Section 2.8.2. The host structure properties were kept constant (2 mm aluminium layer), whereas the stiffness of the build-up was varied from $E_{\mathrm{AL}} = 0.1$ GPa to $E_{\mathrm{AL}} = 10$ GPa, with fixed $\rho_{\mathrm{AL}} = 900$ kg/m^3, $\nu_{\mathrm{AL}} = 0.351$ and $h_{\mathrm{AL}} = 2$ mm. The procedure remains the same (as in Section 2.8.2) with the exception that the generated stress is shown as contributions of propagating waves for a given direction of excitation assuming that the line source supplies 1 W m^{-1} of mechanical power. Hence, all stress values quoted hereafter are given per $\sqrt{1\mathrm{W m}^{-1}}$. The results are presented in Fig. 3.5. The maximum stress was chosen with respect to the sum of all stress components accounting for the phase difference. However, to facilitate presentation particular waves' contributions to stress are plotted as magnitudes (neglecting the phase difference). Hence it is expected that the total stress values presented below are overestimated, especially for mid-stiffness build-ups.

Two effects lie behind the shape of the bars in Fig. 3.5: one is power partitioning, i.e. how strongly particular waves are excited with respect to the power flow, whereas the other is how 'good' are particular waves in generating interface shear stress. For example, it has already been shown in Fig. 3.2 that the out-of-plane forcing (along y) excites almost only the first Lamb wave (flexural), whereas the in-plane loading (along z) excites both the first and the second (compressional) Lamb waves with the compressional wave being dominant at low frequencies. However, as the compressional Lamb wave provides much lower interface shear stress, the stress resulting from an in-plane forcing for $E_{\mathrm{AL}} = 0.1$ GPa appears as predominantly associated with the 1^{st} Lamb mode in Fig. 3.5.

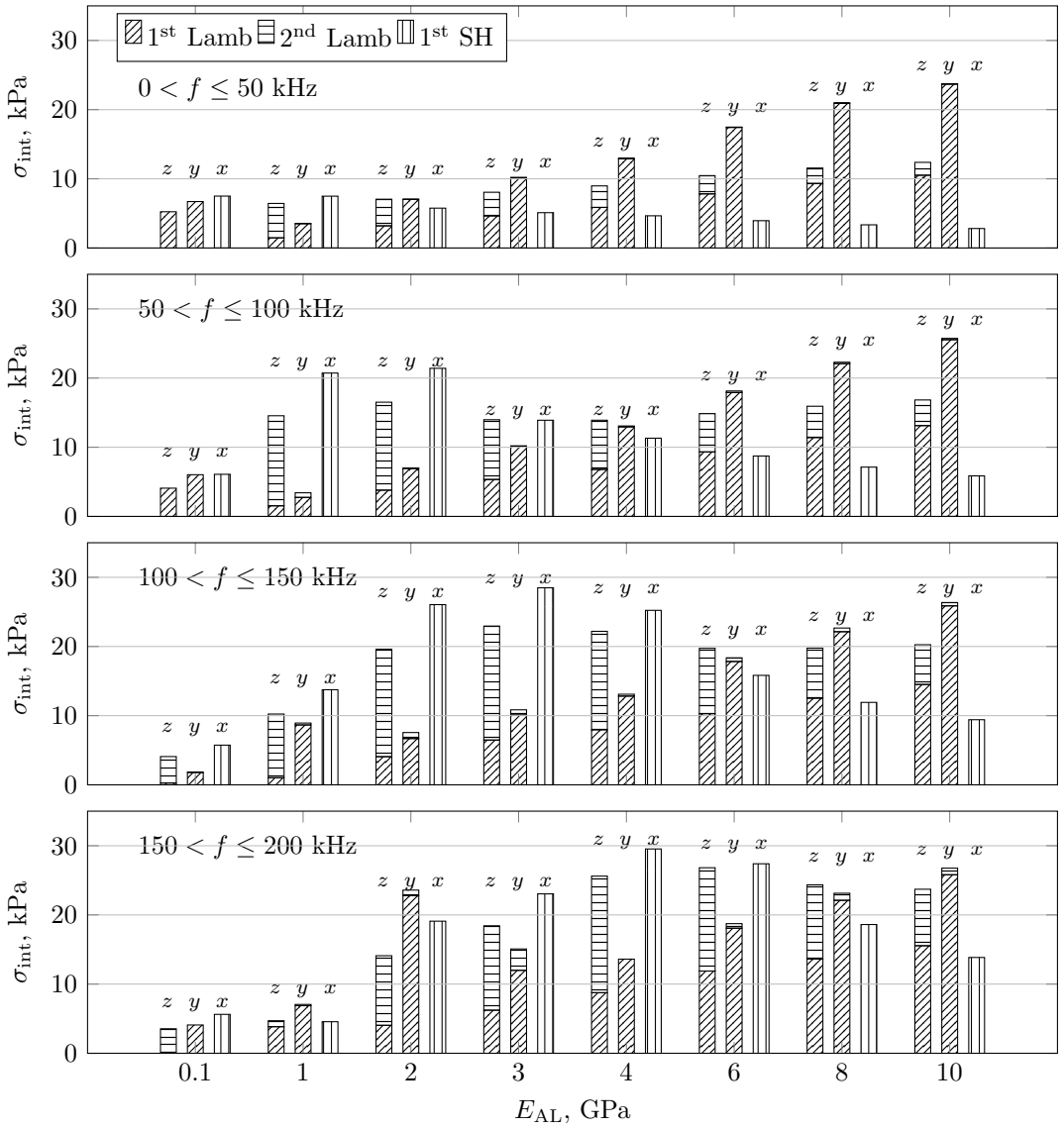

Figure 3.5: Maximum transverse interface shear stress that can be obtained in the stated frequency ranges due to a line force of input power 1 W m^{-1} acting along the x, y or z direction (as denoted over the bars). Structural configuration and parameters are outlined in Section 2.8.2.

A line force oriented along y-axis excites mainly the flexural Lamb wave which was shown to accommodate high interface shear stress in Section 2.8.2. The stress generation capability grows with the accretion stiffness E_{AL} (except two cases) and is predominant among other loading variants for high E_{AL} (8, 10 GPa). Contribution of the second Lamb waves for this excitation is insignificant.

An in-plane loading along z and x axes excites both Lamb waves and the SH wave, respectively. The contributions to the total interface shear stress associated with the compressional Lamb wave and the fundamental SH wave grow with frequency, whereas the one due to the flexural wave propagation grows with E_{AL}. As shown in Section 2.8.2

the compressional Lamb wave is associated with a relatively low interface shear stress unless close to the build-up dominated asymptote. This explains why at higher frequencies, i.e. when more higher-order modes propagate, the stress generated by the 2$^{\text{nd}}$ Lamb wave grows with frequency.

The interface stress associated with the in-plane waves drops with the increase in E_{AL} in the first frequency range from ca. 7.5 kPa for $E_{\text{AL}} = 0.1$ GPa to ca. 2.8 kPa for $E_{\text{AL}} = 10$ GPa (these are related to the SH wave, see Fig.3.5). Furthermore, the stress generated by both the SH and the second Lamb waves experiences a peak that shifts toward higher E_{AL} with the increase of frequency (at $E_{\text{AL}} = 2$ for $50 < f \leq 100$ kHz, at $E_{\text{AL}} = 3$ for $100 < f \leq 150$ kHz, at $E_{\text{AL}} = 4$ for $150 < f \leq 200$ kHz).

Surprisingly, for low values of E_{AL} the generated interface stress drops with frequency. Subsequent bilayer waves start to propagate and draw most of the power supplied, thus less power can contribute to invoking delamination.

The aforementioned analysis indicates that an in-plane omnidirectional actuation could give promising results, as the effects of both Lamb and SH waves would be superimposed. Following Fig. 3.5, for glaze ice accretion it would be possible to achieve the interface shear stress of ca. 1.5 MPa if 1.2 kW m^{-1} is applied in the fourth frequency range (this corresponds to 24 W over a 20 mm wide line). The flexural Lamb wave excited by an out-of-plane or in-plane force is found to accommodate the highest stress for high-stiffness accretions.

The in-plane waves are better suited to be applied to mid-stiffness accretions where the influence of the build-up dominated modes is significant. It is observed, however, that the SH wave seems to provide better results than the compressional Lamb wave.

In some cases the line force excites waves that do not generate high interface stress but draw significant power from the source. Furthermore, if a lossy accretion is considered this power is dissipated. The optimal design of the excitation would prohibit the power flow into these waves and enhance the excitation of waves that provide high interface stress, so that the maximum power available from the source can be utilised for invoking delamination.

3.2 Excitation of structural waves by piezoelectric actuators

Line forces provide a means of conducting a qualitative analysis accounting for modal excitability but lacks in a direct reference to a several aspects of practical excitation are

lacking in the model. As a step towards this aim, a piezoelectric actuator is introduced in this section. Piezoelectric actuators have become a standard for NDT/SHM solutions and they are particularly widely used for exciting structural waves. Various approaches for modelling wave excitation with piezoelements were discussed in Section 1.2.3.2. In the following paragraphs the analytical excitability (NME) approach to piezo-actuation is presented under the assumption that the dynamics of the piezo and the structure are fully uncoupled.

3.2.1 Piezoelectric constitutive equations

The piezoelectric actuator modelled is not modelled per se in this chapter, as under the aforementioned assumption it is represented by a set/distribution of equivalent mechanical forces. However, for the sake of consistency the basic relationships are outlined here. The piezoelectric effect briefly introduced in Section 1.2.3 is mathematically described by the constitutive equations of the piezoelectric material. Four forms of the constitutive equations referring to various configurations of the coefficients are used in the literature [120], of which two are recalled below:

- e form (stress form):

$$\begin{Bmatrix} \boldsymbol{\sigma} \\ \mathbf{D} \end{Bmatrix} = \begin{bmatrix} \mathbf{C}^{\mathrm{E}} & -\mathbf{e}^{\top} \\ \mathbf{e} & \boldsymbol{\varepsilon}^{\epsilon} \end{bmatrix} \begin{Bmatrix} \boldsymbol{\epsilon} \\ \mathbf{E} \end{Bmatrix} \tag{3.19}$$

- d form (strain form):

$$\begin{Bmatrix} \boldsymbol{\epsilon} \\ \mathbf{D} \end{Bmatrix} = \begin{bmatrix} \mathbf{S}^{\mathrm{E}} & \mathbf{d} \\ \mathbf{d} & \boldsymbol{\varepsilon}^{\sigma} \end{bmatrix} \begin{Bmatrix} \boldsymbol{\sigma} \\ \mathbf{E} \end{Bmatrix} \tag{3.20}$$

In the above $\mathbf{E}$ represents the electric field, $\mathbf{D}$ represents the dielectric displacement, $\mathbf{C}^{\mathrm{E}}$ and $\mathbf{S}^{\mathrm{E}}$ are the stiffness and compliance matrices measured at zero electric field, $\mathbf{e}$ and $\mathbf{d}$ are the piezoelectric stress and piezoelectric strain coefficient matrices, respectively and finally $\boldsymbol{\varepsilon}^{\epsilon}$ and $\boldsymbol{\varepsilon}^{\sigma}$ are the permittivity matrices measured at zero strain and zero stress conditions, respectively.

The material structure of typical piezoceramics can be classified as transversely isotropic, therefore 5 stiffness constants suffice to describe their elastic behaviour. PZT actuators are usually poled along the axis corresponding to the material axis of symmetry. Given the coordinate system adopted in this thesis (z is aligned with the waveguide), the stiffness matrix for the piezoelectric with respect to the material symmetry can be written

Table 3.1: Subscripts for piezoelectric material constants in physical and material coordinates.

physical	xx	yy	zz	yz	xz	xy
material	11	33	22	5 or 31	6 or 12	4 or 32

as:

$$\mathbf{C} = \begin{bmatrix} C_{xx} & C_{xy} & C_{xz} & 0 & 0 & 0 \\ C_{xy} & C_{yy} & C_{xz} & 0 & 0 & 0 \\ C_{xz} & C_{xz} & C_{zz} & 0 & 0 & 0 \\ 0 & 0 & 0 & C_{xyxy} & 0 & 0 \\ 0 & 0 & 0 & 0 & \frac{C_{xx}-C_{xz}}{2} & 0 \\ 0 & 0 & 0 & 0 & 0 & C_{xyxy} \end{bmatrix} \tag{3.21}$$

where y is the poling axis.

The piezoelectric coefficient matrix is not fully populated and usually takes on of the following forms (with respect to the above):

$$\mathbf{e} = \begin{bmatrix} 0 & e_{yxx} & 0 \\ 0 & e_{yyy} & 0 \\ 0 & e_{yxx} & 0 \\ 0 & 0 & e_{zyz} \\ 0 & 0 & 0 \\ e_{xxy} & 0 & 0 \end{bmatrix} \quad \text{or} \quad \mathbf{d} = \begin{bmatrix} 0 & d_{yxx} & 0 \\ 0 & d_{yyy} & 0 \\ 0 & d_{yxx} & 0 \\ 0 & 0 & d_{zyz} \\ 0 & 0 & 0 \\ d_{xxy} & 0 & 0 \end{bmatrix} \tag{3.22}$$

Finally the permittivity matrix,

$$\boldsymbol{\varepsilon}^{\epsilon} = \begin{bmatrix} \varepsilon_{xx} & & \\ & \varepsilon_{yy} & \\ & & \varepsilon_{xx} \end{bmatrix} \tag{3.23}$$

The above equations are written with respect to the physical coordinate system adopted in this thesis. The corresponding subscripts in local material coordinates (which are usually used by the manufacturers) are listed in Tab. 3.1.

One needs to pay particular attention to the labelling convention when using any commercial software as it varies significantly. A common oversight regarding reducing the 3D piezoelectric equation under plane strain or plane stress assumption has been recently reported in [121] pointing out that in many cases only one of the equations is used for reduction.

3.2.2 Analytical excitability for modelling piezo-actuation

The piezo-actuated wave amplitudes can be calculated using the excitability approach only if the interaction between the actuator and the structure and the actuator dynamics are neglected. The effect of the actuation is represented by a traction distribution and is frequency invariant. Both the mechanical waveguide and the actuator are modelled in plane strain. The following derivations are based on [93, 122]. It should also be stated that the actuator is assumed to operate linearly.

3.2.2.1 Mechanical wave response under pin-force assumption

A typical PZT monolithic actuator is poled along the thickness and the dimensions of the actuator are such that the thickness is much smaller than the other dimensions (this is often called a d_{31} or 3–1 configuration). The two faces perpendicular to the thickness are covered with electrodes and one of these electrodes is bonded to the surface of the waveguide. The actuator, when driven with voltage deforms inducing traction in the substrate. For d_{31} actuators the piezo-induced traction acts along the z axis and only Lamb waves can be excited.

The pin-force model enables adopting a simplified representation of the effect of piezoelectric actuation. The pin-force assumptions are the following: (i) the actuator's dynamics is neglected; (ii) the coupling with the structure is assumed to have no effect on the strain induced in the actuator; (iii) the bonding layer is of negligible thickness. Practically the above assumptions indicate that the Young's modulus–thickness product of the actuator is considerably smaller than the one of the structure so that they may be treated as decoupled. The predicted response is valid only at low frequencies when the dynamics of the actuator does not play a significant role.

The excited wave amplitude as a response to a z-oriented surface traction t applied over length L along the waveguide can be calculated from excitability functions. Let us recall Eq. (3.12):

$$a_z^{(n)}(z) = \frac{v_z^{(n)*}(h)\exp\left[-\jmath k^{(n)} z\right]}{4} \int_{-L/2}^{L/2} \exp\left[\jmath k_n \gamma\right] t(\gamma)\,\mathrm{d}\gamma \tag{3.24}$$

The desired traction distribution that represents piezoelectric actuator can be readily substituted. If the bonding layer is assumed to be very thin or neglected, piezo-induced traction is confined to the edges of the actuator (the pin-force assumption). In this case the spatial traction distribution is written as:

$$\sigma = t_0\left[\delta(z - L/2) + \delta(z + L/2)\right] \tag{3.25}$$

where t_0 is the amplitude of the traction under the pin-force assumption (in this case it is a force per unit width).

The integral from the right hand side of Eq. (3.24) becomes

$$\int_{-L/2}^{L/2} \exp\left[\jmath k_n \gamma\right] t(\gamma)\, \mathrm{d}\gamma = \int_{-L/2}^{L/2} \exp\left[\jmath k_n \gamma\right] t_0 \left[\delta(\gamma - L/2) + \delta(\gamma + L/2)\right]\, \mathrm{d}\gamma = 2\jmath t_0 \sin k_n L/2 \tag{3.26}$$

The amplitude of the traction t_0 can be found if the character of the actuator-structure interaction is assumed to be quasi-static and the actuator is modelled as uni-axial (rod-like) with linear through-thickness strain distribution. The free displacement at its end can be found from the constitutive equations,

$$u_{\mathrm{PZT,\ free}} = \epsilon_{zz} L = d_{yz} E_y L = \frac{d_{yz} v}{h_{\mathrm{PZT}}} L \tag{3.27}$$

where h_{PZT} is the thickness of the actuator, d_{yz} is the piezoelectric strain coefficient, E_y is the electric field across the thickness of the actuator and v is the driving voltage.

If bonded to a waveguide the actuator sees the substrate as a constraining stiffness. The force transmitted to the substrate is related to the mechanical stiffness of the actuator and the difference between the free displacement and the induced displacement (note the difference with [122]).

$$t_0 = k_{\mathrm{PZT}} \left[u_{\mathrm{PZT,\ free}} - u(L/2, h)\right] \tag{3.28}$$

where k_{PZT} is the static stiffness of the uniaxial PZT actuator (in plane strain) given as (from the constitutive equations):

$$k_{\mathrm{PZT}} = \frac{h_{\mathrm{PZT}}}{S_{zz}^E L} \tag{3.29}$$

with S_{zz}^E being the element of the compliance matrix.

It is common to express Eq. (3.28) in terms of the ratio between the dynamic stiffness of the structure and the static stiffness of the actuator. The former is straightforwardly obtained from Eq. (3.14) which describes the wave receptance

$$k_{\mathrm{structure}} = \frac{1}{\sum_{n=1}^{N} A_z^{(n)}} \tag{3.30}$$

so that the stiffness ratio becomes

$$r(\omega) = \frac{k_{\mathrm{structure}}}{k_{\mathrm{PZT}}} \tag{3.31}$$

Finally, the piezoelectric equivalent force is given as

$$t_0 = \frac{r(\omega)}{1 + r(\omega)} k_{\mathrm{PZT}} u_{\mathrm{PZT,\ free}} \tag{3.32}$$

Now the amplitude of the equivalent traction from Eq. (3.32) is substituted into Eq. (3.26) and Eq. (3.24) The excited wave amplitude at the edge of the actuator in the positive wave direction becomes

$$a_+^{(n)}(L/2) = \frac{2\jmath v_z^{(n)*}(h) \exp\left[-\jmath k^{(n)} L/2\right] r(\omega) \sin\left(k_n L/2\right)}{4\left[1 + r(\omega)\right]} k_{\mathrm{PZT}} u_{\mathrm{PZT,\ free}} \tag{3.33}$$

Eq. (3.33) indicates a well-known criterion for choosing the size of the actuator which is related to the $\sin k_n L/2$ term. In order to maximise the energy propagating along the waveguide one must choose the working dimension of the actuator (here it is the length L) to be any of the odd multiples of the half-wavelength of interest. By the same token, the excitation is found to be ineffective if the length of the actuator is a multiple of the excited wavelength.

The response at a desired location along the waveguide is calculated by multiplying the power-normalised mode shape by the excited wave amplitudes vector from Eq. (3.33). The phase change related to the distance from the edge of the actuator is accounted for by multiplying by the space-harmonic term:

$$\mathbf{v}^{(n)} = \mathbf{v}_{\mathrm{modal}}^{(n)} a_+^{(n)} \exp\left[-\jmath k^{(n)} z\right] \tag{3.34}$$

As an example, numerical results for velocity at the mid-plane of a 3 mm aluminium plate induced by a piezoelectric actuator and read at 0.1 m from the actuator are presented in Fig. 3.6 and Fig. 3.7. The properties of the actuator ($L = 0.05$ m, $h_{\mathrm{PZT}} = 0.5$ mm) refer to the NCE40 material constants after appropriate dimensional reduction (1D uniaxial plane strain). For these values the ratio of the Young's modulus–thickness products between the structure and the actuator is 4.5. The total velocity shown in Fig. 3.6 is split into single wave contributions in Fig. 3.7. Note that only the magnitude is shown as the phase differences between the waves does not seem to be particularly interesting in the example. At low frequencies, as expected, the flexural Lamb wave is predominant in the out-of-plane($|v_y|$) response, whereas the compressional Lamb wave is prevalent in the in-plane response($|v_z|$). Higher-order waves are not particularly strongly excited by the piezoelectric actuator and contribute mainly to the in-plane velocity. The peak of $|v_z|$ at ca. 950 kHz is associated with the zero group velocity effect. The dips and peaks along the velocity FRFs are related to the $\sin\left(k_n L/2\right)$ term from Eq. (3.33). The response experiences a dip if $k_n L/2$ is a multiple of π, i.e. when the length of the actuator

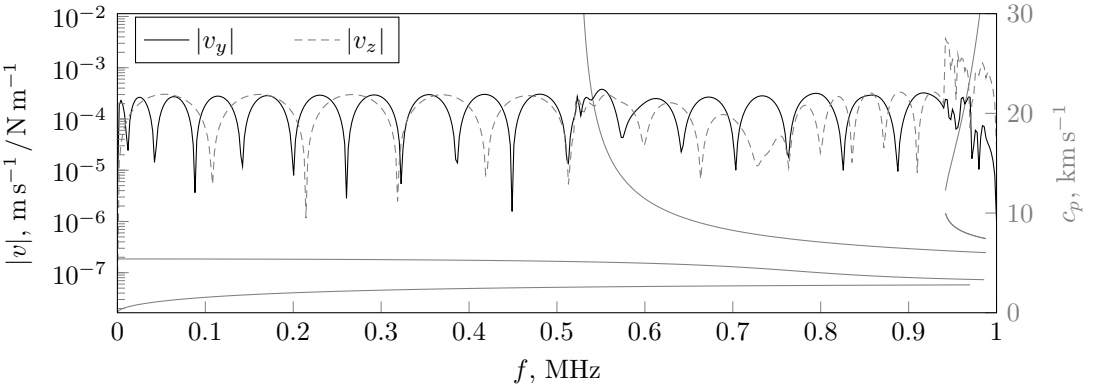

Figure 3.6: Total velocity at the mid-plane of a 3 mm aluminium plate induced by a piezoelectric actuator and read at 0.1 m from the actuator (pin-force model). Plate dispersion curves are drawn in light grey for reference (right axis).

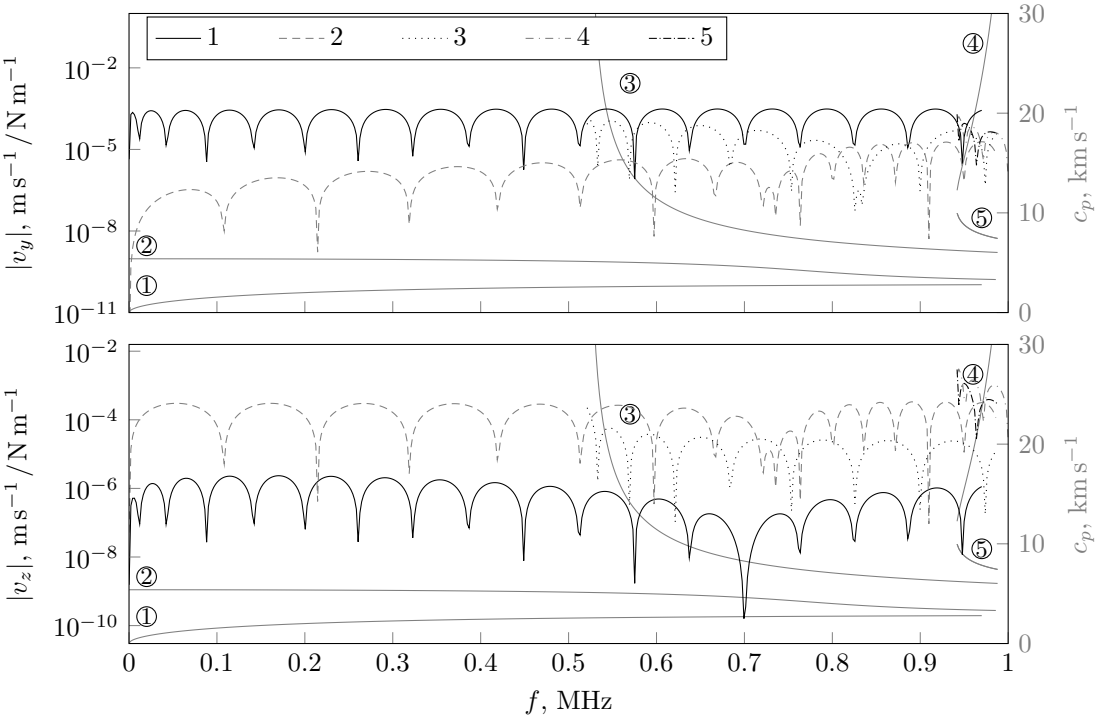

Figure 3.7: Velocity at the mid-plane of a 3 mm aluminium plate associated with each of the propagating waves induced by a piezoelectric actuator and read at 0.1 m from the actuator (pin-force model). Plate dispersion curves are drawn in light grey for reference (right axis).

is a multiple of the excited wavelength. The response is at maximum when $k_n L/2$ is an odd multiple of half-wavelength of interest. In Fig. 3.6 at the frequency of the first dip in $|v_y|$ the wavelength of the flexural Lamb wave equals the length of the actuator L. Similarly, at the frequency of the first dip in $|v_z|$ the wavelength of the compressional Lamb wave equals L.

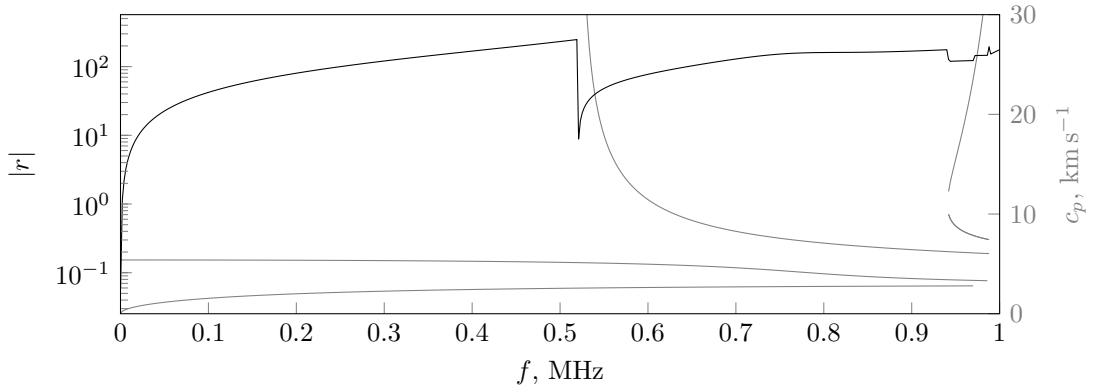

Figure 3.8: The ratio between the dynamics stiffness of the structure and the static stiffness of the actuator r (pin-force model). Plate dispersion curves are drawn in light grey for reference (right axis).

In Fig. 3.8, the ratio between the stiffnesses of the actuator and the structure (r) is shown. Since the actuator is considerably thinner than the structure, this ratio for vast majority of frequencies is significantly greater than one.

3.2.2.2 Electrical power supply under pin-force assumption

Electrical power requirement is a quantity of the greatest interest from the viewpoint of invoking delamination with piezo-actuated structural waves. Assuming constant driving voltage, the active power that is consumed during oscillations of the actuator attached to structural waveguide is calculated as

$$P_R = \frac{1}{2}\mathrm{Re}\{v(\omega) \cdot i(\omega)^*\} \tag{3.35}$$

where v is the constant driving voltage and $i(\omega)$ is the frequency dependent current drawn by the actuator. Under the pin-force assumption the current drawn by the actuator is obtained from [122] (details of the derivation in [93]):

$$i(\omega) = \jmath\omega C_0 v \left[1 - k_{31}^2 \frac{r(\omega)}{1 + r(\omega)}\right] \tag{3.36}$$

where k_{31} is the electromechanical coupling coefficient of the piezoelectric material to be obtained from the manufacturer.

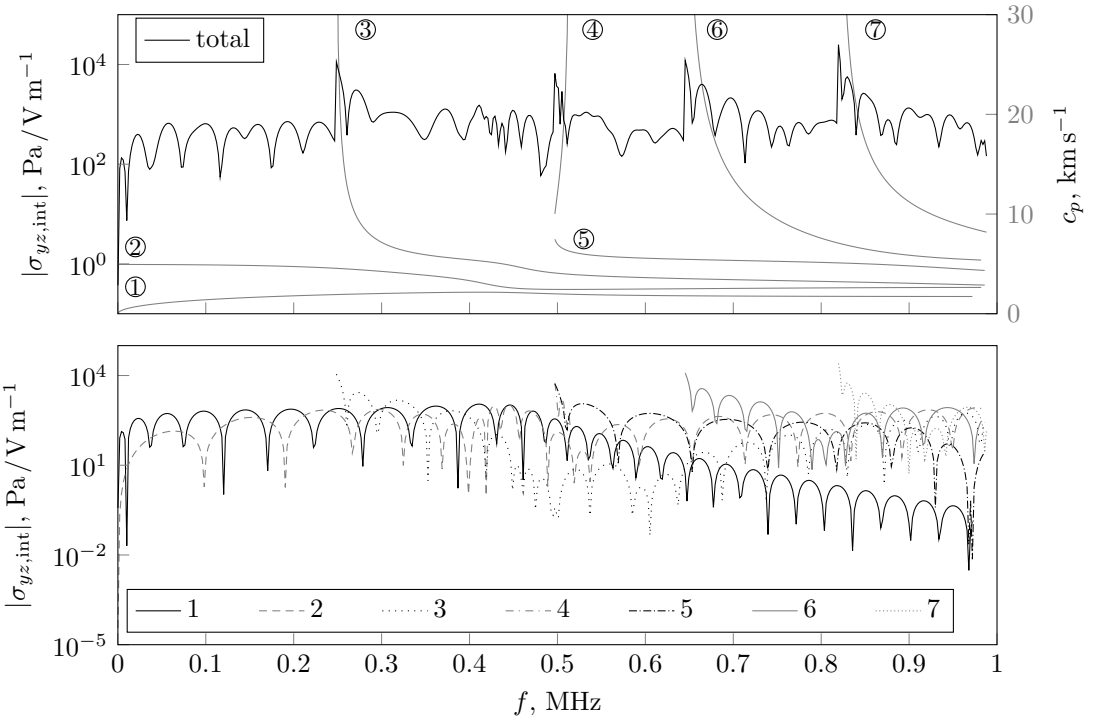

Figure 3.9: Interface shear stress in a 2 mm aluminium plate with a 2 mm glaze ice accretion at 0.1 m from the actuator (pin-force model) with respect to the driving voltage: superimposed (top) and single wave contributions (bottom). Plate dispersion curves are drawn in light grey for reference (right axis).

3.2.3 Interface shear stress in piezo-actuated waveguides with accretion

The approach outlined above is now employed for the analysis of stress generation capability of piezo-actuated waves with respect to the electrical power consumed. Bearing in mind that power is not linearly related to the wave field, the shear stress is normalised with respect to the square root of electrical active power. To start with, a 2 mm aluminium plate with a 2 mm thick glaze ice accretion is considered. The plate is excited with an actuator made of Noliac NCE40 material ($L = 0.05$ m, $h_{\mathrm{PZT}} = 0.0005$ m). The transverse shear stress at the interface resulting from the piezoelectric actuation is presented in Fig. 3.9 (with respect to the driving voltage) and Fig. 3.10 (with respect to the square root of electrical power consumed).

The maximum interface shear stress is observed either near the cut-off frequencies or close to the zero group velocity modes. It is expected that these waves might attenuate rapidly if the accretion is lossy. However, at the same time they seem to be the most appropriate candidates for invoking delamination. If the desired transverse shear stress is chosen to be 1.5 MPa which refers to the reported ice bond shear strength [2], one will need to supply around 130 W m^{-1} at frequencies corresponding to the peaks in

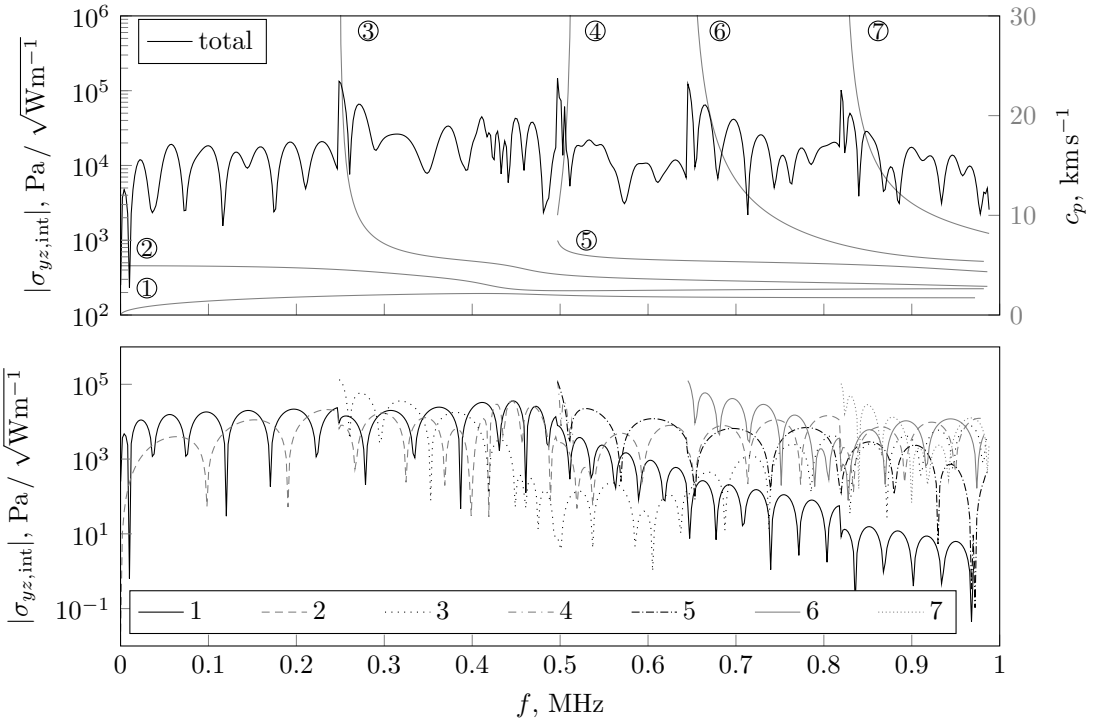

Figure 3.10: Interface shear stress in a 2 mm aluminium plate with a 2 mm glaze ice accretion at 0.1 m from the actuator (pin-force model) with respect to the square root of consumed electrical power: superimposed (top) and single wave contributions (bottom). Plate dispersion curves are drawn in light grey for reference (right axis).

Fig. 3.10 which refers to 2.5 W of electrical power applied to a 20 mm wide strip actuator. However, if the frequency range is restricted to 200 kHz, so that no higher-order waves are present, then the required electrical power grows to 5.3 kW m^{-1} (106 W per 20 mm wide strip) for the most optimistic case at 193 kHz.

The numbers presented above include the effect of the electrical to mechanical energy conversion in the piezoelectric actuator, which is accounted for in Eq. (3.36) [93] but do not account for the energy distribution and possible attenuation of waves. Therefore, the same conditions as used in Section 2.8.2 are introduced (only waves that propagate less than 60% of the energy along the build-up are considered) and an analogous parametric study is conducted. The properties of the structure and the actuator are kept constant, whereas the accretion's Young's modulus is varied. The actuator is allowed to deform exclusively uniaxially, therefore only Lamb waves are excited. In fact, shear horizontal waves are not expected to be excited with 3–1 PZT actuators.

The results of the study are presented in Fig. 3.11. The generated stress is a superposition of the flexural and the compressional Lamb wave contributions. Note that the

labelling '1st' or '2nd Lamb wave' in Fig. 3.11 refers to the bilayer wave modes that are close to the corresponding 1st or '2nd Lamb waves in a free-free host.

It is quite evident that the flexural Lamb wave (1st) is more effective for high stiffness accretions, whereas the compressional Lamb wave (2nd) for the low stiffness ones. As mentioned in Section 2.8.2 it is related to the fact that higher-order, build-up dominated waves cut off at low frequencies if the stiffness is low. These waves couple with the compressional Lamb waves first. They are associated with high interface shear stress, although are likely to attenuate quickly if a lossy accretion is considered. Nevertheless, the energy criterion allows them to be included in the comparative analysis.

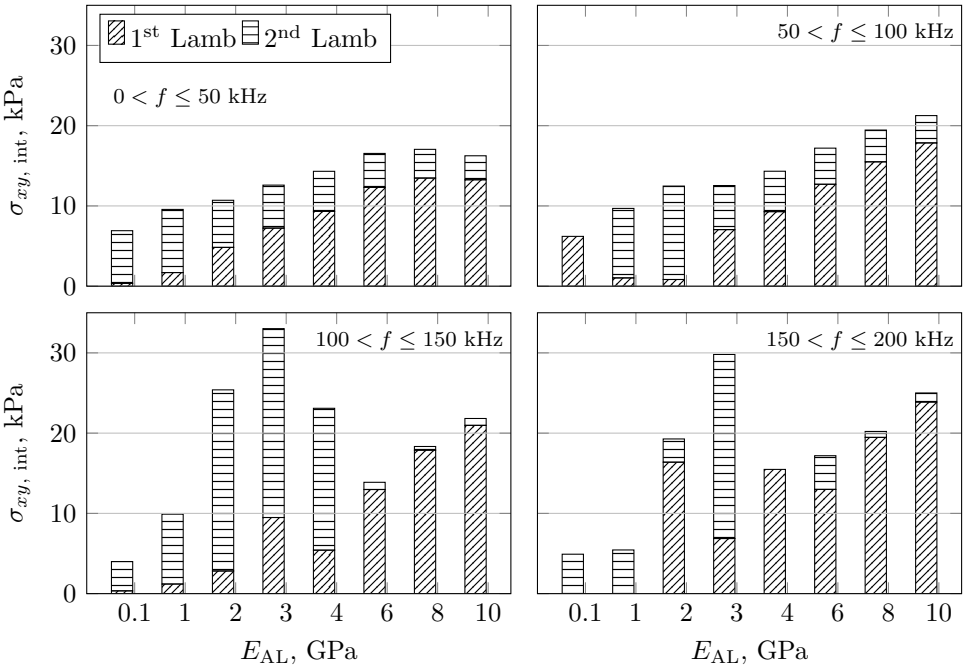

Figure 3.11: Maximum transverse interface shear stress achievable using the PZT actuator (NCE40, $L = 0.05$ m, $h_{\mathrm{PZT}} = 0.0005$ m) in the stated frequency ranges with respect to the square root of consumed electrical power.

Using the above model, a rough estimate of the electrical power requirements can be stated (that includes both Lamb waves contributions). A glaze ice accretion (assuming breaking stress $\sigma_{\mathrm{b}} = 1.5$ MPa requires around 112 W to be applied to a 20 mm wide strip (as given above). A lower stiffness accretion close to the range of values corresponding to rime ice ($E = 2$ GPa) benefits from the prevalence of the build-up dominated modes requiring ca. 70 W per a 20 mm wide strip assuming the same strength of the bond as for glaze ice. A very low stiffness accretion ($E = 0.1$ GPa), assuming the bond strength of 0.1 MPa, is found to be removed at ca. 4 W per a 20 mm wide strip. Finally, a mid-stiffness build-up ($E = 4$ GPa) creating a bond with shear strength of 0.5 MPa is expected to be shed when between 9 and 22 W are applied to a 20 mm wide strip (with

or without the flexural wave contribution, respectively). These numbers seem to be quite promising and feasible to achieve, but one needs to bear in mind the assumptions made when building the model and assess them for conformity with the actual practical case. Note, however, that to facilitate presentation the stress contributions coming from particular waves were added without accounting for phase difference between them. This may have caused the total stress to be slightly overestimated.

3.2.4 Limitations of the approach

The modelling strategy presented in the previous sections provides a relatively simple tool for the analysis of piezo-actuation in structural waveguides. However, both the wave modelling approach used up to this point in the thesis and the pin-force assumption employed for including the piezoelectric actuation are not well-suited for the study on invoking delamination. Although they support a general understanding and insight into various aspects of the physics of the phenomenon, they are not able to represent the considered cases accurately enough. In the following paragraphs the limitations of the Global Matrix Method and pin-force model, respectively, are discussed.

The accretion is usually of significantly different properties to the host structure. The GMM model is based on solving the system equation by searching for roots of a nonlinear equation which is often a tedious task. Particularly it is very prone to fail for a waveguide composed of very different materials unless the frequency step is very small (resulting in long computation time). Furthermore, implementing damping or the ability to predict evanescent waves requires a significant work done on the implementation. Therefore, the method was found to be very well suited for the analysis of particular features of wave propagation but not versatile enough to be used for a comprehensive study aimed at drawing a direct reference to a practical scenario.

In the experiments on invoking delamination reported in the literature [2, 24], as well as in the preliminary experiment described in the Appendix, the actuator's thickness is comparable or higher than that of the structure. However, the pin-force model employed above is based on the quasi-static assumption that requires the thickness of the actuator to be negligible compared to the structure. The pin-force model is valid only if the strain distribution in the actuator can be approximated as uniform and its interaction with the host structure treated as quasi-static (far from the resonances). Since it is expected that the actuators used for removal of an unwanted accretion will be relatively thick in order to be able to induce desired high strain, they will significantly change the behaviour of the host violating the pin-force assumption. Furthermore, the influence of the bonding

layer which is known to have a notable effect on the response is difficult to account for using the pin-force approach.

3.3 Conclusions

Wave excitation in structures covered with accretion were considered in this chapter. Firstly, the excitability functions originating from the guided waves complex reciprocity were recalled. They enabled calculation of the waves amplitudes as a response to applied mechanical force. The excitability functions provided also means of evaluating how the injected power is partitioned between the propagating waves.

With respect to the above a parametric study was performed showing the maximum achievable interface shear stress in particular frequency ranges for different types of accretions with respect to the injected mechanical power. It was shown that the out-of-plane excitation accommodates the highest interface shear stress for high stiffness accretions (such as e.g. glaze ice). Mid- and low stiffness build-ups were demonstrated to experience higher stress with an in-plane excitation.

The excitability functions were employed for implementing the simplest PZT excitation model, namely pin-force. The mathematical origin of the approach and the mathematical formulae for electrical power drawn by the actuator were outlined. The piezo-actuation was applied structures with accretions yielding approximate electrical power requirements for removing sample build-ups. The limitations of the analysis tools developed so far were discussed in the last section. The range of applicability of the pin-force assumption and numerical difficulties associated with implemented models are highlighted as important issues hinder a direct application to real practical cases.

Therefore, an alternative, more versatile methodology is sought. The appealing modelling approach would be able to represent the dynamic character of the piezo-structure interaction accurately remaining valid at high frequencies. It would also be advantageous if the methodology could be directly related to a practical experimental case since this is possible only indirectly using a plane wave model. An attempt to meet these requirements is presented in the subsequent chapters.

Chapter 4

Semi-analytical finite elements for modelling structural wave propagation

The approach based on the partial waves technique and the global matrix method is physically insightful, but practically limited for the following reasons: (i) the root tracing routines are quite sensitive to the choice of the initial guesses and root searching radii which varies significantly from structure to structure; (ii) the methodology enables calculating waves only in infinite structures under the plane strain assumption. One of the alternatives that has been chosen in this thesis is the semi-analytical finite element (SAFE) method. The base concept of the method is to use a finite element approximation to the wave field over the cross section allowing an additional degree of freedom (DOF) in the direction of propagation and solving the wave propagation problem assuming its space-harmonic form. The resulting wave equations are formulated as an eigenvalue problem which can be solved using any of the standard methods. SAFE method can be employed for both free and forced steady-state wave calculations on a lossless or damped waveguide. Thanks to its versatility, the method was found to be helpful in assessing the results developed so far and developing new modelling strategies presented in the subsequent chapters.

This chapter provides the introduction to the SAFE method. Firstly, the notation and labelling conventions are introduced. Then, the derivation of the SAFE element and solution procedure is outlined. The convergence of the free wave solution is verified against global matrix method benchmark. In the second part the forced response wave problem is analysed using SAFE formulation and wave approach. Two ways of calculating the excited waves amplitudes are presented and compared with the analytical

excitability-based solution. Finally, the model is validated with an experiment on a beam-like waveguide with emulated anechoic terminations.

4.1 SAFE formulation

The SAFE framework has been probably proposed in the 1970s [57, 58]. The method is suitable for solving one dimensional wave propagation problems for structures of an arbitrary cross-section - zero- (beam, string, rod theories), one- (infinite plate under plane strain/stress condition), or two-dimensional, which is its great advantage over the analytical partial waves approach. It utilises an FE-like procedure to discretise the plane cross-section and assumes a space-harmonic variation of the displacement along the out-of-plane (waveguide) direction to find a steady-state solution of the equations of motion. The SAFE element has finite dimensions in the cross-section plane and is of an indefinite extent along the propagation direction. The equations of motion are derived from the virtual work principle, as done for FE. The dispersion curves are found as a solution to a resulting eigenvalue problem, therefore the method of determining them does not require tedious and complicated root tracing algorithms. Further details of the method can be found in the literature, e.g. [64–66, 71, 123].

The mathematical framework for the SAFE method for mechanical waveguides is briefly presented below. It is assumed that the cross-section of the structure lies in the x-y plane and that the wave propagates along the z direction. The following derivation is written for a two-dimensional element, however other cases can easily be recovered by removing appropriate degrees of freedom and altering the element shape functions. Lamb/SH wave problems are usually solved using mono-dimensional elements as shown in [66, 123], for example. A schematic diagram showing the coordinate system, labelling convention and nodal degrees of freedom is presented in Fig. 4.1.

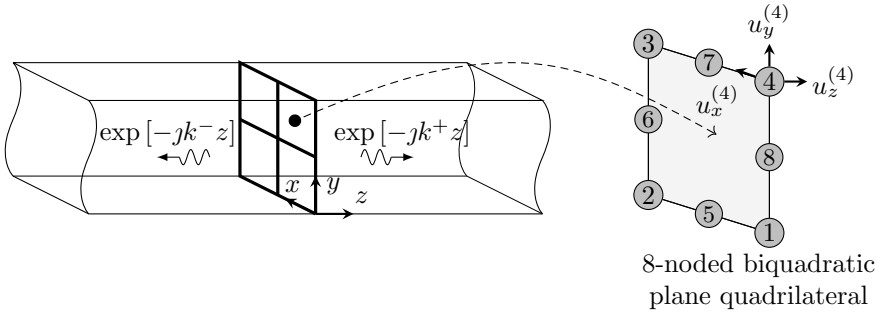

Figure 4.1: Waveguide modelled with SAFE - the coordinates system, labelling convention and degrees of freedom.

4.1.1 Cross-section discretisation

The displacement, strain and stress fields over a SAFE element are defined as [64]

$$\begin{aligned}\mathbf{u} &= \begin{bmatrix} u_x & u_y & u_z \end{bmatrix}^\top \\ \boldsymbol{\epsilon} &= \begin{bmatrix} \epsilon_{xx} & \epsilon_{yy} & \epsilon_{zz} & \gamma_{yz} & \gamma_{xz} & \gamma_{xy} \end{bmatrix}^\top \\ \boldsymbol{\sigma} &= \begin{bmatrix} \sigma_{xx} & \sigma_{yy} & \sigma_{zz} & \sigma_{yz} & \sigma_{xz} & \sigma_{xy} \end{bmatrix}^\top \end{aligned} \tag{4.1}$$

where the time-harmonic term $\exp[\jmath\omega t]$ is omitted for brevity.

The cross-section of the SAFE element is discretised in an FE-like manner using elements and shape functions chosen according to the type of the analysis. In this work an 8-node quadrilateral biquadratic element was used for which the shape functions may be found in any standard textbook on the finite element method, e.g. [124]. The field variables from Eq. (4.1) are expressed using element shape functions (in the cross-section plane) and nodal degrees of freedom (DOFs) as it follows from the FE approximation.

Given that the nodal displacements vector for an element is written as

$$\mathbf{q}(z) = \begin{bmatrix} q_x^{(1)} & q_y^{(1)} & q_z^{(1)} & \dots & q_x^{(8)} & q_y^{(8)} & q_z^{(8)} \end{bmatrix}^\top \tag{4.2}$$

The displacement at any point within the SAFE element is

$$\mathbf{u}(x, y, z) = \mathbf{N}(x, y)\mathbf{q}(z) \tag{4.3}$$

where $\mathbf{N}(x, y)$ is the displacement shape function matrix.

Note that in Eq. (4.3) the nodal amplitude vector depends on the position along the propagation direction z. Following from Eq. (4.3) one writes the strain in terms of the shape functions and the nodal DOFs

$$\begin{aligned}\boldsymbol{\epsilon}(x, y, z) &= \left[\mathbf{L}_x \frac{\partial}{\partial x} + \mathbf{L}_y \frac{\partial}{\partial y} + \mathbf{L}_z \frac{\partial}{\partial z}\right] \mathbf{u}(x, y, z) = \left[\mathbf{L}_x \frac{\partial}{\partial x} + \mathbf{L}_y \frac{\partial}{\partial y} + \mathbf{L}_z \frac{\partial}{\partial z}\right] \mathbf{N}(x, y)\mathbf{q}(z) \\ &= \left[\mathbf{L}_x \mathbf{N}_{,x} + \mathbf{L}_y \mathbf{N}_{,y} + \mathbf{L}_z \frac{\partial}{\partial z}\mathbf{N}\right] \mathbf{q}(z) = \mathbf{B}_1 \mathbf{q} + \mathbf{B}_2 \frac{\partial}{\partial z}\mathbf{q}(z)\end{aligned} \tag{4.4}$$

where $\mathbf{N}_{,x} = \frac{\partial}{\partial x}\mathbf{N}$ and $\mathbf{L}_x$, $\mathbf{L}_y$, $\mathbf{L}_z$, are

$$\mathbf{L}_x = \begin{bmatrix} 1 & 0 & 0 \\ 0 & 0 & 0 \\ 0 & 0 & 0 \\ 0 & 0 & 0 \\ 0 & 0 & 1 \\ 0 & 1 & 0 \end{bmatrix} \quad \mathbf{L}_y = \begin{bmatrix} 0 & 0 & 0 \\ 0 & 1 & 0 \\ 0 & 0 & 0 \\ 0 & 0 & 1 \\ 0 & 0 & 0 \\ 1 & 0 & 0 \end{bmatrix} \quad \mathbf{L}_z = \begin{bmatrix} 0 & 0 & 0 \\ 0 & 0 & 0 \\ 0 & 0 & 1 \\ 0 & 1 & 0 \\ 1 & 0 & 0 \\ 0 & 0 & 0 \end{bmatrix} \tag{4.5}$$

4.1.2 Constitutive equations

For elastic waveguides the stress-strain constitutive relationship is given by the Hooke's Law. For the sake of completeness let us write it in matrix form

$$\boldsymbol{\sigma} = \mathbf{C}\boldsymbol{\epsilon} \tag{4.6}$$

Substituting Eq. (4.4) into Eq. (4.6) one gets the constitutive equations expressed in terms of nodal degrees of freedom and element shape functions

$$\boldsymbol{\sigma} = \mathbf{C}\left(\mathbf{B}_1\mathbf{q} + \mathbf{B}_2\frac{\partial}{\partial z}\mathbf{q}\right) \tag{4.7}$$

4.1.3 Virtual work principle

The governing equations for wave propagation are obtained with the aid of the virtual work principle for deformable bodies. The analysed section of the waveguide occupies volume V which is formed by a cross-section Ω extruded through length L and is bounded by surface Γ. The boundary conditions on Γ are the following:

- Essential mechanical boundary condition on Γ_u (Dirchelet boundary condition): $u = \underline{u}$
- Natural mechanical boundary condition on Γ_σ (Neumann boundary condition): $\sigma_{ij}n_j = t_i$

where $\underline{u}$ is the prescribed displacement and t_i is the applied surface traction.

The respective bounding surfaces related to each pair of the boundary conditions are exclusive and their unions form the whole surface, i.e. $\Gamma_u \cup \Gamma_\sigma = \Gamma$, $\Gamma_u \cap \Gamma_\sigma = 0$.

Given the constitutive equations, the mechanical equilibrium condition, and the essential boundary conditions given above the virtual work principle states that for every time t

$$\overbrace{\int_{\Gamma_\sigma} \delta\mathbf{u}^\top \mathbf{t}\,\mathrm{d}\Gamma_\sigma}^{\substack{\text{work done by}\\ \text{external surface}\\ \text{tractions}}} + \overbrace{\delta\mathbf{q}^\top \mathbf{f}_i}^{\substack{\text{work done by}\\ \text{nodal forces}}} = \overbrace{\int_{\mathrm{V}} \delta\mathbf{u}^\top(\rho\ddot{\mathbf{u}})\,\mathrm{d}V}^{\substack{\text{work done by}\\ \text{inertia body forces}}} + \overbrace{\int_{\mathrm{V}} \delta\boldsymbol{\epsilon}^\top \boldsymbol{\sigma}\,\mathrm{d}V}^{\substack{\text{work done by}\\ \text{the stress field}}} \tag{4.8}$$

where $\mathbf{t}$ is the external tractions vector, $\mathbf{f}_i$ is the vector of nodal forces applied at the ends of the considered section of the waveguide of length L and ρ is the density of the material.

The constitutive equations from Eq. (4.7) are substituted into each of the components in Eq. (4.8). The detailed algebraic manipulations for all of the components are omitted below for the sake of clarity. The work done by the inertia body forces is given by

$$\int_{\mathrm{V}} \delta\mathbf{u}^\top(\rho\ddot{\mathbf{u}})\,\mathrm{d}V = \int_{\Omega}\int_{\mathrm{L}} \delta\mathbf{q}^\top \mathbf{N}^\top \rho\mathbf{N}\frac{\partial^2}{\partial t^2}\mathbf{q}\,\mathrm{d}z\,\mathrm{d}\Omega \tag{4.9}$$

The work done on the stress field by the strain field is given by

$$\begin{aligned}\int_{\mathrm{V}} \delta\boldsymbol{\epsilon}^\top \boldsymbol{\sigma}\,\mathrm{d}V = &\int_{\Omega}\left[\delta\mathbf{q}^\top\left(\mathbf{B}_2^\top\mathbf{C}\mathbf{B}_1\mathbf{q} + \mathbf{B}_2^\top\mathbf{C}\mathbf{B}_2\frac{\partial}{\partial z}\mathbf{q}\right)\right]\mathrm{d}\Omega \\ &+ \int_{\Omega}\int_{\mathrm{L}}\left[\delta\mathbf{q}^\top\mathbf{B}_1^\top\mathbf{C}\mathbf{B}_1\mathbf{q} + \delta\mathbf{q}^\top\left(\mathbf{B}_1^\top\mathbf{C}\mathbf{B}_2 - \mathbf{B}_2^\top\mathbf{C}\mathbf{B}_1\right)\frac{\partial}{\partial z}\mathbf{q}\right. \\ &\left. - \delta\mathbf{q}^\top\mathbf{B}_2^\top\mathbf{C}\mathbf{B}_2\frac{\partial^2}{\partial z^2}\mathbf{q}\right]\mathrm{d}z\mathrm{d}\Omega\end{aligned} \tag{4.10}$$

The distributed tractions term is

$$\int_{\Gamma_\sigma} \delta\mathbf{u}^\top\mathbf{t}\,\mathrm{d}\Gamma_\sigma = \int_{\Gamma_\sigma} \delta\mathbf{q}^\top\mathbf{N}^\top\mathbf{N}\mathbf{t}_i\,\mathrm{d}\Gamma_\sigma \tag{4.11}$$

where $\mathbf{t}$ is lumped at the nodes following the finite element approximation

$$\mathbf{t} = \mathbf{N}\mathbf{t}_i \tag{4.12}$$

with $\mathbf{t}_i$ being the nodal external tractions.

To clarify the formulation, the following notation is adopted which results from the integration of the matrices over the cross-sectional element domain:

$$\begin{aligned} \mathbf{K}_0 &= \int_\Omega \mathbf{B}_1^\top \mathbf{C}\mathbf{B}_1 \,\mathrm{d}\Omega & \mathbf{K}_1 &= \int_\Omega \mathbf{B}_1^\top \mathbf{C}\mathbf{B}_2 - \mathbf{B}_2^\top \mathbf{C}\mathbf{B}_1 \,\mathrm{d}\Omega \\ \mathbf{K}_2 &= \int_\Omega \mathbf{B}_2^\top \mathbf{C}\mathbf{B}_2 \,\mathrm{d}\Omega & \mathbf{M} &= \int_\Omega \mathbf{N}^\top \rho \mathbf{N} \,\mathrm{d}\Omega \\ \mathbf{p} &= \int_{\Gamma_\sigma} \mathbf{N}^\top \mathbf{N}\mathbf{t}_i \,\mathrm{d}\Gamma_\sigma & \mathbf{K}_f &= \int_\Omega \mathbf{B}_2^\top \mathbf{C}\mathbf{B}_1 \,\mathrm{d}\Omega \end{aligned} \tag{4.13}$$

Let us now rewrite both variational equations using the notation from Eq. (4.13) and rearranging the terms:

$$\begin{aligned} \mathbf{0} = \int_L \Bigg\{ \delta\mathbf{q}^\top \left(\mathbf{M}\frac{\partial^2}{\partial t^2}\mathbf{q} + \mathbf{K}_0\mathbf{q} + \mathbf{K}_1\frac{\partial}{\partial z}\mathbf{q} - \mathbf{K}_2\frac{\partial^2}{\partial z^2}\mathbf{q} - \mathbf{p} \right) \Bigg\} \,\mathrm{d}z \\ + \delta\mathbf{q}^\top \left[\mathbf{K}_f\mathbf{q} + \mathbf{K}_2\frac{\partial}{\partial z}\mathbf{q} - \mathbf{f}_i \right] \end{aligned} \tag{4.14}$$

The above variational equation contains two main terms – the first is related to the wave field behaviour over a length L and the second corresponds to every location along L, i.e. every cross-section. Moreover, it needs to hold for every time t and any admissible virtual displacement δq which leads to the governing equation for wave propagation.

4.1.4 Governing equation for wave propagation

From Eq. (4.14) one can conclude the governing equation for wave propagation

$$\mathbf{M}\frac{\partial^2}{\partial t^2}\mathbf{q} + \mathbf{K}_0\mathbf{q} + \mathbf{K}_1\frac{\partial}{\partial z}\mathbf{q} - \mathbf{K}_2\frac{\partial^2}{\partial z^2}\mathbf{q} = \mathbf{p} \tag{4.15}$$

and the natural boundary condition stating that at the ends of the considered section of the waveguide

$$\mathbf{q} = 0 \qquad \text{or} \qquad \mathbf{f}_i = \mathbf{K}_f\mathbf{q} + \mathbf{K}_2\frac{\partial}{\partial z}\mathbf{q} \tag{4.16}$$

which provides the expression for the resultant nodal forces.

It is assumed that displacement in the waveguide direction is space-harmonic

$$\mathbf{q}(z) = \bar{\mathbf{q}} \exp\left[-\jmath k z\right] \tag{4.17}$$

Therefore, Eq. (4.15) is rewritten as

$$\left(-\omega^2\mathbf{M} + \mathbf{K}_0 - \jmath k\mathbf{K}_1 - (-\jmath k)^2\mathbf{K}_2 \right)\bar{\mathbf{q}} = \bar{\mathbf{p}} \tag{4.18}$$

Eq. (4.18) is the governing equation for wave propagation in a mechanical waveguide in the wavenumber-frequency domain. Assuming a space-harmonic character of solutions, the resultant forces over the cross-section are given by (analogous to [119])

$$\bar{\mathbf{f}_i} = \mathbf{K}_f\bar{\mathbf{q}} - \jmath k\mathbf{K}_2\bar{\mathbf{q}} \tag{4.19}$$

4.2 Free wave propagation using SAFE

If the external traction term $\mathbf{p}$ is zero, Eq. (4.18) describes free wave propagation

$$\left(-\omega^2\mathbf{M} + \mathbf{K}_0 - \jmath k\mathbf{K}_1 - (-\jmath k)^2\mathbf{K}_2 \right)\bar{\mathbf{q}} = \mathbf{0} \tag{4.20}$$

Solution of the quadratic eigenvalue problem (QEP) in Eq. (4.20) can be performed using any numerical approach available [125]. The most common is linearisation by doubling the size of the matrix [66]. A new eigenvector is introduced as $\hat{\boldsymbol{\phi}} = \begin{bmatrix}\boldsymbol{\phi} & \lambda\boldsymbol{\phi}\end{bmatrix}^\top$ and the SAFE governing equation from Eq. (4.20) is rewritten as a generalised eigenvalue problem (GEP),

$$\left(\begin{bmatrix} \mathbf{0} & \mathbf{K}_0 - \omega^2\mathbf{M} \\ \mathbf{K}_0 - \omega^2\mathbf{M} & \mathbf{K}_1 \end{bmatrix} - \lambda \begin{bmatrix} \mathbf{K}_0 - \omega^2\mathbf{M} & \mathbf{0} \\ \mathbf{0} & \mathbf{K}_2 \end{bmatrix} \right) \begin{Bmatrix} \boldsymbol{\phi} \\ \lambda\boldsymbol{\phi} \end{Bmatrix} = \mathbf{0} \tag{4.21}$$

or more concisely as

$$\left[\mathbf{A}(\omega) - \lambda\mathbf{B}(\omega)\right]\hat{\boldsymbol{\phi}} = \mathbf{0} \tag{4.22}$$

where $\mathbf{A}$, $\mathbf{B}$ are of dimensions $2n \times 2n$, n is the number of the displacement degrees of freedom in the section and

$$\lambda = -\jmath k \tag{4.23}$$

In Eq. (4.21) matrices $\mathbf{M}$, $\mathbf{K}_0$ and $\mathbf{K}_2$ are symmetric but $\mathbf{K}_1$ is skew-symmetric, hence the linearised eigenproblem is not symmetric. However, as suggested by [65] if one imposes the phase relationships between displacement components (u_z in quadrature with u_x and u_y) which are in general true, a symmetric structure can be obtained.

The GEP from Eq. (4.22) can be readily solved using any of the common scientific computing packages. For a given frequency ω one finds the set of $2n$ eigenvalues $\boldsymbol{\Lambda}$, and

the $2n \times 2n$ matrices of the corresponding right and left eigenvectors denoted by $\hat{\mathbf{\Phi}}$ and $\hat{\mathbf{\Psi}}$, respectively where the right eigenvectors $\hat{\boldsymbol{\phi}}_i$ are columns of $\hat{\mathbf{\Phi}}$ and left eigenvectors $\hat{\boldsymbol{\psi}}_i$ are rows of $\hat{\mathbf{\Psi}}$. The left eigenvectors will be very useful later when their orthogonality with the right eigenvector is exploited.

The wavenumbers can be extracted from the eigenvalues using Eq. (4.23). The modal solutions are associated with positive and negative going waves based on the wavenumber, i.e. there are n positive- and n negative-going waves. The wave is considered to be positive-going if [51]:

$$|\exp[-\jmath k_i z]| < 1 \qquad \text{or} \qquad |\exp[-\jmath k_i z]| = 1 \quad \text{and} \quad p_i > 0 \tag{4.24}$$

where z is a distance (geometrical) smaller than the smallest wavelength of interest and p_i is the modal power flow along the propagation direction adopted from the mechanical complex Poynting theorem [109]. The SAFE formulation provides an elegant expression for the Poynting vector component along the propagation direction [126]:

$$p_i = \omega \frac{\operatorname{Im}\left\{\boldsymbol{\phi}_i^{*\top}\left[\mathbf{K}_f - \jmath k_i \mathbf{K}_2\right]\boldsymbol{\phi}_i\right\}}{2} \tag{4.25}$$

Based on the direction of propagation the corresponding columns and rows of the eigenvectors matrices $\hat{\mathbf{\Phi}}$ and $\hat{\mathbf{\Psi}}$ are rearranged so that:

$$\hat{\mathbf{\Phi}} = \begin{bmatrix} \hat{\mathbf{\Phi}}^{+} & \hat{\mathbf{\Phi}}^{-} \end{bmatrix} \qquad \text{and} \qquad \hat{\mathbf{\Psi}} = \begin{bmatrix} \hat{\mathbf{\Psi}}^{+} \\ \hat{\mathbf{\Psi}}^{-} \end{bmatrix} \tag{4.26}$$

The left and right eigenvectors are normalised according to their orthogonality with respect to the $\mathbf{B}$ matrix (assuming that $\mathbf{B}$ is not rank deficient), so that:

$$\hat{\boldsymbol{\psi}}_i \mathbf{B}(\omega) \hat{\boldsymbol{\phi}}_j = \begin{cases} 1 & \text{if } i = j \\ 0 & \text{otherwise} \end{cases} \tag{4.27}$$

and

$$\hat{\boldsymbol{\psi}}_i \mathbf{A}(\omega) \hat{\boldsymbol{\phi}}_i = \lambda_i \tag{4.28}$$

4.2.1 Wave basis and wave modal properties

The approach presented aims to describe the dynamics of the structure in terms of the travelling waves which in general is known as the wave approach [36, 37] (see Chapter 1). The SAFE formulation provides the means of obtaining the wave modal characteristics

of the waveguide (wavenumbers and wave mode shapes) which form a so-called wave basis [39, 54]. Since the number of waves found using the SAFE method is the same as the number of DOFs of the cross-section, it is usually much higher than required as many DOFs are needed to properly represent complicated wave structures at high frequencies. Therefore, often only a finite number of modal solutions is kept and used in further calculations based on some criterion adopted following the nature of the problem considered. The modal matrices are then no longer square, hence the pseudo-inverse needs to be used [39].

The nodal displacements and nodal resultant forces at any location in the waveguide can be expressed in terms of the wave basis as:

$$\begin{Bmatrix} \mathbf{q}(z) \\ \mathbf{f}(z) \end{Bmatrix} = \begin{Bmatrix} \boldsymbol{\Phi} \\ \boldsymbol{\Theta} \end{Bmatrix} \mathbf{a}(z) = \begin{bmatrix} \boldsymbol{\Phi}^{+} & \boldsymbol{\Phi}^{-} \\ \boldsymbol{\Theta}^{+} & \boldsymbol{\Theta}^{-} \end{bmatrix} \begin{Bmatrix} \mathbf{a}^{+}(z) \\ \mathbf{a}^{-}(z) \end{Bmatrix} \tag{4.29}$$

where $\boldsymbol{\Phi}^{+,-}$ contains positive- and negative-going *displacement wave mode shapes* obtained by taking the upper half of the extended eigenvectors matrix $\hat{\boldsymbol{\Phi}}$, $\boldsymbol{\Theta}^{+,-}$ contains the *force wave mode shapes* obtained from Eq. (4.19):

$$\boldsymbol{\theta}_i = \begin{bmatrix} \mathbf{K}_f & \mathbf{K}_2 \end{bmatrix} \hat{\boldsymbol{\phi}}_\mathbf{i} \tag{4.30}$$

and $\mathbf{a}^{+}(z)$, $\mathbf{a}^{-}(z)$ are the corresponding wave amplitudes.

Wave amplitude change along the waveguide is described by the space-harmonic term called the propagation matrix $\boldsymbol{\tau}(z)$:

$$\mathbf{a}^{+}(z) = \mathbf{a_0}^{+} \mathrm{diag}\left(\exp\left[-\jmath k_i z\right]\right) = \mathbf{a_0}^{+} \boldsymbol{\tau}(z) \tag{4.31}$$

where $\mathbf{a_0}^{+}$ is the wave amplitude at a chosen origin.

For NDT and vibroacoustic applications it is often desired to analyse particular features of guided waves such as the group velocity, the energy carried by a wave mode, the power flow or the energy velocity (which provides the velocity of the wave packet for lossy waveguides). The variational origin of the SAFE equations readily provides a few useful expressions for modal properties of the i^{th} wave mode at a circular frequency ω. They are listed below together with corresponding sources from the literature where the detailed explanation is presented.

Group velocity can be obtained from [59, 66]:

$$c_g^{(i)} = \frac{\boldsymbol{\psi}_i \left(-\jmath \tilde{\mathbf{K}}_1 + 2k_i \tilde{\mathbf{K}}_2\right) \boldsymbol{\phi}_i}{2\omega \boldsymbol{\psi}_i \mathbf{M} \boldsymbol{\phi}_i} \tag{4.32}$$

The total strain energy associated with an element follows from Eq. (4.10):

$$e_{\mathrm{u}}^{(i)} = \frac{\boldsymbol{\phi}_i^{*\top}\left(\tilde{\mathbf{K}}_0 - \jmath k_i \tilde{\mathbf{K}}_1 + k_i^2 \tilde{\mathbf{K}}_2\right)\boldsymbol{\phi}_i}{4} \tag{4.33}$$

The total kinetic energy associated with an element follows from Eq. (4.9):

$$e_{\mathrm{k}}^{(i)} = \omega^2 \frac{\boldsymbol{\phi}_i^{*\top}\mathbf{M}\boldsymbol{\phi}_i}{4} \tag{4.34}$$

Power flow along the propagation direction can be calculated from[126]:

$$p^{(i)} = -\omega \frac{\mathrm{Im}\left\{\boldsymbol{\phi}_i^{*\top}\left[\tilde{\mathbf{K}}_f - \jmath k_i \tilde{\mathbf{K}}_2\right]\boldsymbol{\phi}_i\right\}}{2} \tag{4.35}$$

And finally, the energy velocity [66, 109] is calculated using the above equations:

$$v_e^{(i)} = \frac{p^{(i)}}{e_{\mathrm{u}}^{(i)} + e_{\mathrm{k}}^{(i)}} \tag{4.36}$$

where it needs to be kept in mind that energy and power are cyclic quantities, hence the above equations involve integrals over one period.

4.2.2 Convergence of the SAFE method

Fig. 4.2 shows how the SAFE method solution converges with the increasing number of elements. It can be deduced from Fig. 4.2 that in order to determine how many elements are needed to get accurate results in a desired frequency range one can check the convergence of the cut-off frequencies of the higher-order wave modes. This can be conveniently performed if one recalls the SAFE governing equation from Eq. (4.20)

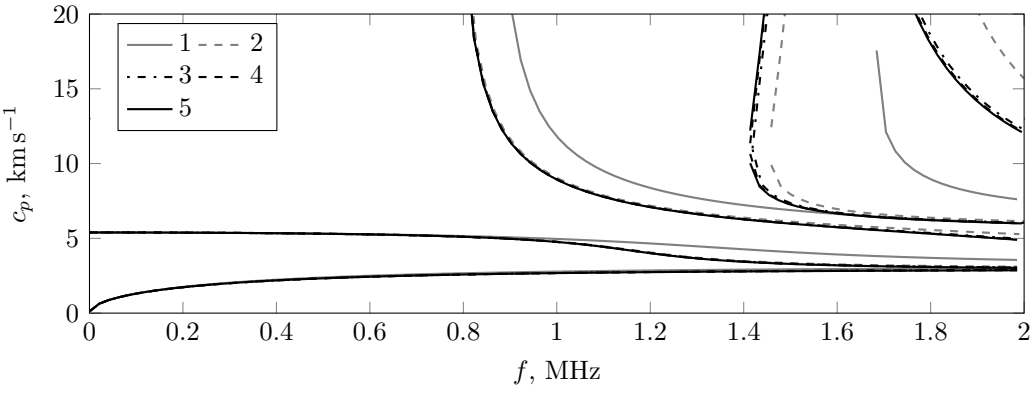

Figure 4.2: Convergence of the SAFE method. Dispersion curves for a 2mm aluminium free-free plate using an increasing number of SAFE elements across the thickness.

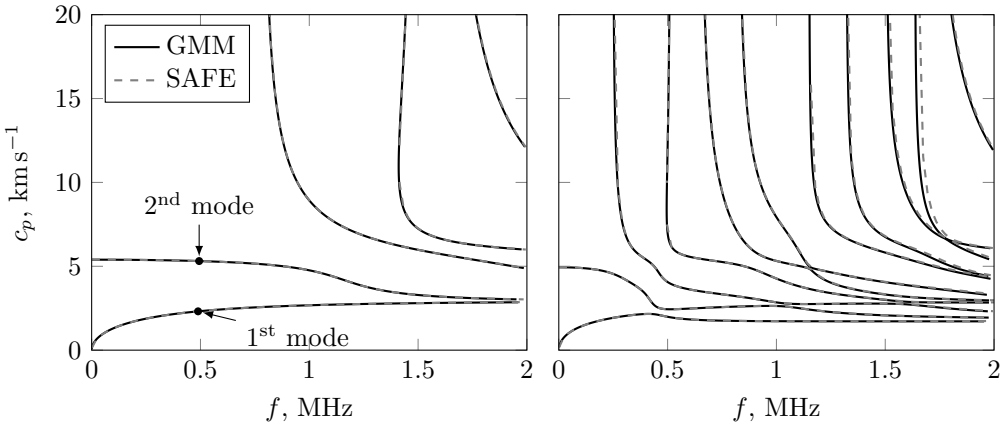

Figure 4.3: Dispersion curves as computed using the global matrix method and SAFE; 2 mm aluminium free-free plate (SAFE: 5 elements) on the left, 2mm aluminium covered with 2mm glaze ice free-free plate (SAFE: 10 elements) on the right.

keeping in mind that at the cut-off frequencies the wavenumber is zero (the wavelength is infinite, i.e. the whole structure is vibrating in phase). Therefore the cut-off frequencies are the eigenvalues of the following GEP:

$$\left(\mathbf{K}_0 - \omega^2 \mathbf{M}\right) \bar{\mathbf{q}} = \mathbf{0} \tag{4.37}$$

In Fig. 4.3 the results of the SAFE and the global matrix method are compared. The GMM solution is exact since no approximation of the wave field is employed here, whereas the SAFE solution is converging to GMM as the number of elements increases. It is shown that an excellent agreement can be obtained, however, the more complex the structure is, the more elements are needed.

4.3 Excitation of structural waves using SAFE

In this section a methodology for steady-state forced response wave calculation using a semi-analytical finite element model is presented for the case of an infinite waveguide. For simplicity the external force vector (either line or point force, depending on the dimension of the model) is assumed to act only on the plane of the cross-section so that its spatial distribution along the propagation axis z is described by a delta function $\delta(z)$:

$$\mathbf{f}_{\text{ext}}(z) = \mathbf{f}_0 \delta(z) \tag{4.38}$$

Two different ways of calculating the excited wave amplitudes are presented in the subsequent paragraphs.

4.3.1 Direct solution of the SAFE governing equations

The wave amplitudes can be found by solving the SAFE equation in the wavenumber - frequency domain directly (see [65]), given the fact that a point excitation as defined in Eq. (4.38) is a constant in wavenumber domain.

The solution is performed using the Spatial Fourier Transform (SFT) defined as:

$$\mathcal{F}\{\mathbf{q}\} = \bar{\mathbf{q}} = \int_{-\infty}^{\infty} \mathbf{q} \exp[\jmath k z]\, \mathrm{d}z \qquad \text{and} \qquad \mathbf{q} = \frac{1}{2\pi} \int_{-\infty}^{\infty} \bar{\mathbf{q}} \exp[-\jmath k z]\, \mathrm{d}k \tag{4.39}$$

which yields that the SFT of the space derivative of a quantity is given by:

$$\mathcal{F}\left\{\frac{\partial}{\partial z}\mathbf{q}\right\} = -\jmath k \mathcal{F}\{\mathbf{q}\} = -\jmath k \bar{\mathbf{q}} \tag{4.40}$$

Let us recall the governing equation for wave propagation in an elastic waveguide in Eq. (4.20), in which the right-hand-side is now given by the SFT of $\mathbf{f}_{\text{ext}}(z)$:

$$\left(-\omega^2 \mathbf{M} + \mathbf{K}_0 - \jmath k \mathbf{K}_1 - (-\jmath k)^2 \mathbf{K}_2 \right) \bar{\mathbf{q}} = \mathbf{f}_0 \tag{4.41}$$

The solution is performed on the linearised form of Eq. (4.41) which brings the benefit of applicability of the GEP properties:

$$\left[\mathbf{A}(\omega) - (-\jmath k)\mathbf{B}(\omega)\right] \bar{\mathbf{q}} = \begin{bmatrix} 0 \\ \mathbf{f}_0 \end{bmatrix} = \widehat{\mathbf{f}}_0 \tag{4.42}$$

where $\mathbf{A}$ and $\mathbf{B}$ are defined by Eq. (4.21) and Eq. (4.22).

The displacement vector $\bar{\mathbf{q}}$ can be written as an expansion in terms of eigenvectors. After pre-multiplying by $\hat{\boldsymbol{\psi}}_\mathbf{i}$ and exploiting the orthogonality of the eigenvectors with respect to $\mathbf{B}$ (Eq. (4.27), Eq. (4.28)) one writes the solution as follows:

$$\bar{\mathbf{q}} = \sum_{i=1}^{2n} \frac{\widehat{\mathbf{f}}_0}{\jmath k (k - k_i)} \hat{\boldsymbol{\psi}}_\mathbf{i} \hat{\boldsymbol{\phi}}_\mathbf{i} \tag{4.43}$$

The form of Eq. (4.43) is similar in appearance to the wave basis expressions in Eq. (4.29), i.e. the solution to the forced wave problem is already written as a weighted superposition of the travelling waves. Their associated mode shapes $\hat{\boldsymbol{\phi}}_\mathbf{i}$, $\hat{\boldsymbol{\psi}}_\mathbf{i}$ and wavenumbers k_i are calculated from Eq. (4.22). The modal weighting factor represents the amplitude of the wave. The amplitude of wave mode i in the space domain can be found via the inverse

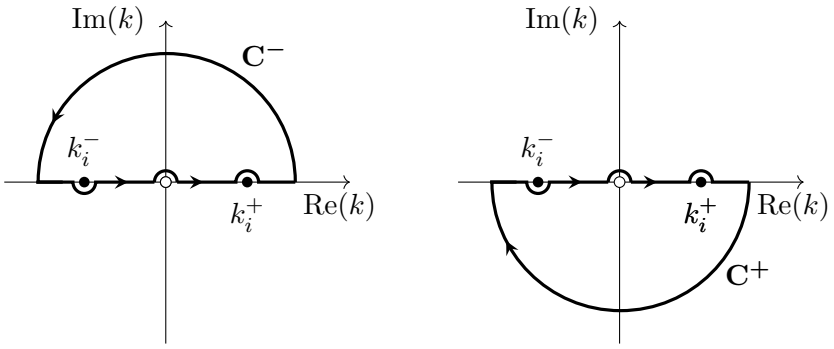

Figure 4.4: Contours for integration.

SFT defined in Eq. (4.39):

$$a_i(z) = \frac{1}{2\pi}\int_{-\infty}^{+\infty} \bar{a}_i \exp[-\jmath k z]\,\mathrm{d}k = \frac{1}{2\pi}\int_{-\infty}^{+\infty} \frac{\widehat{\mathbf{f}}_0}{k-k_i}\hat{\boldsymbol{\psi}}_\mathbf{i} \exp[-\jmath k z]\,\mathrm{d}k \tag{4.44}$$

The above complex integral has simple poles at k_i and a removable singularity at $k = 0$ (since the limit for k approaching 0 is 1). Therefore it is evaluated using Cauchy's residue theorem which states that the complex integral along a chosen contour is the sum of the residues at the poles within the contour [127]. The choice of the contour of integration depends on the solutions of interest. They can be split into two groups. For positive-going waves (right to the force) the integral is evaluated along the semicircle enclosing the lower half of the Re$\{k\}$-Im$\{k\}$ plane, whereas the for the negative-going waves the contour is a semicircle enclosing the upper half of the complex wavenumber plane. In the case of an undamped waveguide the contours need to be properly amended to classify the purely real wavenumbers appropriately using the criterion from Eq. (4.24) or group velocity [128] (see Fig. 4.4 after [54]). Given the notation from Fig. 4.4, the residue theorem can be written as follows [127]:

$$\int_{-\infty}^{+\infty} F(k)\exp[-\jmath k z]\,\mathrm{d}k = \begin{cases} -2\jmath\pi \sum \mathrm{Res}(k_i) & \text{where } k_i \text{ are poles within } \mathbf{C}^+ \quad \text{if } z > 0 \\ 2\jmath\pi \sum \mathrm{Res}(k_i) & \text{where } k_i \text{ are poles within } \mathbf{C}^- \quad \text{if } z < 0 \end{cases} \tag{4.45}$$

where the residues are calculated as [129]:

$$\mathrm{Res}\left(\frac{a(k)}{b(k)}, k_0\right) = \frac{a(k_0)}{b'(k)|_{k=k_0}} \tag{4.46}$$

Thus, after evaluating the integral one gets the excited wave amplitudes in the space domain:

$$\begin{aligned} a_i^+(z) &= -\widehat{\mathbf{f}}_0 \hat{\boldsymbol{\psi}}_\mathbf{i}^+ \exp[-\jmath k_i^+ z] \\ a_i^-(z) &= \widehat{\mathbf{f}}_0 \hat{\boldsymbol{\psi}}_\mathbf{i}^- \exp[-\jmath k_i^- z] \end{aligned} \tag{4.47}$$

4.3.2 Wave approach solution

Alternatively, the excited wave amplitudes can be obtained from displacement continuity and force equilibrium conditions for a section of the waveguide of an infinitesimal length to which the external force is applied. A schematic diagram for the excited wave amplitudes calculation via the wave approach is presented in Fig. 4.5. The cross-hatched section is treated as a rigid body at $z = 0$, hence the displacement resultant from wave propagation in positive and negative directions must be equal and forces must be in equilibrium. Recalling the wave basis expressions that write the displacement and force associated with the propagating wave in terms of wave mode shapes and wave amplitudes one can write:

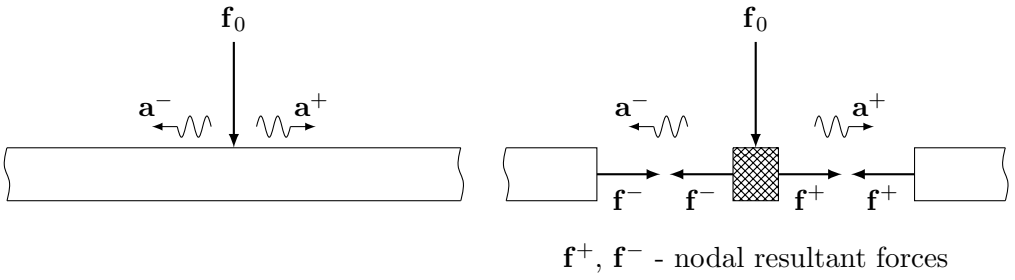

Figure 4.5: Excited waves calculation via wave approach.

$$\begin{bmatrix} \mathbf{\Phi}^+ & -\mathbf{\Phi}^- \\ \mathbf{\Theta}^+ & -\mathbf{\Theta}^- \end{bmatrix} \begin{Bmatrix} \mathbf{a}^+ \\ \mathbf{a}^- \end{Bmatrix} = \begin{Bmatrix} \mathbf{0} \\ \mathbf{f}_0 \end{Bmatrix} \tag{4.48}$$

Eq. (4.48) can then be rearranged using inverse, pseudo-inverse or any other technique exploiting the properties of the mode shapes (e.g. orthogonality [39]) to obtain the excited waves amplitudes:

$$\begin{Bmatrix} \mathbf{a}^+ \\ \mathbf{a}^- \end{Bmatrix} = \begin{bmatrix} \mathbf{\Phi}^+ & -\mathbf{\Phi}^- \\ \mathbf{\Theta}^+ & -\mathbf{\Theta}^- \end{bmatrix}^{-1} \begin{Bmatrix} \mathbf{0} \\ \mathbf{f}_0 \end{Bmatrix} \tag{4.49}$$

Note that both the wave approach and direct solutions described in the preceding sections refer to steady-state excitation of an infinite waveguide. In other words, they constitute the particular solution of the non-homogeneous partial differential equation Eq. (4.15). If a waveguide of finite length is considered, the complementary function must be calculated. This can be done by solving the boundary conditions at the ends of the waveguide directly [130] or, alternatively using the methodology from e.g. [39] preferred in this thesis and referred to as 'wave approach'.

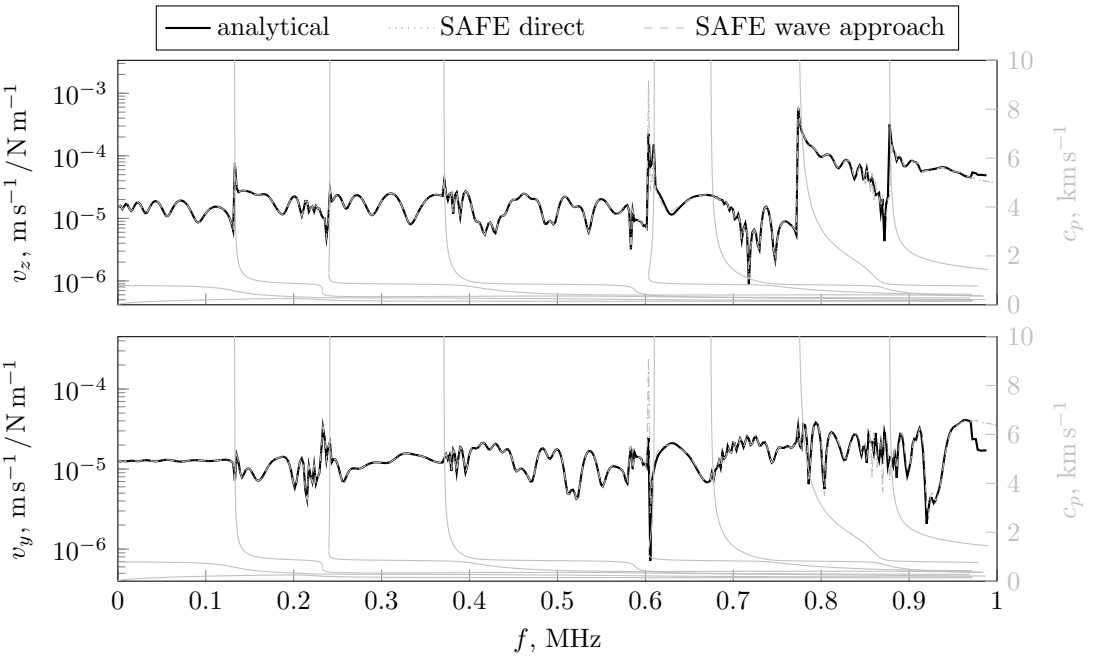

Figure 4.6: Comparison of transfer wave mobilities observed 0.1 m from the force location obtained using different methods (see legend) with the dispersion curves for the waveguide - in-plane line force exciting a 2 mm aluminium plate covered with a 2 mm rime ice accretion.

4.3.3 Comparison with the analytical excitability approach

Provided that a sufficiently fine mesh is used in the SAFE discretisation, the results obtained using the semi-analytical approach agree perfectly with the excitability-based calculations. An illustrative comparison is presented in Fig. 4.6, where transfer mobilities are compared.

The FRFs agree very well. The effect of the waves that cut-off is clearly visible as a sudden jump in the response and noticeable change in the 'peaks and dips' pattern at the following frequencies.

A combination of the two approaches with a particular focus on calculation of the excitability of a lossy waveguide has been recently done by Treyssède [119]. The excitability approach presented here is valid only for lossless waveguides, as is cannot handle the non-propagating waves. Therefore, an alternative approach based on the real reciprocity relation [109] is proposed in [119]. It is expected that excitation of the damped waveguides can be analysed with the SAFE calculation outlined above as it makes no restrictions on the wave type considered.

However, the main disadvantage of the SAFE method can be an insufficiently accurate representation of the wave field distribution over the cross-section. Originating from

variational principles the SAFE formulation provides a very good approximation to total wave energy and power but not necessarily for stress distribution (except Gauss integration points) which is of main interest in this thesis. Therefore, an alternative approach can be employed – SAFE is used for calculating the dispersion curves and excited wave amplitudes, but the wave mode shapes are extracted from the GMM method given the frequency and the wavenumber of a point of interest. By doing so, the sensitivity to the initial guess and step size characteristic for the GMM is circumvented with no loss in the accuracy of the wave field representation.

4.4 Experimental validation on a beam with anechoic terminations

4.4.1 Experimental setup

The SAFE model for calculating the response of the waveguide to a mechanical excitation is validated with a simple experiment. The setup is schematically presented in Fig. 4.7. An impact micro-hammer was used to excite a steel beam with a rectangular cross-section. The response of the waveguide was captured using a laser vibrometer at 0.1025 m from the excitation point. The signal analyser module of the Polytec PSV300 was used to capture the signals.

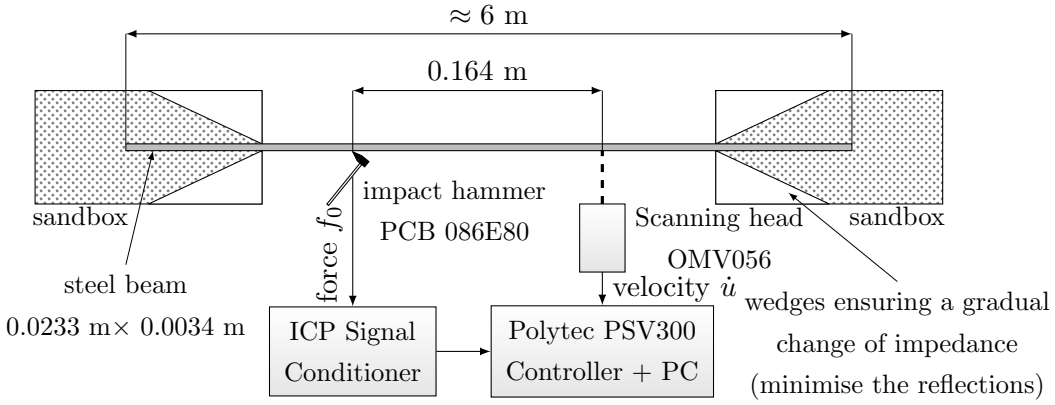

Figure 4.7: Experimental setup for measuring the wave mobility of a beam excited with an impact hammer.

In order to minimise reflections the ends of a 6 m long beam were placed in sandboxes imitating anechoic boundary conditions. The beam was additionally suspended at a few points to keep it in one position as the sand did not provide enough support. The sandboxes are constructed in a way that provides a gradual increase of the sand 'coating' which is expected to minimise the reflections resulting from the sudden change in the

impedance of the waveguide. A significant length of the beam (ca. 0.5 m) was placed in the sandboxes ensuring that as many wavelengths of interest as possible were covered. All these are known to maximise the absorption of the flexural waves by the terminations and enable experimental work on an infinite-like structure.

The material properties for steel are shown in Tab. 2, whereas the dimensions are given in Fig. 4.7. Direct identification of the constants was not performed, falling outside the scope of this thesis. Furthermore, the beam was a standard rolled mild steel profile for which the dimensions vary considerably along the length. Therefore, noting that the model resembles the fundamental physical characteristics of the waveguide correctly, the beam properties were adjusted to provide a good match with the experimental data.

4.4.2 Results and discussion

The comparison between the experimental results and the results obtained from the implemented SAFE model are shown in Fig. 4.8. The corresponding higher order wave mode shapes that cut-off in the considered frequency range are presented in Fig. 4.9. In general, the numerical results represent the experimentally observed response correctly and the first higher-order transverse bending wave is predicted accurately. Nevertheless, some features and ambiguities need to be addressed. The impact hammer has a limited capability of reproducing a perfect impulse. Apart from the common difficulty in avoiding multiple taps, one needs to keep in mind that the real hammer impact acts as a low-pass filter - see the input spectrum in Fig. 4.8. Therefore, the 'usable' frequency range includes regions where the input spectrum is reasonably high. For example between 44–49 kHz the input spectrum experiences a dip and a discrepancy between the model and the experiment is more apparent.

The two peaks marked as the cut-off frequencies of higher-order modes in Fig. 4.8 correspond probably to the cut-off of the two higher-order waves. The cut-off frequencies predicted by the SAFE model together with the mode shapes are shown in Fig. 4.9. They should not be observed if both the excitation and the laser beam were perfectly normal to the plane of the beam and located precisely at the middle of its width. These conditions were difficult to meet in the given experimental setup, hence the peaks in the response.

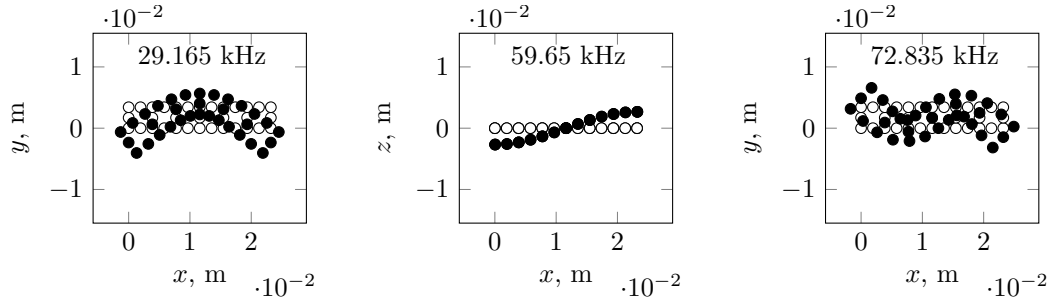

Figure 4.9: Wave mode shapes in beam as used in the experiment computed using SAFE wave model.

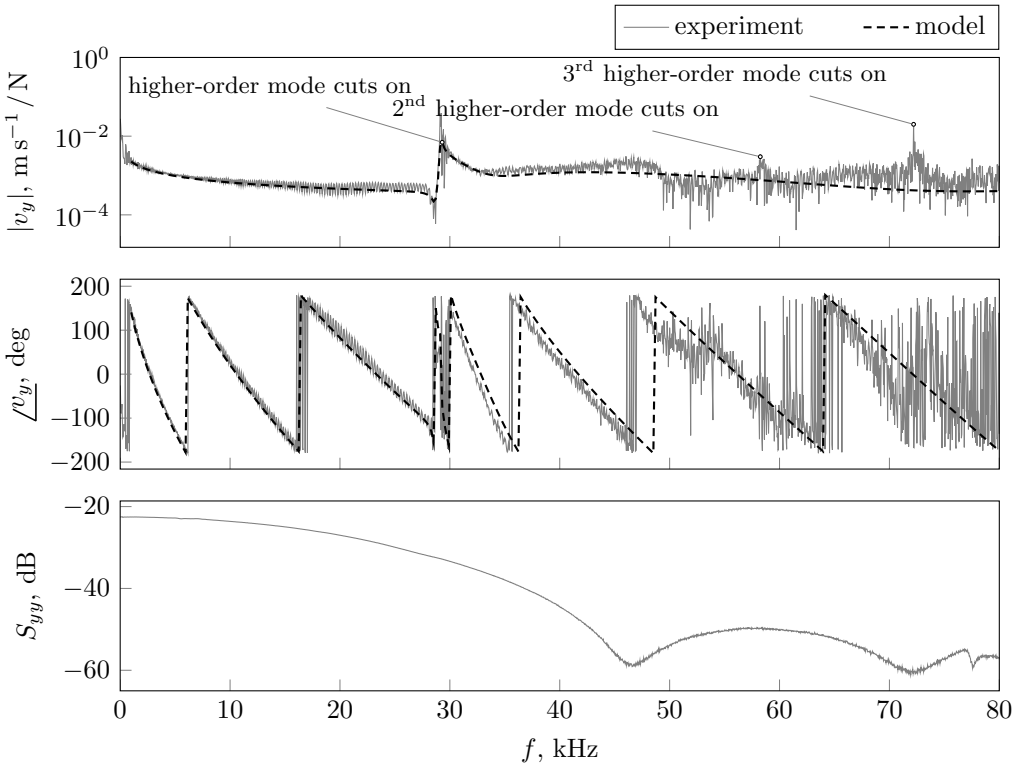

Figure 4.8: Wave mobility of a beam excited with an impulse hammer.

The performance of the sandboxes is acceptable for the purpose of distinguishing the propagating wave contribution from the standing waves, but it is clear that perfect anechoity was not achieved. The ripples on the FRF up to ca. 50 kHz are the imprints of very highly damped standing waves. Around the first cut-off frequency (29.165 kHz), when the magnitude of the response is very high, the waves are exceptionally poorly absorbed at the terminations. At higher frequencies the ripples are also related to the fact that the input level provided by the hammer is very low, hence the response is of a very low magnitude and prone to be affected by noise.

4.5 Assessment of the mode selection criteria for invoking delamination using SAFE

In Chapter 1 the criteria for selecting waves likely to invoke delamination were specified. Since the implementation of the GMM model did not allow the inclusion of material damping, an arbitrarily chosen energy condition was used to account for wave attenuation based on the energy propagation analysis. The SAFE model with complex stiffness (hysteretic damping) now enables these criteria to be assessed.

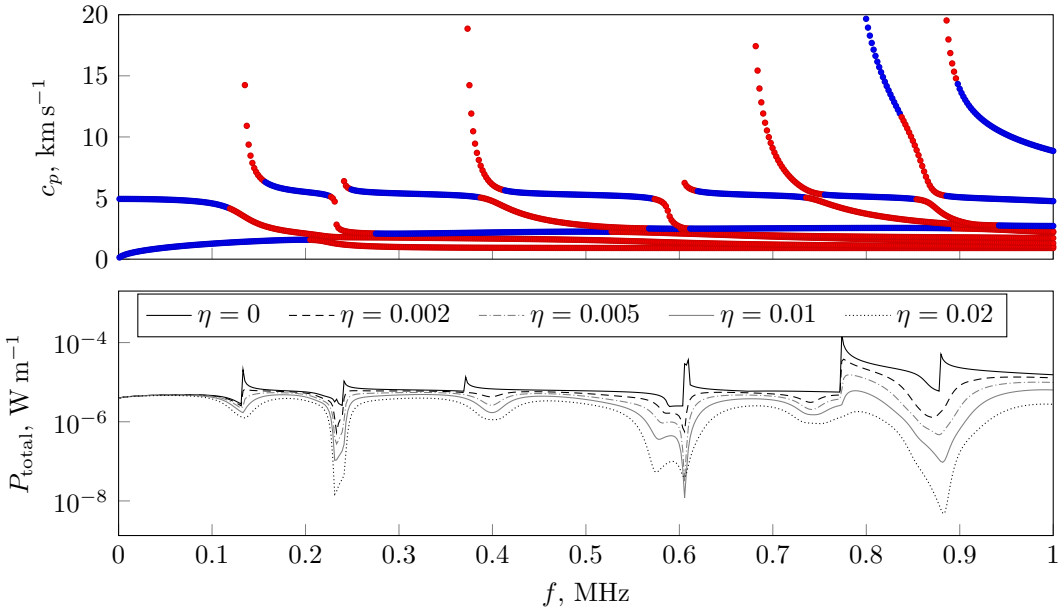

Figure 4.10: Bottom graph–total wave power injected by an in-plane unit line force as seen 0.2 m from the excitation for different rime ice loss factors; top graph–corresponding dispersion curves for an undamped case with colours denoting - blue: ENR < 0.6 and red: ENR ≥ 0.6.

In order to do this, the total wave power injected by a line in-plane force ($F_z = 1$ N m^{-1}) was computed for a 2 mm aluminium plate covered with a 2 mm rime ice accretion with different loss factors using SAFE. As a reference the distribution of values of the energy ratio ENR as defined in Section 2.3 was calculated for an undamped accretion. The aim was to determine whether the waves with ENR > 0.6 carry any significant power, i. e. if not taking them into account as done in Chapter 2 is justifiable. In order to provide a direct relevance to the corresponding GMM results, mono-dimensional plane strain quadratic elements were used in SAFE. The results are presented in Fig. 4.10.

The peaks in power-frequency curves correspond to the cut-off frequencies of higher-order waves. Apart from the one cutting off at around 800 kHz they are all build-up dominated, thus likely to be heavily attenuated if damping is considered. This can be

observed in Fig. 4.10 - the peaks diminish if the loss factor increases and even transform into valleys for large η. The wave cutting off at around 800 kHz is host dominated, so is quite well excited even if the host is covered by a lossy accretion. It is associated with the highest peak in the undamped case and retains the status of the maximum of the power-frequency curve even for a damped waveguide.

These simple results prove the approach adopted in Chapter 1 correct and valid as an indicator. Therefore, high interface stress associated with waves that cut-off can only be efficiently exploited for host dominated waves. The regions with ENR > 0.6 do not carry power in a damped waveguide and therefore are not to be considered for removing structural accretions.

4.6 Conclusions

The semi-analytical finite elements enable modelling of structural wave propagation in waveguides of an arbitrary cross-section. It also allows modelling of damped waveguides with no change to the solution algorithms. The methodology was introduced and implemented. Various aspects including the free wave modal properties and convergence criteria were discussed. The excitation of structural waves was considered using two different techniques, namely direct solution of the SAFE equation and the analytical wave approach. Both of them were compared and proven to be equivalent.

An experimental validation of the implemented SAFE model was performed on a beam-like waveguide with emulated anechoic terminations. The results agreed very well with the numerical simulation. The wave nature of the model was exploited to show various wave modes present in the response.

Finally, the criteria for wave mode selection employed in Chapter 1 and Chapter 2 are assessed with the aid of the SAFE model. The chosen energy distribution criterion is shown to be appropriate.

Some drawbacks of the analytical modelling from the previous chapters were successfully addressed above. The next step is to incorporate a piezoelectric actuator in the SAFE-based model in a way that enables dropping the quasi-static assumption.

Chapter 5

Semi-analytical finite elements for modelling piezoelectric excitation

The common modelling strategies for piezoelectric excitation in waveguides as described in Chapter 1 are not applicable to a large class of problems containing removal of unwanted accretions using structural waves among others. The assumptions in place (e.g. in pin-force model) put into question the validity of these approaches when the actuator's thickness is comparable to the one of the waveguide and when it is driven at high frequencies, possibly close to its resonances. One could then choose costly finite element models that are potentially not bound by the aforementioned limitations, however they require implementing cumbersome techniques in order to provide absorbing boundaries for wave calculations.

An alternative methodology exploiting the versatility of the SAFE formulation and the generality of the wave approach is proposed in this chapter. It starts from the development of a new piezoelectric SAFE element for modelling electroded piezo elements and formulating the framework for calculating the steady-state response to a distributed voltage excitation, which to the best knowledge of the author have not been done to date. The SAFE model is coupled with the analytical wave approach, which accommodated calculations in the wave domain and supports modelling scattering at the discontinuities. Thanks to the piezoelectric SAFE element the dynamics of the actuator can be accounted for and bonding conditions can freely be represented either by additional layer of elastic/viscoelastic SAFE elements or spring SAFE elements as discussed in [68].

The workflow describing the methodology for a simple example of an infinite waveguide with a finite piezoelectric actuator is shown in Fig. 5.1. The diagram outlines the main

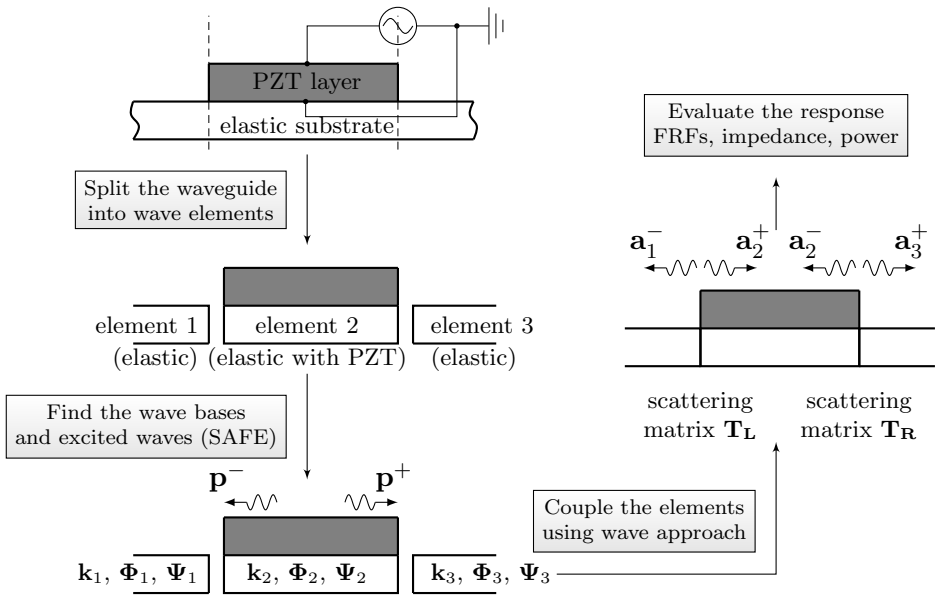

Figure 5.1: The workflow for calculating the response to the piezoelectric excitation using the piezoelectric SAFE method and wave approach.

stages of the calculation. After the structure is split into homogeneous wave elements, the wave basis (i.e. dispersion curves and wave mode shapes) and excited wave amplitudes are obtained for each of them. At the later stage all wave elements are coupled together using the analytical wave approach and the desired response is computed in the wave domain.

In the following sections the mathematical derivation of the piezoelectric SAFE element and excited wave calculation methods are presented. The limitations and numerical issues related to the implementation are briefly discussed. Finally, the model is successfully validated with an experiment.

5.1 Semi-analytical finite element formulation for an elastic waveguide with piezoelectric coupling

The mathematical framework for the SAFE method for the piezoelectric waveguide is developed below. Some parts of the equations and the flow of argument is similar to the ones presented for mechanical SAFE in Chapter 4. Any repetitions are left for the convenience of the reader.

The model presented below involves the following assumptions and limitations:

- the allowable deformation of the cross-section is dictated by the finite element approximation (convergence needs to be ensured),

- the piezoelectric is assumed to be polarised along y direction,
- the electric field vector is assumed to *quasi*-static,
- the electric field in the direction of propagation is assumed to be zero (the effect of one of the shear piezoelectric coefficients is neglected).

5.1.1 Derivation of the piezoelectric SAFE element

It is assumed that the cross-section of the structure lies in the x-y plane and that the wave propagates along the z direction (see labelling conventions in Fig. 5.2). The cross-section in general can be zero-, one- or two-dimensional. Only the two dimensional case is presented in the thesis, however the other cases can easily be recovered by removing appropriate degrees of freedom and altering the element shape functions.

5.1.1.1 Cross-section discretisation

The displacement and strain fields over a wave element are defined analogously to as Eq. (4.1) [64]

$$\mathbf{u} = \begin{bmatrix} u_x & u_y & u_z \end{bmatrix}^\top$$
$$\boldsymbol{\epsilon} = \begin{bmatrix} \epsilon_{xx} & \epsilon_{yy} & \epsilon_{zz} & \gamma_{yz} & \gamma_{xz} & \gamma_{xy} \end{bmatrix}^\top$$
$$\boldsymbol{\sigma} = \begin{bmatrix} \sigma_{xx} & \sigma_{yy} & \sigma_{zz} & \sigma_{yz} & \sigma_{xz} & \sigma_{xy} \end{bmatrix}^\top$$

where the time-harmonic term $\exp[\jmath\omega t]$ is omitted for brevity.

Similarly to Chapter 4, the cross-section is discretised in an FE-like manner using 8-node quadrilateral biquadratic element, however the choice of the element is dictated by the considered case. Linear elements can also be used, however an accurate approximation of the wave field at high frequencies can be achieved at lower cost with quadratic elements.

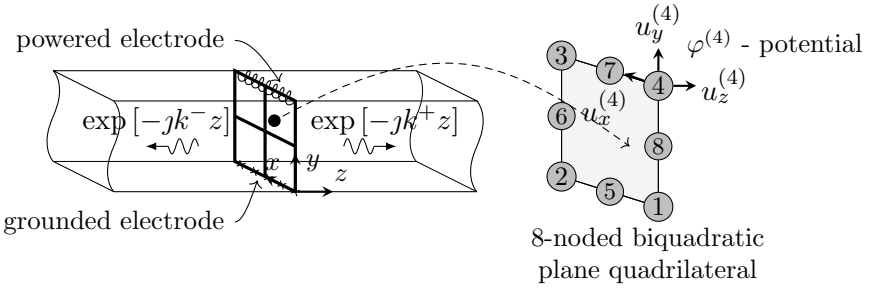

Figure 5.2: Piezoelectric SAFE element - the coordinates and degrees of freedom.

The field variables from Eq. (4.1) are expressed using the element shape functions (in the cross-section plane) and the nodal degrees of freedom (DOFs) as implied by the FE approximation. Given the nodal displacements vector $\mathbf{q}$, the displacement at any point within the SAFE element is

$$\mathbf{u}(x,y,z) = \mathbf{N}(x,y)\mathbf{q}(z) \tag{5.1}$$

where $\mathbf{N}(x,y)$ is the displacement shape function matrix.

Following from Eq. (4.3) one writes the strain in terms of the shape functions and the nodal DOFs

$$\begin{aligned}\boldsymbol{\epsilon}(x,y,z) = \left[\mathbf{L}_x\frac{\partial}{\partial x} + \mathbf{L}_y\frac{\partial}{\partial y} + \mathbf{L}_z\frac{\partial}{\partial z}\right]\mathbf{u}(x,y) = \\ \left[\mathbf{L}_x\mathbf{N}_{,x} + \mathbf{L}_y\mathbf{N}_{,y} + \mathbf{L}_z\frac{\partial}{\partial z}\mathbf{N}\right]\mathbf{q}(z) = \mathbf{B}_1\mathbf{q} + \mathbf{B}_2\frac{\partial}{\partial z}\mathbf{q}(z)\end{aligned} \tag{5.2}$$

where $\mathbf{N}_{,x} = \frac{\partial}{\partial x}\mathbf{N}$ and $\mathbf{L}_x$, $\mathbf{L}_y$, $\mathbf{L}_z$, are given in Eq. (4.5).

In a piezoelectric element each node has an additional degree of freedom representing the electrical potential φ. Therefore, the electrical potential in the waveguide ϑ is expressed as

$$\boldsymbol{\vartheta} = \mathbf{N}_\varphi\boldsymbol{\varphi} \tag{5.3}$$

5.1.1.2 Constitutive equations

The constitutive equations governing the behaviour of the piezoelectric material are written in matricial 'e' form [131]:

$$\begin{aligned}\boldsymbol{\sigma} &= \mathbf{C}^{\mathrm{E}}\boldsymbol{\epsilon} - \mathbf{e}^\top\mathbf{E} \\ \mathbf{D} &= \mathbf{e}\boldsymbol{\epsilon} + \boldsymbol{\varepsilon}^{\epsilon}\mathbf{E}\end{aligned} \tag{5.4}$$

where $\mathbf{C}^{\mathrm{E}}$, $\mathbf{e}$, $\mathbf{E}$, $\mathbf{D}$, $\boldsymbol{\varepsilon}^{\epsilon}$ are the stiffness matrix measured under zero-electric field (short-circuit) condition, piezoelectric stress coefficient matrix, electric field vector, electric displacement vector and permittivity matrix measured at zero-strain (clamped) condition, respectively.

The electromagnetic behaviour of a piezoelectric material is described via Maxwell's equations. However, since no time-varying magnetic field is assumed, *curl* $\mathbf{E}$ is zero. This is commonly referred to as the *quasi*-static (or *quasi*-electrostatic) approximation,

even though $\mathbf{E}$ is time-varying [109, 132]. Thanks to that, the electric field can be expressed as a scalar gradient of the potential

$$\mathbf{E}(x,y,z) = -\nabla\boldsymbol{\vartheta} \tag{5.5}$$

Given the discretisation of the cross-section one writes [133–135]

$$\mathbf{E}(x,y,z) = -\nabla\boldsymbol{\vartheta} = -\begin{bmatrix}\frac{\partial}{\partial x} & \frac{\partial}{\partial y} & \frac{\partial}{\partial z}\end{bmatrix}^{\top}\mathbf{N}_{\varphi}\boldsymbol{\varphi} \tag{5.6}$$

where the electrical potential shape functions $\mathbf{N}_{\boldsymbol{\varphi}}$ are chosen to be the same as the displacement shape functions $\mathbf{N}$.

In this work piezoelectric elements are developed to be used for modelling actuators made of bulk piezoelectric ceramic (PZT) with two electroded surfaces. A driving voltage is applied across the thickness of the PZT element (y direction) and the electric field is assumed not to change along the propagation direction z. The SAFE matrices related to the electric field will then be z-invariant, which facilitates condensation of the potentials. By doing so, the contribution of the piezoelectric coefficient associated with the voltage gradient along z is neglected, which is not expected to invoke a significant error for wave excitation calculation (the voltage is applied along the direction y). Eq. (5.6) is rewritten as

$$\mathbf{E}(x,y,z) = -\begin{bmatrix}\mathbf{N}_{\varphi,x} & \mathbf{N}_{\varphi,y} & 0\end{bmatrix}^{\top}\boldsymbol{\varphi} = -\mathbf{B}_{\varphi}\boldsymbol{\varphi} \tag{5.7}$$

Substituting Eqs. (4.4), (5.7) into Eq. (5.4) one gets the constitutive equations expressed in terms of nodal degrees of freedom and element shape functions

$$\begin{aligned}\boldsymbol{\sigma} &= \mathbf{C}^{\mathrm{E}}\left(\mathbf{B}_1\mathbf{q} + \mathbf{B}_2\frac{\partial}{\partial z}\mathbf{q}\right) + \mathbf{e}^{\top}\mathbf{B}_{\varphi}\boldsymbol{\varphi}\\ \mathbf{D} &= \mathbf{e}\left(\mathbf{B}_1\mathbf{q} + \mathbf{B}_2\frac{\partial}{\partial z}\mathbf{q}\right) - \boldsymbol{\varepsilon}^{\epsilon}\mathbf{B}_{\varphi}\boldsymbol{\varphi}\end{aligned} \tag{5.8}$$

If one sets the piezoelectric coefficients in $\mathbf{e}$ and dielectric constants in $\boldsymbol{\varepsilon}^{\epsilon}$ to zero, standard elastic Hooke's Law equations are recovered.

5.1.1.3 Virtual work principle for piezoelectric semi-analytical finite element

The governing equations for wave propagation are obtained with the aid of the virtual work principle for deformable bodies and the analogous principle of virtual electric potentials [132, 134, 135]. The analysed section of a piezoelectric waveguide occupies volume

V which is formed by a cross-section Ω extruded through length L and is bounded by surface Γ. The boundary conditions (BC) on Γ are the following:

- Essential mechanical BC on Γ_u (Dirchelet BC): $u = \underline{u}$
- Essential electrical BC on Γ_φ (Dirchelet BC): $\varphi = \underline{\varphi}$
- Natural mechanical BC on Γ_σ (Neumann BC): $\sigma_{ij} n_j = t_i$
- Natural electrical BC on Γ_ϱ (Neumann BC): $n_i D_i = \varrho_i$

where $\underline{u}$ and $\underline{\varphi}$ are the prescribed displacement and potential, respectively, and t_i, ϱ_i are the applied surface traction and the applied surface charge, respectively. The respective bounding surfaces related to each pair of the boundary conditions are exclusive and their unions form the whole surface, i.e. $\Gamma_u \cup \Gamma_\sigma = \Gamma$, $\Gamma_u \cap \Gamma_\sigma = 0$ and analogously $\Gamma_\varphi \cup \Gamma_\varrho = \Gamma$, $\Gamma_\varphi \cap \Gamma_\varrho = 0$.

Given the constitutive equations, the mechanical equilibrium condition, and the essential boundary conditions given above the virtual work principle states that for every time t

$$\overbrace{\int_{\Gamma_\sigma} \delta \mathbf{u}^\top \mathbf{t} \, \mathrm{d}\Gamma_\sigma}^{\substack{\text{work done by} \\ \text{external surface} \\ \text{tractions}}} + \overbrace{\delta \mathbf{q}^\top \mathbf{f}_i}^{\substack{\text{work done by} \\ \text{nodal forces}}} = \overbrace{\int_{\mathrm{V}} \delta \mathbf{u}^\top (\rho \ddot{\mathbf{u}}) \, \mathrm{d}V}^{\substack{\text{work done by} \\ \text{inertia body forces}}} + \overbrace{\int_{\mathrm{V}} \delta \boldsymbol{\epsilon}^\top \boldsymbol{\sigma} \, \mathrm{d}V}^{\substack{\text{work done by} \\ \text{the stress field}}} \tag{5.9}$$

where $\mathbf{t}$ is the external tractions vector, $\mathbf{f}_i$ is the vector of nodal forces applied at the ends of the considered section of the waveguide of length L and ρ is the density of the material.

Similarly, under the essential boundary conditions, the virtual electric potentials principle states that for every time t

$$-\overbrace{\int_{\Gamma_\varrho} \delta \boldsymbol{\varphi}^\top \boldsymbol{\varrho} \, \mathrm{d}\Gamma_\varrho}^{\substack{\text{work done by} \\ \text{external surface} \\ \text{charges}}} = \overbrace{\int_{\mathrm{V}} \delta \mathbf{E}^\top \mathbf{D} \, \mathrm{d}V}^{\substack{\text{work done by} \\ \text{the electric} \\ \text{displacement field}}} \tag{5.10}$$

where $\boldsymbol{\varrho}$ is the external surface charge vector.

The constitutive equations from Eq. (5.8) are substituted into each of the components in Eqs. (5.9) and (5.10) along with the finite element approximations given in Eqs. (4.3), (4.4), (5.7). The detailed algebraic manipulations for all of the components are omitted below for the sake of clarity but only the final equations for each component are given.

The work done on the stress field by the strain field is given by

$$\begin{aligned}\int_{\mathrm{V}} \delta\boldsymbol{\epsilon}^{\top}\boldsymbol{\sigma}\,\mathrm{d}V = &\int_{\Omega}\left[\delta\mathbf{q}^{\top}\left(\mathbf{B}_2^{\top}\mathbf{C}\mathbf{B}_1\mathbf{q}+\mathbf{B}_2^{\top}\mathbf{C}\mathbf{B}_2\frac{\partial}{\partial z}\mathbf{q}+\mathbf{B}_2^{\top}\mathbf{e}^{\top}\mathbf{B}_{\varphi}\boldsymbol{\varphi}\right)\right]\mathrm{d}\Omega\\ &+\int_{\Omega}\int_{\mathrm{L}}\left[\delta\mathbf{q}^{\top}\mathbf{B}_1^{\top}\mathbf{C}\mathbf{B}_1\mathbf{q}+\delta\mathbf{q}^{\top}\left(\mathbf{B}_1^{\top}\mathbf{C}\mathbf{B}_2-\mathbf{B}_2^{\top}\mathbf{C}\mathbf{B}_1\right)\frac{\partial}{\partial z}\mathbf{q}\right.\\ &\left.-\delta\mathbf{q}^{\top}\mathbf{B}_2^{\top}\mathbf{C}\mathbf{B}_2\frac{\partial^2}{\partial z^2}\mathbf{q}+\delta\mathbf{q}^{\top}\mathbf{B}_1^{\top}\mathbf{e}^{\top}\mathbf{B}_{\varphi}\boldsymbol{\varphi}-\delta\mathbf{q}^{\top}\mathbf{B}_2^{\top}\mathbf{e}^{\top}\mathbf{B}_{\varphi}\frac{\partial}{\partial z}\boldsymbol{\varphi}\right]\mathrm{d}z\mathrm{d}\Omega\end{aligned} \tag{5.11}$$

The work done on the electric displacement field by the electric field is given by

$$\int_{\mathrm{V}}\delta\mathbf{E}^{\top}\mathbf{D}\,\mathrm{d}V=\int_{\mathrm{V}}\left[\delta\boldsymbol{\varphi}^{\top}\mathbf{B}_{\varphi}^{\top}\boldsymbol{\varepsilon}^{\mathrm{s}}\mathbf{B}_{\varphi}\boldsymbol{\varphi}-\delta\boldsymbol{\varphi}^{\top}\mathbf{B}_{\varphi}^{\top}\left(\mathbf{e}\mathbf{B}_{\mathbf{1}}\mathbf{q}+\mathbf{B}_{\varphi}^{\top}\mathbf{e}\mathbf{B}_{\mathbf{2}}\frac{\partial}{\partial z}\mathbf{q}\right)\right]\mathrm{d}V \tag{5.12}$$

The work done by the intertia forces and the distributed tractions term are the same as in Eq. (4.9) and Eq. (4.11), respectively.

In order to clarify the formulation the following notation is adopted which results from the integration of the matrices over the cross-sectional element domain:

$$\begin{aligned}\mathbf{M}&=\int_{\Omega}\mathbf{N}^{\top}\rho\mathbf{N}\,\mathrm{d}\Omega & \mathbf{K}_f&=\int_{\Omega}\mathbf{B}_2^{\top}\mathbf{C}\mathbf{B}_1\,\mathrm{d}\Omega\\ \mathbf{K}_0&=\int_{\Omega}\mathbf{B}_1^{\top}\mathbf{C}\mathbf{B}_1\,\mathrm{d}\Omega & \mathbf{K}_0^{u\varphi}&=\mathbf{K}_0^{\varphi u\top}=\int_{\Omega}\mathbf{B}_1^{\top}\mathbf{e}^{\top}\mathbf{B}_{\varphi}\,\mathrm{d}\Omega\\ \mathbf{K}_1&=\int_{\Omega}\mathbf{K}_f^{\top}-\mathbf{K}_f\,\mathrm{d}\Omega & \mathbf{K}_1^{u\varphi}&=\mathbf{K}_1^{\varphi u\top}=\int_{\Omega}\mathbf{B}_2^{\top}\mathbf{e}^{\top}\mathbf{B}_{\varphi}\,\mathrm{d}\Omega\\ \mathbf{K}_2&=\int_{\Omega}\mathbf{B}_2^{\top}\mathbf{C}\mathbf{B}_2\,\mathrm{d}\Omega & \mathbf{K}^{\varphi\varphi}&=\int_{\Omega}\mathbf{B}_{\varphi}^{\top}\boldsymbol{\varepsilon}^{\mathrm{s}}\mathbf{B}_{\varphi}\,\mathrm{d}\Omega\\ \mathbf{p}&=\int_{\Gamma_{\sigma}}\mathbf{N}^{\top}\mathbf{N}\mathbf{t}_i\,\mathrm{d}\Gamma_{\sigma} & \boldsymbol{\Upsilon}&=\int_{\Gamma_{\varrho}}\boldsymbol{\varrho}\,\mathrm{d}\Gamma_{\varrho}\end{aligned} \tag{5.13}$$

Let us now rewrite both variational equations Eq. (5.9) and Eq. (5.10) using the notation from Eq. (4.13). Rearranging the terms one obtains

$$\begin{aligned}\mathbf{0}=\int_{L}\Big\{&\delta\mathbf{q}^{\top}\Big(\mathbf{M}\frac{\partial^2}{\partial t^2}\mathbf{q}+\mathbf{K}_0\mathbf{q}+\mathbf{K}_1\frac{\partial}{\partial z}\mathbf{q}-\mathbf{K}_2\frac{\partial^2}{\partial z^2}\mathbf{q}\Big)+\\ &\delta\mathbf{q}^{\top}\Big(\mathbf{K}_0^{u\varphi}\boldsymbol{\varphi}-\mathbf{K}_1^{u\varphi}\frac{\partial}{\partial z}\boldsymbol{\varphi}\Big)-\delta\mathbf{q}^{\top}\mathbf{p}\Big\}\,\mathrm{d}z+\\ &\delta\mathbf{q}^{\top}\left[\mathbf{K}_f\mathbf{q}+\mathbf{K}_2\frac{\partial}{\partial z}\mathbf{q}+\mathbf{K}_1^{u\varphi}\boldsymbol{\varphi}-\mathbf{f}_i\right]\end{aligned} \tag{5.14}$$

and

$$0 = \int_L \left\{ \delta\boldsymbol{\varphi}^\top \mathbf{K}^{\varphi\varphi}\boldsymbol{\varphi} - \delta\boldsymbol{\varphi}^\top \left(\mathbf{K}_0^{\varphi u}\mathbf{q} + \mathbf{K}_1^{\varphi u}\frac{\partial}{\partial z}\mathbf{q} \right) + \delta\boldsymbol{\varphi}^\top \boldsymbol{\Upsilon} \right\} \mathrm{d}z \tag{5.15}$$

Eq. (4.14) contains two main terms – the first is related to the wave field behaviour over the length L and the second corresponds to cross-sections at the ends of L. Both equations contain terms reflecting the electromechanical coupling. They need to hold for every time t and any admissible virtual displacement δq and virtual potential $\delta\varphi$, which leads to the governing equation for wave propagation in a waveguide with .

5.1.1.4 Governing equations for wave propagation and resultant nodal forces

From Eqs. (5.14), (5.15) one can conclude the set of the governing equations for wave propagation

$$\begin{aligned} \mathbf{M}\frac{\partial^2}{\partial t^2}\mathbf{q} + \mathbf{K}_0\mathbf{q} + \mathbf{K}_1\frac{\partial}{\partial z}\mathbf{q} - \mathbf{K}_2\frac{\partial^2}{\partial z^2}\mathbf{q} + \mathbf{K}_0^{u\varphi}\boldsymbol{\varphi} - \mathbf{K}_1^{u\varphi}\frac{\partial}{\partial z}\boldsymbol{\varphi} &= \mathbf{p} \\ \mathbf{K}_0^{\varphi u}\mathbf{q} + \mathbf{K}_1^{\varphi u}\frac{\partial}{\partial z}\mathbf{q} - \mathbf{K}^{\varphi\varphi}\boldsymbol{\varphi} &= \boldsymbol{\Upsilon} \end{aligned} \tag{5.16}$$

and the natural boundary condition stating that at the ends of the considered section of the waveguide

$$\mathbf{q} = 0 \qquad \text{or} \qquad \mathbf{f}_i = \mathbf{K}_f\mathbf{q} + \mathbf{K}_2\frac{\partial}{\partial z}\mathbf{q} + \mathbf{K}_1^{u\varphi}\boldsymbol{\varphi} \tag{5.17}$$

which directly provides the expression for the resultant nodal forces.

Solution to Eq. (5.16) is performed using the Spatial Fourier Transform (SFT) defined in Eq. (4.39)

$$\mathcal{F}\{\mathbf{q}\} = \bar{\mathbf{q}} = \int_{-\infty}^{\infty} \mathbf{q}\exp\left[\jmath kz\right]\mathrm{d}z \text{ and } \mathbf{q} = \frac{1}{2\pi}\int_{-\infty}^{\infty} \bar{\mathbf{q}}\exp\left[-\jmath kz\right]\mathrm{d}k$$

which yields that the SFT of the space derivative of a quantity is given by Eq. (4.40)

$$\mathcal{F}\left\{\frac{\partial}{\partial z}\mathbf{q}\right\} = -\jmath k\mathcal{F}\{\mathbf{q}\} = -\jmath k\bar{\mathbf{q}}$$

Applying Eqs. (4.39) and (4.40) to Eq. (5.16) and performing the time derivation under the harmonic motion assumption, one writes

$$\left(\begin{bmatrix} -\omega^2\mathbf{M} & \mathbf{0} \\ \mathbf{0} & \mathbf{0} \end{bmatrix} + \begin{bmatrix} \mathbf{K}_0 - \jmath k\mathbf{K}_1 - (-\jmath k)^2\mathbf{K}_2 & \mathbf{K}_0^{u\varphi} + \jmath k\mathbf{K}_1^{u\varphi} \\ \mathbf{K}_0^{\varphi u} - \jmath k\mathbf{K}_1^{\varphi u} & -\mathbf{K}^{\varphi\varphi} \end{bmatrix} \right) \begin{Bmatrix} \bar{\mathbf{q}} \\ \bar{\boldsymbol{\varphi}} \end{Bmatrix} = \begin{Bmatrix} \bar{\mathbf{p}} \\ \bar{\boldsymbol{\Upsilon}} \end{Bmatrix} \tag{5.18}$$

Eq. (5.18) is the governing equation for wave propagation in a piezoelectric waveguide in the wavenumber-frequency domain. After same transformations the resultant forces over the cross-section are given by

$$\bar{\mathbf{f}}_i = \mathbf{K}_f \bar{\mathbf{q}} - \jmath k \mathbf{K}_2 \bar{\mathbf{q}} + \mathbf{K}_1^{u\varphi} \bar{\boldsymbol{\varphi}} \tag{5.19}$$

5.1.1.5 Static condensation of the internal potentials

The focus of the procedure is the application to piezoelectric actuators where the outer surfaces perpendicular to the propagation direction are electroded. One of the electrodes is grounded and the other one is driven with voltage v. It is therefore advantageous to express the above equation in terms of driving voltage which can be done by condensing out the potentials at the internal nodes via static condensation [133, 134, 136]. For sake of brevity we write the SAFE matrices in the following manner:

$$\begin{aligned} \mathbf{K}^{uu}(k) &= \mathbf{K}_0 - \jmath k \mathbf{K}_1 - (-\jmath k)^2 \mathbf{K}_2 \\ \mathbf{K}^{u\varphi}(k) &= \mathbf{K}_0^{u\varphi} + \jmath k \mathbf{K}_1^{u\varphi} \\ \mathbf{K}^{\varphi u}(k) &= \mathbf{K}_0^{\varphi u} - \jmath k \mathbf{K}_1^{\varphi u} \end{aligned} \tag{5.20}$$

In the following the index i denotes the internal nodes, index v denotes the nodes on the powered electrode and finally the index 0 denotes the nodes on the grounded electrode. Eq. (4.20) is then rewritten as

$$\begin{bmatrix} \mathbf{K}^{uu}(k) - \omega^2 \mathbf{M} & \mathbf{K}_v^{u\varphi}(k) & \mathbf{K}_0^{u\varphi}(k) & \mathbf{K}_i^{u\varphi}(k) \\ \mathbf{K}_v^{\varphi u}(k) & -\mathbf{K}_{vv}^{\varphi\varphi} & -\mathbf{K}_{v0}^{\varphi\varphi} & -\mathbf{K}_{vi}^{\varphi\varphi} \\ \mathbf{K}_0^{\varphi u}(k) & -\mathbf{K}_{0v}^{\varphi\varphi} & -\mathbf{K}_{00}^{\varphi\varphi} & -\mathbf{K}_{0\mathrm{i}}^{\varphi\varphi} \\ \mathbf{K}_i^{\varphi u}(k) & -\mathbf{K}_{iV}^{\varphi\varphi} & -\mathbf{K}_{\mathrm{i}0}^{\varphi\varphi} & -\mathbf{K}_{ii}^{\varphi\varphi} \end{bmatrix} \begin{Bmatrix} \bar{\mathbf{q}} \\ \bar{\boldsymbol{\varphi}}_v \\ \bar{\boldsymbol{\varphi}}_0 \\ \bar{\boldsymbol{\varphi}}_i \end{Bmatrix} = \begin{Bmatrix} \bar{\mathbf{p}} \\ \bar{\boldsymbol{\Upsilon}}_v \\ \mathbf{0} \\ \mathbf{0} \end{Bmatrix} \tag{5.21}$$

We assume that there are no external forces and remove rows and columns associated with the grounded electrode $\bar{\boldsymbol{\varphi}}_\mathbf{0}$ since $\bar{\boldsymbol{\varphi}}_\mathbf{0} = 0$. Potentials at the internal nodes can be extracted from the third equation

$$\bar{\boldsymbol{\varphi}}_i = \left(\mathbf{K}_{ii}^{\varphi\varphi}\right)^{-1} \left(\mathbf{K}_i^{\varphi u}(k) \bar{\mathbf{q}} - \mathbf{K}_{iV}^{\varphi\varphi} \bar{\boldsymbol{\varphi}}_v\right) \tag{5.22}$$

And finally the governing equation can be rewritten using the condensed potentials

$$\begin{bmatrix} \mathbf{K}^{uu}(k) & \mathbf{K}_v^{u\varphi}(k) \\ -\omega^2\mathbf{M} + \mathbf{K}_i^{u\varphi}(k)\left(\mathbf{K}_{ii}^{\varphi\varphi}\right)^{-1}\mathbf{K}_i^{\varphi u}(k) & -\mathbf{K}_i^{u\varphi}(k)\left(\mathbf{K}_{ii}^{\varphi\varphi}\right)^{-1}\mathbf{K}_{iV}^{\varphi\varphi} \\ \mathbf{K}_v^{\varphi u}(k) & -\mathbf{K}_{vv}^{\varphi\varphi} \\ -\mathbf{K}_{vi}^{\varphi\varphi}\left(\mathbf{K}_{ii}^{\varphi\varphi}\right)^{-1}\mathbf{K}_i^{\varphi u}(k) & +\mathbf{K}_{vi}^{\varphi\varphi}\left(\mathbf{K}_{ii}^{\varphi\varphi}\right)^{-1}\mathbf{K}_{iV}^{\varphi\varphi} \end{bmatrix} \cdot \begin{Bmatrix} \bar{\mathbf{q}} \\ \bar{\boldsymbol{\varphi}}_v \end{Bmatrix} = \begin{Bmatrix} \mathbf{0} \\ \bar{\boldsymbol{\Upsilon}}_v \end{Bmatrix} \tag{5.23}$$

The matrices above are expanded according to the shorthand notation introduced in Eq. (5.20) and the resulting equations rearranged and grouped with respect to the order of the wavenumber. All components of the driving voltage subvector $\boldsymbol{\varphi}_v$ are equal since voltage is constant over the driving electrode. Hence, the contributions of all nodes on the powered electrode can be summed up providing an elegant equation with only one electrical driving voltage v. Similarly, the reaction charge is summed across the 'line' electrode yielding total reaction charge q that is straightforwardly related to the current drawn by the actuator

$$i = \jmath\omega q \tag{5.24}$$

After some algebraic manipulations the condensed matrices can be written in the form

$$\begin{aligned} \tilde{\mathbf{K}}_0 &= \mathbf{K}_0 + \mathbf{K}_{0i}^{u\varphi}\left(\mathbf{K}_{ii}^{\varphi\varphi}\right)^{-1}\mathbf{K}_{0\mathrm{i}}^{\varphi u} \\ \tilde{\mathbf{K}}_1 &= \mathbf{K}_1 + \left[\mathbf{K}_{0i}^{u\varphi}\left(\mathbf{K}_{ii}^{\varphi\varphi}\right)^{-1}\mathbf{K}_{1i}^{\varphi u} - \mathbf{K}_{1i}^{u\varphi}\left(\mathbf{K}_{ii}^{\varphi\varphi}\right)^{-1}\mathbf{K}_{0i}^{\varphi u}\right] \\ \tilde{\mathbf{K}}_2 &= \mathbf{K}_2 + \mathbf{K}_{1i}^{u\varphi}\left(\mathbf{K}_{ii}^{\varphi\varphi}\right)^{-1}\mathbf{K}_{1i}^{\varphi u} \\ \tilde{\mathbf{K}}_0^{u\varphi} &= \tilde{\mathbf{K}}_0^{\varphi u^\top} = \left[\mathbf{K}_{0v}^{u\varphi} - \mathbf{K}_{0i}^{u\varphi}\left(\tilde{\mathbf{K}}_{ii}^{\varphi\varphi}\right)^{-1}\mathbf{K}_{iv}^{\varphi\varphi}\right]\mathbf{I}_\mathbf{v} \\ \tilde{\mathbf{K}}_1^{u\varphi} &= \tilde{\mathbf{K}}_1^{\varphi u^\top} = \left[\mathbf{K}_{1v}^{u\varphi} - \mathbf{K}_{1i}^{u\varphi}\left(\mathbf{K}_{ii}^{\varphi\varphi}\right)^{-1}\mathbf{K}_{iV}^{\varphi\varphi}\right]\mathbf{I}_\mathbf{v} \\ \tilde{\mathbf{K}}^{\varphi\varphi} &= \mathbf{I}_\mathbf{v}{}^\top\left[\mathbf{K}_{vv}^{\varphi\varphi} - \mathbf{K}_{Vi}^{\varphi\varphi}\left(\mathbf{K}_{ii}^{\varphi\varphi}\right)^{-1}\mathbf{K}_{iV}^{\varphi\varphi}\right]\mathbf{I}_\mathbf{v} \\ \tilde{\mathbf{K}}_f &= \mathbf{K}_f + \mathbf{K}_{1i}^{u\varphi}\left(\mathbf{K}_{ii}^{\varphi\varphi}\right)^{-1}\mathbf{K}_{0i}^{\varphi u} \end{aligned} \tag{5.25}$$

where $\mathbf{I}_\mathbf{v} = \begin{bmatrix} 1 & 1 & \dots & 1 \end{bmatrix}^\top$ is the vector of the length equal to the number of nodes on the powered piezoelectric electrode [134].

The governing equations can be finally written in terms of the condensed matrices

$$\begin{bmatrix} \tilde{\mathbf{K}}_0 - \jmath k\tilde{\mathbf{K}}_1 - (-\jmath k)^2\tilde{\mathbf{K}}_2 - \omega^2\mathbf{M} & \tilde{\mathbf{K}}_0^{u\varphi} + \jmath k\tilde{\mathbf{K}}_1^{u\varphi} \\ \tilde{\mathbf{K}}_0^{\varphi u} - \jmath k\tilde{\mathbf{K}}_1^{\varphi u} & -\tilde{\mathbf{K}}^{\varphi\varphi} \end{bmatrix} \begin{Bmatrix} \bar{\mathbf{q}} \\ v \end{Bmatrix} = \begin{Bmatrix} \bar{\mathbf{p}} \\ q \end{Bmatrix} \tag{5.26}$$

where q is the total reaction charge over the powered electrode and v is the driving voltage. The tilde $\tilde{\{\}}$ symbol indicates that the matrix is amended to account for the condensed potentials.

Analogously, the internal forces vector is rewritten as

$$\bar{\mathbf{f}}_i = \tilde{\mathbf{K}}_f \bar{\mathbf{q}} - \jmath k \tilde{\mathbf{K}}_2 \bar{\mathbf{q}} + \tilde{\mathbf{K}}_1^{u\varphi} v \tag{5.27}$$

5.1.2 Free elastic waves in a waveguide with piezoelectric coupling

Let us now look at the free wave propagation in an elastic waveguide with piezoelectric coupling. As a consequence of the *quasi*-electrostatic assumption, only elastic waves are permitted. The role of the piezoelectric coupling is to provide means of exciting the waveguide, sensing the travelling waves, harvesting the mechanical energy or stiffening the waveguide with the spatially-static nature of voltage kept in mind.

Before the response to the distributed voltage is introduced we look at the calculation and basic characteristics of the free waves which form a basis for the forced response solution. The SAFE equations for an elastic waveguide can be recovered from Eqs. (5.26), (5.27) by setting all the piezoelectric material constants to zero. The solution procedure for free waves remains the same.

5.1.2.1 Electrical conditions

Free waves in a waveguide with piezoelectric coupling can be considered either in the short-circuit or in the open-circuit condition. The former implies that the voltage in the powered electrode is set to zero ($v = 0$) resulting in the quadratic eigenvalue problem (QEP)

$$\left[\tilde{\mathbf{K}}_0 + \lambda \tilde{\mathbf{K}}_1 - \lambda^2 \tilde{\mathbf{K}}_2 - \omega^2 \mathbf{M}\right] \boldsymbol{\phi} = \mathbf{0} \tag{5.28}$$

where $\boldsymbol{\phi}$ is the eigenvector.

Conversely, for the open-circuit electrodes the 'driving' charge Q is set to zero. The modal potential at the powered electrode is then extracted from the second row of

Eq.(5.26): $v = \left(\tilde{\mathbf{K}}^{\varphi\varphi}\right)^{-1}\left(\tilde{\mathbf{K}}_0^{\varphi u} + \jmath k\tilde{\mathbf{K}}_1^{\varphi u}\right)\boldsymbol{\phi}$, and substituted back in the first row equation. After some manipulation one obtains

$$\begin{aligned}&\left\{\left[\tilde{\mathbf{K}}_0 + \tilde{\mathbf{K}}_0^{u\varphi}\left(\tilde{\mathbf{K}}^{\varphi\varphi}\right)^{-1}\tilde{\mathbf{K}}_0^{\varphi u} - \omega^2\mathbf{M}\right] + \right.\\ &\lambda\left[\tilde{\mathbf{K}}_1 + \tilde{\mathbf{K}}_0^{u\varphi}\left(\tilde{\mathbf{K}}^{\varphi\varphi}\right)^{-1}\tilde{\mathbf{K}}_1^{\varphi u} - \tilde{\mathbf{K}}_1^{u\varphi}\left(\tilde{\mathbf{K}}^{\varphi\varphi}\right)^{-1}\tilde{\mathbf{K}}_0^{\varphi u}\right] - \\ &\left.\lambda^2\left[\tilde{\mathbf{K}}_2 + \tilde{\mathbf{K}}_1^{u\varphi}\left(\tilde{\mathbf{K}}^{\varphi\varphi}\right)^{-1}\tilde{\mathbf{K}}_1^{\varphi u}\right]\right\}\boldsymbol{\phi} = 0\end{aligned} \tag{5.29}$$

The form of the eigenvalue problem is similar to Eq. (5.28) with the stiffness matrices enhanced. Therefore, Eq. (5.29) indicates that in the open-circuit condition the structure is stiffened compared to the short-circuit case. This is a well-known effect of the piezoelectric coupling on the elastic behaviour of the material.

In this thesis the voltage is the 'driving' variable. The charge is a response variable associated with how the actuator-structure system responds to the applied voltage. Therefore, the short-circuit condition equations are considered hereafter. However, the procedure outlined below can be applied to both aforementioned cases.

5.1.2.2 Free wave solution

Similarly to Chapter 4, the solution to the QEP in Eq. (5.28) is performed using linearisation by doubling the size of the system. A new eigenvector is introduced as $\hat{\boldsymbol{\phi}} = \begin{bmatrix}\boldsymbol{\phi} & \lambda\boldsymbol{\phi}\end{bmatrix}^\top$ and the SAFE governing equation from Eq. (5.28) is rewritten as a generalised eigenvalue problem (GEP)

$$\left(\begin{bmatrix}\mathbf{0} & \tilde{\mathbf{K}}_0 - \omega^2\mathbf{M}\\ \tilde{\mathbf{K}}_0 - \omega^2\mathbf{M} & \tilde{\mathbf{K}}_1\end{bmatrix} - \lambda\begin{bmatrix}\tilde{\mathbf{K}}_0 - \omega^2\mathbf{M} & \mathbf{0}\\ \mathbf{0} & \tilde{\mathbf{K}}_2\end{bmatrix}\right)\begin{Bmatrix}\boldsymbol{\phi}\\ \lambda\boldsymbol{\phi}\end{Bmatrix} = \mathbf{0} \tag{5.30}$$

or more concisely as

$$\left[\mathbf{A}(\omega) - \lambda\mathbf{B}(\omega)\right]\hat{\boldsymbol{\phi}} = \mathbf{0} \tag{5.31}$$

where $\mathbf{A}$, $\mathbf{B}$ are of dimensions $2n \times 2n$, n is the number of the displacement degrees of freedom in the cross-section and

$$\lambda = -\jmath k$$

Since there is no difference in the description of the free wave solution, the matrices and eigenvectors structure and the modal solution properties, the reader is referred to Section 4.2 where these matters were discussed for SAFE elements for mechanical waveguides.

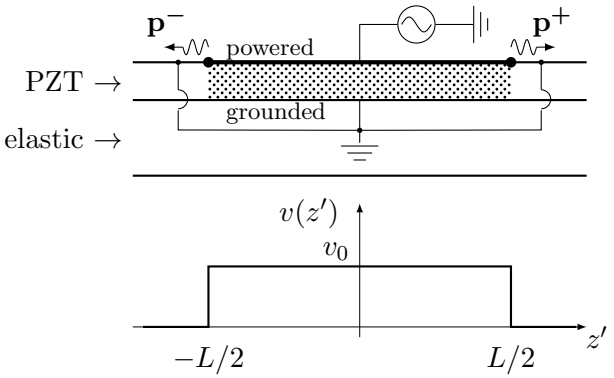

Figure 5.3: Piezoelectric waveguide driven electrically over a finite length. Excited waves amplitudes and voltage spatial distribution.

5.1.3 Excitation of structural waves in an elastic waveguide covered with a piezoelectric layer powered over a finite length

In this section the piezoelectric wave element developed above is used to study structural waves excitation as a response to a spatially distributed voltage. We consider a steady-state response in an infinite elastic layer covered over its whole length by an electroded piezoelectric layer (Fig. 5.3). A finite section of the electrode is driven with time-harmonic voltage v_0. Note that the 'driving' section is electrically isolated from adjacent parts of the waveguide. The hatched region represents the section of the piezoelectric layer under electrical excitation. The adjacent sections of the waveguide are in the short-circuit condition. Vectors $\mathbf{p}^-$ and $\mathbf{p}^+$ represent the waves generated by the distributed patch-like piezoelectric excitation as they enter the non-powered region. A local coordinate system (z') is introduced with the origin in the middle of the length of the piezoelectric actuator. The spatial distribution of voltage $v(z')$ is a rectangular box function as shown in Fig. 5.3, such that

$$v(z') = \begin{cases} v_0 & \text{if } z' \leq |L/2| \\ 0 & \text{otherwise} \end{cases} \tag{5.32}$$

5.1.3.1 Direct solution of the SAFE equation

The wave amplitudes can be found by solving the SAFE equation in the wavenumber - frequency domain directly, given the spatial distribution of voltage (the approach similar to [54] where the response to a distributed pressure is considered). Let us recall the top row of the governing equation for wave propagation in the piezoelectric waveguide in

Eq. (5.26), assuming no external tractions for the sake of clarity of the formulation

$$\left(\tilde{\mathbf{K}}_0 - \jmath k\tilde{\mathbf{K}}_1 - (-\jmath k)^2\tilde{\mathbf{K}}_2 - \omega^2\mathbf{M}\right)\bar{\mathbf{q}} = \left(-\tilde{\mathbf{K}}_0^{u\varphi} - \jmath k\tilde{\mathbf{K}}_1^{u\varphi}\right)\bar{v} \tag{5.33}$$

where $\bar{v}$ is the SFT of the voltage spatial distribution given by

$$\bar{v} = \int_{-\infty}^{\infty} v(z')\exp\left[\jmath kz'\right]\mathrm{d}z' = 2v_0\frac{\sin\left(kL/2\right)}{k} \tag{5.34}$$

The solution is performed on the linearised form of Eq.(5.33) which enables the use of GEP properties

$$\left[\mathbf{A}(\omega) - (-\jmath k)\mathbf{B}(\omega)\right]\bar{\mathbf{q}} = \begin{bmatrix} 0 \\ -\tilde{\mathbf{K}}_0^{u\varphi} - \jmath k\tilde{\mathbf{K}}_1^{u\varphi} \end{bmatrix}\bar{v} \tag{5.35}$$

The displacement vector $\bar{\mathbf{q}}$ can be written as an expansion in terms of eigenvectors. After pre-multiplying by $\hat{\boldsymbol{\psi}}_\mathbf{i}$ and exploiting the orthogonality of the eigenvectors with respect to $\mathbf{B}$ (Eq. (4.27)) one writes the solution as

$$\bar{\mathbf{q}} = \sum_{i=1}^{2n}\frac{2v_0\sin\left(kL/2\right)}{\jmath k(k-k_i)}\hat{\boldsymbol{\psi}}_\mathbf{i}\begin{bmatrix} 0 \\ -\tilde{\mathbf{K}}_0^{u\varphi} - \jmath k\tilde{\mathbf{K}}_1^{u\varphi} \end{bmatrix}\hat{\boldsymbol{\phi}}_\mathbf{i} = \sum_{i=1}^{2n}\hat{\boldsymbol{\phi}}_i\bar{p}_i \tag{5.36}$$

where the $\bar{v}$ was substituted with the expression from Eq. (5.34).

The form of Eq. (5.36) is similar in appearance to the wave basis expressions in Eq. (4.29), i.e. the solution to the voltage excited wave problem is already written as a weighted superposition of the travelling waves. The modal weighting factor representing the amplitude of wave i in the space domain is found via the inverse SFT defined in Eq. (4.39)

$$\begin{aligned} p_i(z') = \frac{1}{2\pi}\int_{-\infty}^{+\infty}\bar{p}_i\exp[-\jmath kz']\,\mathrm{d}k = \\ \frac{1}{2\pi}\int_{-\infty}^{+\infty}\frac{2v_0\sin\left(kL/2\right)}{\jmath k(k-k_i)}\hat{\boldsymbol{\psi}}_\mathbf{i}\begin{bmatrix} 0 \\ -\tilde{\mathbf{K}}_0^{u\varphi} - \jmath k\tilde{\mathbf{K}}_1^{u\varphi} \end{bmatrix}\exp[-\jmath kz']\,\mathrm{d}k \end{aligned} \tag{5.37}$$

The above complex integral has simple poles at k_i and a removable singularity at $k = 0$ (since the limit for k approaching 0 is 1) and therefore it is evaluated using Cauchy's residue theorem [127] outlined in Section 4.3.1. The contours of integrations are shown again in Fig. 5.4 [54] for reference. The Cauchy's residue theorem can be written as

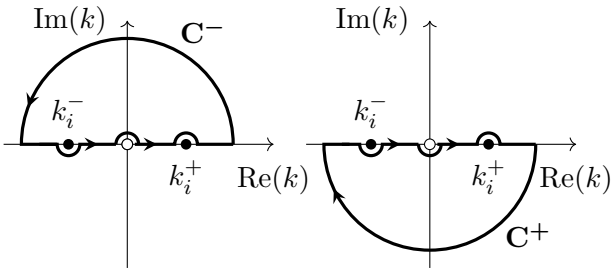

Figure 5.4: Contours for integration.

follows [127]

$$\int_{-\infty}^{+\infty} F(k)\exp[-\jmath k z']\,\mathrm{d}k = \begin{cases} -2\jmath\pi\sum \mathrm{Res}(k_i) & \text{where } k_i \text{ are poles within } \mathbf{C}^+ \quad \text{if } z'>0 \\ 2\jmath\pi\sum \mathrm{Res}(k_i) & \text{where } k_i \text{ are poles within } \mathbf{C}^- \quad \text{if } z'<0 \end{cases} \tag{5.38}$$

where the residues are calculated as [129]

$$\mathrm{Res}\left(\frac{a(k)}{b(k)}, k_0\right) = \frac{a(k_0)}{b'(k)|_{k=k_0}} \tag{5.39}$$

After evaluating the integral one obtains the excited wave amplitudes in the space domain

$$\begin{aligned} p_i^+(z') &= -\frac{2v_0\sin\left(k_i^+ L/2\right)}{k_i^+}\hat{\boldsymbol{\psi}}_{\mathbf{i}}^+ \begin{bmatrix} 0 \\ -\tilde{\mathbf{K}}_0^{u\varphi} - \jmath k_i^+ \tilde{\mathbf{K}}_1^{u\varphi} \end{bmatrix} \exp[-\jmath k_i^+ z'] \\ p_i^-(z') &= \frac{2v_0\sin\left(k_i^- L/2\right)}{k_i^-}\hat{\boldsymbol{\psi}}_{\mathbf{i}}^- \begin{bmatrix} 0 \\ -\tilde{\mathbf{K}}_0^{u\varphi} - \jmath k_i^- \tilde{\mathbf{K}}_1^{u\varphi} \end{bmatrix} \exp[-\jmath k_i^- z'] \end{aligned} \tag{5.40}$$

Note that the excited wave amplitudes $p_i^+(z')$, $p_i^-(z')$ are expressed with reference to the local coordinate system as depicted in Fig. 5.3. In order to obtain the excited waves amplitudes as they appear at the ends of the electrically driven region, they need to be multiplied by appropriate space harmonic term representing propagation over $L/2$, yielding

$$\begin{aligned} p_i^+ &= -\frac{v_0\left(1-\exp\left[-\jmath k_i^+ L\right]\right)}{\jmath k_i^+}\hat{\boldsymbol{\psi}}_{\mathbf{i}}^+ \begin{bmatrix} 0 \\ -\tilde{\mathbf{K}}_0^{u\varphi} - \jmath k_i^+ \tilde{\mathbf{K}}_1^{u\varphi} \end{bmatrix} \\ p_i^- &= \frac{v_0\left(\exp\left[\jmath k_i^- L\right]-1\right)}{\jmath k_i^-}\hat{\boldsymbol{\psi}}_{\mathbf{i}}^- \begin{bmatrix} 0 \\ -\tilde{\mathbf{K}}_0^{u\varphi} - \jmath k_i^- \tilde{\mathbf{K}}_1^{u\varphi} \end{bmatrix} \end{aligned} \tag{5.41}$$

Eq. (5.41) provides expressions for wave amplitudes excited by a voltage uniformly distributed over L in an infinite piezo-covered waveguide as they appear at the ends of the

driving section. Identical expressions can be found from convolving the response to a point voltage excitation with the spatial voltage distribution.

5.1.3.2 Solution via convolution of point excitations

Alternatively, the wave amplitudes generated by the electrical excitation over a finite length can be expressed as a superposition of voltage point excitations defined as

$$v(z') = v_0\delta(z') = \begin{cases} v_0 & \text{if } z' = 0 \\ 0 & \text{otherwise} \end{cases} \tag{5.42}$$

The response to a single point voltage excitation is calculated from the SAFE equation in a manner similar to the one presented above. Since the SFT of a delta function as defined in Eq. (5.42) is v_0, the excited wave amplitudes are

$$\begin{aligned} d_i^+ &= -v_0\hat{\boldsymbol{\psi}}_\mathbf{i}^+ \begin{bmatrix} 0 \\ -\tilde{\mathbf{K}}_0^{u\varphi} - \jmath k_i^+ \tilde{\mathbf{K}}_1^{u\varphi} \end{bmatrix} \\ d_i^- &= v_0\hat{\boldsymbol{\psi}}_\mathbf{i}^- \begin{bmatrix} 0 \\ -\tilde{\mathbf{K}}_0^{u\varphi} - \jmath k_i^- \tilde{\mathbf{K}}_1^{u\varphi} \end{bmatrix} \end{aligned} \tag{5.43}$$

The resultant generated wave amplitudes as they appear at the ends of the excited region are obtained by convolving the point excitation wave amplitudes with the spatial distribution of voltage Eq. (5.32)

$$\begin{aligned} p_j^+ &= \int_0^L d_j^+ \exp[-\jmath k_j^+ z'] \,\mathrm{d}z' = \frac{d_j^+}{-\jmath k_j^+}(\exp[-\jmath k_j^+ L] - 1) \\ p_j^- &= \int_0^L d_j^- \exp[\jmath k_j^- z'] \,\mathrm{d}z' = \frac{d_j^-}{\jmath k_j^-}(\exp[\jmath k_j^- L] - 1) \end{aligned} \tag{5.44}$$

Expressions for wave amplitudes after substituting Eq. (5.43) are identical with the ones given in Eq. (5.41).

5.2 Wave approach

The semi-analytical finite element approach *per se* is only applicable to infinite waveguides with a uniform cross-section. In order to accommodate modelling structural wave excitation with finite piezoelectric actuators, but also more complex structures in general, the analytical wave approach is employed. The SAFE model serves as a kernel

module that provides the wave bases (see Section 4.2.1) and excited wave amplitudes for each wave element, i.e. each homogeneous section of the complex waveguide under consideration. The further solution is conducted in the wave domain using analytical relationships representing scattering and reflection.

5.2.1 Wave basis

The wave basis for a piezoelectric waveguide is the same as for the elastic waveguide since only elastic waves are permitted in the former. Let us recall it for convenience

$$\begin{Bmatrix} \mathbf{q}(z) \\ \mathbf{f}(z) \end{Bmatrix} = \begin{Bmatrix} \boldsymbol{\Phi} \\ \boldsymbol{\Theta} \end{Bmatrix} \mathbf{a}(z) = \begin{bmatrix} \boldsymbol{\phi}^{+} & \boldsymbol{\phi}^{-} \\ \boldsymbol{\theta}^{+} & \boldsymbol{\theta}^{-} \end{bmatrix} \begin{Bmatrix} \mathbf{a}^{+}(z) \\ \mathbf{a}^{-}(z) \end{Bmatrix}$$

where $\boldsymbol{\phi}^{+,-}$ are positive- and negative-going *displacement wave mode shapes* obtained by taking the upper half of the extended eigenvector $\hat{\boldsymbol{\phi}}_{\mathbf{i}}$; $\boldsymbol{\theta}^{+,-}$ are the *force wave mode shapes* obtained from Eq. (5.27): $\boldsymbol{\theta} = \begin{bmatrix} \tilde{\mathbf{K}}_f & \tilde{\mathbf{K}}_2 \end{bmatrix} \hat{\boldsymbol{\phi}}$, and $\mathbf{a}^{+}(z)$, $\mathbf{a}^{-}(z)$ are the corresponding wave amplitudes.

As in Chapter 4 the wave amplitude change along the waveguide is described by the space-harmonic term called the propagation matrix $\boldsymbol{\tau}(z)$

$$\mathbf{a}^{+}(z) = \mathbf{a_0}^{+} \mathrm{diag}\left(\exp\left[-\jmath k_i z\right]\right) = \mathbf{a_0}^{+} \boldsymbol{\tau}(z)$$

where $\mathbf{a_0}^{+}$ is the wave amplitude at a chosen origin.

5.2.2 Wave scattering and reflection

The wave approach involves coupling together wave elements that have different dimensions and properties. The wave elements are required to be meshed in such a way that all the nodes from the overlapping regions of two adjacent waveguides are coincident. Wave scattering at discontinuities and reflection at the boundaries is represented here in the same way as proposed in [38, 39].

When incident on the junction, the wave scatters into reflected and transmitted components. The frequency dependent scattering matrix can be found by solving simultaneously the conditions of displacement continuity and force equilibrium between the adjacent sections [38]. With reference to Fig. 5.5b, let us write them in the matrix form using the wave basis defined in Eq. (4.29)

$$\begin{bmatrix} -\mathbf{C}_1 \boldsymbol{\phi}_1^{-} & \mathbf{C}_2 \boldsymbol{\phi}_2^{+} \\ -\mathbf{E}_1 \boldsymbol{\theta}_1^{-} & \mathbf{E}_2 \boldsymbol{\theta}_2^{+} \end{bmatrix} \begin{Bmatrix} \mathbf{g}^{-} \\ \mathbf{f}^{+} \end{Bmatrix} = \begin{bmatrix} \mathbf{C}_1 \boldsymbol{\phi}_1^{+} & -\mathbf{C}_2 \boldsymbol{\phi}_2^{-} \\ \mathbf{E}_1 \boldsymbol{\theta}_1^{+} & -\mathbf{E}_2 \boldsymbol{\theta}_2^{-} \end{bmatrix} \begin{Bmatrix} \mathbf{g}^{+} \\ \mathbf{f}^{-} \end{Bmatrix} \tag{5.45}$$

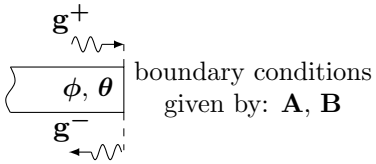

(a) wave reflection at the boundary

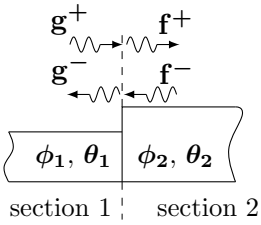

(b) wave scattering at a junction between two waveguides

Figure 5.5: Schematic wave diagrams for calculation of wave scattering at discontinuities.

where $\mathbf{C}_1$, $\mathbf{C}_2$ are continuity matrices that provide information about the coincident nodes in both sections and leaving the uncoupled nodes free, whereas $\mathbf{E}_1$, $\mathbf{E}_2$ are equilibrium matrices that are balancing the nodal resultant forces at the coincident nodes and setting the resultant nodal forces at the uncoupled nodes to zero.

By inverting the matrix on the right hand side of Eq. (5.45) one can express the waves leaving the junction in terms of the waves incident upon the junction by means of the scattering matrix $\mathbf{T}$

$$\begin{Bmatrix} \mathbf{g}^- \\ \mathbf{f}^+ \end{Bmatrix} = \begin{bmatrix} -\mathbf{C}_1\boldsymbol{\phi}_1^- & \mathbf{C}_2\boldsymbol{\phi}_2^+ \\ -\mathbf{E}_1\boldsymbol{\theta}_1^- & \mathbf{E}_2\boldsymbol{\theta}_2^+ \end{bmatrix}^{-1} \begin{bmatrix} \mathbf{C}_1\boldsymbol{\phi}_1^+ & -\mathbf{C}_2\boldsymbol{\phi}_2^- \\ \mathbf{E}_1\boldsymbol{\theta}_1^+ & -\mathbf{E}_2\boldsymbol{\theta}_2^- \end{bmatrix} \begin{Bmatrix} \mathbf{g}^+ \\ \mathbf{f}^- \end{Bmatrix} = \begin{bmatrix} \mathbf{R}^{11} & \mathbf{T}^{21} \\ \mathbf{T}^{12} & \mathbf{R}^{22} \end{bmatrix} \begin{Bmatrix} \mathbf{g}^+ \\ \mathbf{f}^- \end{Bmatrix} = \mathbf{T} \begin{Bmatrix} \mathbf{g}^+ \\ \mathbf{f}^- \end{Bmatrix} \tag{5.46}$$

where the structure of the scattering matrix is clearly shown in the last step.

Similarly, wave reflection at the boundary can be determined using the wave basis. Depending on the type of the boundary condition either the displacement or force degree of freedom is set to zero. With reference to Fig. 5.5a this can be represented in a matrix form as [39]

$$\mathbf{A}\mathbf{f} + \mathbf{B}\mathbf{q} = 0 \tag{5.47}$$

which in terms of the wave basis defined in Eq. (4.29) is written as

$$\mathbf{A}\left[\boldsymbol{\theta}^+\mathbf{g}^+ + \boldsymbol{\theta}^-\mathbf{g}^-\right] + \mathbf{B}\left[\boldsymbol{\phi}^+\mathbf{g}^+ + \boldsymbol{\phi}^-\mathbf{g}^-\right] = 0 \tag{5.48}$$

The reflection matrix relates the wave leaving the boundary to the wave incident upon the boundary, such that $\mathbf{g}^- = \mathbf{R}\mathbf{g}^+$ (for the 'right' boundary). After rearranging Eq. (5.48) one obtains an expression for a reflection matrix at the 'right' boundary,

i.e. with positive-going wave incident, given the characteristics of the boundary $\mathbf{A}$, $\mathbf{B}$

$$\mathbf{R} = -\left[\mathbf{A}\boldsymbol{\theta}^{-} + \mathbf{B}\boldsymbol{\phi}^{-}\right]^{-1}\left[\mathbf{A}\boldsymbol{\theta}^{+} + \mathbf{B}\boldsymbol{\phi}^{+}\right] \tag{5.49}$$

5.3 Structural waves excitation using a piezoelectric actuator

The approach is demonstrated on a simple model of an infinite waveguide with a rectangular cross-section equipped with a finite piezo actuator (see Fig. 5.1). The structure is first subdivided into 3 wave elements, i.e. two (identical) elastic elements and one elastic element covered with a piezoelectric layer. Each wave element is analysed using a SAFE model in order to find the wave bases and the amplitudes of waves generated by the voltage excitation. Afterwards, the coupling between the wave elements is implemented using scattering matrices. Finally, the desired response is computed in the wave domain. The scattering matrices for the two junctions are calculated according to Eq. (5.46) at each frequency.

Calculation of the response of a waveguide of either finite or indefinite length is essentially solving a non-homogeneous partial differential equation. Its solution has two parts: particular integral and complementary function. Particular integral represents the response of the waveguide to forcing as if the waveguide was infinite, whereas complementary function represents free waves travelling between the boundaries (and therefore required to fulfil the boundary conditions) [137]. Two approaches to the solution method can be adopted.

In the first approach (as done for example in [130] both particular integral and complementary function are calculated separately – particular integral via e.g. spatial Fourier transform and complementary function by ensuring that the free wave solution fulfils the boundary conditions.

The other approach, referred to as wave approach and adopted in this thesis, follows the perspective of a wave travelling through the structure. Similarly to the previous case, the response to the excitation (excited wave) is calculated first as if the waveguide was infinite. Then the response right to the forcing location is written as a sum of the excited wave and the travelling wave coming from the left boundary. Travelling waves are propagated through the structure and appropriate reflection and scattering matrices are applied. Although possibly not evident at first, this technique leads to the same

solution as that previously described. Travelling waves represent the complementary function and they are obtained with the aid of simple matrix algebra.

Although the approach is demonstrated on a very simple example below, it can be extended to enable modelling a multi-component waveguide. The only condition that needs to be ensured is the conformity of the meshes of the overlapping parts of the subsequent adjacent cross-sections. A generalised piece-wise formulation is given in Appendix B.

There are two possible desired outputs of such a calculation, namely either the excited wave field propagating in the elastic substrate or the electrical impedance of the actuator. Both cases are considered below.

5.3.1 The response outside the piezo-covered region

The interest is in finding the wave amplitudes induced in the substrate waveguide at a position z_r to the right of the actuator, denoted hereafter by $\mathbf{b}^+$. The travelling waves at different stages and the excited waves at the ends of the actuator are depicted in Fig. 5.6.

The wave amplitudes resulting from the distributed voltage excitation $\mathbf{p}^-$, $\mathbf{p}^+$ as found in Section 5.1.3 are immediately incident upon the discontinuities at the ends of the piezoelectric actuator, and therefore scattered according to the appropriate scattering matrix for the junction.

Since the right boundary condition is ideally absorbing (located at ∞) there is no negative-going wave in element 3. Thus, the response of the structure at z_r is written in wave domain as

$$\mathbf{q}(z_r) = \boldsymbol{\phi}^+ \mathbf{b}^+(z_r) = \boldsymbol{\phi}^+ \boldsymbol{\tau}(z_r) \mathbf{a}_3^+ \tag{5.50}$$

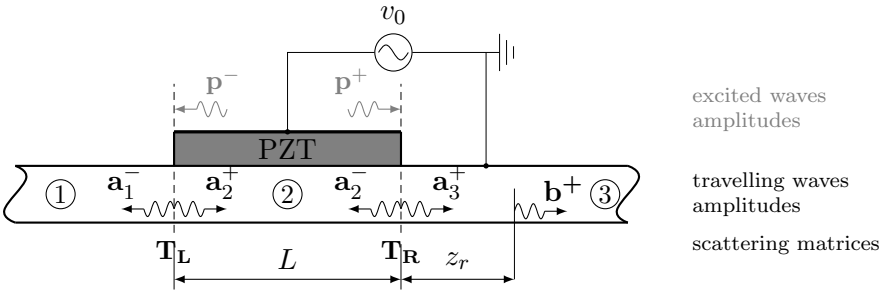

Figure 5.6: Infinite waveguide excited with a piezoelectric actuator - schematic diagrams for calculating the travelling waves outside the PZT-covered section; the excited waves $\mathbf{p}^+$, $\mathbf{p}^-$ are defined at the edges of the actuator just before they are incident on the discontinuity.

In order to obtain the response at a desired location z_r one needs to find the travelling wave amplitude $\mathbf{a_3}^+$ first

$$\mathbf{a}_3^+ = \mathbf{T}_{\mathrm{R}}^{12}\mathbf{p}^+ + \mathbf{T}_{\mathrm{R}}^{12}\boldsymbol{\tau}(L)\mathbf{a}_2^+ \tag{5.51}$$

where

$$\mathbf{a}_2^+ = \mathbf{R}_{\mathrm{L}}^{22}\mathbf{p}^- + \mathbf{R}_{\mathrm{L}}^{22}\boldsymbol{\tau}(L)\mathbf{a}_2^- \tag{5.52}$$

and

$$\mathbf{a}_2^- = \mathbf{R}_{\mathrm{R}}^{11}\mathbf{p}^+ + \mathbf{R}_{\mathrm{R}}^{11}\boldsymbol{\tau}(L)\mathbf{a}_2^+ \tag{5.53}$$

Therefore,

$$\mathbf{a}_2^+ = \mathbf{R}_{\mathrm{L}}^{22}\mathbf{p}^- + \mathbf{R}_{\mathrm{L}}^{22}\boldsymbol{\tau}(L)\left[\mathbf{R}_{\mathrm{R}}^{11}\mathbf{p}^+ + \mathbf{R}_{\mathrm{R}}^{11}\boldsymbol{\tau}(L)\mathbf{a}_2^+\right] \tag{5.54}$$

and

$$\mathbf{a}_2^+ = \left[\mathbf{I} - \mathbf{R}_{\mathrm{L}}^{22}\boldsymbol{\tau}(L)\mathbf{R}_{\mathrm{R}}^{11}\boldsymbol{\tau}(L)\right]^{-1}\left[\mathbf{R}_{\mathrm{L}}^{22}\mathbf{p}^- + \mathbf{R}_{\mathrm{L}}^{22}\boldsymbol{\tau}(L)\mathbf{R}_{\mathrm{R}}^{11}\mathbf{p}^+\right] \tag{5.55}$$

Finally,

$$\begin{aligned}\mathbf{a}_3^+ = \mathbf{T}_{\mathrm{R}}^{12}\mathbf{p}^+ + \mathbf{T}_{\mathrm{R}}^{12}\boldsymbol{\tau}(L)\big[\mathbf{I} - \mathbf{R}_{\mathrm{L}}^{22}\boldsymbol{\tau}(L)\mathbf{R}_{\mathrm{R}}^{11}\boldsymbol{\tau}(L)\big]^{-1}\cdot \\ \big[\mathbf{R}_{\mathrm{L}}^{22}\mathbf{p}^- + \mathbf{R}_{\mathrm{L}}^{22}\boldsymbol{\tau}(L)\mathbf{R}_{\mathrm{R}}^{11}\mathbf{p}^+\big]\end{aligned} \tag{5.56}$$

which after substituting into Eq. (5.50) leads to the desired response.

5.3.2 The response within the piezo-covered region: electrical impedance extraction

Many engineering applications take advantage of the electromechanical coupling in piezoelectric elements to sense the dynamic behaviour of the structure by means of the frequency dependent electrical impedance of the PZT element $z(\omega) = \frac{v(\omega)}{i(\omega)}$. Although only the electrical quantities are measured directly (voltage, current), it is often referred to as an electrical impedance since the backward current generated by the vibrating substrate imposes its dynamic characteristics on the electric output of the piezoelectric.

The driving voltage v is kept fixed, whereas the current drawn is obtained from the second row of Eq. (5.26) which provides an expression for the total reaction charge on the electrode

$$\begin{bmatrix}\tilde{\mathbf{K}}_0^{\varphi u} - \jmath k\tilde{\mathbf{K}}_1^{\varphi u} & -\tilde{\mathbf{K}}^{\varphi\varphi}\end{bmatrix}\begin{Bmatrix}\bar{\mathbf{q}} \\ v\end{Bmatrix} = -q \tag{5.57}$$

It is evident from Eq. (5.57) that the total reaction charge consists of two parts: the component resulting from the electrical properties of the piezoelectric ($\tilde{\mathbf{K}}^{\varphi\varphi}$) which has a capacitive nature, and the component resulting from the mechanical deformation of the element generating charge via piezoelectric electromechanical coupling ($\tilde{\mathbf{K}}_0^{\varphi u} - \jmath k\tilde{\mathbf{K}}_1^{\varphi u}$).

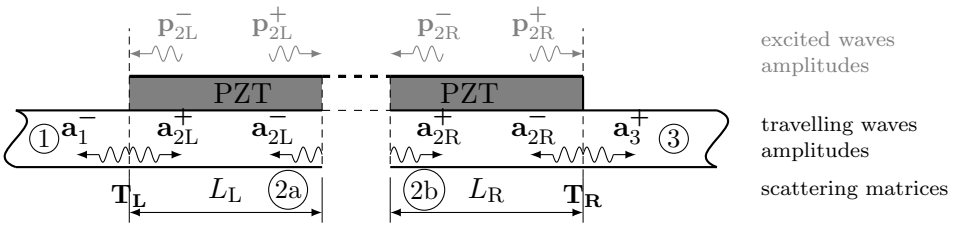

Figure 5.7: Infinite waveguide excited with a piezoelectric actuator - schematic diagrams for calculating the travelling waves inside the PZT-covered section; the excited waves $\mathbf{p}^+_{2L}$, $\mathbf{p}^-_{2L}$, $\mathbf{p}^+_{2R}$, $\mathbf{p}^-_{2R}$ are defined at the edges of the actuator just before they are incident on the discontinuity.

Since the reaction charge needs to be summed over the length of the actuator, a methodology for evaluating the response inside the actuator is required. At each location z_i along the length of the PZT-covered wave element we split it into two parts: the one to the left from z_i and that to the right from z_i. The excited waves are calculated separately for each part using the framework presented in the previous paragraphs and substituting the correct lengths depending on z_i. A schematic diagram for the calculation is shown in Fig. 5.7.

The excited waves $\mathbf{p}^+_{2L}$, $\mathbf{p}^-_{2L}$, $\mathbf{p}^+_{2R}$, $\mathbf{p}^-_{2R}$ as depicted in Fig. 5.7 are the wave amplitudes excited in an infinite waveguide covered by the piezoelectric layer powered over a finite length (Section 5.1.3) and in case of a finite piezoelectric layer the are immediately incident upon a discontinuity.

One starts the calculation from writing the expressions for travelling waves at different stages as

$$\begin{aligned} \mathbf{a}^+_{2R} &= \mathbf{p}^+_{2L} + \boldsymbol{\tau}(L_L)\mathbf{a}^+_{2L} \quad & \mathbf{a}^-_{2R} &= \mathbf{R}^{11}_R \mathbf{p}^+_{2R} + \mathbf{R}^{11}_R \boldsymbol{\tau}(L_R)\mathbf{a}^+_{2R} \\ \mathbf{a}^-_{2L} &= \mathbf{p}^-_{2R} + \boldsymbol{\tau}(L_R)\mathbf{a}^-_{2R} \quad & \mathbf{a}^+_{2L} &= \mathbf{R}^{22}_L \mathbf{p}^-_{2L} + \mathbf{R}^{22}_L \boldsymbol{\tau}(L_L)\mathbf{a}^-_{2L} \end{aligned} \tag{5.58}$$

After some algebraic manipulations of the above equations one gets the expressions for the positive- and negative-going waves at a location z_i within the piezoelectric actuator

$$\begin{aligned} \mathbf{a}^-_{2L} = &\left[\mathbf{I} - \boldsymbol{\tau}(L_R)\mathbf{R}^{11}_R \boldsymbol{\tau}(L)\mathbf{R}^{22}_L \boldsymbol{\tau}(L_L)\right]^{-1} \\ &\left\{\mathbf{p}^-_{2R} + \boldsymbol{\tau}(L_R)\left[\mathbf{R}^{11}_R \mathbf{p}^+_{2R} + \mathbf{R}^{11}_R \boldsymbol{\tau}(L_R)\left(\mathbf{p}^+_{2L} + \boldsymbol{\tau}(L_L)\mathbf{R}^{22}_L \mathbf{p}^-_L\right)\right]\right\} \\ \mathbf{a}^+_{2R} = &\mathbf{p}^+_{2L} + \boldsymbol{\tau}(L_L)\mathbf{R}^{22}_L \mathbf{p}^-_{2L} + \boldsymbol{\tau}(L_L)\mathbf{R}^{22}_L \boldsymbol{\tau}(L_L)\mathbf{a}^-_{2L} \end{aligned} \tag{5.59}$$

Therefore the total charge is

$$Q = \tilde{\mathbf{K}}^{\varphi\varphi} vL - \int_0^L \left[\tilde{\mathbf{K}}^{\varphi u}_0 \mathbf{q}(z) - \jmath k \tilde{\mathbf{K}}^{\varphi u}_1 \mathbf{q}(z)\right] \mathrm{d}z \tag{5.60}$$

where

$$\mathbf{q}(z_i) = \boldsymbol{\Phi}^+ \mathbf{a}^+_{2R} + \boldsymbol{\Phi}^- \mathbf{a}^-_{2L} \tag{5.61}$$

The integral in Eq. (5.60) can be evaluated numerically.

5.4 Numerical issues and implementation

The motivation for the wave-based methodology is twofold. Firstly, it enables conducting calculations in the wave domain with no need for cumbersome absorbing boundary development or applying hybrid techniques. Secondly, it is aimed at reducing the required computational time for high frequency dynamic analysis of structures equipped with piezoelectric active elements. It is important to state that the approach outlined in this chapter offers a potential for efficient simulations but this is subject to the implementation. With regard to this comment, we would like to raise the importance of the SAFE system solution.

SAFE equations take the form of QEP (quadratic eigenvalue problem) which is commonly solved by linearisation [125] and recasting to first order GEP (generalised eigenvalue problem). The solution can benefit from the computational savings offered by sparse matrix algebra if the matrices are appropriately formulated (see e.g discussions in [59, 75]). Nevertheless, special attention needs to be given to current research on QEP solution procedures especially those of a particular structure. The solution time can also be optimised by using shape functions more suitable for high frequency problems (Lobatto or Chebyshev polynomials) is proposed in the time-domain spectral element method [78].

Although the choice of the numerical techniques is outside of the scope of this thesis, it should be noted that the methodological potential of the modelling strategy presented largely depends on the wise implementation.

5.5 Experimental validation

The framework proposed in this chapter was validated with an experiment on a piezo-equipped beam with emulated anechoic terminations. A schematic diagram of the experimental set-up is shown in Fig. 5.8. The piezoelectric actuator (0.076 m $\times$ 0.0232 m $\times$ 0.0022 m made of Noliac NCE40 material - see Table 5.1) was driven by a signal from the generator module of a Polytec PSV300 controller amplified with a PCB 790 Series power amplifier.

Prior to bonding to the beam the impedance of the free-free actuator was measured. Corresponding numerical results were obtained from the wave model consisting of one

Table 5.1: Material constants used for experimental validation.

Property	Steel	Epoxy	NCE40
E, GPa	163	15	n/a
ν	0.3	0.4	n/a
ρ, $\mathrm{kg\,m^{-3}}$	8000	1000	7850
η	0.0001	0.0001	0.007
$c^E_{xx} = c^E_{zz}$, GPa	n/a	n/a	126.35
$c^E_{xy} = c^E_{yz}$, GPa	n/a	n/a	58.68
c^E_{yy}, GPa	n/a	n/a	99.88
c^E_{xz}, GPa	n/a	n/a	62.93
c^E_{xz}, GPa	n/a	n/a	31.71
$c^E_{yz} = c^E_{xy}$, GPa	n/a	n/a	36.77
$\varepsilon^\epsilon_{xx} = \varepsilon^\epsilon_{zz}$, $\mathrm{F\,m^{-1}}$	n/a	n/a	5.5e-09
$\varepsilon^\epsilon_{yy}$, $\mathrm{F\,m^{-1}}$	n/a	n/a	5.196e-09
$e_{yxx} = e_{yzz}$, $\mathrm{N\,V^{-1}\,m^{-1}}$	n/a	n/a	-3.239
$e_{zyz} = e_{xyx}$, $\mathrm{N\,V^{-1}\,m^{-1}}$	n/a	n/a	13.075
e_{yyy}, $\mathrm{N\,V^{-1}\,m^{-1}}$	n/a	n/a	16.335

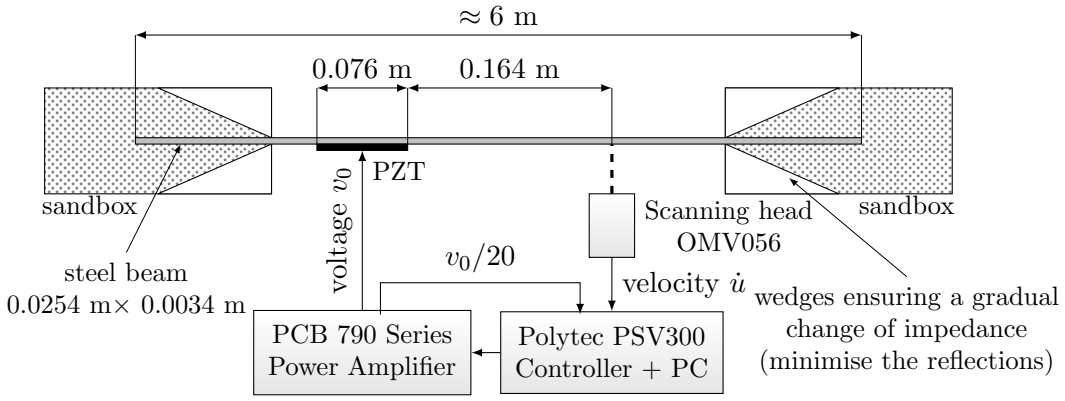

Figure 5.8: Experimental setup.

0.076 m long wave element with free-free boundaries. The impedance was extracted from the wave model according to the technique outlined in Section 5.3.2.

The manufacturer of the piezoelectric actuators states clearly that the properties listed in the datasheet [138] are for reference purposes only and the actual value depends on various conditions such as shape, finishing, electrode type etc. The quoted standard tolerances are ±10% for electrical properties and ±5% for mechanical properties. Moreover, the manufacturer does not provide a full set of material constants. The missing values were chosen by analogy to similar materials of other manufacturers and based on the relationships between various components of the matrices. Finally, the properties of NCE40 were further updated based on the free-free actuator impedance measurement to provide the closest match (within stated tolerances).

The updated SAFE-wave model prediction is compared with the measured data in

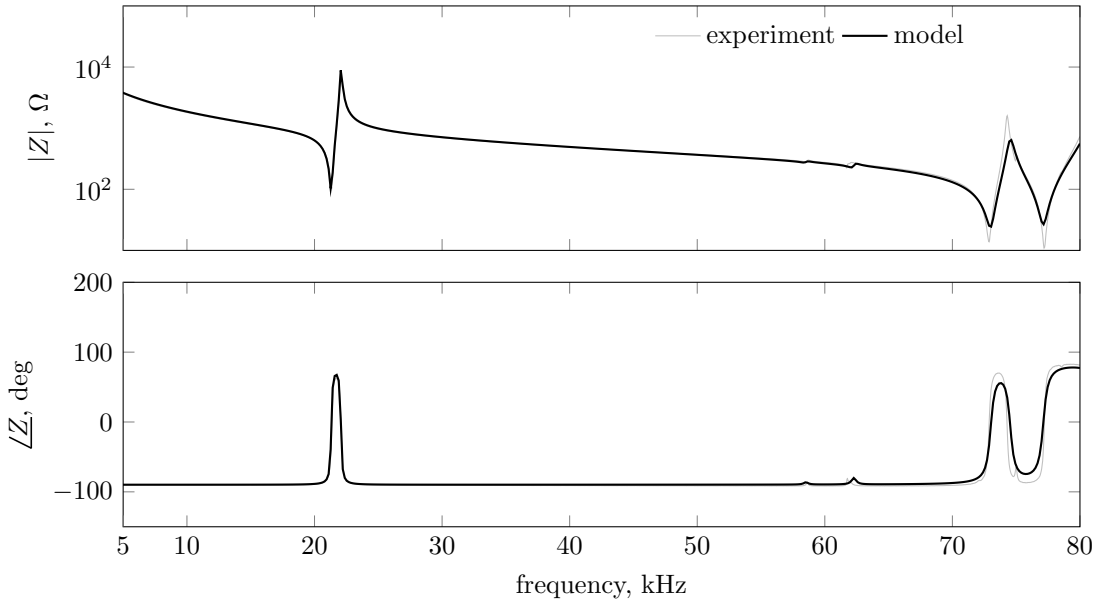

Figure 5.9: The electrical impedance of the free-free actuator prior to bonding.

Fig. 5.9. The electrical impedance contains imprints of all strain components, therefore can serve as a validity indicator for a 3D wave field. The response obtained from the wave model is slightly overdamped at high frequencies which is attributed to the effect of the constant loss factor used in the SAFE routine to represent damping as proposed by [66].

The actuator was attached to the beam using a thin (ca. 0.1 mm) layer of silvered epoxy (CircuitWorks CW2400 - properties of the epoxy were not measured and standard values were adopted instead). Since the beam was a standard rolled mild steel profile its cross-section was not ideally rectangular (see Fig 5.10) and the actuator needed to be cut to a slightly smaller dimension than the maximum width of the beam. The SAFE-wave model represents the cross-section with a rectangle, therefore in order to account for that the width in the model was amended and taken to be 0.024 m. All relevant material properties are listed in Table 5.1.

During the test the response to the electrical excitation was measured at 0.164 m from the actuator and at a few locations along the width of the beam using a Polytec PSV300 laser vibrometer. The grid of scanner points was chosen to be close to the positions of the nodes in the wave model. The ends of the beam were placed in boxes filled with sand in such a way that the thickness of the sand cover was gradually increased to ensure a smooth change in the mechanical impedance of the boundary and minimise any reflections.

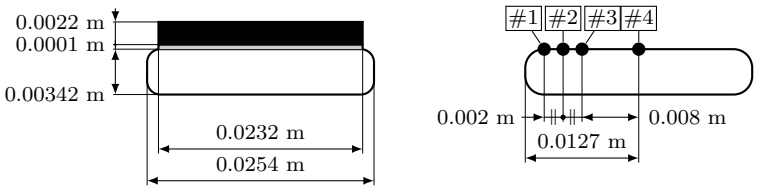

Figure 5.10: Cross-section of the beam with and without the PZT layer - dimensions and scan points locations.

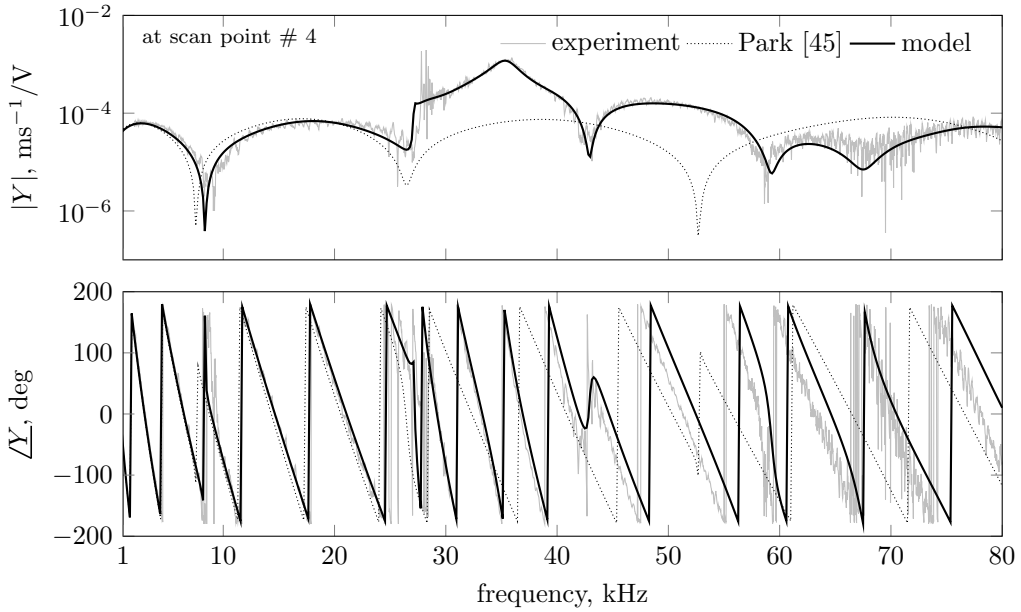

Figure 5.11: Magnitude and phase of the mobility with respect to the driving voltage measured at scan point #4 (see Fig. 5.10).

The relevant wave model consisted of 3 wave elements (as described in Section 5.3): two single-layer (steel) sections and one three-layer (piezo-bonding-steel) section. Appropriate continuity conditions at the junctions of the wave elements were specified. Each cross-section was modelled with six 8-node biquadratic quadrilateral elements across the width and one element across the thickness of each layer.

Recorded mobilities are compared with the wave model predictions in Figs. 5.11–5.14. If the terminations were perfectly anechoic, the measured response would only show the waves passing through the position of the laser dot. In reality, the absorption is not perfect which imposes the fluctuations on the response. Nevertheless, the mobilities presented in Figs. 5.11–5.14 show predominantly the effect of the propagating waves.

The response at the center of the width of the beam (point # 4) shown in Fig. 5.11 is discussed first. At low frequencies the mobility follows the behaviour expected from the approximate theories with simple bending being dominant. The first sudden jump in magnitude at around 27 kHz corresponds to the cut-off frequency of the first transverse bending mode in the steel beam. At around 35 kHz the mobility reaches its maximum

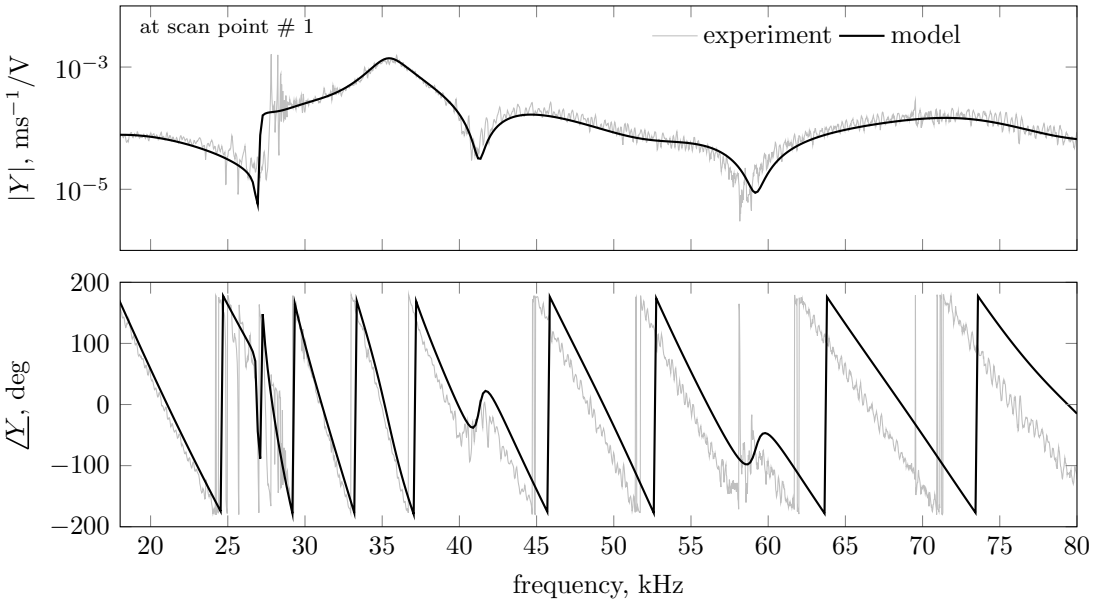

Figure 5.12: Magnitude and phase of the mobility with respect to the driving voltage measured at scan point #1 (see Fig. 5.10).

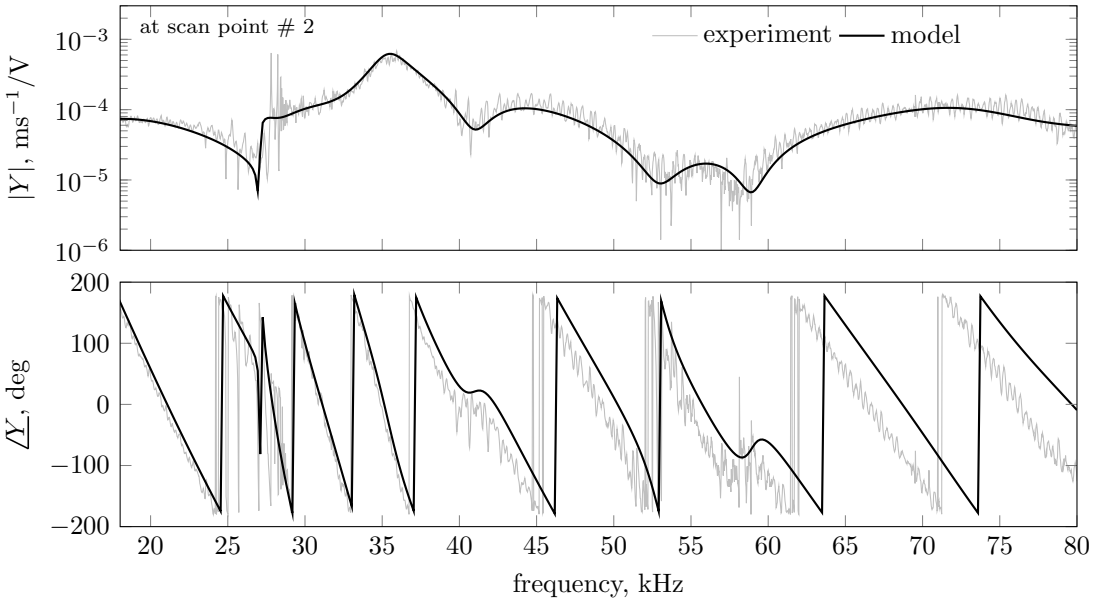

Figure 5.13: Magnitude and phase of the mobility with respect to the driving voltage measured at scan point #2 (see Fig. 5.10).

which is related to the cut-off frequency of the first transverse bending wave in the PZT-covered section. This corresponds to the through-width resonance of the steel-epoxy-PZT composite cross-section. The response experiences a dip whenever the length of the actuator matches with a multiple of the predominantly excited wavelength.

In order to show the potential of the proposed approach the experimental and numerical

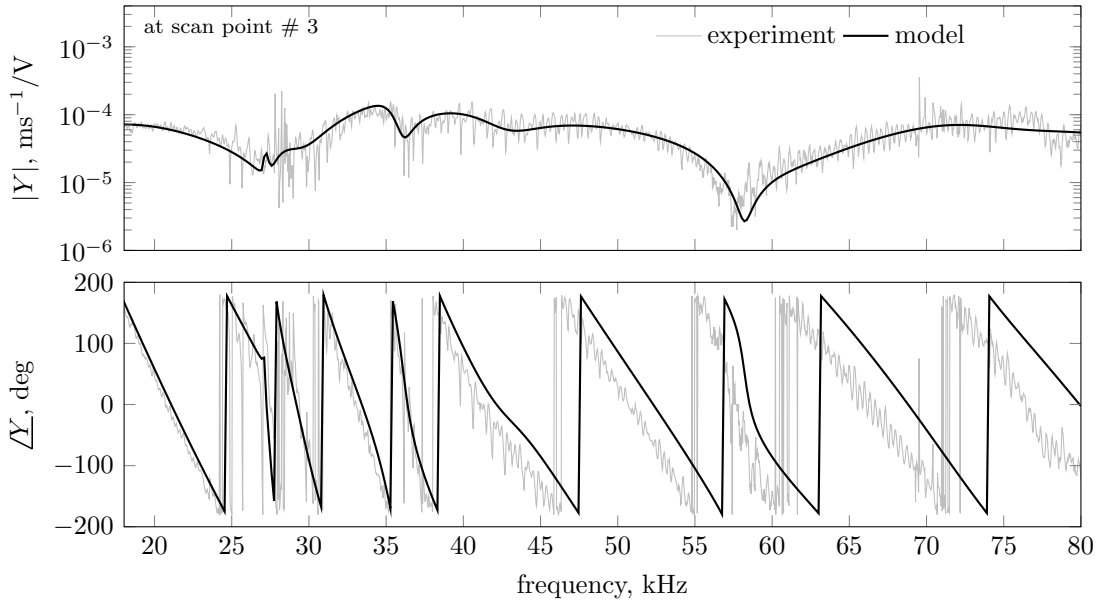

Figure 5.14: Magnitude and phase of the mobility with respect to the driving voltage measured at scan point #3 (see Fig. 5.10).

mobilities are supplemented with the results obtained from a model adopted from the literature. Park and co-workers [45] proposed a Timoshenko-Mindlin-Hermann formulation for coupled flexural-longitudinal-shear vibration of beam-like structures excited with PZT actuators. Predictions obtained with [45] agree well with the experiment up to ca. 5 kHz but deviate at higher frequencies. It is noted that the model from [45] is developed under the plane stress assumption which is typical for conventional beam theories, whereas the wave model proposed in this chapter captures the full 3D response of the structure. Accounting for that difference we note that the proposed model enables gaining more physical insight into wave motion than the conventional approaches for modelling piezoelectric excitation. The conventional approaches are not able to capture higher-order waves (e.g. the one cutting of at ca. 35 kHz) which in structural waveguides often govern the response at ultrasonic frequencies.

Figs. 5.12–5.14 show the response measured at different locations across the width of the beam (as indicated). The parts of the mobilities where simple bending is dominant (< 20 kHz) are not presented for these points, but it does not differ from Fig. 5.11 (when only fundamental waves are present the motion of the cross-section motion has the form of the rigid body modes).

The comparison shows a very good agreement between the wave model and the experiment verified for different locations. A slight drift in the phase at high frequencies can be partially attributed to the phase wrapping routines and difficulty in capturing the

phase change at cut-off frequencies correctly. The fact that the phase slopes of both lines are almost identical is a better indication of the correspondence of the two results.

It was observed that the wave absorption in the sandboxes has a nonlinear character and largely depends on the amplitude of the waves. Near the cut-off frequency of the transverse bending mode in the steel section the resonances (of the 6 m beam) are clearly visible in the response. This is attributed to the fact that near the cut-off frequency the amplitude of the wave is very large and therefore poorly absorbed by the sandboxes. Experiments performed with different excitation levels confirmed that the absorption in the emulated anechoic terminations drops with the increase of the amplitudes of the waves.

5.6 Wave analysis of the experimental case

In this section the experimental case is analysed from a wave perspective using the SAFE model.

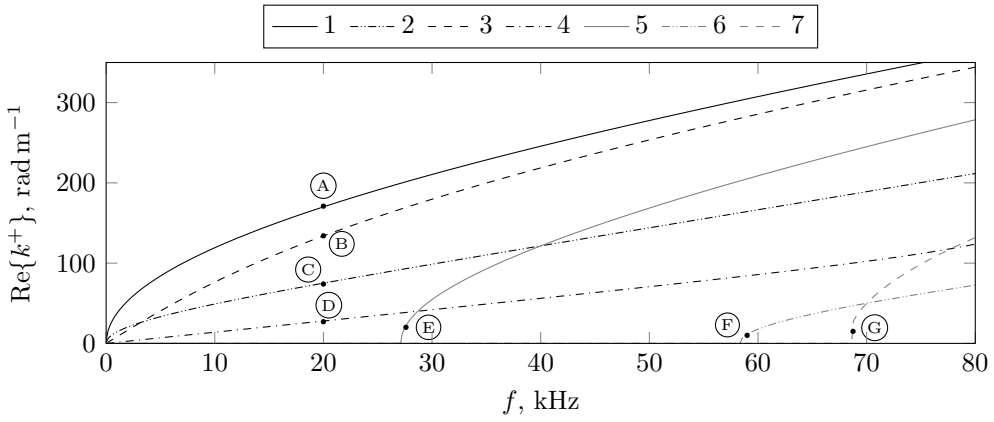

(a) steel beam

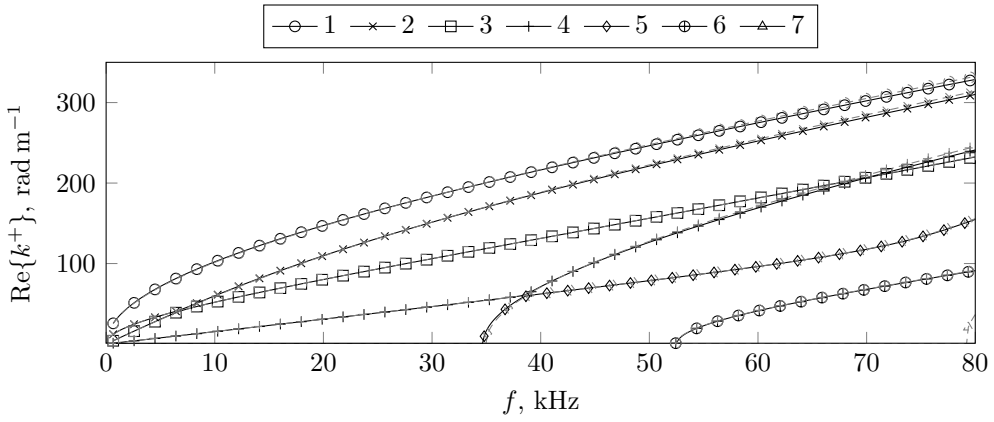

(b) PZT-steel beam (black solid) and PZT-epoxy-steel beam (grey dashed)

Figure 5.15: Dispersion curves for the sections used in the validation experiment.

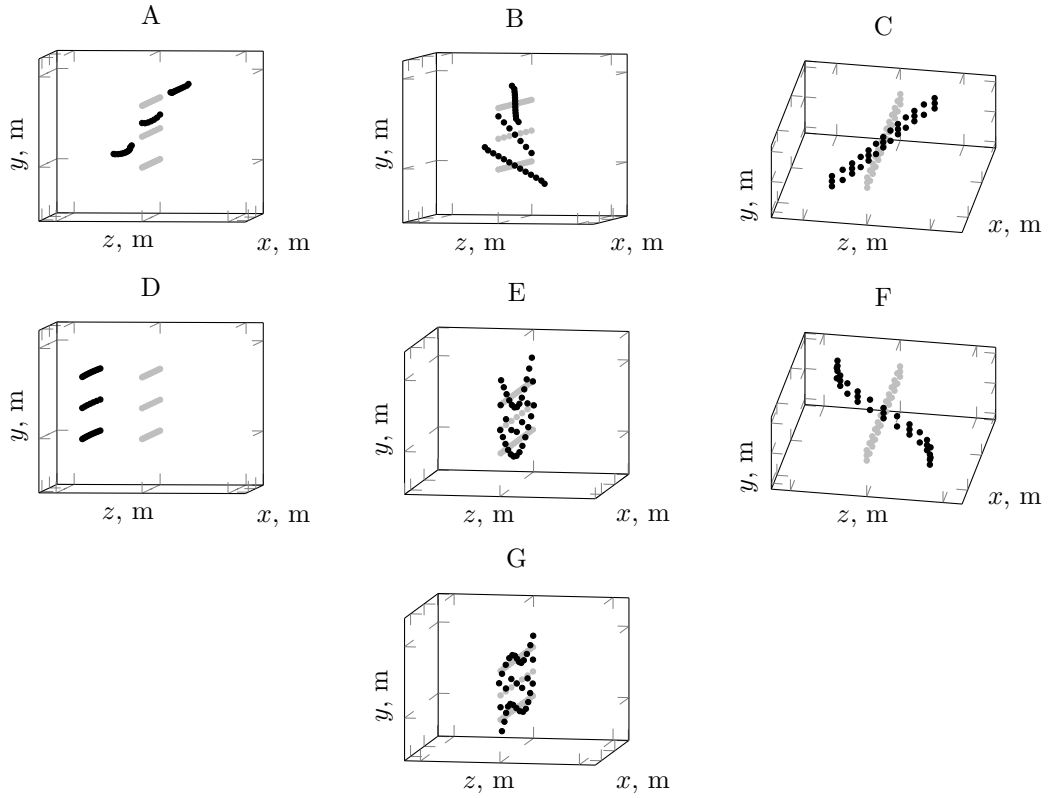

Figure 5.16: Wave displacement mode shapes for the steel beam used in the experiment associated with the points highlighted in Fig. 5.15. The geometry scale is not preserved in order to facilitate the visualisation.

The wave-based nature of the proposed model enables gaining insight into the wave characteristics of the structure and the wave composition of the FRF. The dispersion curves for the cross-sections used in the experiment are presented in Fig. 5.15. At each frequency the wavenumbers are arranged according to the WAC matrix (Wave Assurance Criterion [39, 139]; an alternative more accurate formulation can be found in [140]) ensuring the continuity of the wave mode shape along the dispersion curve. In the case of a steel beam the wave modes are very weakly coupled therefore unless a very small frequency increment is taken, the WAC criterion makes the dispersion curves cross each other which is not physical. However, for a multilayered cross-section the WAC criterion does not bring a clear separation of the curves based on the wave mode shape any more. Since the coupling between the wave modes is stronger in a multi-layered structure, the veering phenomenon of the dispersion curves can be observed.

Points A-G as marked in Fig. 5.15 are used to present the displacement wave mode shape associated with particular waves in a steel beam (Fig. 5.16). There are four fundamental waves in the steel beam under consideration: two bending waves - one around the x-axis (A) and the other around the y-axis (C), one compressional wave (D) and one torsional wave (B). Two higher-order across-width transverse bending modes cut off at 27.113

Table 5.2: Cut-off frequencies for higher-order wave modes in considered waveguides calculated from the wave model (in kHz).

waveguide	mode 5	mode 6	mode 7	mode 8
steel-epoxy-PZT	34.946	52.479	79.069	88.334
steel-PZT	34.700	52.536	79.945	88.589
steel	27.113	58.324	68.229	98.432

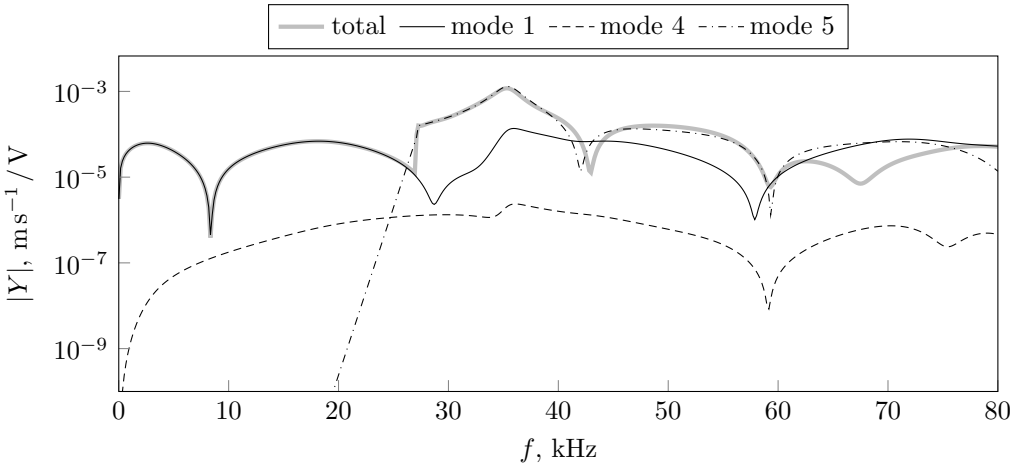

Figure 5.17: Wave decomposition of the magnitude of the mobility measured at scan point #4 (Fig. 5.10).

kHz (E) and 68.229 kHz (G). Finally, a higher-order bending wave (around the y-axis) starts propagating at 58.324 kHz (F).

When PZT layer is present (Fig. 5.15b) the transverse across-width bending waves cut-off frequencies are shifted up since the bending stiffness of the cross-section is increased (see Table 5.2). The presence of the bonding layer does not change the dispersion curves considerably.

The wave model enables decomposition of the mobility into contributions from particular waves. The piezoelectric actuator is able to activate only three of the seven waves in the frequency range of interest (Fig. 5.15). The velocities associated with each single propagating wave (as magnitudes) are shown in Fig. 5.17 with the legend and labelling convention adopted from Fig. 5.15. The FRF corresponds to the surface out-of-plane velocity at scan point #4. One can observe that at low frequencies the fundamental flexural wave (around x-axis) is prevalent in the response. When the across-width bending wave cuts off at 27.11 kHz it locally dominates the total FRF and from that frequency onwards it is mainly the two aforementioned waves that contribute to similar extents to the overall response. The influence of the compressional wave is very small as expected from the direction of the velocity measurement (out-of-plane).

5.7 Conclusions

The methodology for modelling piezoelectric excitation in structural waveguides was developed and validated in the previous chapter. The coupling of SAFE and the wave approach enables dropping the commonly used quasi-static and pin-force assumptions and include the actuator as a active electromechanical component in the wave model. Thanks to that the actuator is allowed to be thick (convergence of SAFE must be ensured though) and to operate at frequencies close to its resonance. The mathematical framework for calculation of the steady-state response to distributed voltage excitation is outlined.

The electromechanical wave model is validated with an experiment. The piezo-actuated structural waves in a beam-like waveguide with emulated anechoic terminations are captured using a laser vibrometer at different locations and compared with the numerical calculation. The comparison shows a very good agreement.

Chapter 6

Power and energy propagation in structures excited with piezoelectric actuators

The efficiency of structural wave excitation with piezoelectric actuators can be insightfully analysed by looking at the relationship between the mechanical wave power and the electrical power supplied to the actuator. Driving voltage as an input parameter of an electromechanical model of a structure equipped with piezoelectric active elements is indicative but assumes that the electrical driving source has an infinite power delivery capability. In the real world this is seldom the case and the power transduction efficiency is limited by the specification of the electrical driving source. Power transfer is particularly important for removal of unwanted accretions using structural waves when one needs to ensure that sufficient mechanical power is injected to the waveguide. Therefore, the electrical power seems to be a more practically insightful input variable for the electromechanical model than the driving voltage.

In this chapter the issues related to power conversion are addressed using the SAFE and wave approach methodology developed in the previous chapter. It is assumed that the actuator operates in the linear region, which may be questionable for high power excitation. The basic relationships and observations are discussed with reference to the validation case of an infinite beam with a finite PZT actuator. The practicalities of driving a complex load and associated perspective on the electrical power requirements of the actuator are outlined and used to refine the understanding of the power transfer between the piezoelectric and the mechanical waveguide. Finally, a parametric study is performed to show the influence of the actuator's dimensions and bonding layer's thickness on the efficiency of wave excitation from a power perspective.

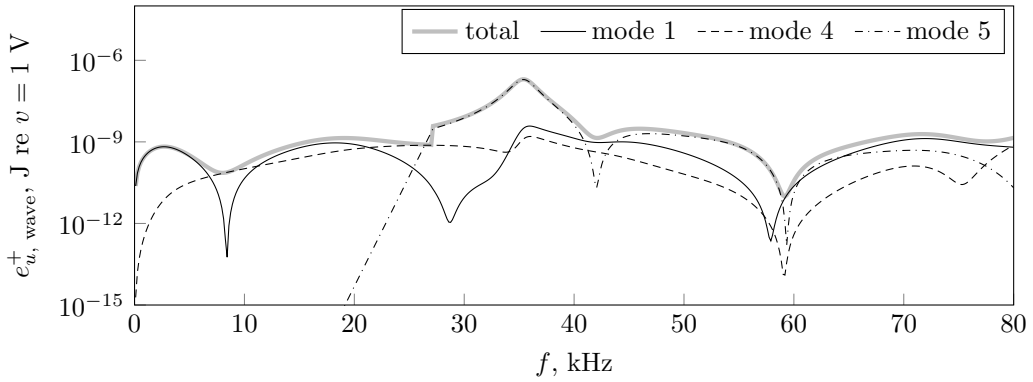

Figure 6.1: Strain energy per propagating wave induced by a piezoelectric actuator in a steel beam with emulated anechoic terminations (structural configuration as in Section 5.5).

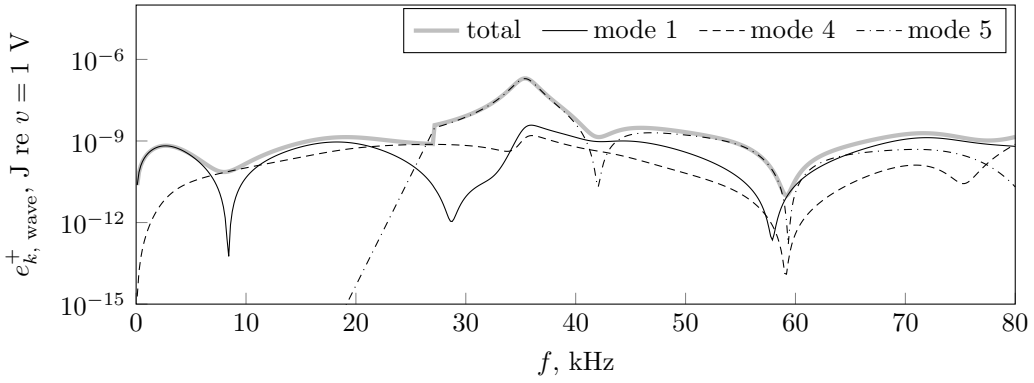

Figure 6.2: Kinetic energy per propagating wave induced by a piezoelectric actuator in a steel beam with emulated anechoic terminations (structural configuration as in Section 5.5).

6.1 Energy and power propagation in a structural waveguide

The wave composition of the FRF presented in Fig. 5.17 shows how particular waves contribute to the velocity measured at a particular point, however it does not bring insight into the efficiency with which they are excited or, in other words, how the supplied energy is partitioned between the waves. In this section power and energy are analysed for the beam-like structure used in the validation case in Chapter 5.

In Fig. 6.1 and Fig. 6.2 the wave contributions to the strain and kinetic energies (time-averaged) at the edge of the actuator are plotted, respectively. The wave energy is fully exchanged between its strain and kinetic forms over one cycle hence, as one would expect, the curves in Fig. 6.1 and Fig. 6.2 are identical. It is noted that these are not frequency response functions as the relationship between the energy or power and voltage is not linear. Therefore, the graphs are annotated with a reference driving voltage.

Strain energy e_u is related to the deformation associated with a wave and is defined as a sum of stress-strain products for corresponding components, whereas the kinetic energy e_k reflects the motion of the mass. The SAFE formulation provides simple expressions for strain and kinetic energies associated with a wave mode which can be found in Eq. (4.33) and Eq. (4.34).

Let us now look how the energy is distributed among the modes. At the low frequencies the flexural wave (mode 1) carries the most of the energy. The compressional wave (mode 4) contribution at low frequencies is very small, however it reaches a level similar to the flexural wave over the frequency range considered. The pattern of peaks and dips for these waves is associated with a certain relationship between the wavelength and the length of the actuator. Whenever the length of the actuator is close to the multiple of the excited wavelength, the response outside the PZT-covered region is minimised. Conversely, the response is maximum when the length of the actuator is close to an odd multiple of the excited half-wavelength.

The dips associated with the compressional wave are spaced more widely in frequency as its wavelength is considerably longer than the one of the flexural wave in the frequency range considered. A small jump in the total energy is observed when the first-order mode (mode 5) cuts-on in the steel beam at 27.12 kHz. The maximum of the energy curve occurs around 35 kHz, i.e close to the cut-off frequency of the first-order across-width bending wave in the PZT-covered section (see Fig. 5.15). Wave power considered in this thesis originates from the Poynting vector that describes the rate of energy transfer per unit area (energy flux). The expression resulting from the SAFE formulation gives the value for the Poynting vector component along z integrated over the cross-section of the waveguide, i. e. the total energy flux.

The power carried by each of the waves and their superposition as seen at the edge of the actuator are presented in Fig. 6.3. The shape of the curves is very similar to the ones in Fig. 6.1 and Fig. 6.2 and the difference originates from the definitions of the quantities. The strain energy takes into account all stress and deformation components and refers to the whole cross section. The wave power is a component of a Poynting vector which represents power flow in the direction of propagation (z), so only the components interfering with the z direction are included.

At low frequencies the fundamental flexural wave (mode 1) absorbs most of the injected power. The power consumed by the fundamental compressional wave (mode 4) grows with frequency and follows its dips and peaks pattern as discussed above. Fig. 6.3 shows that a single PZT actuator excites both flexural and compressional waves to a similar extent, although this is not always obvious due to the difference in the patterns of peaks and valleys. For example, at particular frequencies (for instance 8.5 kHz) the total

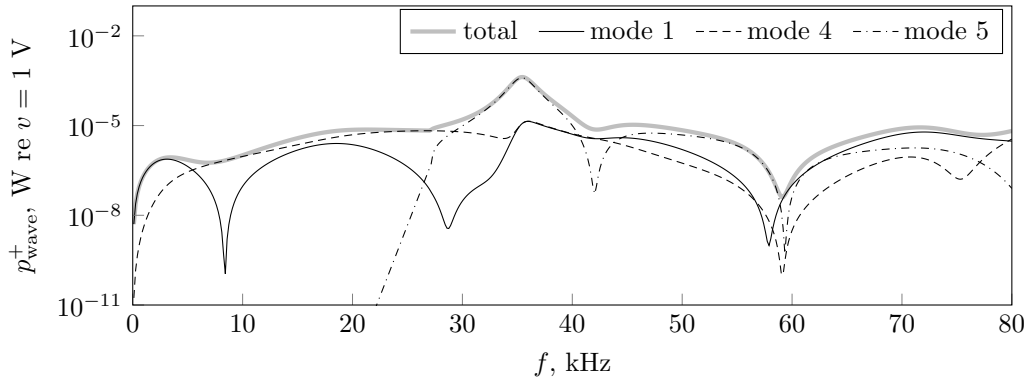

Figure 6.3: Wave power induced by a piezoelectric actuator and carried by waves propagating in a steel beam with simulated anechoic terminations (structural configuration as in Section 5.5).

power is almost entirely related to propagation of the compressional wave. The wave power reaches its peak around 35 kHz and is dominated by the higher-order across-width bending wave (mode 5).

The transduction efficiency in a waveguide with electromechanical coupling can be perceptively analysed in the light of the electrical power supplied to the actuator. In fact, the electrical power is the most practical measure for the requirements of a piezo-driven smart structure.

6.2 Electrical power supplied to a piezoelectric actuator exciting a structural waveguide

In the following paragraphs the electrical viewpoint perspective on the operation of the piezoelectric actuator is explored. Firstly, the electrical characteristics of the actuator are analysed in order to be relate them to the driving electrical system afterwards. Then, the impedance mismatch and power reflection are briefly discussed bringing general guidelines to understanding the power requirements of a piezoelectric actuator.

6.2.1 Characteristics of a complex load

The most typical quantity characterising an electric load is its impedance Z understood as a ratio between the applied voltage and current drawn. If the load is purely resistive, the current is in phase with the voltage and the impedance is real and frequency-independent. The capacitive or inductive components alter the phase relationship between the voltage and the current. The impedance becomes complex and frequency dependent.

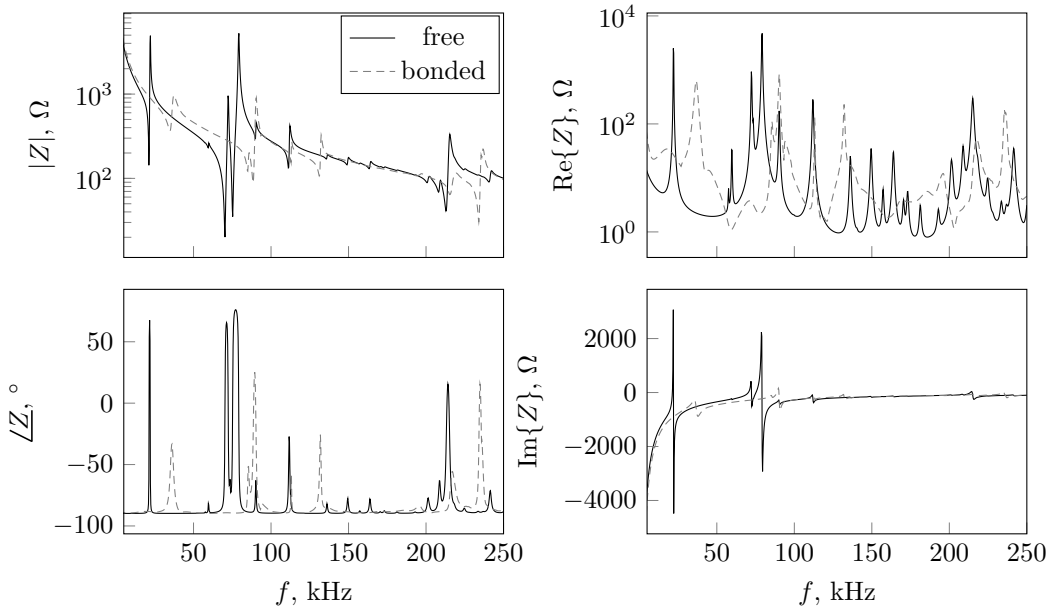

Figure 6.4: Electrical impedance of the actuator used in the validation experiment (see Section 5.5) computed using presented wave model. Comparison between the results for the free actuator and the actuator bonded to the beam

In the DC regime or at low frequencies the piezoelectric actuator acts as a capacitor, i.e. a dielectric between two conducting plates (silvered electrodes) in series with a resistance representing dielectric loss and current leakage (see Fig. 1.1). Low frequencies here means frequencies far below the mechanical resonances of the actuator. The piezoelectric effect in the material results in coupling the electric driving field with the strain field associated with the induced vibration [93]. With increasing frequency a vibrating structure encounters subsequent mechanical resonances of which some are evident for a piezoelectric actuator. As the voltage is applied to the electrode (which in this thesis is assumed to cover the whole face of the actuator), it is able to excite only those vibration modes which are associated with a symmetric strain distribution [93]. As a consequence of the piezoelectric effect, a large strain field at a resonance makes the actuator draw large current from the source. When these conditions are met an electromechanical resonance occurs which is visible on the impedance plot as a dip. While passing through subsequent resonances the phase relationship between the voltage and the current changes resulting in complex and frequency dependent impedance.

In Fig. 6.4 the electrical impedance of a free actuator as used in the validation experiment is presented and compared to its impedance when bonded to the waveguide. At low frequencies, before the electromechanical resonances of the actuator occur, it acts as a capacitor with almost purely imaginary (negative) impedance $Z_C = (\jmath\omega C_0)^{-1}$. The behaviour of the actuator is more complex around its resonance - the magnified impedance curves for the free actuator are shown in Fig. 6.5. At the resonance the load

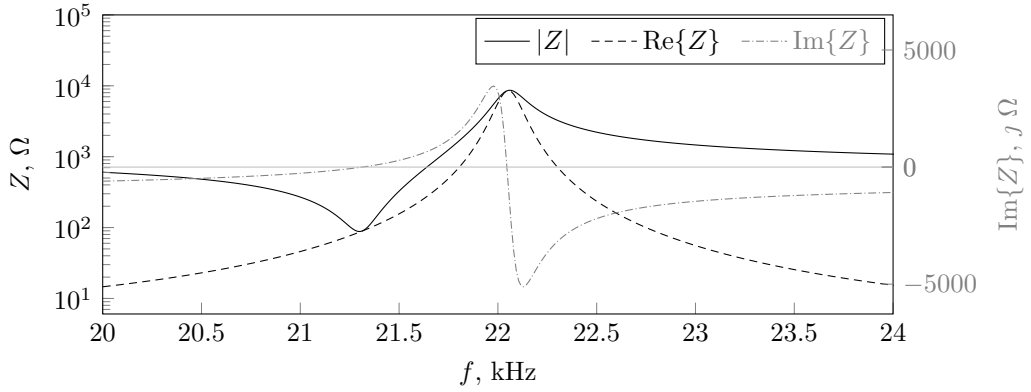

Figure 6.5: Electrical impedance of a free actuator as used in the validation experiment (see Section 5.5) computed using presented wave model zoomed around the first resonance; note the double y-axis.

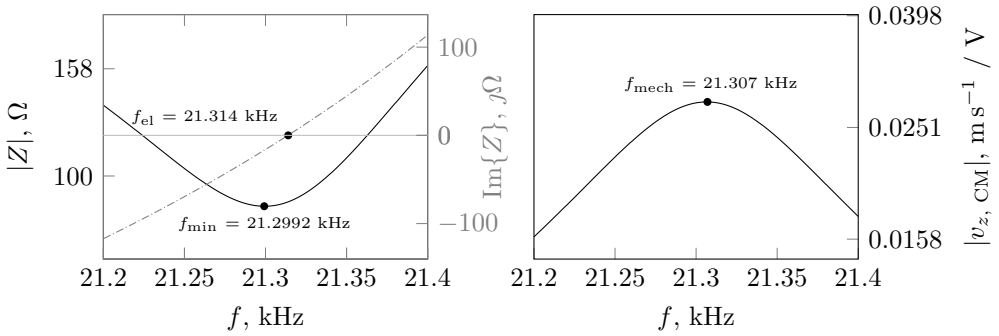

Figure 6.6: Frequencies at which the events associated with actuator's resonance occur - on the left: the modulus of the impedance and velocity of the center of mass of the cross-section; on the right: imaginary part of the impedance.

becomes purely resistive, and $|Z|$ experiences a dip which is usually associated with the maximum of the mechanical deformation. At resonance the actuator draws very large current from the source. The imaginary part of the impedance crosses the zero axis again at a slightly higher frequency (22.06 kHz) which is an anti-resonance.

In fact, the effects that are usually attributed to the resonance of the actuator happen at three different frequencies [81] as depicted in Fig. 6.6. The lowest in frequency is the minimum of the magnitude of the impedance $|Z|$ (f_{min}). The mechanical resonance frequency (f_{mech}), i.e. the frequency at which the velocity at the edge of the actuator is maximised is slightly higher. Finally the highest is the electrical resonance frequency (f_{el}) which corresponds to Im$\{Z\}$ crossing zero. At this point the current and voltage are in phase so that the current drawn is at maximum. As these are very close to each other they are often represented by a single frequency.

When attached to a structure the actuator's response changes and encapsulates the imprints of the dynamics of the host. In Fig. 6.7 the impedance is presented for the

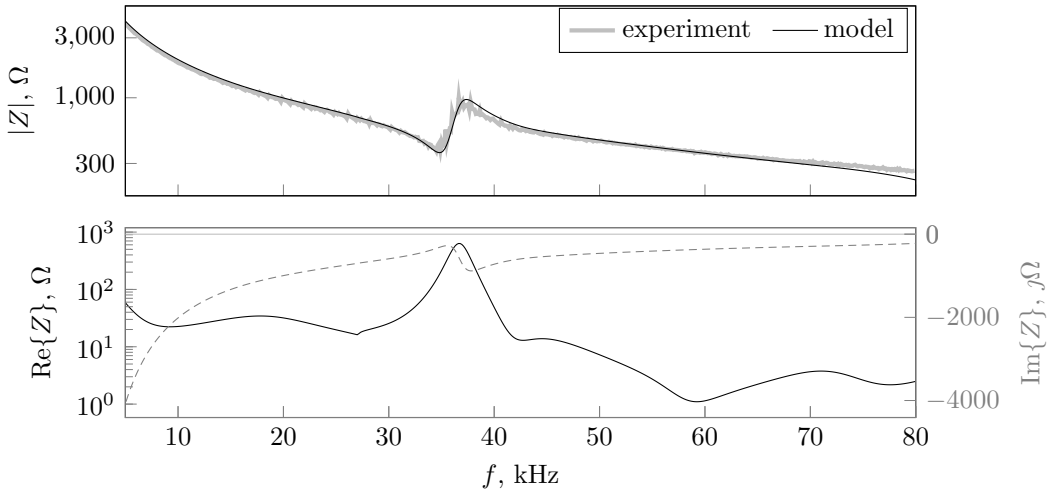

Figure 6.7: Electrical impedance of the piezoelectric actuator bonded to the beam with simulated anechoic terminations as in the validation experiment (see Section 5.5).

Table 6.1: Resonance-related frequencies for the actuator bonded to the beam as in the experimental validation case (see: Fig. 6.7).

	$\min(\lvert Z\rvert)$	$\max(\mathrm{Im}\{Z\})$	$\max(\lvert v_{(79)}\rvert)$
f, kHz	34.85	35.49	35.28

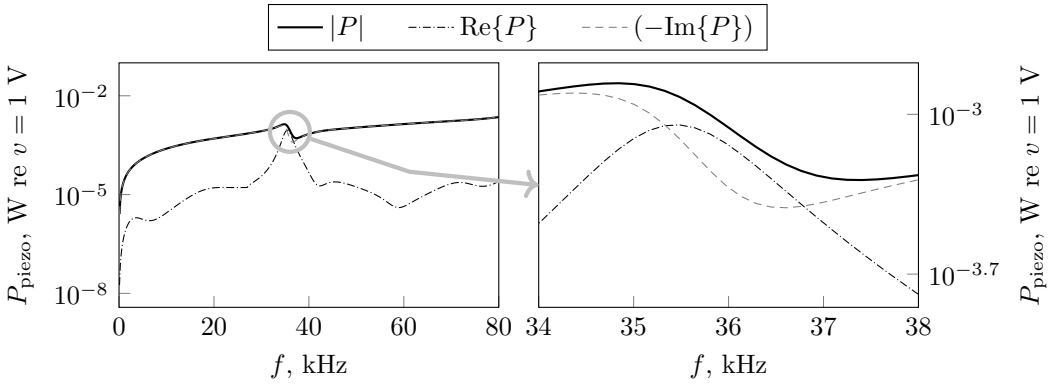

Figure 6.8: Active, reactive and apparent power in a piezoelectric actuator bonded to the beam with simulated anechoic terminations as in the validation experiment (see Section 5.5).

actuator bonded to the beam with emulated anechoic boundaries as used in the validation experiment. The resonance dip in Fig. 6.7 is related to the cut-off of the first-order across-width bending wave in the PZT-covered section of the waveguide (see Section 5.6). Note that no other resonances (e. g. no resonance related to the length or the thickness of the actuator) are observed in the frequency range considered. The three frequencies described in the previous paragraph for the experimental case are listed in Tab. 6.1.

The power quantities related to a load of complex impedance are discussed below. As the

load is complex, the electrical power required by the load is also complex. Both voltage and current are first written using the complex exponential notation as $V\exp[\jmath\omega t]$ and $I\exp[\jmath\omega t]$, respectively, with V and I being complex amplitudes defined as

$$\begin{aligned} V &= |V|e^{\jmath\phi_v} \\ I &= |I|e^{\jmath\phi_i} \end{aligned} \tag{6.1}$$

The physical voltage and current in time domain can then be written as

$$\begin{aligned} v(t) &= |V|\cos(\omega t+\phi_v) = \frac{Ve^{\jmath\omega t}+V^*e^{-\jmath\omega t}}{2} = \mathrm{Re}\{Ve^{\jmath\omega t}\} \\ i(t) &= |I|\cos(\omega t+\phi_i) = \frac{Ie^{\jmath\omega t}+I^*e^{-\jmath\omega t}}{2} = \mathrm{Re}\{Ie^{\jmath\omega t}\} \end{aligned} \tag{6.2}$$

Instantaneous power is calculated as

$$p(t) = v(t)i(t) \tag{6.3}$$

Adopting the complex-exponential notation and setting the phase angle of one of the quantities to zero (in this case voltage - ϕ_v) one can expand Eq. (6.3) to [109]

$$p(t) = \mathrm{Re}\left\{\frac{VI^*}{2}\right\}(1+\cos 2\omega t) + \mathrm{Im}\left\{\frac{VI^*}{2}\right\}\sin 2\omega t \tag{6.4}$$

From Eq. (6.4) it is clear that the instantaneous power contains a pulsating power flow with the time-average

$$P_R = \mathrm{Re}\left\{\frac{VI^*}{2}\right\} \tag{6.5}$$

and a periodic power flow with peak value

$$P_I = \mathrm{Im}\left\{\frac{VI^*}{2}\right\} \tag{6.6}$$

Therefore, instantaneous power waveform is completely specified by the average resistive power and the peak reactive power [109]. Hence, complex power is defined using the above as

$$P = P_R + \jmath P_I \tag{6.7}$$

As explained in [109] P_R supplies resistive losses and is consumed by the actuator during operation, whereas P_I is absorbed and released by the energy storing elements (mass, stiffness, inductance, capacitance) interchangeably over a cycle. The magnitude of the complex power is often referred to as the apparent power P_{app} or power rating, which

can be alternatively written as

$$P_{\text{app}} = |P| = |V||I| \tag{6.8}$$

In Fig. 6.8 the discussed power quantities are plotted for the bonded actuator. The reactive power dominates except near the resonance, when the actuators consumes significant active power. The implications of these facts on the practicalities of high power excitation and the efficiency of power transduction between the actuator and the waveguide are discussed in the next section.

6.2.2 Complex load driving and power transfer

Efficient driving of a complex load requires a thoughtful choice of the amplifier. Piezoelectric actuators are usually powered by RF (radio frequency) amplifiers as they work over a broad frequency range, provide high enough power and are able to handle capacitive loads and impedance mismatch. In this work a 1020L amplifier from Electronics & Innovation was used. It can provide up to 200 W with low harmonic distortion at frequencies from 10 kHz to 5 MHz. The amplifier gain as stated by the manufacturer is 53 dB. The input and output terminals impedance is 50 Ω and the allowed input voltage range is 0 to 1 V RMS.

The input waveform is fed into amplifier using a TTI TGA1240 Series Arbitrary Waveform Generator. It has a useful feature of specifying the 50 Ω load that ensures that the voltage as seen on the display is the actual voltage sent to the amplifier. Since a PZT actuator is a complex electrical load the power transfer issues have to be accounted for. The efficiency of the electrical power transfer between an ultrasonic source and a receiver (here: the PZT actuator) depends on the impedances of the elements. Since the at frequencies of interest the electromagnetic wavelength is very large, the system can be well represented by a simple lumped parameter circuit (Fig. 6.9), where v_S is the voltage of the Thévenin's equivalent voltage source, Z_S is the impedance of the source and Z_L is the impedance of the load. Voltage across the load can be calculated as

$$v_L = v_S \frac{Z_L}{Z_L + Z_S} \tag{6.9}$$

and current flowing through the circuit as

$$I = v_S \frac{1}{Z_L + Z_S} \tag{6.10}$$

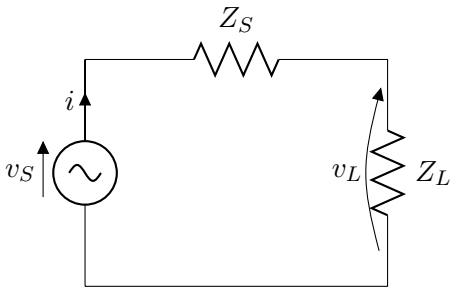

Figure 6.9: Lumped parameter circuit representing the power source–actuator system.

Power absorbed by the load (active) is obtained from

$$P_R = \frac{1}{2}\mathrm{Re}\{v_L I^*\} = \frac{1}{2}\mathrm{Re}\left\{\left(v_S\frac{Z_L}{Z_L+Z_S}\right)\left(v_S\frac{1}{Z_L+Z_S}\right)^*\right\} = \frac{1}{2}|v_S|^2\frac{\mathrm{Re}\{Z_L\}}{|Z_L+Z_S|^2} \tag{6.11}$$

Eq. (6.11) indicates that power transfer is maximum is the impedance of the load is a conjugate of the impedance of the source. If this is the case, power absorbed by the load becomes

$$P_R^{\max} = \frac{|v_S|^2}{8\mathrm{Re}\{Z_S\}} \tag{6.12}$$

In order to make the power from Eq. (6.11) available for the load, the amplifier needs to be capable of delivering $\frac{1}{2}v_S I^* = \frac{1}{2}\frac{|v_S|^2}{Z_L+Z_S}$. As for complex loads, the power rating of the amplifier seems to be a practical measure. Thus, a required power capability of the amplifier is defined here as required power rating of the amplifier with output impedance Z_S that ensures delivery of certain active power P_R to the load of impedance Z_L

$$P_{\mathrm{capab}} = \left|\frac{Z_L+Z_S}{\mathrm{Re}\{Z_L\}}\right| P_R \tag{6.13}$$

Likewise, the power rating of the actuator itself can be defined as

$$P_{\mathrm{app}} = |P_R + \jmath P_I| \tag{6.14}$$

Piezoelectric actuators are often driven using RF amplifiers which have a standardised output impedance of 50 Ω. Since these devices are usually designed to work with microwave units and very long connections, they adopt a transmission line theory viewpoint to power transfer (see e.g. [141]). Voltage is represented as a superposition of waves that travel through the cables. Like in mechanical waveguides, any discontinuity in the waveguide is related to localised impedance change. Voltage wave and associated power is partly reflected and partly transmitted through the discontinuity.

The forward and reflected powers are often measured by RF amplifiers (e.g. 1020L

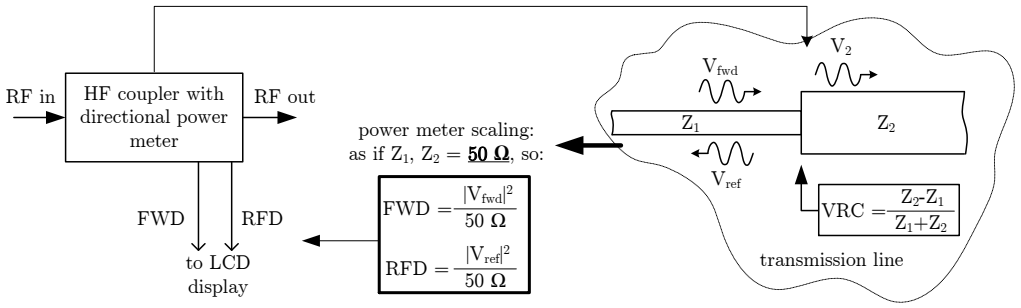

Figure 6.10: Forward and reflected power measurement in a typical RF amplifier (such as E&I 1020L) and the meaning of figures measured by directional power meters.

amplifier from Electronics and Innovation Ltd.). However, it is important to understand clearly the indications given by the equipment. In fact, the directional power meters as used in HF couplers measure the amplitude of two voltage waves: the wave incident upon the discontinuity v_{FWD} and the wave reflected back to the source v_{RFD}. Based on measured figures they calculate forward and reflected powers assuming that those voltage waves are incident upon a standardised impedance, usually 50 Ω (see Fig. 6.10)

$$P_{\mathrm{FWD}} = \frac{|V_{\mathrm{FWD}}|^2}{50\Omega} \tag{6.15}$$

$$P_{\mathrm{RFD}} = \frac{|V_{\mathrm{RFD}}|^2}{50\Omega} \tag{6.16}$$

Therefore, readings from such devices should not be taken literally as indication of power in the system. They have to be properly scaled according to the actual impedances in place. It should also be noticed that the forward power denotes the power incident on the discontinuity and not the power absorbed by the load. However, it is straightforward to show that the difference between P_{FWD} and P_{RFD} gives the active power consumed by the load, no matter what the load impedance is [142].

The power quantities discussed above are shown for the experimental validation case in Fig. 6.11. The actuator is driven with 1 V and during operation consumes real power represented by the black solid line. However, in order for this to happen the 50 Ω source must be capable of producing power indicated by the grey dashed line. Finally the apparent power (P_{app}) that tells about the load rating, i.e. the powers that will be both consumed and exchanged with the network is shown by the black dash-dotted line.

The major challenge in driving piezoelectric actuators is the ability of handling large reactive, capacitive loads, which can only be achieved by specialised high power amplifiers.

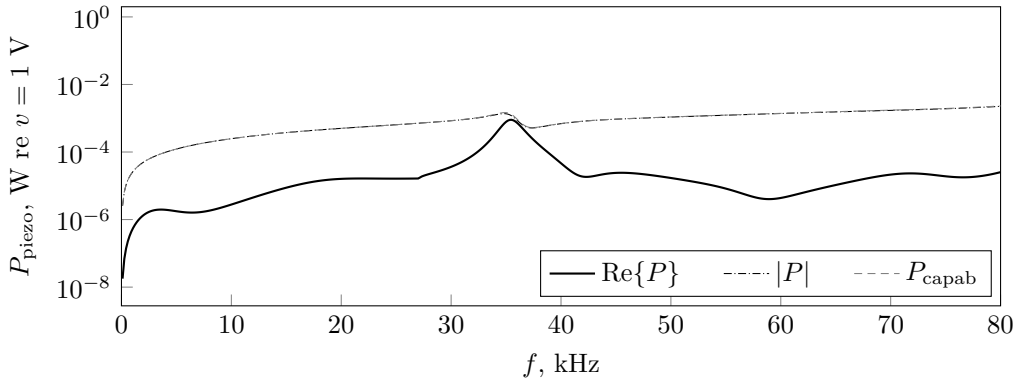

Figure 6.11: Comparison between the discussed power quantities for a piezoelectric actuator bonded to the beam with anechoic terminations as in the validation experiment (see Section 5.5).

6.3 Power transduction

6.3.1 Electrical to mechanical wave power conversion

When a piezoelectric actuator is attached to a structure and supplied with some power it induces mechanical waves in a structure. From a power transfer viewpoint the mechanical waveguide is absorbing mechanical power that the electrical driving power was converted to via electromechanical piezoelectric coupling (radiation damping). Therefore the power associated with propagating waves is a part of the active electrical power consumed by the actuator (P_R). Other effects associated with drawing power from P_R are various loss phenomena such as mechanical material damping resulting in elevated temperature or dielectric loss. In general, the active electrical power is converted into mechanical power of which one part is propagating and and the other dissipated within the actuator.

The optimal electrical-to-mechanical power transduction occurs when P is purely resistive, i.e. the reactive part P_I is small or close to zero. Therefore, if the output impedance of the source can be arbitrarily chosen one would aim to minimise the reactive power. If this is the case the driving voltage is in phase with the current drawn, hence the instantaneous power reaches its maximum [81].

Whether the consumed active power is converted into propagating wave power is closely related to the dimensions of the actuator. If the length of the actuator contains a multiple of excited wavelengths, the response is greatly diminished as the waves cancel each other within the actuator-covered region. In this case, the active power is predominantly dissipated within the actuator. Furthermore, if the actuator is driven at frequencies at

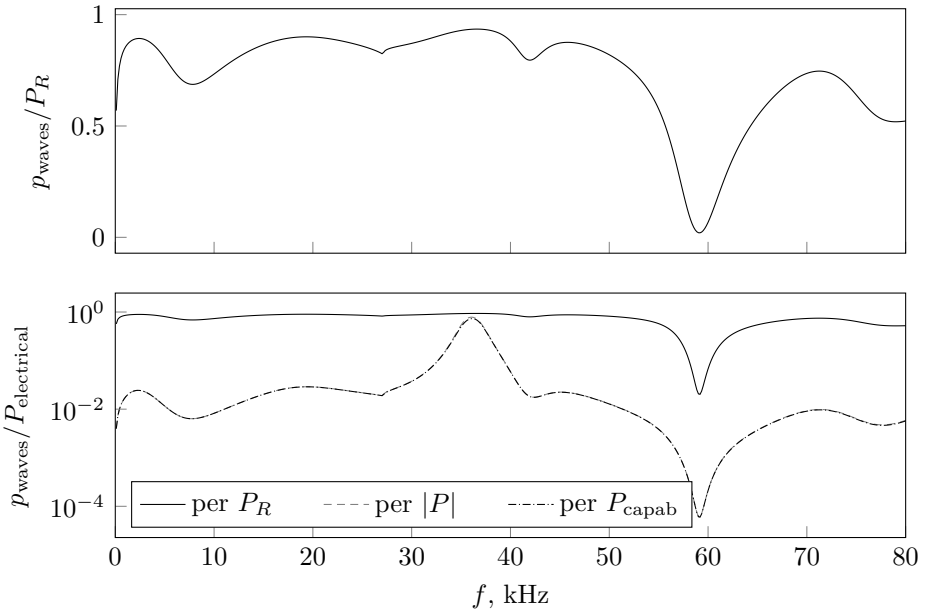

Figure 6.12: Electrical power conversion to propagating wave power (both positive and negative) for the experimental validation case (see Section 5.5) - comparison with reference to the considered power quantities.

Table 6.2: Electrical to wave power conversion maxima with respect to different power quantities (see: Fig. 6.12).

	P_R	$\lvert P\rvert$	P_{capab}
$f_{\max}$, kHz	36.61	36.13	36.13
$P_{\text{wave}}/P_{\text{electrical}}$	0.935	0.782	0.733

the zero group velocity waves exist in waveguide, the power injected to the waveguide does not propagate giving rise to localised resonance around the actuating region.

Let us first look at the example of the structure used in the validation experiment (Section 5.5). The ratio between the total mechanical wave power (superposition of all modes) and the electrical power is presented in Fig. 6.12. The curve corresponding to the ratio between the wave power and consumed (real) electrical power is magnified in the top sub-figure for convenience. Firstly, it is clear that not all active electrical power is converted to propagating waves. This is attributed to the mechanical damping (see Tab. 5.1) and to the specific relationship between the wavelength of the propagating waves and the size of the actuator as explained above. The dip around 60 kHz corresponds to the region where all propagating waves match this criterion, hence the drop in the wave power and consequently in power transduction is very evident.

The top sub-figure in Fig. 6.12 shows that most of the electrical power consumed by a PZT-equipped structure is converted into mechanical wave power in the frequency range under consideration. The optimal power transfer occurs at 36.61 kHz where almost 94%

of the electrical active power is converted into wave power. This frequency is associated with the higher-order wave cutting-off in the PZT-covered section and consequently, a dip in the electrical impedance curve.

If one takes into account the complex character of the PZT actuator as an electric load, the apparent power (sometimes called the power rating) becomes a figure more appropriately defining the actual power requirement. The analysis can be further refined by considering the impedance matching between the components of the electrical driving system. Including these effects strongly changes the perspective and it is expected that the insight it provides is closer to practical scenarios.

The two curves representing the ratio between mechanical wave power and both the apparent power and the required source power capability (assuming 50 Ω output source impedance) are compared with the former in the bottom sub-figure of Fig. 6.12. The power transduction efficiency with respect to these quantities is substantially lower and gets close to the real power curve only near the resonance frequency. The maximum power transduction coefficients for each curve are presented in Tab. 6.2. Note that only up to 73% of the available electrical power can be accommodated in mechanical wave power for the chosen source output impedance. Away from the resonance the power transduction efficiency is very low ($< 10^{-2}$), and so these frequencies are not generally used since in power ultrasonics the actuators usually work at their resonances. Nevertheless, it is significant that in this illustrative case the ultrasonic source needs to be capable of delivering electrical power that is almost 140% of the desired injected mechanical wave power. It is also clear, that the required power capability of the source is very close to the power rating (apparent power) of the actuator.

In order to facilitate understanding of the results presented hereafter, a few general comments on the typical characteristics of structural waveguides with PZT in plane strain are made below. The efficiency of power transduction is closely related to the impedance of the actuator. The impedance of a typical PZT actuator polarised in the through-thickness direction can be viewed as the reactive impedance due to capacitance (electrical) with imprints of subsequent resonances related to standing structural waves (mechanical). The resonance is related to standing wave across a particular finite dimension of the waveguide. Accounting for the fact that standing waves along the length are largely affected by radiation damping, the imprints of the structural resonances on the electrical impedance curve are related to the cross-section resonances, i.e. cut-off frequencies of the higher-order wave modes.

At a cut-off frequency the cross-section of the waveguide resonates and the spatial variation of this disturbance is uniform since the wavenumber is zero (or close to zero). Only those cross-section resonances that couple well with the applied electric field are picked

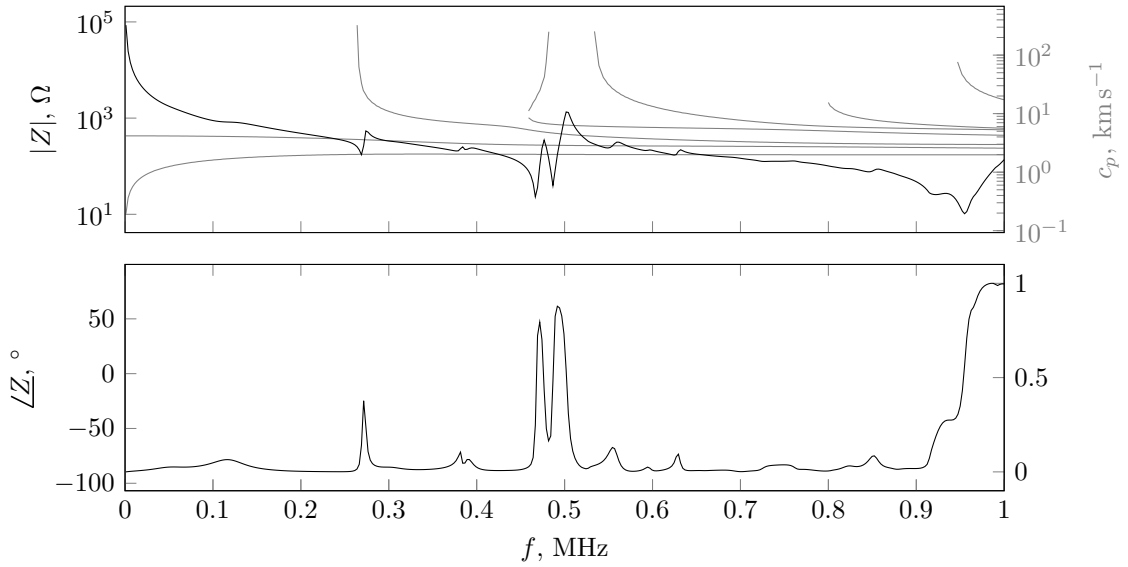

Figure 6.13: Electrical impedance of an actuator ($L = 0.02$ m, $h = 0.002$ m, $w = 0.02$ m) bonded to the 3 mm aluminium plate in plane strain (SAFE); the dispersion curves of the PZT-aluminium cross-section are shown in light gray on the top figure.

by the actuator. The dominant resonance of an actuator bonded to a plate in all cases refers to the 'thickness resonance' of the actuator. This is associated with the cut-off frequency of the bulging-contracting wave which propagates predominantly along the actuator layer. The modulus of the impedance $|Z|$ at the thickness resonance is very low, i.e. from zero up to few volts depending on the damping in the PZT material.

As an illustration to the above, the impedance for one of the cases considered below is presented in Fig. 6.13. The dips refer to the cut-off or zero-group-velocity frequencies associated with the PZT-aluminium cross-section. Since the waveguide is damped the actual cross-section resonance happens at a frequency slightly higher than the one determined by $k = 0$, as wave attenuation is very high around that point. There are four clearly visible dips in the electrical impedance curve: at 280 kHz(cut-off), at 466 kHz (zero group velocity), 486 kHz (cut-off) and at 955 kHz (cut-off). The dominant resonance occurs at 955 kHz with $|Z| = 10\ \Omega$ and corresponds to the thickness resonance of the actuator. The other resonances at 466 and 486 kHz bring the drop of $|Z|$ to 22 and 40 Ω, respectively. Keeping in mind the source impedance $Z_L = 50\ \Omega$ and the relationship between the power transfer and the impedance mismatch, one can notice that not all cross-section resonances will promote power transduction. Instead, the optimal frequencies will sometimes occur between the resonances.

The above explanation is to bring the reader's attention to the number of factors that are associated with the power transduction efficiency and point out that it is strongly

dependent on the impedance of the ultrasonic driving source.

6.3.2 Frequency response function with reference to power quantities

As a last example the point mobility at the middle of the width of the beam with respect to the power quantities is presented in Fig. 6.14. Power and velocity are not linearly related, therefore the *quasi*-FRF is calculated with respect to the square root of electrical power. Although similarly to the previous section the least optimistic case is the curve with respect to the apparent power and power capability of the source, these are expected to be the most practical power requirement measure. The global surface velocity with respect to active power, apparent power and the power capability of the source occur at 34.05 kHz, 35.97 kHz and 36.13 kHz, respectively.

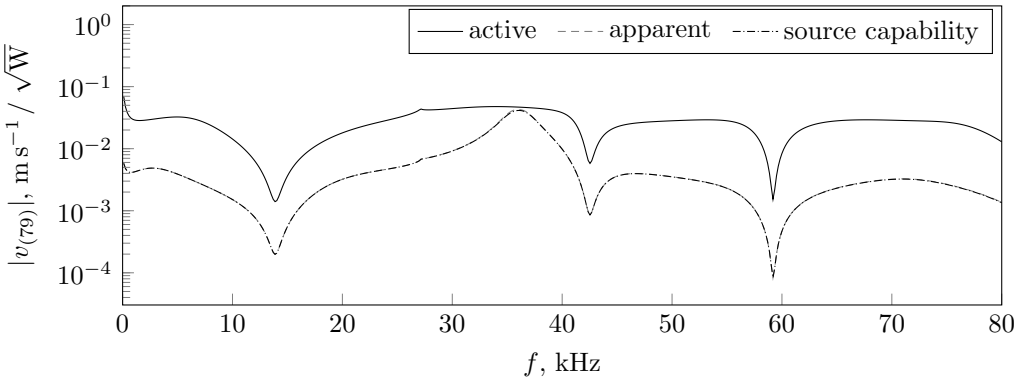

Figure 6.14: FRFs with reference to the square root of active power, apparent power and power capability of a 50 Ω source for the experimental validation case (Section 5.5).

6.4 The influence of the actuator and bonding layer parameters on the efficiency of power conversion

The above sections discuss the power conversion in waveguides excited with piezoelectric actuators. The power capability of the electrical driving source that accounts for the impedance mismatch and the complex character of the load was found to be the most practical yet the least optimistic measure of the power requirements of a smart structure. The current section is concerned with evaluating how the dimensions of the actuator and the bonding layer influence the power transduction efficiency in th light of the methodology developed in Chapter 5. A similar question motivated the work on power and energy transduction by Lin *et al.* [122, 143], however they modelled the actuator under the pin-force assumption and presented rather limited results.

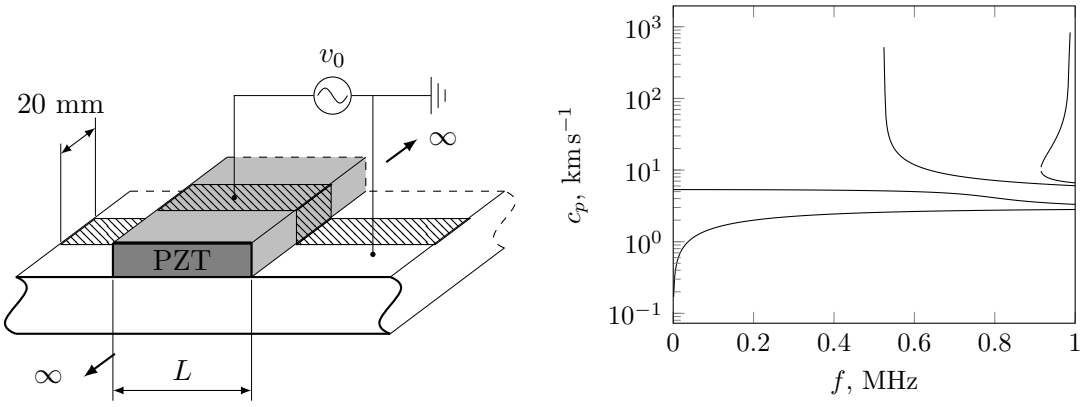

(a) Infinite plate in plane strain equipped with a PZT actuator.

(b) Phase velocity dispersion curves for a 3 mm aluminium plate - the illustrative waveguide for the parametric study.

Figure 6.15: Parametric study setup.

The current study is performed on an infinite 3 mm aluminium plate in plane strain (which confines the analysis to Lamb waves) equipped with a PZT actuator made of NCE40 material. All structural components are modelled using mono-dimensional quadratic plane strain SAFE elements. The dimensions (length - Section 6.4.1 and thickness - Section 6.4.2) of the actuator are varied accordingly in each run. In Section 6.4.3 the thickness and the loss factor associated with the bonding layer are examined.

For each case the following quantities are illustrated: (i) wave power with respect the driving voltage; (ii) wave power with respect to the active electrical power; (iii) wave power with respect to the apparent power; (iv) wave power with respect to the power capability of the amplifier. Note that for calculation of these quantities some arbitrary width of the plate has to be chosen since the plane strain model extends to infinity in the x-direction. In the following the output of the computation is scaled to represent a 20 mm wide strip (see Fig. 6.15a). For the calculation of P_{capab} it is assumed that the driving source output impedance is 50 Ω. Thus, the reader should be aware that the P_{capab} results represent a particular case that could be significantly different if the source impedance were changed.

6.4.1 Actuator's length

In this set of numerical experiments the length of the actuator was varied between 0.004 m and 0.1 m and its influence on power transduction efficiency was analysed. The results corresponding to the total wave power are shown in Fig. 6.16, whereas the contributions to wave power associated with the fundamental flexural and compressional waves are presented in Fig. 6.17, Fig. 6.18, respectively. On each graph the colour represents the

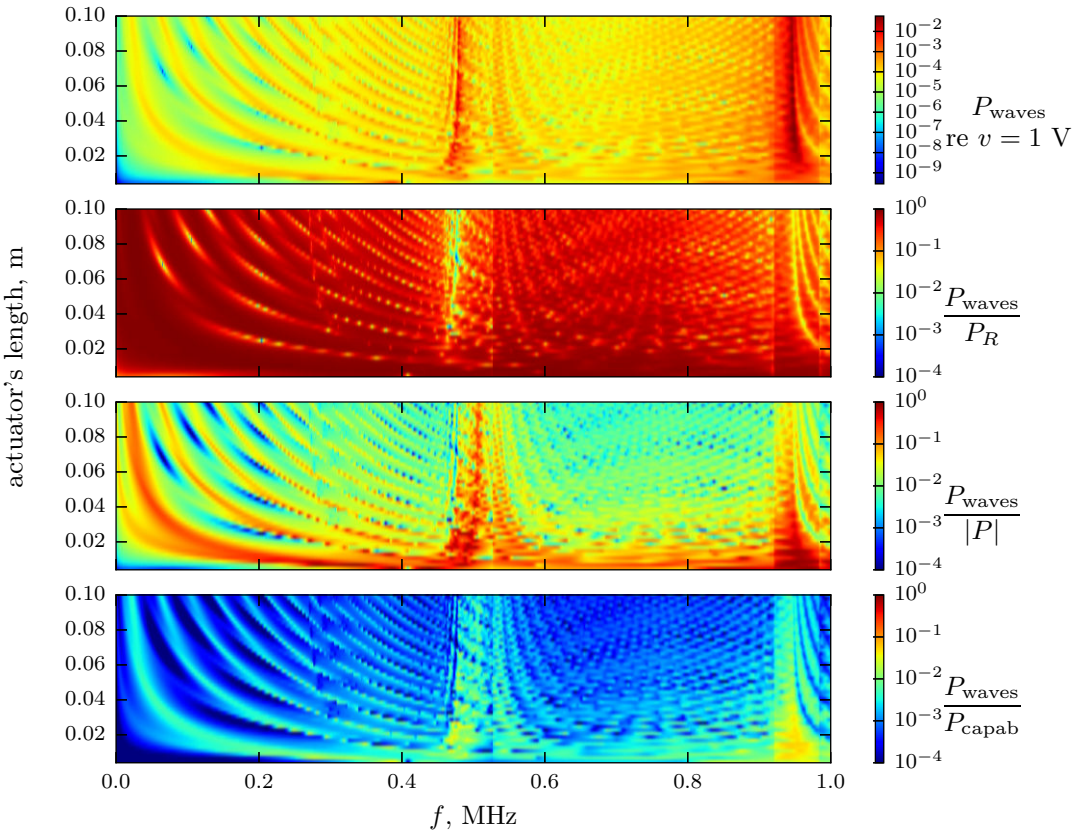

Figure 6.16: Total power transduction efficiency of a PZT actuator bonded to a 3 mm thick aluminium plate as a function of the length of the actuator; the transduction efficiency is computed with reference to the driving voltage, the active consumed power, the power rating of the actuator and the required driving source capability.

wave power computed with reference to a quantity denoted on the colour bar. Both the appearance and the analysis of the figures might seem quite formidable, however a few fundamental observations and conclusions can be stated.

The wave power is 'measured' in the plate, at the edge of the PZT-covered section. There are four waves propagating in the plate in the considered frequency range as shown in Fig. 6.15b – two fundamental and two higher-order. The relationship between the excited wavelengths and the length of the actuator leaves a clear imprint up to the first cut-off frequency in Fig. 6.16. This is sometimes referred to as wave tuning curves [93]. Whenever the length of the actuator matches a multiple of an excited wavelength the response is very small.

At low frequencies the active electrical power is almost entirely converted into mechanical wave power. However, given the chosen output impedance of the driving source (50 Ω) in most cases a very large amplifier is needed in order to induce such power. Interestingly, a larger actuator does not imply higher induced wave power (spotted also in

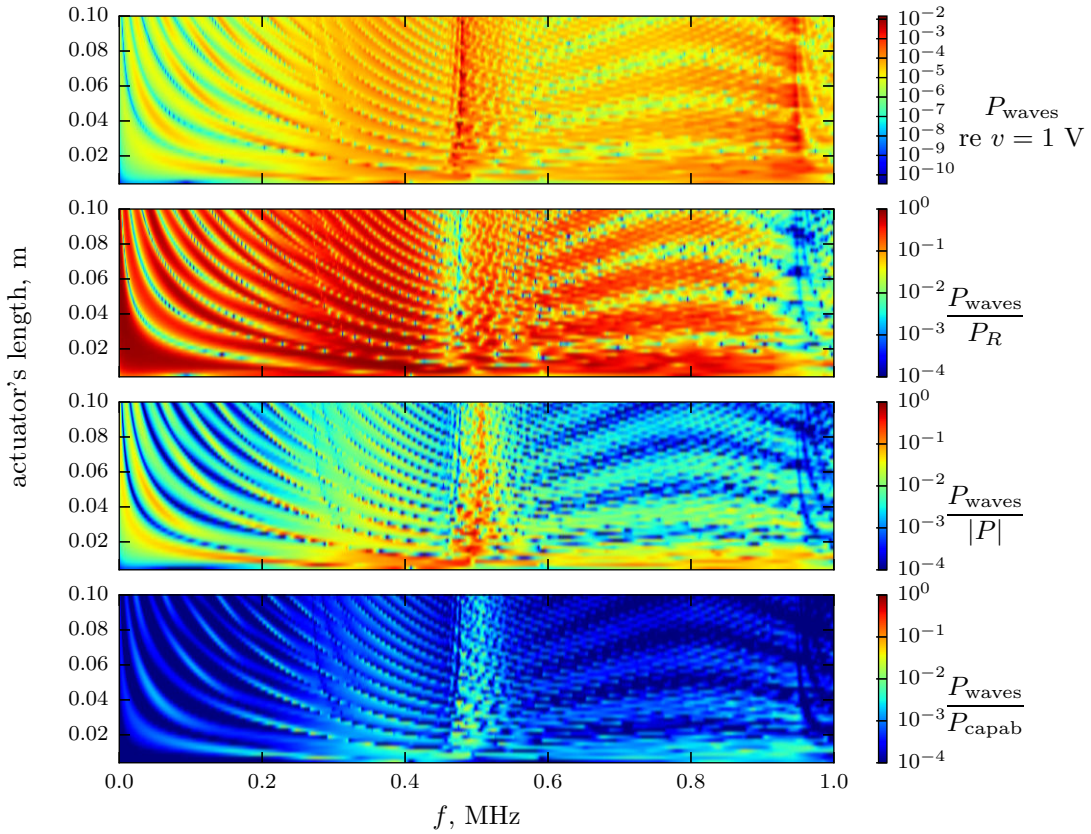

Figure 6.17: Power transduction efficiency of a PZT actuator bonded to a 3 mm thick aluminium plate as a function of the length of the actuator for the fundamental flexural (A_0) wave; the transduction efficiency is computed with reference to the driving voltage, the active consumed power, the power rating of the actuator and the required driving source capability.

[122]). Conversely, smaller actuators can operate over larger bandwidths effectively and the red spots denoting good power transduction cover wider frequency ranges. Large actuators are affected by the wave tuning pattern more strongly, so achieving a good power transduction requires more precise frequency tuning.

The cut-off frequencies in the PZT-covered section can be visible in Fig. 6.16 – the first at around 265 kHz, then around 486 kHz and finally at around 800 and 955 kHz. The zero-group velocity mode related to high localised deformation (and hence large power consumption) is expected to be responsible for the local drop in the P_{waves}/P_R ratio at around 466 kHz. Closely after that, at around 486 kHz, the higher order bending cuts off and is accompanied by the rise in the power conversion efficiency with respect to $|P|$ and P_{capab}. The cut-off frequency around 955 kHz is related to a wave that gives a very large through-thickness deformation in the PZT-covered section and is linked to the thickness resonance of the PZT actuator. The imaginary part of the impedance is minimised and the real part of the impedance is maximised, but a significant amount of

the active power P_R is dissipated within the vibrating actuator. Note that the efficiency of power conversion at those frequencies drops with the increase of the length of the actuator. The power loss in a long vibrating actuator is more prominent.

On the other hand, primarily resistive electrical impedance near the cut-off frequencies facilitates power transfer between the electrical components. Short actuators, which are not that strongly affected by the power loss due to localised resonance can then be driven very efficiently.

The cut-off frequencies in the aluminium plate are very close to those in the PZT-aluminium bilayer. A vertical distinguishable strip between ca. 920 and 980 kHz of increased power conversion efficiency in Fig. 6.16 is related to a higher-order wave in the aluminium plate. The group velocity of that wave is of the opposite sign to the phase velocity (compare with Fig. 6.15b remembering that only positive phase velocities are pictured there). The electrical power is absorbed by that wave efficiently, but does not propagate over a long distance as the imaginary part of the dominant wavenumber is at best $-5\jmath$.

Over the whole frequency range considered it is worth noticing that if the source with a standard output impedance is used (50 Ω) smaller actuators ($L < 0.06$ m) are able to convert the electrical power into the wave power more effectively.

In Fig. 6.17 and Fig. 6.18 it is shown how the electrical power is converted into the two fundamental waves. Up to the cut-off of the first higher-order wave in the PZT-covered section (around 265 kHz) the wave tuning curves for both waves can easily be noticed. The peaks and dips patterns and the increase of their density with the length of the actuator are apparent. As in this frequency range the compressional wavelength is longer than the flexural wavelength, the peaks are more widely spaced for the compressional wave.

After the first cut-off frequency the higher-order waves are the dominant energy carriers in the PZT-covered section. From 265 kHz up to 466 kHz the higher-order wave in the PZT-covered section converts predominantly into the flexural wave in the plate. At higher frequencies the higher order waves in the plate propagate most of the energy. The graphs associated with the higher-order waves are not presented for the sake of brevity.

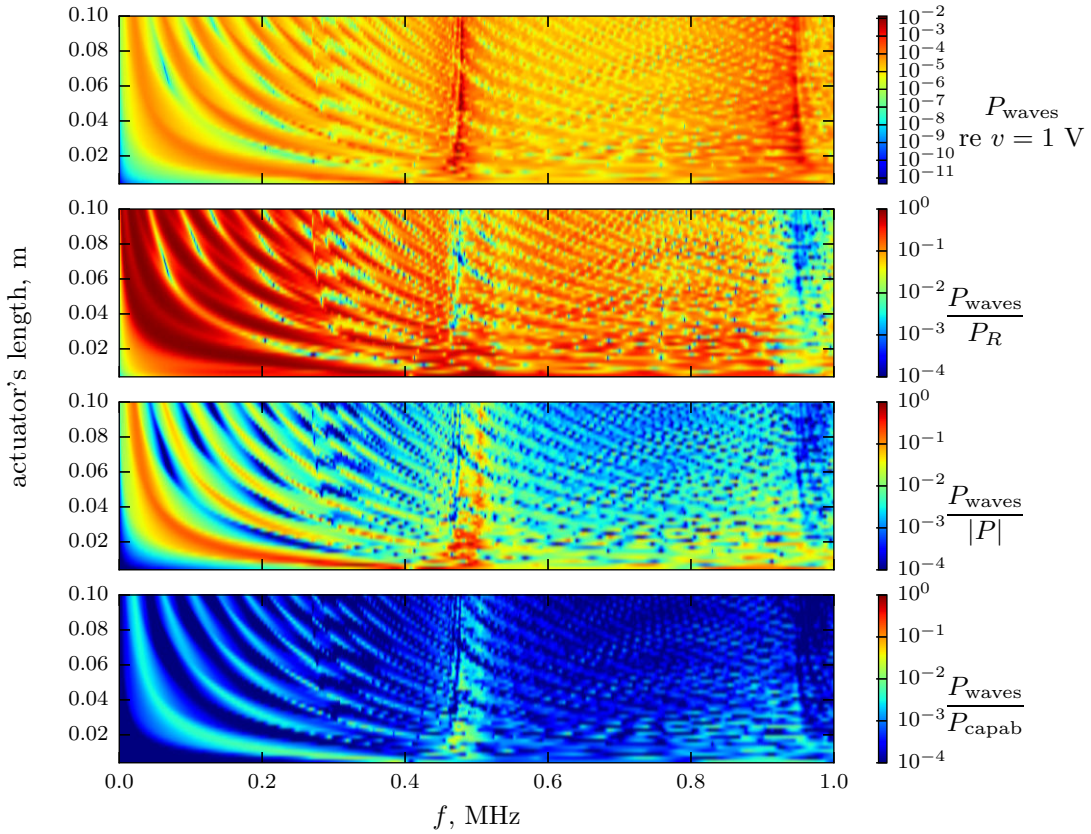

Figure 6.18: Power transduction efficiency of a PZT actuator bonded to a 3 mm thick aluminium plate as a function of the length of the actuator for the fundamental longitudinal (S_0) wave; the transduction efficiency is computed with reference to the driving voltage, the active consumed power, the power rating of the actuator and the required driving source capability.

6.4.2 Actuator's thickness

In this section the actuator's thickness is varied between 0.0001 and 0.004 m, keeping the length of the actuator fixed at $L = 0.025$ m. The results corresponding to the total wave power are shown in Fig. 6.19, whereas the contributions to wave power associated with the fundamental flexural and compressional waves are presented in Fig. 6.20, Fig. 6.21, respectively.

The change in the thickness of the actuator affects the wave spectrum and the dispersion curves, therefore it is difficult to clearly distinguish between the factors affecting power transduction. From the electrical viewpoint, varying the thickness contributes to two effects: the change of the static capacitance of the actuator (inversely proportional to the thickness) and a smaller electric field gradient (more voltage is needed for a thick actuator to generate the same electric field).

At low frequencies the efficiency of the power conversion increases with the thickness of the actuator. The thicker the actuator, the smaller is the capacitance and therefore the reactive power required by the PZT. On the other hand thick actuators have higher resistance (as opposed to thin actuators which behave as almost pure capacitors). This makes the impedances of the typical source and of the load match more closely promoting an efficient power transfer. Note that very thin actuators (< 0.5 mm) are very difficult to drive with standard off-the-shelf amplifiers due to large static capacitance and very small resistance. Although thick actuators perform better, they involve very high voltages in order to invoke high enough electric field which often acts as a limitation.

Increasing thickness of the actuator affects the dispersion curves of the PZT-covered section, and hence the wave tuning curves (the effect of the relationship between the excited wavelengths and the length of the actuator). This is clear up to the first cut-off frequency (around 260 kHz). The wavelength of the fundamental flexural wave increases with the thickness of the actuator, hence the regions corresponding to good power conversion

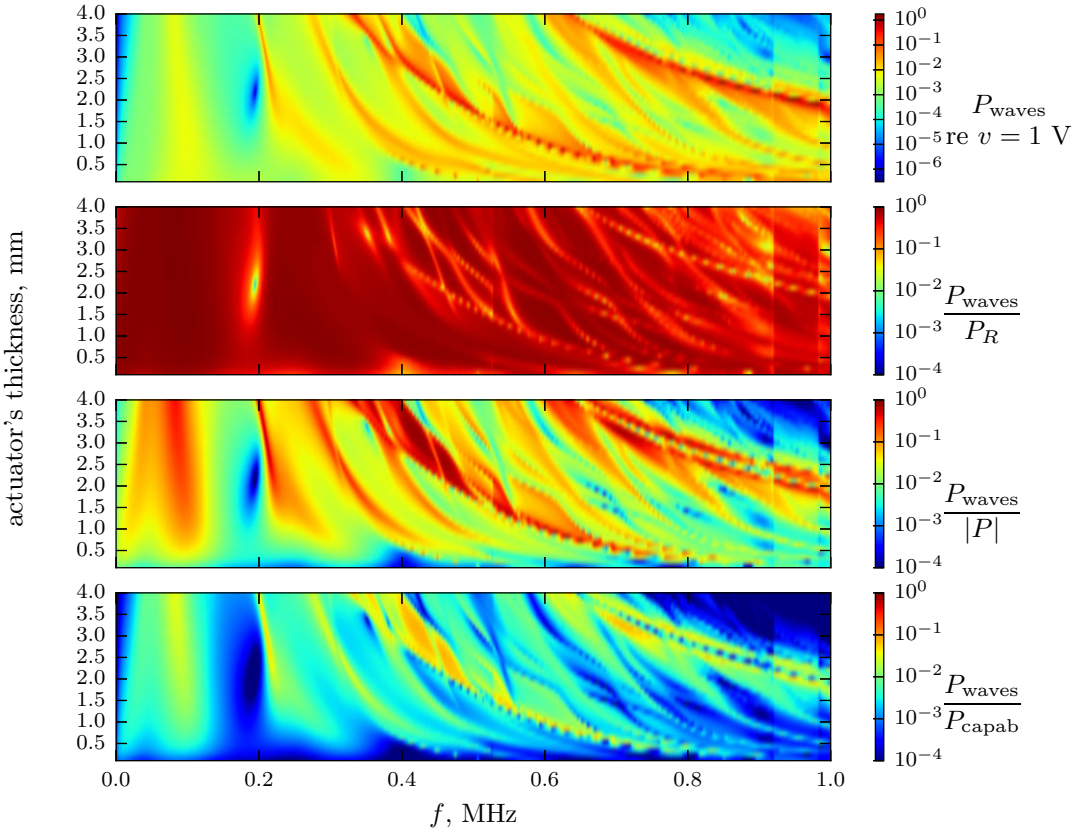

Figure 6.19: Total power transduction efficiency of a PZT actuator bonded to a 3 mm thick aluminium plate as a function of the thickness of the actuator; the transduction efficiency is computed with reference to the driving voltage, the active consumed power, the power rating of the actuator and the required driving source capability.

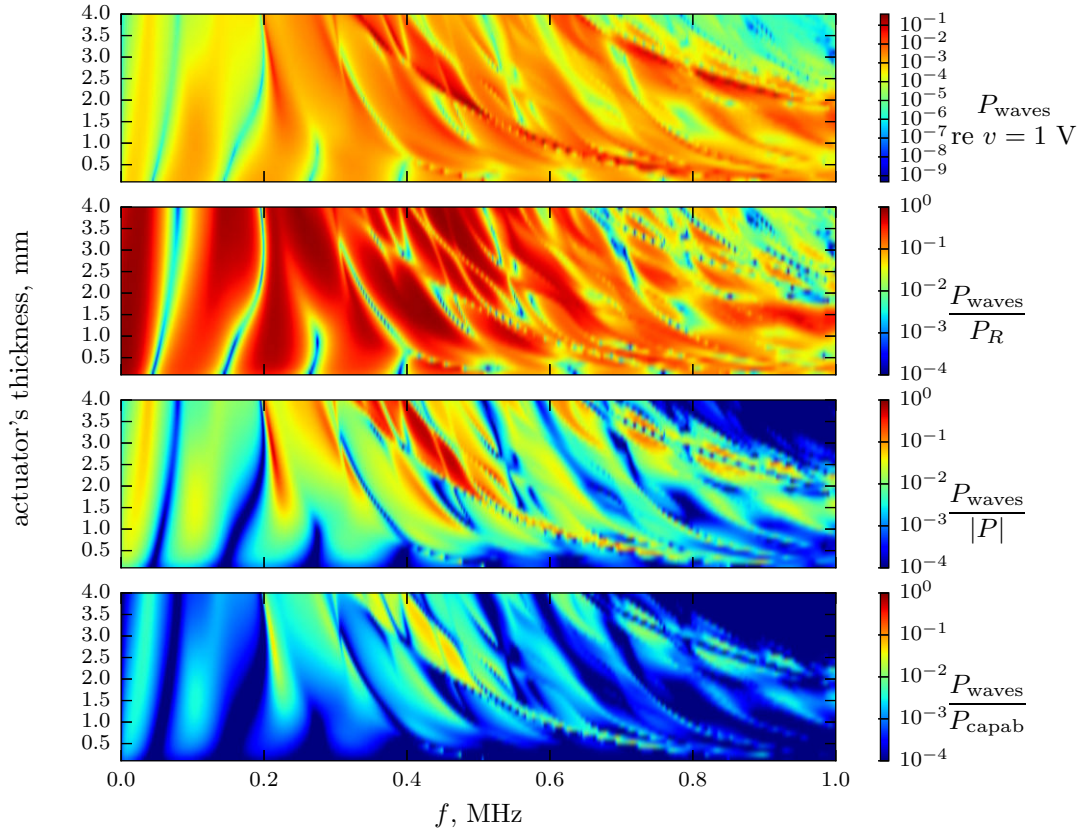

Figure 6.20: Power transduction efficiency of a PZT actuator bonded to a 3 mm thick aluminium plate as a function of the thickness of the actuator for the fundamental flexural (A_0) wave; the transduction efficiency is computed with reference to the driving voltage, the active consumed power, the power rating of the actuator and the required driving source capability.

become wider and shift slightly toward higher frequencies (see Fig. 6.20). Conversely, the wavelength associated with the fundamental compressional wave becomes shorter for thicker actuators which results in narrowing the optimal power conversion area towards the top of Fig. 6.21.

There is a uniform stop-band between 150 and 200 kHz which corresponds to the region where both excited wavelengths are such that their whole multiples are equal to the length of the actuator. This stop-band does not change significantly with the thickness of the actuator, as its effect on the location of the stop-bands for particular waves is not strong enough.

The dominant bright tongues originating from the top of the graphs in refer to the cut-off frequencies of the waves in the PZT-covered section. Close to the cut-off frequencies actuators tend to behave as resistive loads (which helps with the efficient power transfer between electrical components) and invoke high amplitude wave field (large deformation

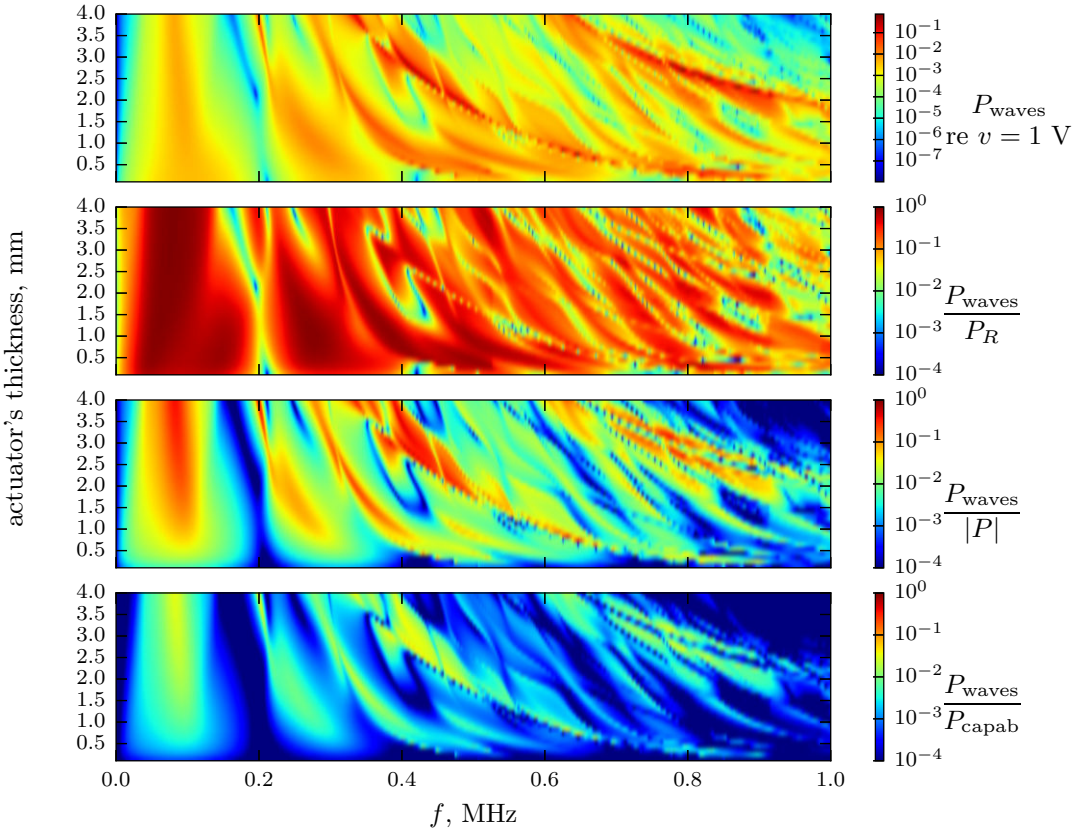

Figure 6.21: Power transduction efficiency of a PZT actuator bonded to a 3 mm thick aluminium plate as a function of the thickness of the actuator for the fundamental longitudinal (S_0) wave; the transduction efficiency is computed with reference to the driving voltage, the active consumed power, the power rating of the actuator and the required driving source capability.

is associated with cut-off frequencies). When the thickness increases, higher-order waves start to propagate earlier in frequency, hence the negative slope of the tongues.

The other multiple narrow orange/red regions corresponding to good power transduction in Fig. 6.19, Fig. 6.21, Fig. 6.21 are expected to originate from across-length resonances of the actuator. As they can be largely affected by radiation damping their effect is smaller than those related to the cut-off frequencies.

The power conversion efficiency generally drops towards higher frequencies (except near some of the cut-off frequencies) and thicker actuators (see the second graph of Fig. 6.19). If the ability to drive the actuators with commercial amplifiers is taken as a criterion this effect becomes even more evident. Moreover, the blue area near the bottom axis of the fourth figure in Fig. 6.19 indicates that very thin surface bonded actuators are not very practical power converters.

6.4.3 Bonding layer's thickness and loss factor

In the last part of the parametric study the influence of the bonding layer is discussed. Two variables are varied, namely the thickness and the loss factor of the bonding layer. The other properties of the bond material are taken from Tab. 2. The NCE40 PZT actuator is 0.025 m long and 2 mm thick. The results for bonding layer thickness are shown in Fig. 6.22 and for the loss factor in Fig. 6.23. Since the effects of both properties are not very significant, only the superimposed power graphs are given.

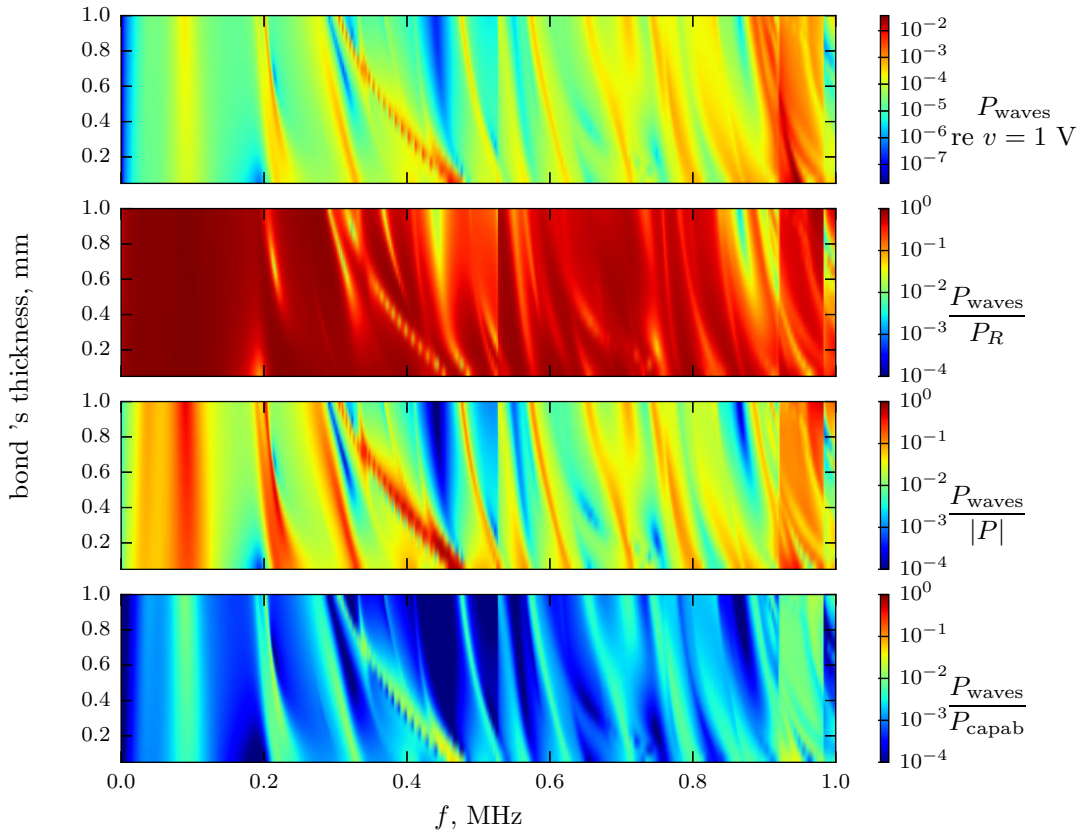

Figure 6.22: Total power transduction efficiency of a PZT actuator bonded to a 3 mm thick aluminium plate as a function of the thickness of the bonding layer; the transduction efficiency is computed with reference to the driving voltage, the active consumed power, the power rating of the actuator and the required driving source capability.

The thickness of the bonding layer does not affect the power transfer considerably up to 200 kHz. Above that frequency the 'orange/red tongues' indicating an efficient power transfer are shifted towards low frequencies with the increase of the bond thickness. This can be attributed to the fact that at high frequencies the thickness of the bonding layer affects the wavelength more strongly. Consequently, the frequencies at which the relationship between the excited wavelength and the length of the actuator correspond

to efficient power conversion are changed. One can also notice that the tongues are wider for thin bonds and narrower for thick bonds. This implies that thick bonds require more precise frequency tuning in order to achieve good power transduction efficiency.

Fig. 6.23 indicates that the loss factor of the epoxy used for bonding the actuator does not affect the power transfer notably (given that the bonding layer is 0.1 mm thick). It is expected that in the considered frequency range the bond-dominated waves do not exist, therefore only small part of the strain energy is confined in the bond and prone to dissipation.

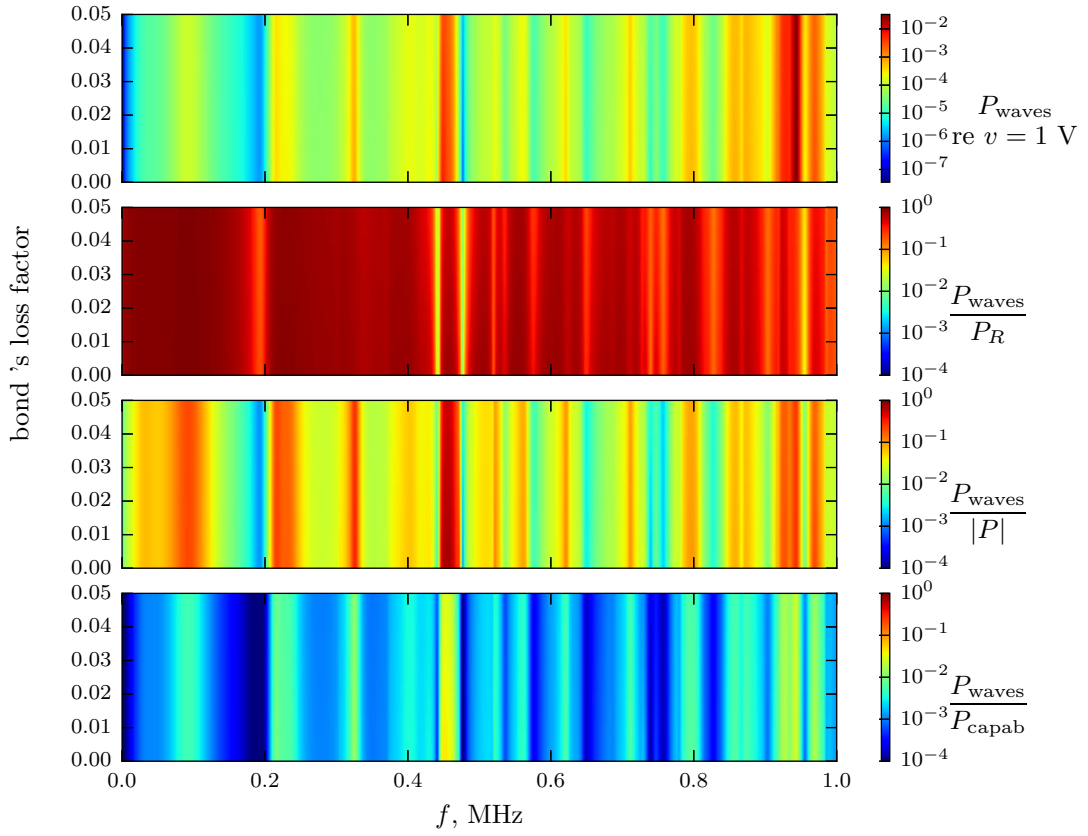

Figure 6.23: Total power transduction efficiency of a PZT actuator bonded to a 3 mm thick aluminium plate as a function of the loss factor of the bonding layer; the transduction efficiency is computed with reference to the driving voltage, the active consumed power, the power rating of the actuator and the required driving source capability.

6.5 Conclusions

In this chapter the power conversion in waveguides excited with piezoelectric actuators has been analysed. The SAFE/wave model developed in Chapter 5 served as a tool

for calculating both mechanical and electrical powers. Particular attention was given to the issues related to the power transfer between the ultrasonic driving source and the actuator. The frequency dependent voltage reflection coefficient was employed to evaluate the electrical power requirements that include impedance mismatch.

From a physical viewpoint the active (real) power is the most indicative reference quantity that describes how the power consumed by the actuator is used to perform a given task. However, a practical engineering perspective requires including the effects associated with complex load driving which, changes the perspective considerably. The resulting power requirement regarding the capability of the amplifier was found to be the most informative figure for power ultrasonic systems.

The electrical to mechanical wave power transduction was analysed for the configuration used in the validation experiment in Chapter 5. The chapter was concluded with a parametric study showing the dependence of the power conversion efficiency on the dimensions of the actuator and the thickness and loss factor associated with the bonding layer.

Chapter 7

Application of the proposed methodology to interface shear stress prediction

The modelling tools developed in the previous chapters enable an insightful and practical analysis of the interface shear stress in piezo-actuated structural waveguides with respect to the electric power requirements. The qualitative study originating from analytical theories was concluded in Chapter 2 with a set of observations and implications for real world applications. They were subsequently addressed throughout the course of the thesis with more adequate and specialised modelling tools. The essential stage was the development of a wave-based methodology for calculating waves excited by piezoelectric actuators which was not laden with the limitations of the commonly used theories (e.g. the pin-force assumption). Its electromechanical character has been explored in more detail in Chapter 6 where various aspects of electrical-to-mechanical power conversion were discussed.

In this chapter the aforementioned tools are applied to the problem of interface shear stress prediction in structural waveguides with unwanted accretions equipped with piezoelectric actuators. In order to keep both generality and the reference to a practical case, two structural configurations for the host are considered: an aluminium plate in plane strain (1D cross-section) and a steel rectangular beam as used in the validation experiment (Section 5.5 - 2D cross-section). Waveguides fully covered with accretion are considered first. In Section 7.1.1 and Section 7.1.2 it is shown how the interface stress is recovered from the SAFE formulation and how the results of the proposed model compare with conventional FE simulations. The particular wave contributions to the overall stress are discussed in Section 7.1.3 and the interface stress distribution for a 2D

waveguide is presented in Section 7.1.5. The power quantities introduced in Chapter 6 are used as reference quantities for stress analysis in Section 7.1.4. In Section 7.2 the influence of the parameters of the accreted layer is assessed with the new modelling tools. The discussion on other related issues such as the comparison between a fully and partially covered waveguide and the effect of reflections is presented in the following sections. Whenever ice is used as the accretion, the corresponding electrical power requirements are stated.

This chapter is concluded with an experiment on invoking delamination using structural waves in a beam-like waveguide with patches of a model material accretion (building plaster - see Appendix A).

7.1 Interface stress in a waveguide fully covered with accretion under piezoelectric actuation

7.1.1 Stress recovery routine

The cross-section in SAFE is modelled in a similar way to the conventional FE, hence it is bound by the same limitations when stress calculation is desired. FE formulation is based on displacement, i.e. during the element assembly only the displacement degrees of freedom associated with adjacent elements are equated. Moreover the shape functions are required to be continuous up to the $(p-1)$ derivative across the element boundaries where p is the order of approximating polynomial [124]. The strain and stress calculation requires higher-order derivatives of the shape functions which are not necessarily (in practice very seldom) continuous. As a consequence one observes sudden jumps of stress between elements, especially at material boundaries. In order to minimise this effect a sufficiently dense mesh must be used near the region where stress values are to be obtained.

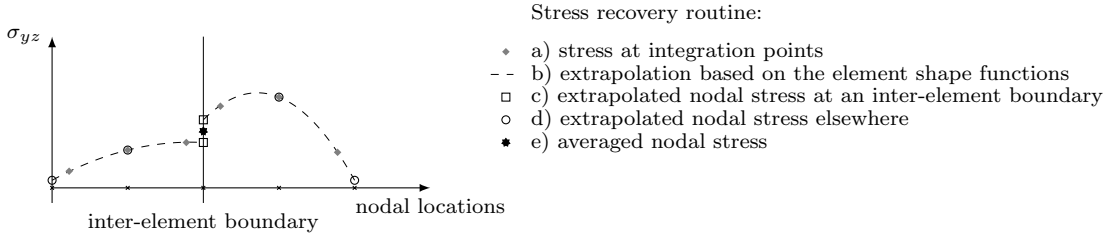

Figure 7.1: Schematic presentation of the stress recovery routine from SAFE model.

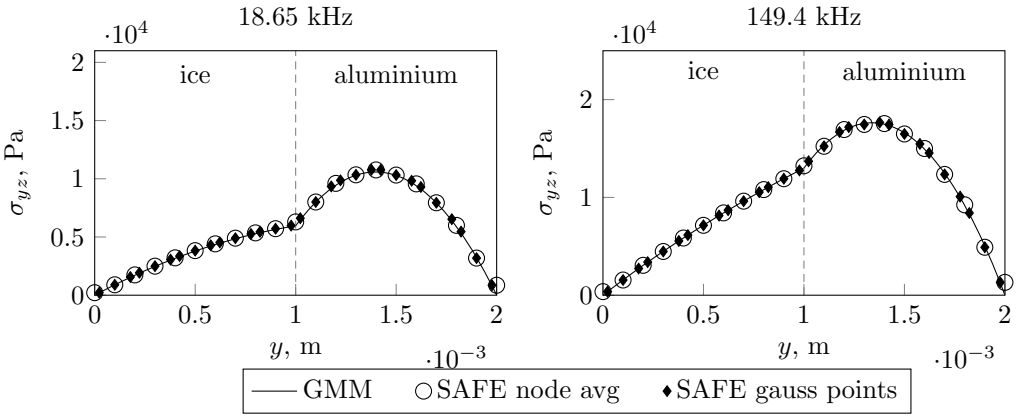

Figure 7.2: Through-thickness stress distribution at two frequencies for an infinite aluminium (1 mm) – glaze ice (1 mm) plate in plane strain. Comparison between distributions from SAFE plotted at integration points and extrapolated to nodes (with averaging) with analytical GMM result.

The derivation of the SAFE elements requires computing the virtual work done by the strain field on the stress field which is integrated over the cross-sectional domain (see Section 4.1.3). The Gauss integration scheme adopted in the implementation of SAFE enables evaluating the integrations by computing the integrands only at a few particular locations called integration points. Therefore, the stress in displacement-based FE is the most accurate at the integration points [124]. If linear elements are used, the stress at the integration point is often referred to as element stress. In the case of quadratic elements there are three integration points for 1D elements and 9 integration points for 2D elements. The stress can be extrapolated to the nodes using the displacement shape functions chosen, however special care must be taken while analysing extrapolated results. Since the stress is expected to be discontinuous at an inter-element boundary, at a node where a few elements meet, a few different values for stress are obtained. An appropriate averaging technique is needed to account for the discontinuity. In this thesis, the simplest method is used, namely a mean of all the contributions is returned as a representative value for a node shared by more than one element.

A schematic presentation of the implemented stress recovery routine can be found in Fig. 7.1. Note that nodal stresses are in general complex numbers, so they are averaged as such. As for FE, increasing mesh density improves the accuracy of the calculated nodal stress. It is worth mentioning that for a 1D cross-section (plate in plane strain) an alternative technique that combines the robustness of SAFE method for determining dispersion curves and accuracy of GMM for calculating through-thickness wave field distributions can be used [123]. The SAFE method is employed to find the dispersion characteristics which then are used in a global matrix assembly according to GMM. The wave field is recovered from the global matrix in the same way as explained in Chapter 1.

Thanks to this technique the strongest advantages of both methods are used at the same time. The main benefit of this approach is that the stress distribution, and therefore the interface shear stress value, is exact. An illustrative result can be found in Fig. 7.2.

Unfortunately the GMM 'extension' can only be applied to one-dimensional cross-sections, for which a GMM formulation exists. If the cross-section is two-dimensional or if the GMM is not used for a one-dimensional cross-section, one must be particularly careful while specifying the mesh density in stress calculations. Note that convergence of the SAFE method for dispersion calculation does not ensure that the stress values are accurate.

7.1.2 Validation with FE

The wave model and the stress recovery routine have been validated with conventional FE simulations. Modelling of anechoic boundaries is quite cumbersome in FE, therefore the comparison has been performed on a finite waveguide (which the wave model can easily handle) – modelled either in plane strain (2D structure, but 1D mesh in SAFE) or as fully three-dimensional (3D structure, but 2D mesh in SAFE).

One of the main simplifications involved in the wave model developed in Chapter 5 is related to the assumption that the electric field in the direction of propagation z is neglected, therefore piezoelectric shear coefficient e_{zyz} plays no role in the constitutive equations in (3.19). The effect of this simplification is demonstrated below as in the FE simulation two variants are considered – with full piezoelectric coefficients matrix and with reduced piezoelectric coefficients matrix (without shear components). It is important to mention that the dimensional reduction of the piezoelectric constitutive equations (from 3D to e.g. 2D plane strain) is not always properly implemented [121] therefore it is advisory to use the d-form of the piezoelectric constants in 2D plane strain FE models.

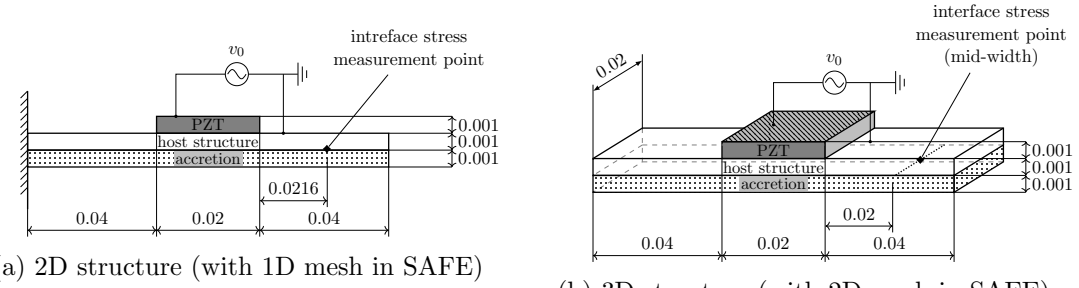

(a) 2D structure (with 1D mesh in SAFE)

(b) 3D structure (with 2D mesh in SAFE)

Figure 7.3: Geometry for the SAFE-FE validation cases.

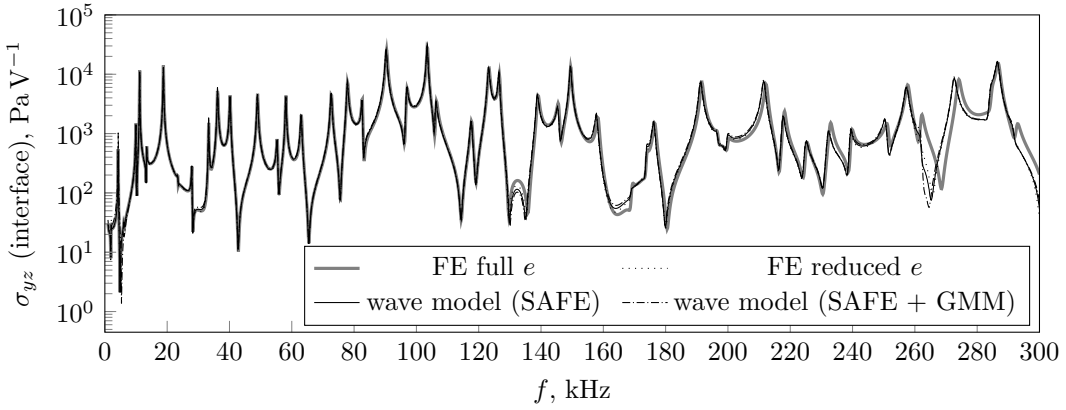

Figure 7.4: Validation with FE of the stress calculation for a 2D structure with 1D mesh in SAFE. See Fig. 7.3a for structural configuration details.

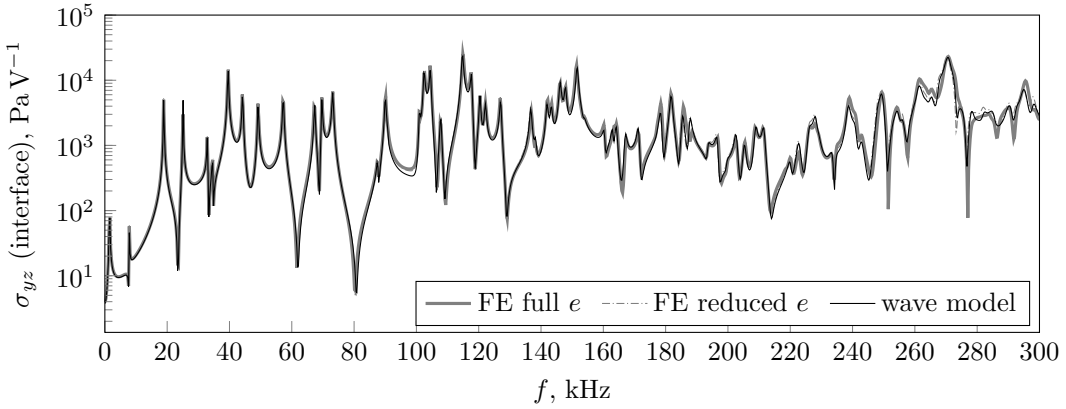

Figure 7.5: Validation with FE of the stress calculation for a 3D structure with 2D mesh in SAFE. See Fig. 7.3b for structural configuration details.

For the 2D variant a finite aluminium (1 mm) – glaze ice (1 mm) plate in plane strain with fixed-free end boundary conditions was used. It was equipped with a Noliac NCE40 1 mm thick and 2 cm long actuator. Both in SAFE and in FE five quadratic elements were used per each layer (mono-dimensional plane strain in SAFE and two-dimensional plane strain in FE). The geometry for the considered case is schematically presented in Fig. 7.3a. Fig. 7.4 shows the results for SAFE, SAFE with GMM for stress calculation and conventional FE (Abaqus). The transfer functions obtained using SAFE and FE with reduced $\mathbf{e}$ matrix are in excellent agreement, however with increasing frequency the effect of neglecting shear piezoelectric coefficients becomes more significant. Nevertheless, the magnitude of the discrepancy confirms that this assumption does not involve significant loss of accuracy.

The comparison for the 3D variant is done on a similar structure, but extended by 20 mm in the x direction and with free-free boundaries. The corresponding geometry is schematically presented in Fig. 7.3b. The cross-section was discretised with 12×1

quadratic elements per material layer both in SAFE and FE (8-node quadratic plane elements in SAFE and 20-node quadratic 3D bricks in FE). In Fig. 7.5 the comparison between SAFE and conventional FE (Abaqus) is presented. Like for the 1D case, a small discrepancy between the FE with full $\mathbf{e}$ matrix and SAFE is observed, but its magnitude is negligible. Otherwise, the agreement is very good, which confirms the validity of the implemented wave model and the associated stress recovery routine.

7.1.3 Contributions of wave types to the overall interface stress

Let us now look at how different waves contribute to the piezo-induced interface shear stress in structures with unwanted accretions when no reflections are present. It is recalled that throughout the thesis the actuator is assumed to be poled along the thickness (y) direction which corresponds to the material 3-3 axis.

The wave-based nature of the model enables separating the stress generated by particular waves. Note that only propagating waves are considered in this comparison which means that the waves that are classified as evanescent are not taken into account. The loss factor for ice adopted in this thesis is high $\eta_{\text{ice}} = 0.01$, so the wave attenuation at high frequencies is expected to be non-negligible. Therefore, specifying at what distance from the actuator the interface stress is analysed is essential for understanding the capabilities of the waves for invoking debonding. The criterion for identifying propagating waves is in general case specific (see Section 4.2, [51]) and below it is assumed that propagating waves are associated with the imaginary part of the wavenumber such that $|\text{Im}\{k\}| < 100$. This is rather generous, since for instance, over a distance of 0.1 m wave amplitude is reduced by a factor of $|\exp[-\jmath(-100\jmath)0.1]| = 4.5 \times 10^{-5}$.

7.1.3.1 Infinite plate in plane strain (1D cross-section)

If the waveguide and the actuator are modelled under the plane strain assumption, only Lamb wave propagation is allowed (i.e. with the motion confined within the y–z plane). The wave composition of the stress FRF is shown in Fig. 7.6. Note that the contributions of particular waves are plotted as a magnitude, whereas the total response is the sum of the contributions which accounts for the phase differences. The phase velocity dispersion curves for the iced plate are plotted in Fig. 7.7 for reference purposes. The highlighted sections of the dispersion curves in Fig. 7.7 correspond to a more strict propagation condition, namely $|\text{Im}\{k\}| < 10$. This illustrates how the attenuation in the accreted layer grows with frequency and confirms that the build-up dominated modes decay very quickly.

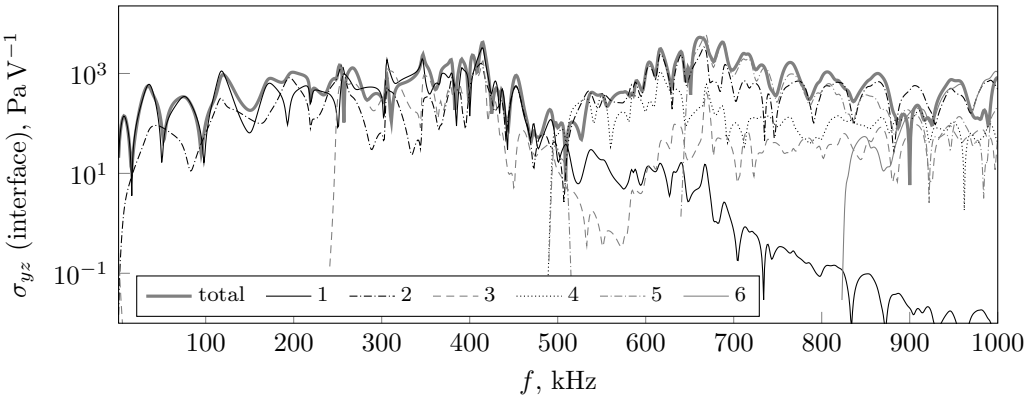

Figure 7.6: Wave contributions to the overall interface shear stress for an infinite aluminium (2 mm) – glaze ice (2 mm) plate in plane strain equipped with a Noliac NCE40 2 mm thick and 5 cm long actuator.

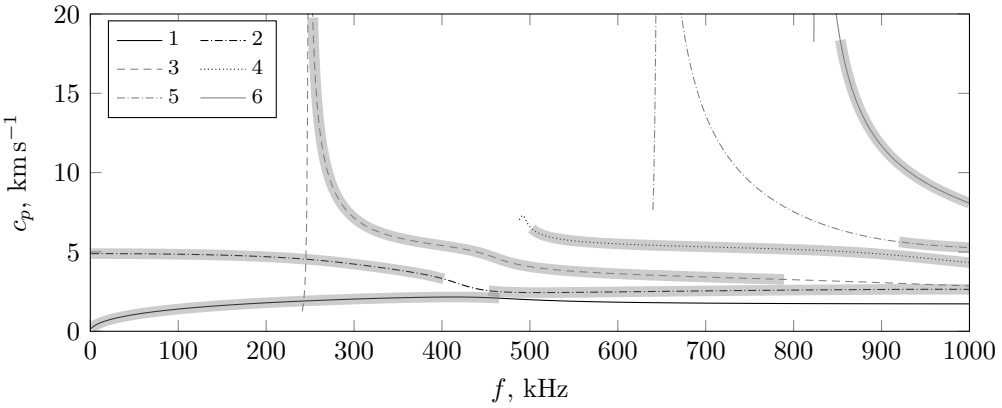

Figure 7.7: Phase velocity dispersion curves for an infinite aluminium (2 mm) – glaze ice (2 mm) plate in plane strain; the highlighted sections of the curves indicate that the condition $|\mathrm{Im}\{k\}| < 10$ is fullfilled; wave mode labelling conforms with Fig. 7.6.

Up to ca. 200 kHz the interface shear stress is predominantly generated by the flexural wave (1$^{\mathrm{st}}$ wave, often called A_0). The contribution of the 2$^{\mathrm{nd}}$ wave becomes stronger at higher frequencies. The maximum is related to the cut-off frequency of wave 5 at around 660 kHz. Higher-order waves give a significant rise to the interface stress over a narrow bandwidth close to the cut-off frequency. Glaze ice stiffness is relatively high, so that mode veering is very smooth in the considered case. However, it can be observed that veering towards the AL (accreted layer) asymptote (see Chapter 2) is associated with high stress, although at the same time associated with large wave attenuation. Note that at a longer distance from the actuator the contributions of waves that are not covered by the highlighted sections in Fig. 7.7 become negligible due to wave decay.

In the frequency range that is expected to be the most practical for wave-induced delamination (wave attenuation grows with frequency - see Chapter 2), i.e. up to around

200-300 kHz the 1st wave (flexural – A_0) provides the highest interface shear stress. The stress given by the compressional wave (2nd) is significantly lower, particularly below 150 kHz (see Fig. 7.6). This agrees quite well with the theoretical predictions from analytical wave models in Chapter 2.

7.1.3.2 Infinite beam-like waveguide as used in the experiment (2D cross-section)

A beam-like waveguide is apparently very similar to the previously considered case, however the associated wave spectrum is much more complex. Mode tracking becomes a cumbersome task since the wave mode shapes are rather complex and difficult to classify as they change along a dispersion curve significantly. A full analysis on which wave (described by the displacement wave mode shape) gives rise to the interface shear stress can only be done at a single frequency.

Nevertheless, for the sake of consistency a representative set of interface shear stress results is presented in Fig. 7.8 and associated dispersion curves shown in Fig. 7.9. At high frequencies the number of waves hinders the analysis of the wave composition of the stress FRF, therefore only a limited frequency range is discussed. Note that what is referred to as a single wave below, does not imply a continuous, single-coloured curve in Fig. 7.8 and Fig. 7.9. The arrows on Fig. 7.9 help associating particular colour with the deformation pattern for the two fundamental and the first higher-order wave.

At low frequencies the interface shear stress is generated predominantly by the fundamental flexural wave (1st in Fig. 7.8). The first higher-order wave cuts off at around 30 kHz and from that point prevails in the response. The global stress peak around

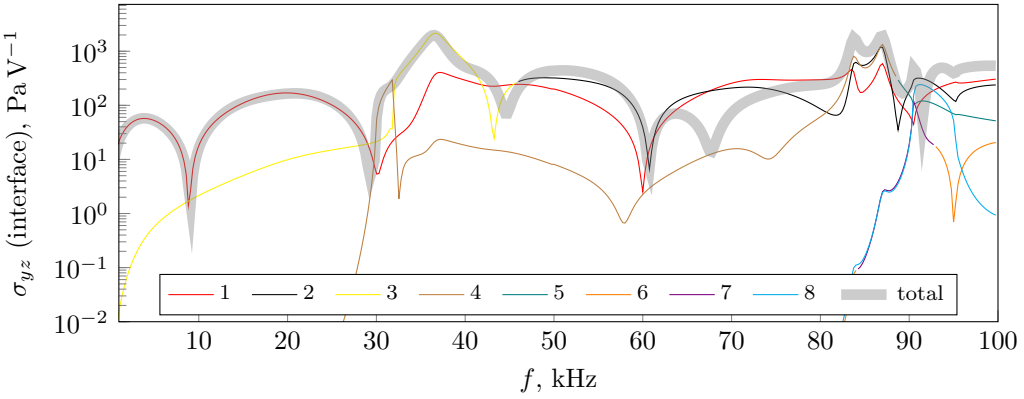

Figure 7.8: Wave contributions to the overall interface shear stress for an infinite steel beam as used in the experiment covered with a 3 mm thick glaze ice layer.

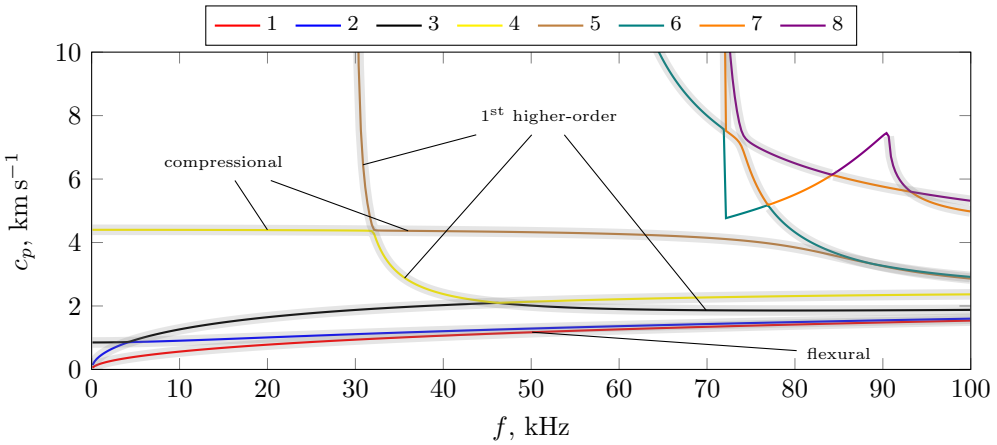

Figure 7.9: Phase velocity dispersion curves for a steel beam as used in the experiment covered with a 3 mm thick glaze ice layer; the highlighted sections of the curves indicate that the condition $|\mathrm{Im}\{k\}| < 10$ is fulfilled; wave mode labelling conforms with Fig. 7.8.

37 kHz) is related to the cut-off frequency of the higher-order wave (across-width bending) in the PZT-covered section. The contribution of the wave associated with a longitudinal deformation becomes significant around 80 kHz. It is worth mentioning that at that frequency the associated deformation pattern is a coupling between flexural and compressional motion.

Up to 80 kHz only the fundamental flexural wave and the first higher-order wave invoke non-negligible interface shear stress. Note that the maxima of the response are usually related to the cut-off frequencies in the PZT-covered section.

7.1.4 Transfer functions between interface stress and electrical input variables

A critical quantity describing the applicability of the wave-based ultrasonic cleaning systems is the electrical power requirement. The power transfer analysis of the piezo-equipped structural waveguides from Chapter 6 raised the importance of the impedance mismatch between the driving source and the actuator and proposed a few reference power quantities for the assessment of the efficiency of the excitation. Although the active power which is consumed by the actuator provides the most physical understanding of the power transduction process, the power capability of a driving source with a fixed impedance is a more practical measure indicating how big and powerful the amplifier needs to be. The interface shear stress generated by the piezoelectric actuation is now presented with the reference to those power quantities. Note that the stress is not linearly related to power, therefore the dimension of the *quasi*-transfer functions shown

below is stress per square root of electrical power. The piezoelectric actuator is assumed to be linear in all cases considered in the thesis.

7.1.4.1 Infinite plate in plane strain (1D cross-section)

Firstly, the Lamb wave (plane strain) case is considered. The results referring to a 20 mm wide strip of an infinite aluminium (2 mm) – glaze ice (2 mm) plate equipped with a Noliac NCE40 2 mm thick and 5 cm long actuator are shown in Fig. 7.10. Assuming the bond strength of the aluminuium–glaze ice bond σ_b to be 1.5 MPa, the corresponding power requirements are presented and plotted in Fig. 7.11. The figures indicated by Fig. 7.11 appear to be practically non-realisable. From the active power perspective the best point is at 268 kHz, requiring 94 W of power to be consumed by the actuator for inducing debonding. If only a 50 Ω driving source is available, one would require its power capability to be higher than a few kilowatts which may put the practicability of the approach in question.

However, two additional aspects need to be taken into account. Firstly, the shear strength bond used in this thesis is obtained statically and is expected to be higher than the dynamic bond strength. Secondly, the power capability is calculated for a 50 Ω source only (the typical off-the shelf characteristics). A dedicated system could have different output impedance adjusted to match the structural configuration, which can possibly lower the P_{capab} indications.

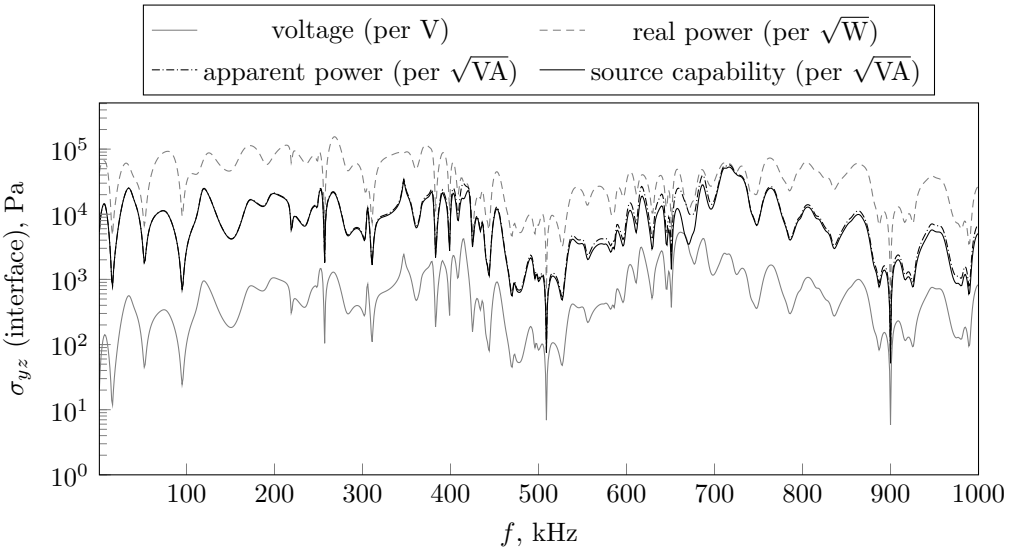

Figure 7.10: Interface shear stress seen 0.1 m from the actuator per applied voltage and per the square root of power quantities considered for an infinite aluminium (2 mm) – glaze ice (2 mm) plate in plane strain equipped with a Noliac NCE40 2 mm thick and 5 cm long actuator; powers are scaled to a 20 mm wide strip.

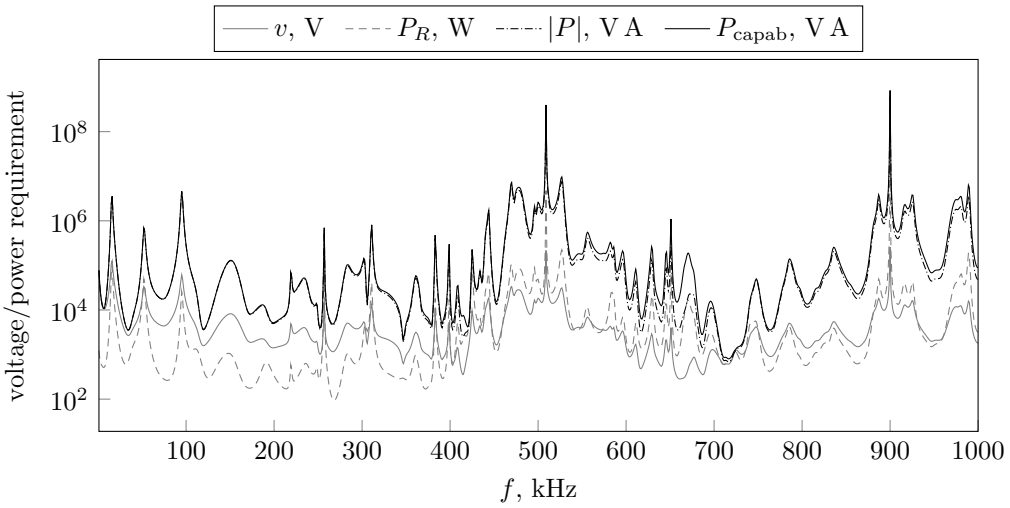

Figure 7.11: Voltage and power required to debond a 2 mm thick glaze ice layer from an infinite 2 mm aluminium plate in plane strain equipped with a Noliac NCE40 2 mm thick and 5 cm long actuator; $\sigma_b = 1.5$ MPa; powers are scaled to a 20 mm wide strip.

7.1.4.2 Infinite beam-like waveguide as used in the experiment (2D cross-section)

Attention is now drawn to a structural waveguide with a rectangular cross-section equipped with a 0.076 m and 2.2 mm thick Noliac NCE40 actuator (as used in the experiment). The beam is covered over its whole length with a 3 mm thick glaze ice layer. The results showing the interface shear stress as a function of the applied voltage and the square root of electrical power are given in Fig. 7.12. On the right y-axes the voltage/power requirements for achieving delamination at the steel–glaze ice interface are depicted (assuming the bond strength σ_b to be 1.5 MPa). Additionally, the values near the through-width resonance of the PZT-covered section, which ensures the power transduction to be optimal (see Chapter 6), are specified. A waveguide with a 2D cross-section benefits from higher order waves that are associated with through-width resonances of the cross-section. These are not available under the plane strain assumptions, although they give a rise to the interface shear stress. The first higher-order wave cuts off at around 37 kHz and is associated with a resonance of the actuator, providing the optimal power conversion between the electrical driving systems and structural waveguide (see Chapter 6). Moreover, at that frequency the transverse shear stress at the interface with respect to $|P|$ and P_{capab} reaches its maximum. It is interesting that the peak around 37 kHz does not appear in the graph where a reference to active power P_R is taken. This is attributed to the fact that since the PZT covered section is at resonance, a relatively large amount of power is lost in the actuator due to the material damping. As a consequence a smaller portion of the consumed electrical power is

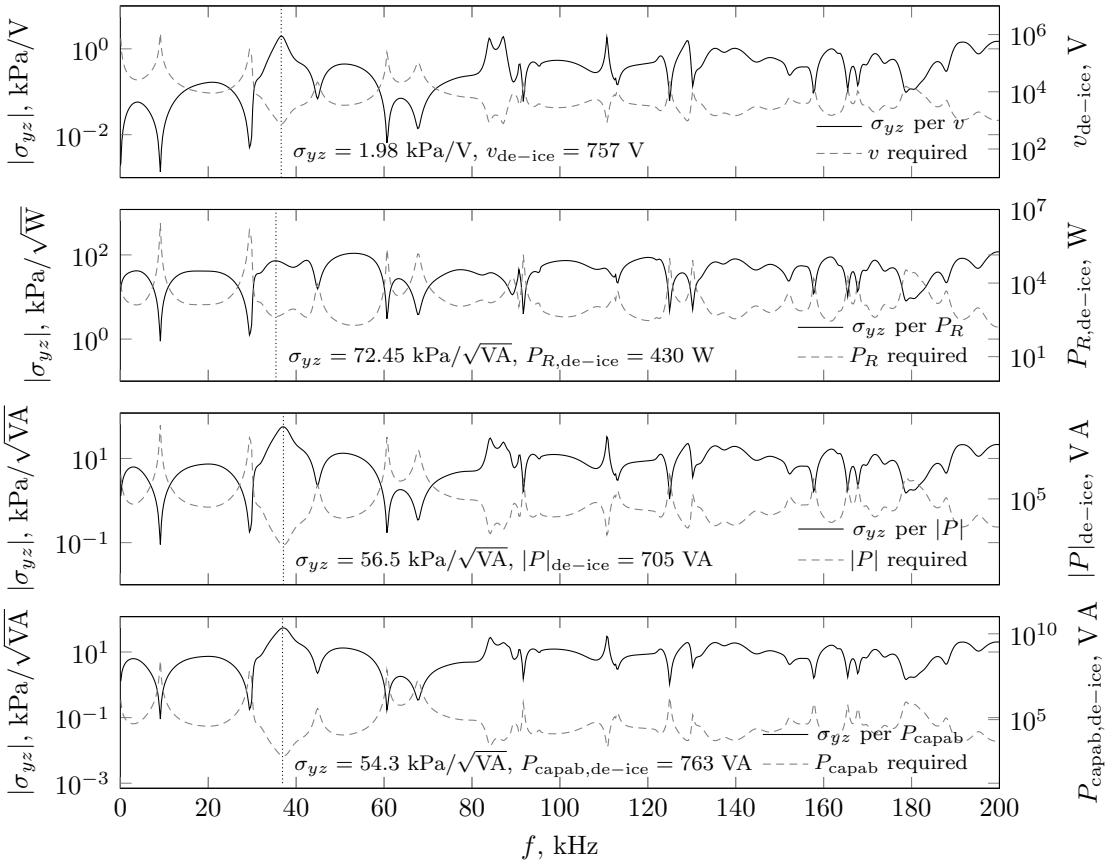

Figure 7.12: Interface shear stress per applied voltage and per the square root of power quantities considered before for the beam as used in the experiment covered with 3 mm layer of glaze ice. On the right hand side y axis, the voltage/power requirement is presented, assuming the ice bond braking stress to be $\sigma_b = 1.5$ MPa.

converted into structural wave power.

The respective power requirements shown in Fig. 7.12 are high and not directly acceptable from a practical perspective. However, it is worth keeping in mind that the ice bond strength (static) reported in the literature is not consistent among the authors and varies from 0.1 to 1.6 MPa. Moreover, the dynamic deformation is expected to break the bond easier, but unfortunately no results on the dynamic strength of the bond are known to the author. If then the actual strength of the bond is two times smaller than the assumed $\sigma_b = 1.5$ MPa, the power requirements drops by a factor of four.

One also needs to bear in mind that the examples presented in this section refer to the worst case scenarios, i.e. when no end reflections are present and the debonding is to be induced only by a propagating wave. The effect of slightly reflective boundaries is discussed later in the chapter.

7.1.4.3 How representative is a 1D cross-section waveguide for a practical 2D cross-section waveguide?

Throughout the thesis the two different structural configurations appear – the beam-like waveguide (2D rectangular cross-section) and the plate in plane strain which is commonly used in ultrasonics (1D line cross-section). It is interesting to investigate how representative is a waveguide with a 1D cross section (infinite width) for a waveguide with a 2D cross-section which is more practical, in general. In order to illustrate it, the interface stress response for the former is compared to the response of the latter, given the same material properties and dimensions. The electrical power for the infinite width case is calculated based on a 24 mm width strip which is the same as the width of the 2D cross-section. The comparison is presented in Fig. 7.13. The responses of the two models are similar up to ca. 30 kHz, when the higher-order wave cuts off in the beam-like waveguide. This wave originates from the through-width bending mode of the cross-section and therefore cannot be captured by a plane strain model. At low

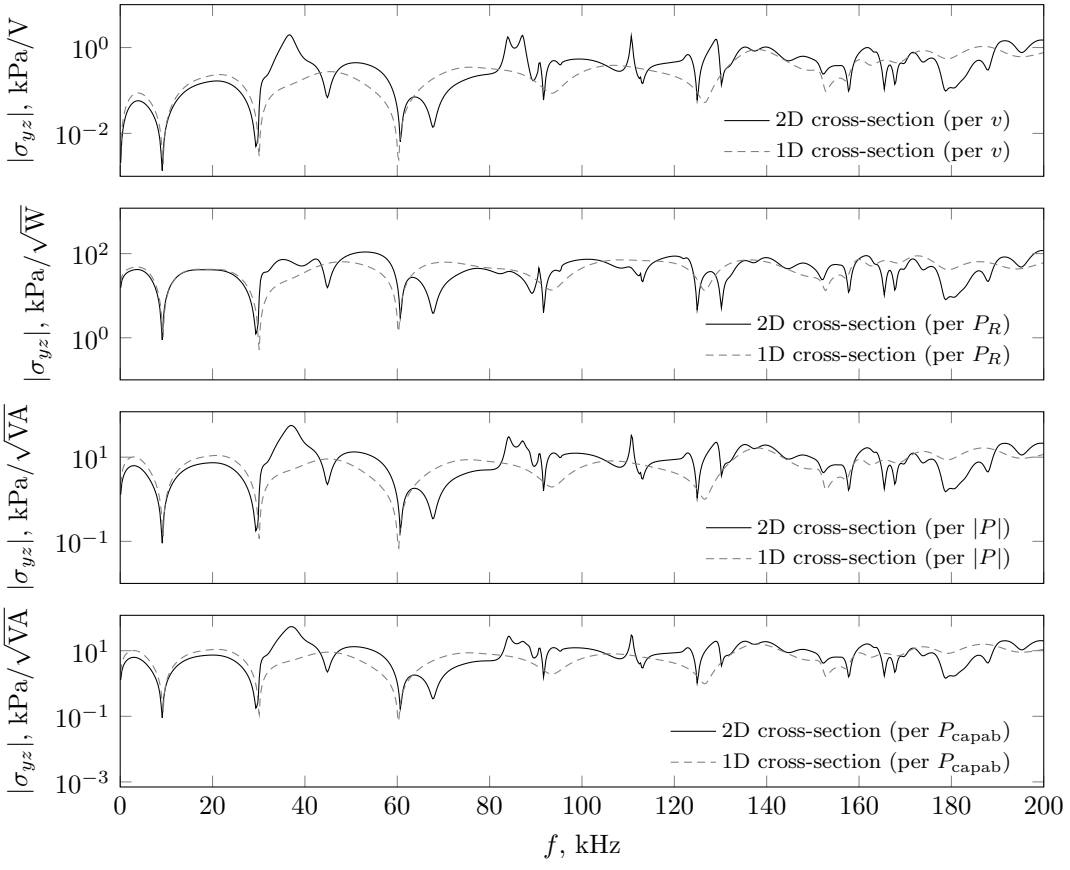

Figure 7.13: The interface shear stress calculated using a model with a 2D cross-section and with a 1D cross-section (plane strain) with width for the power calculation corresponding to the width of the 2D beam; both configurations refer to the beam as used in the experiment covered with a 3 mm accretion.

frequencies, when only the flexural and compressional fundamental waves are present and the shapes of the graphs are very similar, the 1D model gives slightly higher stress than the 2D counterpart. It can be attributed to the fact that the deformation along the width (x) contributes to higher current drawn by the actuator (especially its reactive components). Note that this difference is the least apparent in the active power (P_R) graph, which shows how the delivered active power is consumed on generating stress. In this case the influence of the reactive components is not captured and therefore the responses are very similar.

Concluding, a plane strain model is not able to capture some physical effects that can be very beneficial for the efficiency of the power transfer in a 2D waveguide. However, at low frequencies (i.e. when only the fundamental waves are present) it provides indicative and trustworthy results (although slightly overestimated).

7.1.5 Interface stress through-width distribution as a function of frequency for a beam-like waveguide

The interface shear stress in a beam-like waveguide considered in this chapter usually refers to the interface point at the middle of the width of the cross-section. However, the interface stress distribution in the beam is, of course, not uniform. In some cases the chosen reference point for stress comparison is not leading to the most optimistic conclusions. Therefore, for the sake of completeness the through-width stress distribution for the illustrative beam-like waveguide is discussed in this section. For a specific implementation one could account for the benefits of considering the full through-width distribution.

In a waveguide with a two dimensional cross-section there are two stress components that are likely to promote delamination – σ_{yz} (as for the 1D case) and σ_{yx}. The shear stress σ_{xz} is supposed to contribute to shearing of the vertical planes and hence induce internal cracks (see Fig. 2.17). The through-width distribution of the interface stress components including the effect of combining the two transverse shear stresses is shown in Fig. 7.14. Both σ_{yx} and σ_{xz} are anti-symmetric with respect to the middle of the cross-section. A significant rise in all the stress components is observed with the first higher-order through-width bending wave cuts off at around 35 kHz. At higher frequencies the transverse stresses (σ_{yx}, σ_{xy}) exhibit other sharp peaks at those subsequent cut-off frequencies, whose associated waves are excited by the actuator. The shear stress σ_{xz} achieves the highest values among the three, however according to [21] is not expected to contribute to delamination. Note that the transverse shear stress σ_{yz} is maximum at the edges of the beam at the cut-off frequencies.

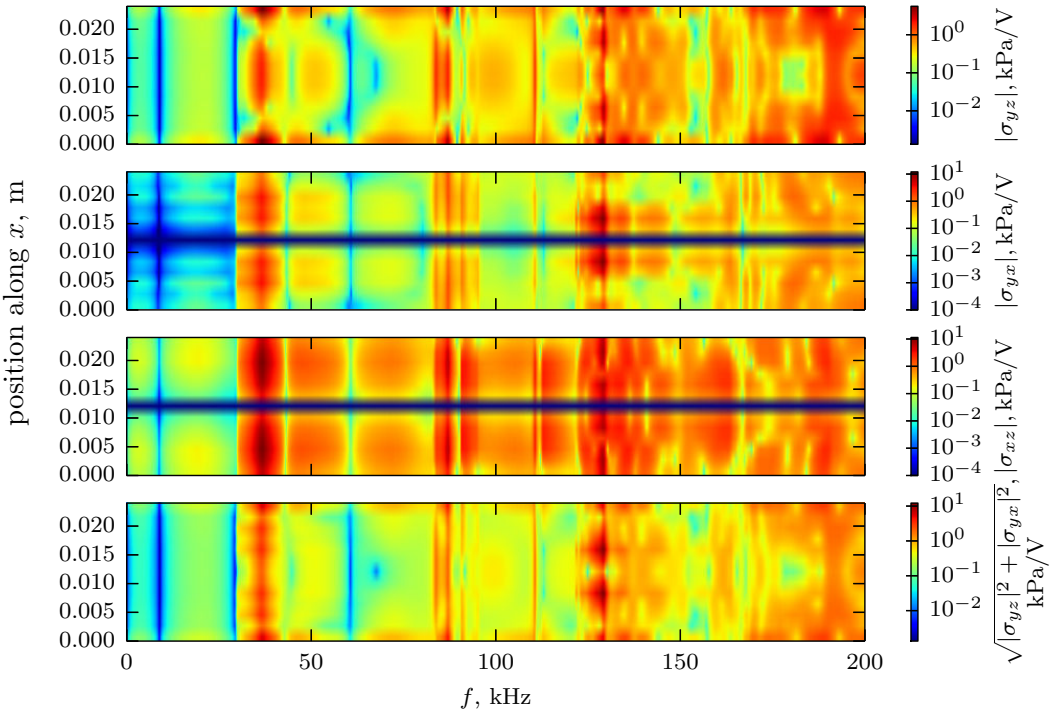

Figure 7.14: Cross-width interface shear stress distributions (components on the colourbars) against frequency for the beam as used in the experiment covered with 3 mm layer of glaze ice.

7.2 Influence of the parameters of the accreted layer on the generated interface stress

Given the numerical tools developed throughout the previous chapters, the influence of the properties (thickness and stiffness) of the accreted layer on stress generation is analysed in a more informed way. Both the effect of wave attenuation and the excitability of particular waves by the PZT actuator can now be addressed directly and not inferred as done in Chapter 2 and Chapter 3. The parametric study is performed on an infinite aluminium plate (2 mm thick) in plane strain equipped with a 5 cm long and 2 mm thick Noliac NCE40 actuator. The stress is extracted at 0.2 m from the actuator and the electrical power is calculated for a 20 mm wide strip (see Fig. 6.15a). Note that the structural configuration permits Lamb wave propagation only.

7.2.1 Thickness of the accretion

In the first part it is analysed how a growing glaze ice accretion affects the stress generation capability of guided waves. The thickness of the glaze ice layer is varied from 0.1 to 4 mm. The results for interface shear stress computed with reference to voltage, active

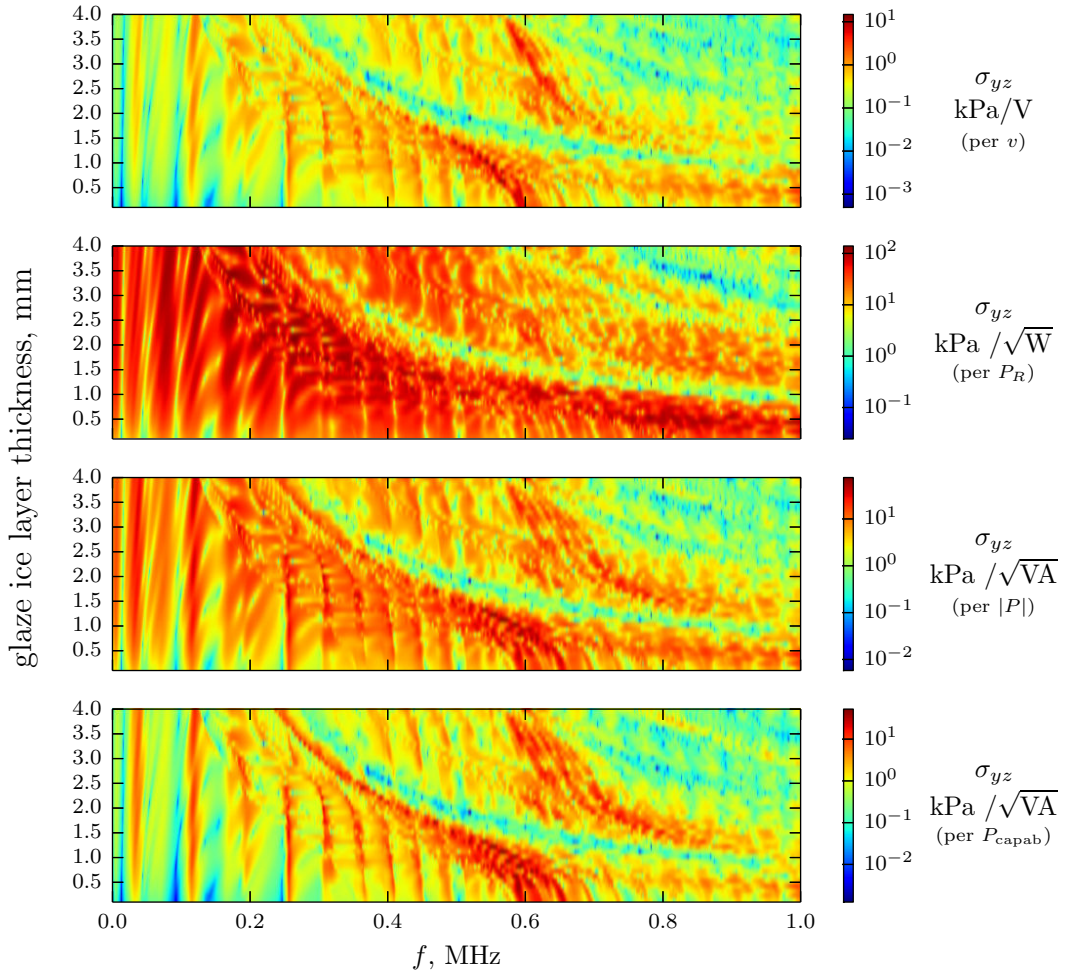

Figure 7.15: Interface shear stress as a function of a growing glaze ice layer on a 2 mm aluminium plate in plane strain with respect to different electric quantities. The structure is excited with a 5 cm long and 2 mm thick Noliac NCE40 actuator.

consumed power, apparent power and the capability of the driving source are shown on the colour maps in Fig. 7.15.

From a physical viewpoint the most useful is the graph scaled with reference to the active power, as it shows how the electrical power consumed by the actuator is used for generating stress. From a practical implementation viewpoint, the graph scaled with reference to the required source capability is the most informative, indicating how easy it is to generate stress with piezo-actuated waves given a standard ultrasonic source.

There are two main related factors that influence the effectiveness of the piezo-actuation for generating interface shear stress. The first is the characteristics of a particular wave field that does or does not invoke high stress at the interface. The second is the frequency dependent characteristics of the actuator and its relation to the electrical driving components which affects the efficiency of the excitation.

In the low frequency regime (up to the first cut-off frequency around 120 kHz for 4 mm thick icing) the thickness of the accretion does not alter the frequency distribution of the generated stress significantly (note the vertical stripes up to ca. 120 kHz). When ice grows the excited wavelengths change, therefore the precise locations of dips and peaks in this region vary with the build-up thickness.

The magnitude of the induced stress increases with the growth of the build-up layer. For example, at the peak region (red stripe) between 75 and 80 kHz one can achieve up to ca. 24 kPa/$\sqrt{\text{W}}$ for the 0.1 mm thick ice layer, and up to ca. 99 kPa/$\sqrt{\text{W}}$ for the 4 mm thick ice layer (with reference to active consumed power – see the second graph in Fig. 7.15). It is noted that according to Fig. 7.6, in this frequency range, the interface shear stress is predominantly generated by the flexural wave (A_0). Hence, the interface shear stress grows with the thickness of the accretion. This confirms that it is more difficult to remove thin ice accretions at low frequencies (before the first cut-off frequency).

The situation becomes more complex when higher-order waves are included. When excited near their cut-off frequencies, higher-order waves generate high interface shear stress, which can clearly be seen in the 'per v' graph of Fig. 7.15 (e.g. the red tongue originating from ca. 600 kHz at 0.1 mm thickness). This effect moves towards low frequencies when the accretion grows since the cut-off frequencies of the higher order waves shift towards lower frequencies with the growth of the accretion.

On the other hand, high deformation incurs high current requirements and hence high power consumption from the driving source. The interface stress is high as is the power consumed by the actuator. This is why on the 'per P_R' graph there is no substantial difference between the stress generated at low frequencies and that achieved near the cut-off frequencies if the reference quantity is the square root of active power.

The ice build-up has a relatively high loss factor (0.01), and therefore the energy loss increases with frequency and the thickness of the accretion. The 'per P_R' graph in Fig. 7.15 becomes lighter towards its top-right corner which corresponds to high frequency and large thickness. The electrical power consumed by the actuator is lost due to various dissipation mechanisms including growing wave attenuation. Although the ice loss factor was chosen arbitrarily to represent a medium damping that has been observed for ice experimentally, the results indicate that high ultrasonic frequencies are not suitable for removal of thick accretions.

A bigger picture can be drawn if one accounts for specific properties of the ultrasonic driving source. The electrical driving system's ability to deliver the desired active power to the actuator depends on the ratio between the impedances of both components and

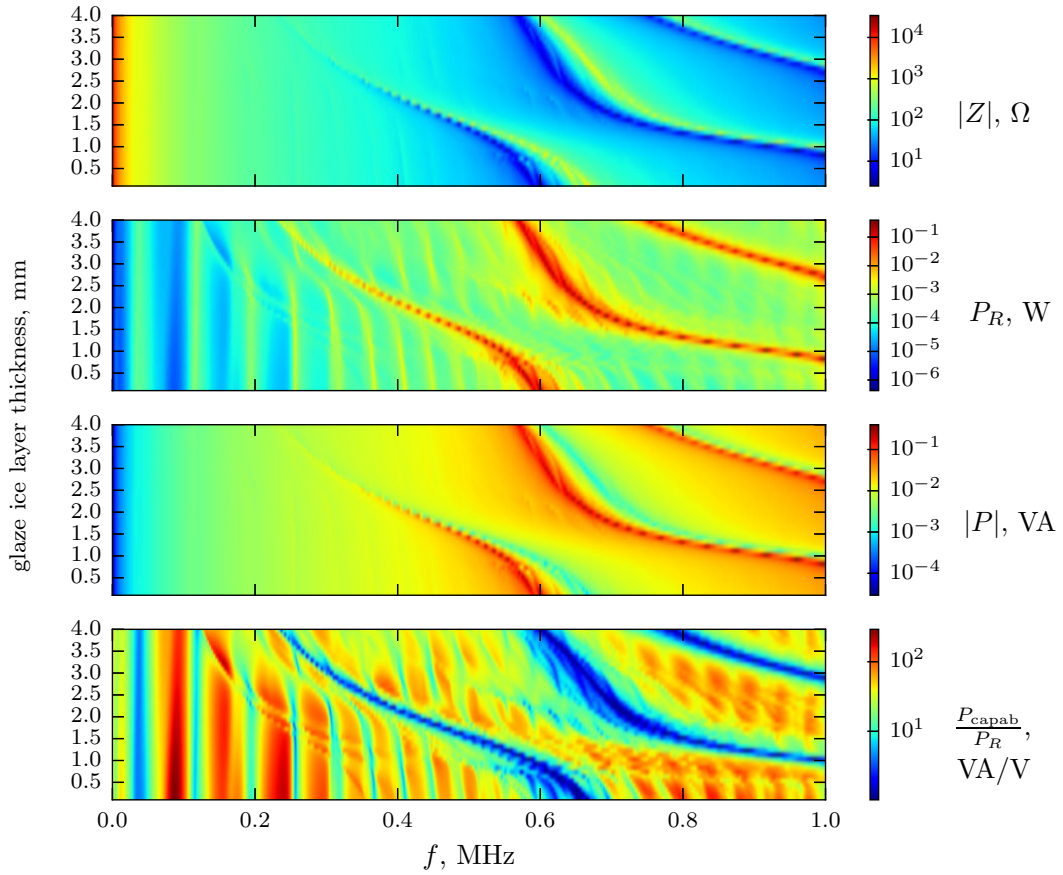

Figure 7.16: Electrical impedance and power quantities discussed in the chapter (reference driving voltage $v = 1$ V) as a function of frequency and thickness of a glaze ice layer growing on a 2 mm aluminium plate in plane strain. The structure is excited with a 5 cm long and 2 mm thick Noliac NCE40 actuator.

the reactance of the actuator. Matched impedances ensure that most of the available power can be utilised and hence that the capability of the source (very close to the power rating of the actuator) is nearly the same as the active power needed by the actuator. In this thesis an arbitrary value of 50 Ω is chosen for the driving source output impedance. This value corresponds to the standard with which most of the off-the-shelf ultrasonic amplifiers conform. The amplitude of the actuator is frequency dependent, therefore only at some frequencies its value can be close to the fixed output impedance of the source.

If the waveguide is infinite, the impedance of the actuator is usually high and predominantly capacitive unless close to the cut-off frequencies. Near the cut-off frequencies the actuator-covered section is in a planar resonance (i.e. the resonance of the cross-section with k=0), therefore both the impedance magnitude and its reactive part drop down. In order to exploit the characteristics of the cut-off frequencies, i.e. high associated

Table 7.1: The maximum interface shear stress achieved above the first cut-off frequency for a few thicknesses of glaze ice accretions.

ice thickness	maximum σ_{yz}	frequency
1.1 mm	71.7 kPa $/\sqrt{\text{VA}}$	467 kHz
2 mm	42.6 kPa $/\sqrt{\text{VA}}$	615 kHz
4 mm	24.2 kPa $/\sqrt{\text{VA}}$	503 kHz

interface shear stress and very low impedance, one would design the amplifier to have a specific output impedance that matches the structural response.

Even though the standard source output impedance is used in Fig. 7.15, the piezo-equipped structure is the easier to drive and more likely to invoke high stress near the cut-off frequencies. These effects are captured on the 'per P_{capab}' graph in Fig. 7.15. Interestingly, it shows that at high frequencies it is easier to remove relatively thin accretions. Some illustrative results corresponding to different ice thicknesses are gathered in Tab. 7.1.

Separating the two aforementioned effects (the wave field promoting high stress and low impedance of the actuator) is rather impossible since the electromechanical coupling makes them strongly dependent on each other. In order to facilitate the analysis, the impedance and corresponding electrical powers are plotted in Fig. 7.16. A very clear imprint associated with three higher-order waves can be observed in Fig. 7.16. The distinct tongues depict how the cut-off frequencies change with the thickness of the accretion. Note, however, that there are other higher-order waves propagating in the considered frequency range but they do not couple well with the electrical characteristics of the actuator at the cut-off frequency resonances. For a plane strain model, as the one used in the current study, only the cross-section resonances with predominant deformation in the thickness direction can be 'picked' by the actuator, because they couple with the electric field applied across the thickness.

7.2.2 Stiffness of the accretion

In the second part the influence of the stiffness of the accreted layer is assessed, assuming that the thickness is kept fixed at 2 mm and that the Young's modulus is varied between 0.1 and 10 GPa. The results of the study with reference to driving voltage, consumed power and the required 50 Ω amplifier capability are presented in Fig. 7.17. The whole stiffness range is divided into two linearly scaled sub-ranges: from 0.1 to 1 GPa and from 1 to 10 GPa.

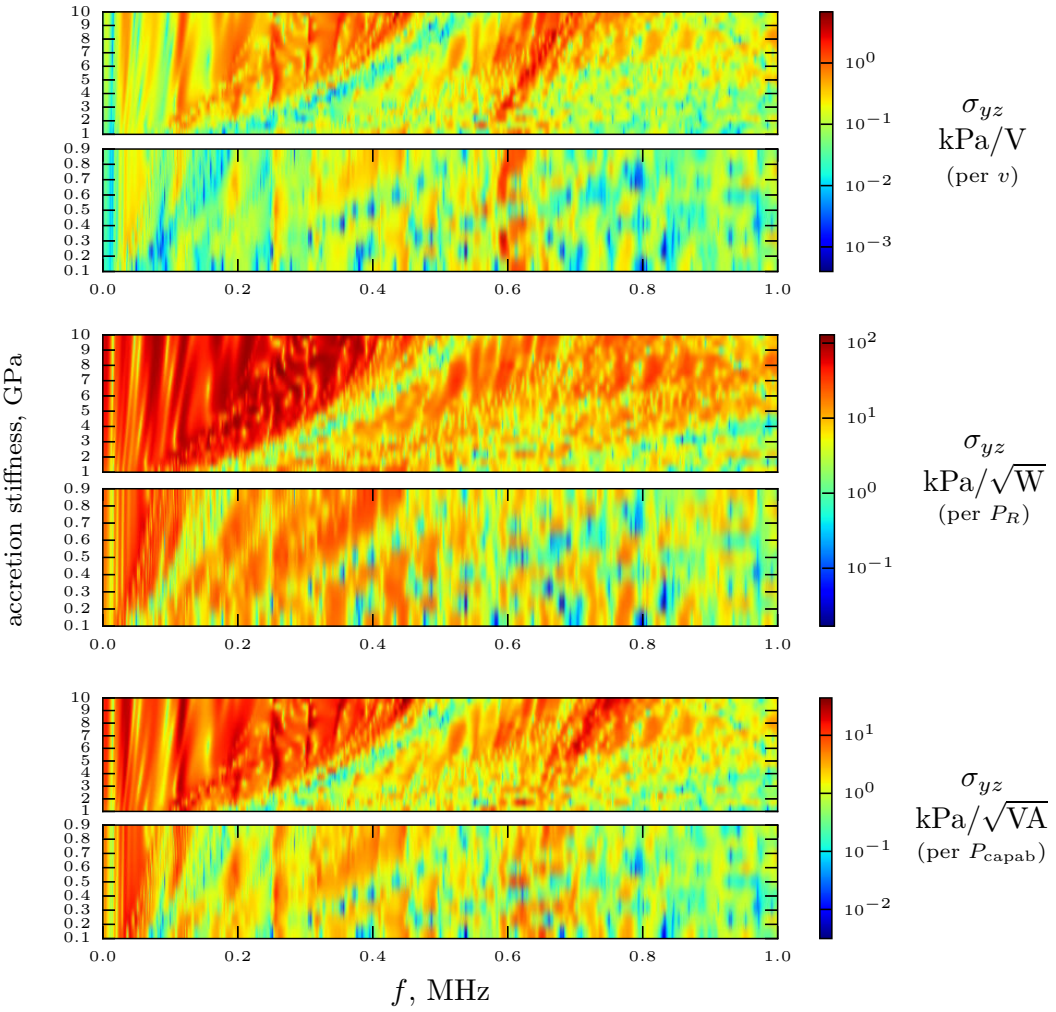

Figure 7.17: Interface shear stress as a function of frequency and build-up stiffness with respect to different electric quantities. The structure (2 mm thick aluminium plate in plane strain covered with 2 mm accretion) is excited with a 5 cm long and 2 mm thick Noliac NCE40 actuator.

In Chapter 2 an intrinsically physical analysis of the influence of the stiffness of the build-up was performed. It was shown that the lower the stiffness of the build-up is, the more strongly the host-accretion bilayer is decoupled. As a consequence of the decoupling, waves in such a waveguide are either originating from the free-free host (as if the accretion was absent) or from the clamped-free build-up. The former are more easily excited, but do not generate high interface shear stress, because the free-free asymptotes are associated with stress-free surfaces in the host. On the other hand, the build-up dominated waves are difficult to excite and highly attenuated which makes the ultrasonic action effective only at limited locations.

Some of these effects can be observed in Fig. 7.17. The generated stress drops significantly with decreasing stiffness of the accretion. One of the main reasons is that the

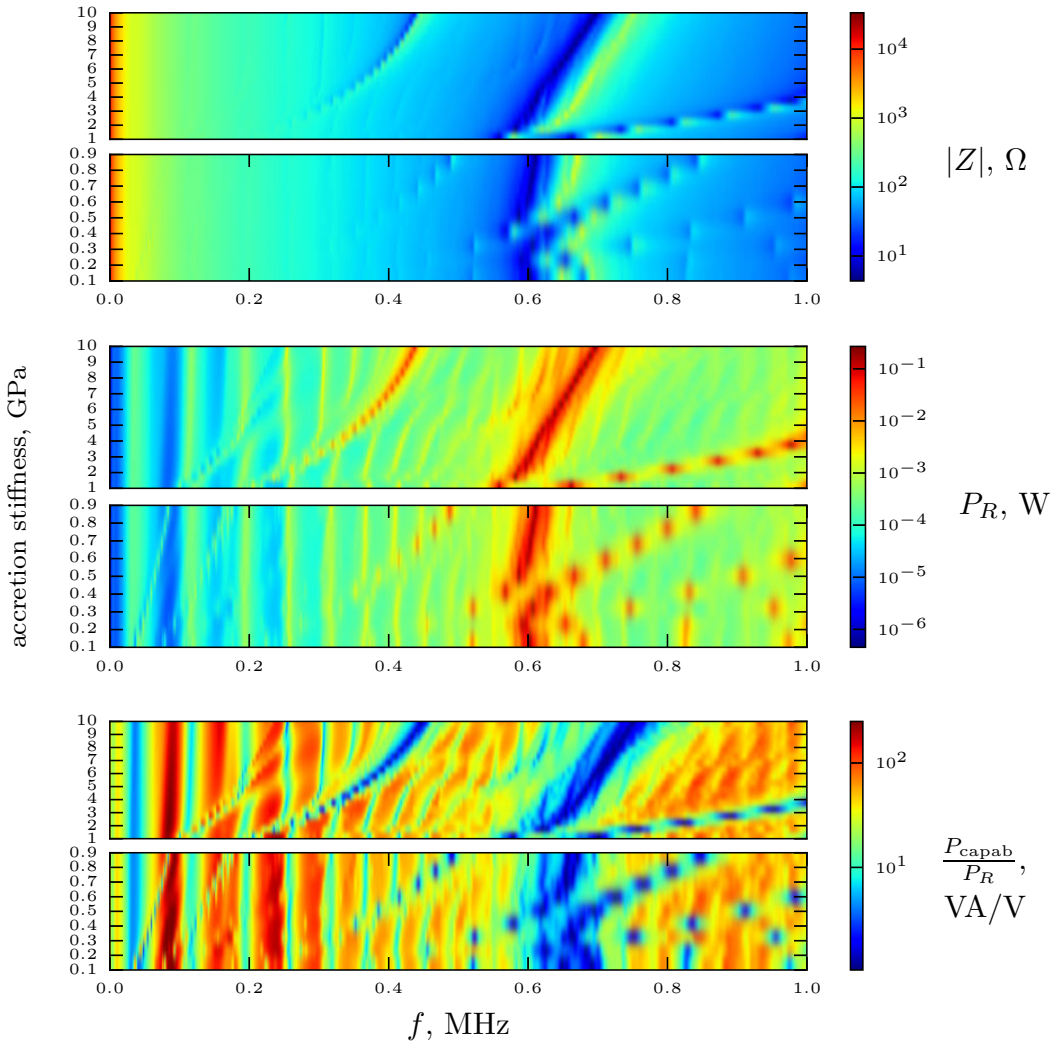

Figure 7.18: Electrical impedance and power quantities discussed in the chapter (reference driving voltage $v = 1$ V) as a function of frequency and build-up stiffness. The structure (2 mm thick aluminium plate in plane strain covered with 2 mm accretion) is excited with a 5 cm long and 2 mm thick Noliac NCE40 actuator.

build-up dominated higher-order waves that are associated with high wave attenuation cut off at low frequencies and absorb a large amount of the injected power. On the 'per P_R' graph in Fig. 7.17 the red region corresponding to efficient stress generation becomes narrower and lighter while moving down the accretion stiffness axis. Moreover, for the whole range of accretion stiffnesses, the stress generation efficiency diminishes while moving towards high ultrasonic frequencies.

Secondly, since the waves that are well excited are mainly host-dominated, the interface stress tends to zero with decreasing stiffness (decoupling of the layers). One can also observe the increasing number of stop-bands, i.e. frequencies at which the stress drops for low stiffness accretions due to high attenuation or layer decoupling at high frequencies.

From the viewpoint of the driving system, the interface shear stress for high stiffness build-ups can be generated efficiently at wider bandwidths. On the contrary, low stiffness build-ups require precise frequency tuning (narrow red regions on the 'per P_{capab}' graph in Fig. 7.17). Although it was said that the efficiency of the interface stress generation drops with increasing frequency, there is a group of 'red areas' around 600 kHz on the 'per P_{capab}' graph in Fig. 7.17 which covers most of the range of accretions. This corresponds to a cut-off frequency which enhances the impedance matching between the driving source and the actuator considerably. Therefore, even though the interface stress with respect to consumed power at those frequencies is not high, delivering such power can be relatively efficient for a standard ultrasonic source.

The associated electrical quantities are presented in Fig. 7.18 for reference.

7.3 Interface stress in a waveguide partially covered by accretion under piezoelectric actuation

Given the big picture on different aspects of using structural waves for invoking delamination outlined in the previous sections, the attention is now confined to the beam-like waveguide with a rectangular cross-section. It is of interest to examine the difference in the generated interface shear stress if the beam is only partially covered with accretion as opposed to the fully covered case considered up to this point. The geometry and structural configurations used for the computation are depicted in Fig. 7.19.

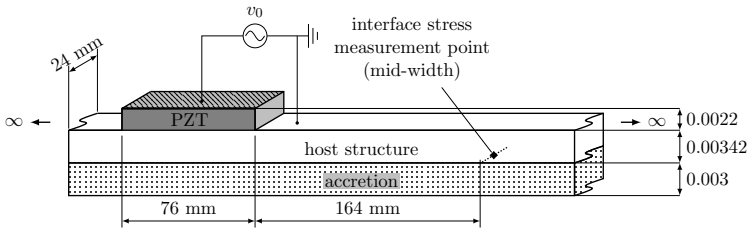

(a) fully covered

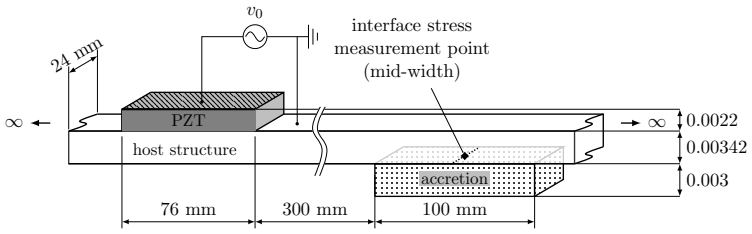

(b) partially covered

Figure 7.19: Structural configuration for simulations of interface shear stress in a beam-like waveguide fully and partially covered with glaze ice accretion.

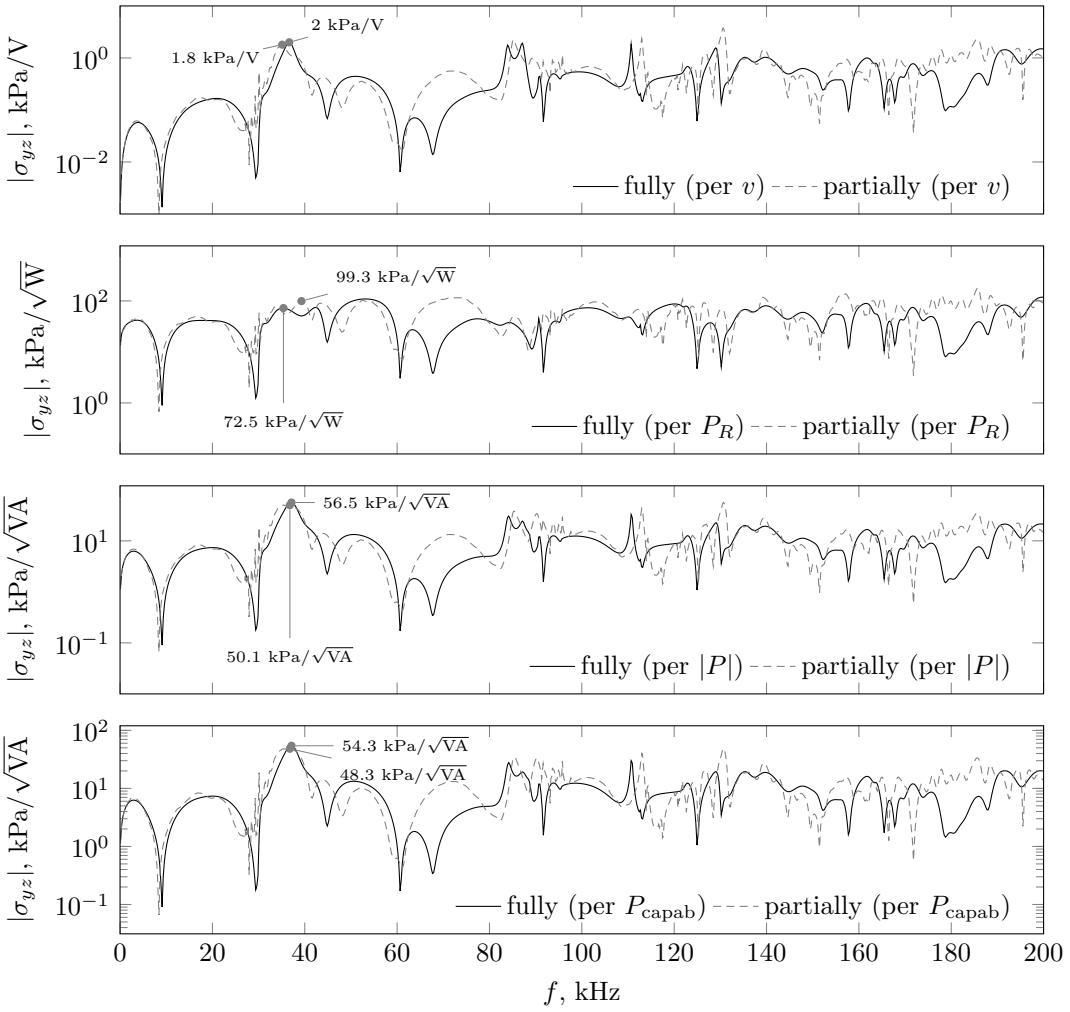

Figure 7.20: Interface shear stress in a waveguide (as used in the experiment) either fully or partially covered with 3 mm glaze ice accretion.

The comparison between the interface shear stress generated for the fully and partially covered cases is presented in Fig. 7.20. Maximum stresses occurring near the across-width resonance of the PZT-covered section are marked explicitly. The discrepancy between the two curves becomes significant from around 60 kHz. Up to that point the difference in acoustic impedances between the steel and steel-ice sections is small and most of the wave energy is successfully transmitted into the section with accretion. From 60 kHz upwards the wave conversion at the discontinuity becomes more complex and at some frequencies gives the advantage to the partially covered case. Note that for the partially covered case the section with the actuator is less stiff as it does not have the ice layer. As a consequence, the across-width resonance happens at a slightly lower frequency that for the waveguide fully covered with accretion.

The corresponding power requirements for de-icing assuming the ice bond breaking stress to be 1.5 MPa are shown in Fig. 7.21.

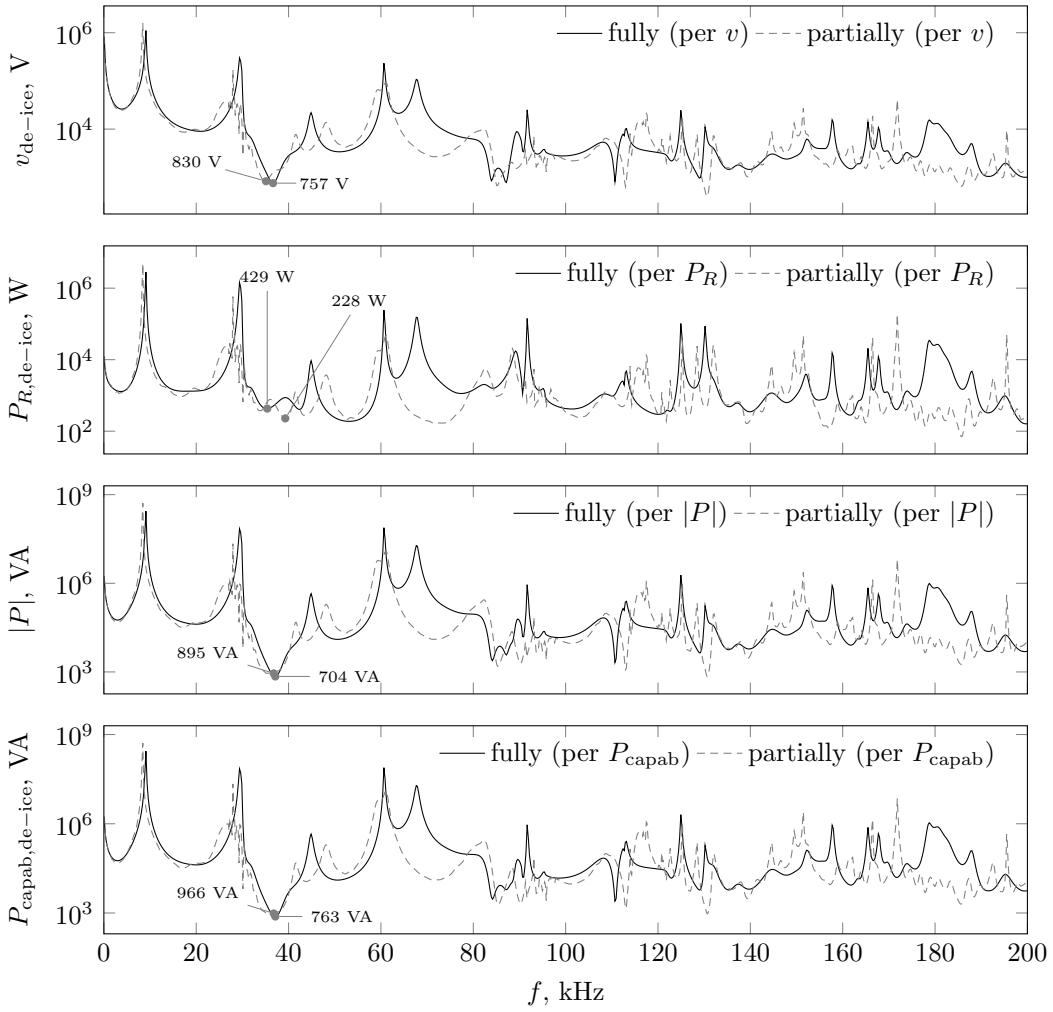

Figure 7.21: Voltage and power requirement for de-icing a waveguide (as used in the experiment) either fully or partially covered with 3 mm glaze ice accretion.

Throughout the thesis, the required driving source power capability (P_{capab}) is promoted as the most practical and indicative quantity describing electrical power requirements for removal of accretions with structural waves. However, one needs to keep in mind that P_{capab} is subject to the choice of the amplifier output impedance. In all the simulations presented up to this point the standard value of 50 Ω was adopted. On the other hand, it is noted that at most frequencies the required capability of the source is very close to the power rating of the actuator P_{app}.

7.4 Influence of the reflections at boundaries on generated interface shear stress

The results presented throughout this thesis are confined to infinite waveguides in which no reflections give rise to the interface shear stress. This rather conservative configuration was chosen, since the real-world structures exposed to accretions (e.g. aircraft panels) were observed to be highly damped due to mounting conditions (e.g. riveting) and wave leakage to the fuselage structure. However, in practice some reflections are almost always present and as seen in the experiments presented in Chapter 5 it is even very difficult to emulate perfectly absorbing conditions on purpose. Therefore, in this section the outlook for practical applications that accounts for reflections is discussed. It is shown how the achievable interface shear stress grows with decreasing absorption at the boundaries.

In order to do this, artificial simplified reflection matrices are used in the simulations for the beam-like waveguide partially covered with a 3 mm thick glaze ice accretion as considered in Section 7.3. The artificial reflection matrices are assumed to be diagonal and take the form

$$\mathbf{R}_{\text{art}} = (1 - \text{absorption})\mathbf{I} \tag{7.1}$$

where $\mathbf{I}$ is the identity matrix.

The form of the reflection matrices indicates that no mode conversion is allowed and that waves are reflected with no phase change, but only with the amplitude diminished according to the arbitrarily chosen absorption coefficient. The interface shear stress with respect to the active power and source capability for different levels of absorption compared with the infinite case are presented in Fig. 7.22. The beam is very long (6 m) so the resonances are very closely spaced. As expected, the line corresponding to the infinite beam is a mean (with in a moving frequency window) of each of the finite beam responses. The presence of reflections significantly facilitates achieving large interface stress. Illustrative results referring to the maximum achievable stress and corresponding power required to induce debonding (assuming ice breaking stress to be 1.5 MPa) around the 36 kHz peak are listed in Tab. 7.2. Note that the quantities presented in Tab. 7.2 were computed for a fixed frequency step, which may have caused the stress to be underestimated yielding overestimated power requirements. Nevertheless, they provide an informative indication on how the reflections (even if very small in amplitude) affect the electrical power requirements for de-icing.

Table 7.2: The maximum interface shear stress achieved between 30 kHz and 40 kHz for the beam partially covered with glaze ice as considered in Section 7.3 for different levels of wave absorption at the boundaries.

absorption at the ends	infinite (100%)	95%	90%	75%	50%	25%c	0%
$\sigma_{yz}/\sqrt{P_R}$ in kPa $/\sqrt{\text{W}}$	99.3	102.8	107.8	124.4	157.3	251.6	500.7
$\sigma_{yz}/\sqrt{P_{\text{capab}}}$ in kPa $/\sqrt{\text{VA}}$	48.3	52.1	56	69.9	102.3	148.7	269.4
$P_{R,\text{de-ice}}$ in W	228	213	194	145	91	36	9
P_{capab} in VA	966	830	717	761	215	102	31

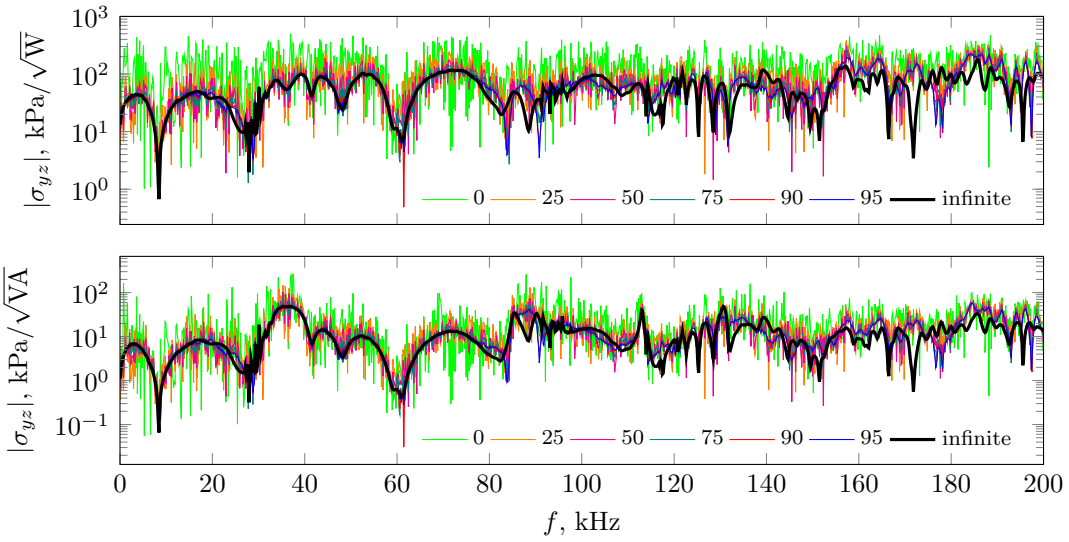

Figure 7.22: PZT induced interface shear stress in a waveguide with artificial boundary conditions; the values for the absorption coefficient are denoted in the legend.

7.5 Experiment on invoking delamination

In this final section of the chapter, the concept of accretion removal using piezo-actuated structural waves is demonstrated experimentally. Following the preliminary experiment reported in Appendix A, the accretion was modelled with a patch of building plaster. The plaster patches were built on the PZT-equipped beam-like waveguide with emulated infinite boundary conditions at some distance from the actuator.

The experimental arrangement is affected by many uncertainties and variabilities, of which the most important are the uniformity of accretion thickness, the rigidity of the bond between the beam and the patch and the properties of plaster when it is set. This is very close to real circumstances in which the ice layer thickness or properties do not form regular patches and are very far from being homogeneous and uniform, however it impedes quantitative comparison with predictions. The experiment serves as a demonstration of the technique, which needs to be specifically adjusted and tested for each particular problem case.

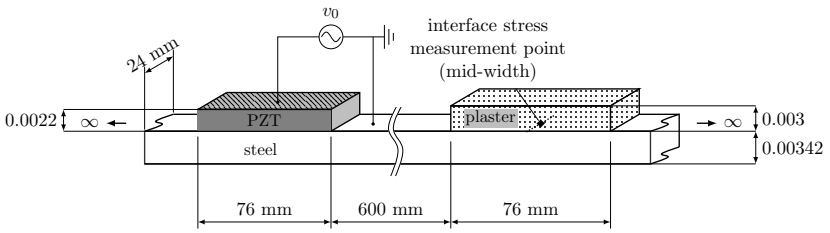

Figure 7.23: Structural configuration for simulations of interface shear stress in a beam-like waveguide covered with a plaster patch.

7.5.1 Interface shear stress in a plaster-covered beam

The experiment is first performed numerically. The interface shear stress induced by the PZT-actuator is simulated using the proposed computational approach. Plaster is treated as an isotropic material. The properties of the plaster are in general unknown and not measured here, but according to the report attached in Appendix A they are assumed as follows: the Young's modulus is 3 GPa, the density is 1000 $\mathrm{kg\,m^{-3}}$, the Poisson's ratio is 0.351 and the loss factor is 0.01. The strength of the bond created by plaster is assumed to be 0.24 MPa. The geometry and structural configuration for the considered case is shown in Fig. 7.23. For reference purposes the interface shear stress for a waveguide fully covered with plaster is also computed (with plaster layer on the opposite surface to the PZT).

The piezo-induced interface shear stress in a waveguide covered with a plaster accretion with respect to different power-related quantities is shown in Fig. 7.24. Up to around 60 kHz both partially and fully covered cases a similar level of interface shear stress is achieved. It is expected that at low ultrasonic frequencies the frequency dependent characteristic impedance of the accretion is considerably smaller that that of the host beam, therefore the waves pass through the accreted region almost unchanged. At higher frequencies, wave scattering at the boundaries of the patch plays a more significant role and makes the overall response more complex. Given the equipment available in the Dynamics Laboratory at ISVR the interest is confined to frequencies below 80 kHz. This also aids physical insight into the phenomenon as only a few waves are present.

The maximum achievable stress if referred to the driving source power capability in the lower part of the frequency range in Fig. 7.24 is associated with the first higher-order wave (across-width bending) that cuts off in the PZT covered section around 35 kHz. The corresponding values for all chosen power reference quantities around that peak are listed in Fig. 7.24. The frequency of the optimal electrical power transfer between the amplifier and the actuator is dictated by the electrical impedance of the actuator. The magnitude of the impedance magnified around its minimum is shown in Fig. 7.25.

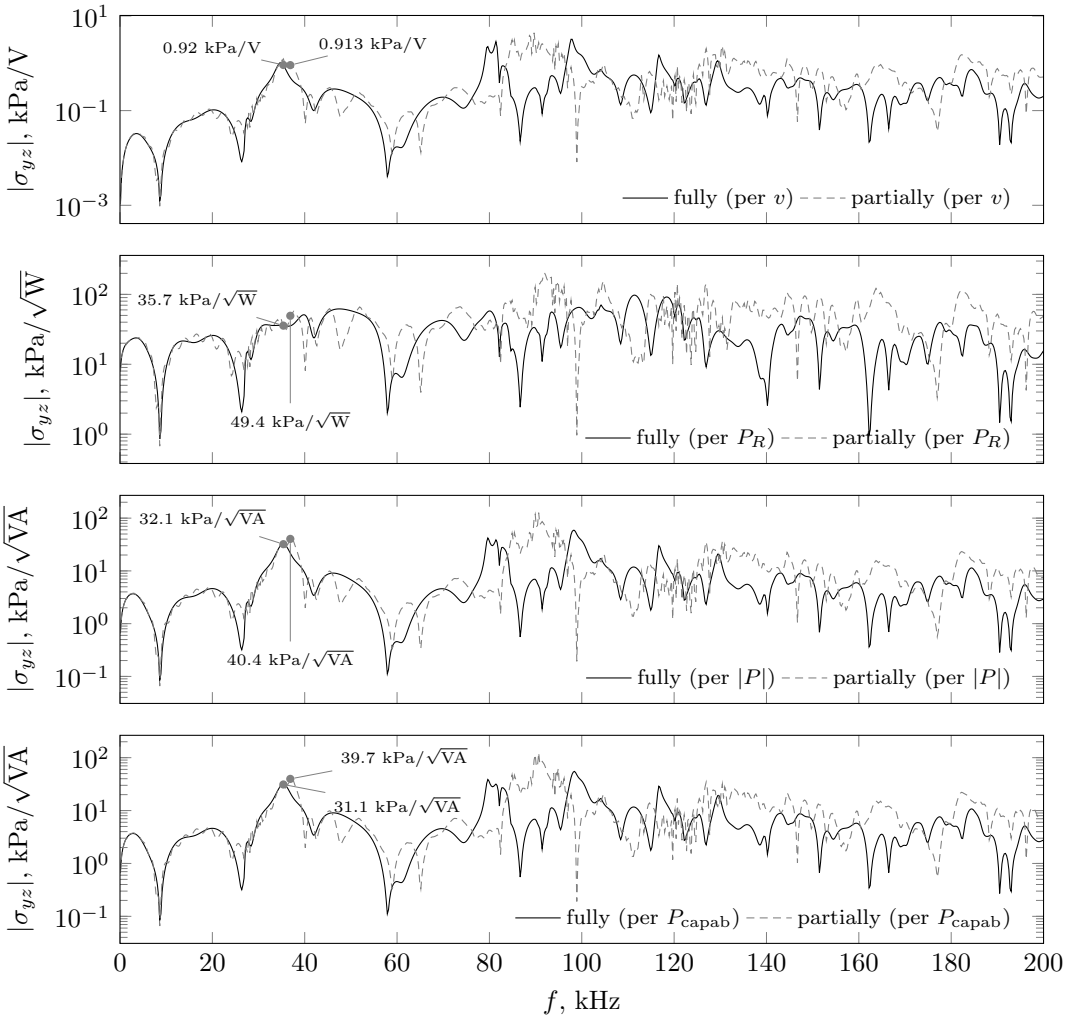

Figure 7.24: Predicted interface shear stress in a waveguide (as used in the experiment) either fully or partially covered with 3 mm plaster accretion.

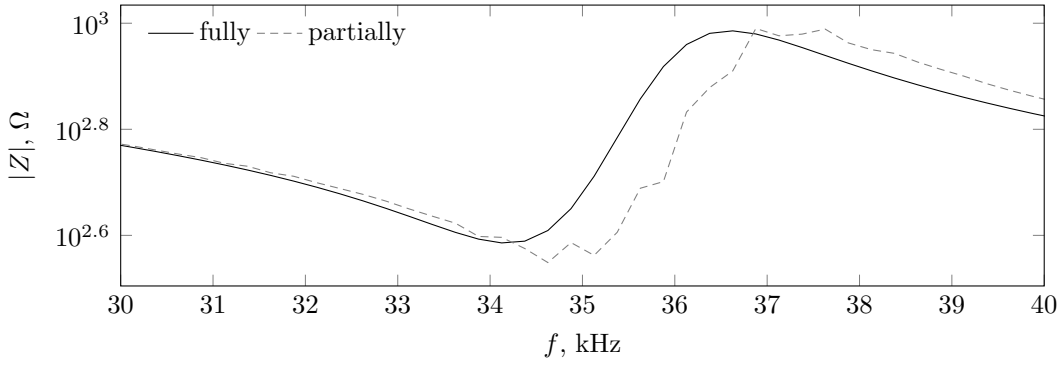

Figure 7.25: Predicted electrical impedance of the actuator bonded to the waveguide (as used in the experiment) either fully or partially covered with 3 mm glaze ice accretion.

The power requirements for the removal of the plaster with reference to the properties of the plaster inferred in Appendix A are presented in Fig. 7.26. As a representative value

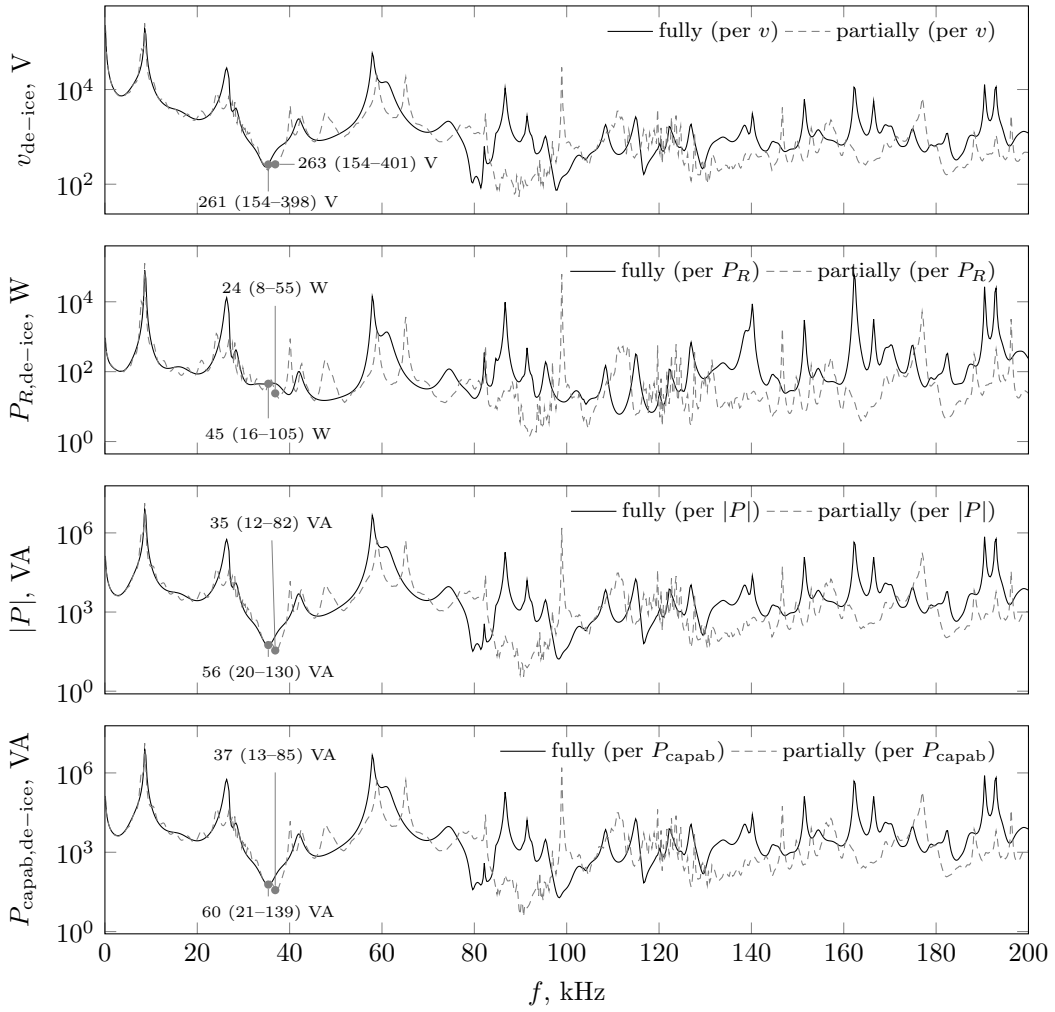

Figure 7.26: Voltage and power requirement for removing the plaster from the waveguide (as used in the experiment) either fully or partially covered with 3 mm plaster accretion. The values are calculated for the plaster bond strength as measured in the experiment (Appendix A) – mean: 0.24 MPa (min: 0.142 MPa, max: 0.366 MPa.

for generated interface shear stress σ_{yz} at the middle of the width is chosen. One could argue that, according to Fig. 7.14, including other stress components and analysing the stress along the whole width of the beam could significantly diminish the power requirements. It is true that at other locations, especially near the edges, the stress is expected to be as much as three times higher. On the other hand, the chosen strategy, yet more conservative, helps to ensure that the whole accretion is debonded. If one based the predictions only on the localised maxima, the structural waves could induce only localised delamination without shedding the accretion. The power requirements calculated for the mid-width point imply that the desired stress is achieved (and exceeded) at other locations across the width as well, which promotes build-up shedding.

The power requirements required to break the bond created by plaster (and assumed to

be $\sigma_b = 0.24$ MPa) in Fig. 7.26 indicate that the ultrasonic action can be successful if the actuator consumes 24 W of active power. It can be delivered to the actuator if the 50 Ω ultrasonic driving source is capable of producing 37 V A (and handle the impedance mismatch).

7.5.2 Experimental setup

The experimental setup for the delamination experiment is shown in Fig. 7.27. The actuator is powered by an RF amplifier from Electronics & Innovation Ltd. (1020L) which is driven by the signal from a TTi TGA1240 arbitrary waveform generator. The generator output impedance can be set to 50 Ω in order to match the 1020L amplifier input impedance. The amplifier is equipped with an LCD display on which the forward and reflected power readings are shown (the meaning of these quantities is explained in Section 6.2.2).

The output of the amplifier is shifted with a DC offset to ensure that the tensile stress within the actuator is minimised. Since PZT ceramics are much stronger in compression than in tension it is desirable to drive them predominantly in compression especially at high excitation levels to avoid tensile cracks (see [24] and Appendix A). Although a rectangular actuator is used here and the DC offset introduce tensile prestress in the width direction, it is not dangerous as the aspect ratio of the actuator is quite high (more than 3), but reduces the tensile stress in the length direction. A simple 'bias T' circuit is used to add the DC offset to the high amplitude signal and prevent feeding it back to the amplifier.

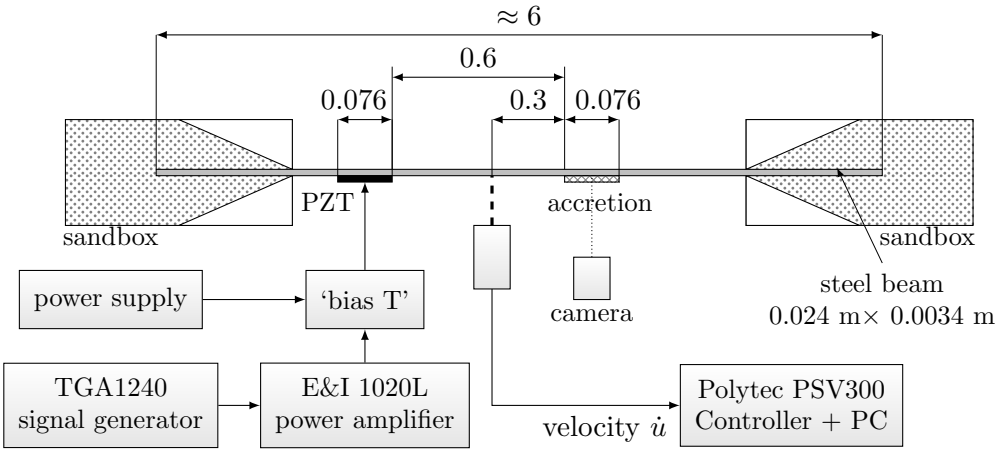

Figure 7.27: Experimental setup for the delamination test. Dimensions of the beam refer to the equivalent values discussed in Section 5.5.

The following experimental procedure was adopted. Firstly, at a low level of excitation the optimum frequency was sought for around the 35 kHz resonance (see Fig. 7.25). The optimal frequency was identified based on the active power delivered to the actuator as indicated by the amplifier's display. After the frequency had been tuned, the driving power was increased up to the point when plaster patch shedding was observed. The reader should pay attention to the following remarks. Firstly, note that the numerical results from the previous section were computed based on the assumed properties (Young's modulus and density) of plaster, which have not been rigorously identified as this is out of the scope of the thesis. Therefore the maximum stress frequency read from Fig. 7.24 serves as an indication only. Secondly, the wave absorption at the boundaries was not ideal in the experimental rig, therefore the delamination experiment is expected to benefit from the effect of reflections even f they are very small in magnitude.

For reference purposes, the surface velocity at a point equidistant from the actuator and the accreted patch was measured using a laser vibrometer for one of the experimental runs.

7.5.3 Experimental results

The delamination was attempted in different runs of which some conformed to the structural configuration showed in Fig. 7.23 and the others did not (e.g. more patches were placed on the beam). The results indicating the active (consumed) power at the instant of delamination are listed in Tab. 7.3, and illustrative video snapshots showing the patches shedding are presented in Fig. 7.28. Piezo-actuated structural waves were proven to be able to invoke delamination and remove model accretion.

After the patches had shed it was observed that some of them were only partially attached to the host beam, which made the debonding very difficult. Imperfect bond between the layers significantly diminishes the generated interface stress which results in higher power requirements.

Table 7.3: Consumed power at the successful delamination attempts. The readings for P_{FWD} and P_{RFD} assume the amplifier to have 50 Ω output impedance.

Run no.	P_{FWD} (amp LCD)	P_{RFD}	P_R	structural configuration
1	83 W	63 W	20 W @ 35.61 kHz	as in Fig. 7.23
2	52 W	32 W	20 W @ 35.32 kHz	as in Fig. 7.23
3	93 W	56 W	37 W	different from Fig. 7.23
4	130 W	81 W	49 W	different from Fig. 7.23
5	18 W	8 W	10 W	different from Fig. 7.23

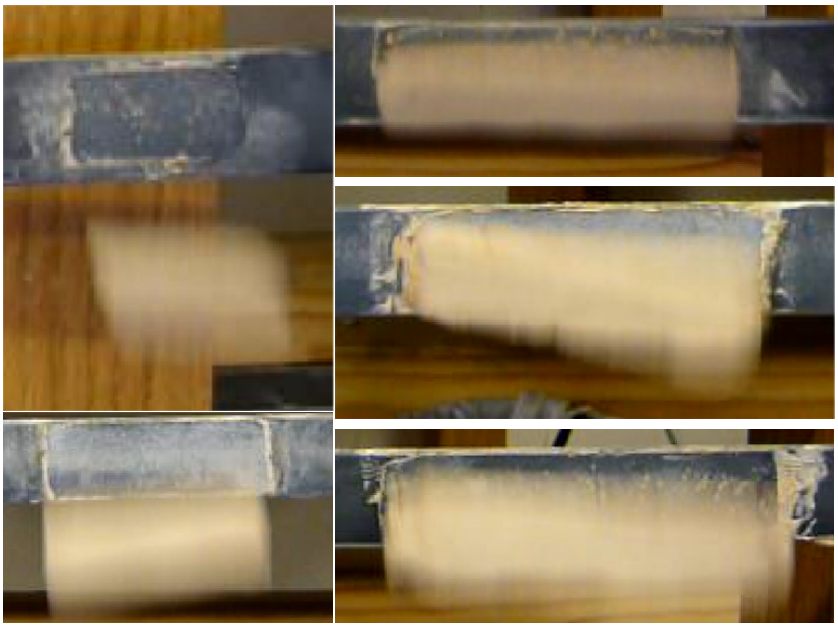

Figure 7.28: Video snapshots showing the plaster patches falling of the beam as a result of the ultrasonic actuation.

For the two runs for which the structural configuration was the same as in the simulations in Fig. 7.26 the active power consumption at the delamination was measured to be 20 W. The corresponding numerical simulation indicates a higher value of 24 W. Given the variability of the shear adhesion strength of plaster, these results seem to be in a good agreement. However, it is noted that the properties of plaster assumed in the simulation were not rigorously measured and that the numerical results assume a perfect bond between the patch and the host structure.

In order to further verify the link between the model and the experimental arrangement, the surface velocity of the beam was monitored during the delamination in run 1. (see Tab. 7.3.) The time history corresponding to the instant when the patch shed is shown in Fig. 7.29. The relevant numerical results computed using the developed wave model are presented in Fig. 7.30.

During successful delamination attempt 20 W of active powered was consumed. Using the data from Fig. 7.30 one can calculate that if the actuator is driven with 20 W of active power the surface velocity is 191.0 mm/s. The observed surface velocity is 432.7 mm/s, which is more than twice the prediction from simulation. This may be attributable to the residual reflections from the sandboxes which give rise to the response. Therefore, the interface shear stress generated by the 20 W ultrasonic actuation is expected to be twice as high as predicted by the model. At 20 W of active power the model predicts the shear stress of 0.16 MPa at the interface. If one follows the observation that response is doubled compared to the numerical prediction, the interface shear stress generated in

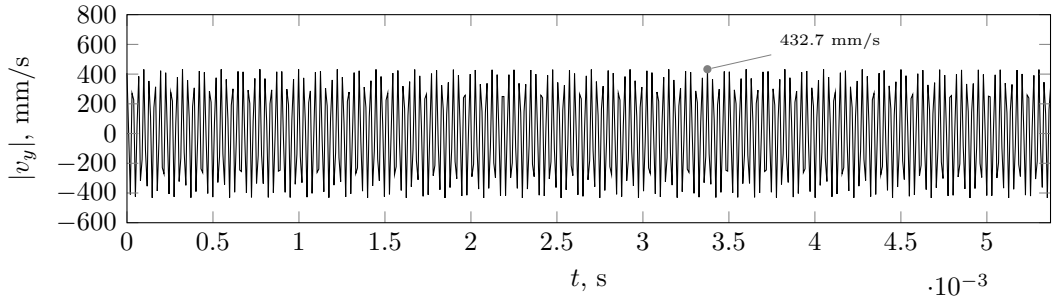

Figure 7.29: Surface velocity at the middle of the width of the steel beam recorded during the successful delamination attempt; real power consumption: 20 W.

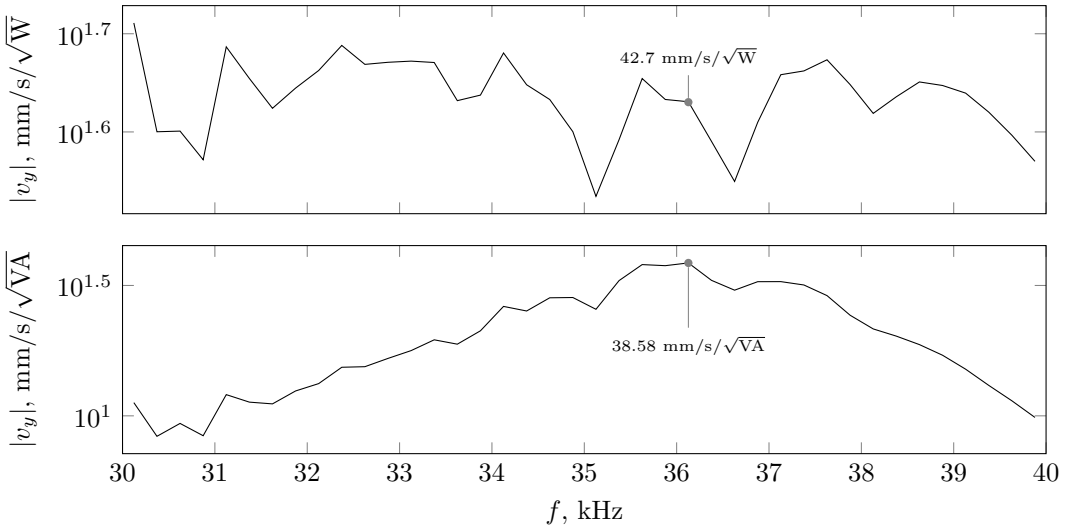

Figure 7.30: Surface velocity at the middle of the width of the steel beam - numerical results with respect to the active power and the power capability of the source.

the experiment was 0.32 MPa which is very close to the upper-bound values measured for plaster bond strength from Fig. A.7.

Given the aforementioned uncertainties in the experimental arrangement of which analysis falls outside of the scope of this thesis, it is acknowledged that piezo-actuated ultrasonic waves were demonstrated to be capable of removing surface accretion. The power requirements observed in the experimental demonstration were of an acceptable level and similar to those predicted by the numerical model (accounting for the differences explained above). This confirms that the modelling technique developed in this thesis can be useful for a class of problems requiring computation of high-power (yet still linear) piezoelectric actuation. Moreover, it shows the potential of high-frequency structural waves for delaminating unwanted build-ups.

7.6 Conclusions

In this chapter the modelling methodologies developed throughout the thesis were applied to the problem of invoking delamination using structural waves. The computational part focused on calculating the interface shear stress generated by piezoelectric actuation and referring it to the electrical power requirements. The stress recovery routine was validated with commercial finite element models for both a plane strain model and full 3D case. The transfer functions and *quasi*-transfer functions between the interface shear stress and voltage and power were presented and contributions from particular wave modes separated.

With the aid of the coupled-field wave model that enables modelling of the actuator including its full dynamics, a parametric study on the effect of the thickness and the stiffness of the accretion was performed. It was shown that low ultrasonic frequencies are better suited to thick ice accretions, whereas the thin accretions are more likely to be removed when the effects associated with the thickness resonance of the actuator are utilised. It was also confirmed that for low stiffness accretions it is difficult to achieve high interface shear stress at high frequencies unless around the thickness resonance of the actuator.

Referring to the practical cases in which often some reflections are present, the outlook for their effect is discussed. The reflections, even if very small, provide considerable boost to the interface shear stress and in consequence lower the power requirements. Since the stress is proportional to the square root of the electrical power even a small enhancement in the generated stress results in significant power requirements reduction.

The chapter is concluded with the experimental demonstration of the concept. Model accretions from plaster were attached to the beam with emulated anechoic terminations. Piezo-actuated structural waves were proven capable of removing the accretions for a few experimental runs. For some of the cases the numerical counterpart was simulated. The computed power requirements corresponded reasonably well with the power consumption associated with delamination observed during the experiment.

Chapter 8

Conclusions

8.1 Review of the thesis

Unwanted accretions on structures are a common machinery maintenance problem, which can pose a serious safety threat if not treated effectively and punctually. The foremost example of the dangerous build-up problem is aircraft icing, however this phenomenon affects many other types of structures such as pipelines, wind turbine blades or material handling systems. Traditionally unwanted build-ups here removed using e.g. chemicals, heat or mechanical cleaning. In recent decades researchers' attention has been directed towards more versatile and low-power systems that could either clean affected structures or prevent the accretion process. Among many interesting concepts the idea of employing the wave-based ultrasonic devices emerged in the aerospace context. Structural waves excited with surface bonded piezoelectric actuators were expected to invoke delamination and shed the unwanted material (in this case - ice). The power requirements of such systems were expected to be significantly lower than the traditional electro-thermal solutions.

Although substantial contributions to the field had been made by a few notable authors, there was still a gap between generic wave models' predictions and experimental work aided with finite element simulations on arbitrary finite structures. Several theoretical studies on the interface shear stress associated with wave propagation in structures with accretion can be found in the literature. However, they lack a direct link with the experimental validation. Since no wave-based model for representing high power piezoelectric excitation in waveguides was available at the time, the authors shifted the course of their analyses onto the ultrasonic vibration of finite plates that can be modelled using conventional FE. Successful attempts to invoke delamination with ultrasonic vibration were reported in the literature, yet the physical insight into the phenomenon was hindered

as the wave perspective was not available any more. A particular emphasis on wave viewpoint is additionally supported by the fact that in many relevant cases the wave leakage into the supporting structure is expected to introduce high radiation damping, largely diminishing the resonance peaks.

This thesis aimed at bridging this gap by keeping the wave-based nature of the approach from the preliminary theoretical analysis to the experimental demonstration. The chosen course helped to understand the conditions that promote high interface shear stress and to obtain realistic electrical power requirements for a piezoelectric actuator that enable excitation structural waves capable of delaminating the accretion. The thesis was constructed around two main research threads. The first was the assessment of the feasibility of the concept of removing accretions with piezo-actuated structural waves. The other was the development of the wave based modelling tools with growing complexity – from a free plane wave model for multilayered plates to a coupled field wave model for waveguides of an arbitrary cross-section excited with piezoelectric actuators.

The study started with the investigation into the physics of free wave propagation in multilayered plates aimed at understanding the conditions and phenomena that promote high interface shear stress (Chapter 2). A standard modelling methodology based on the partial wave technique and the global matrix method for system assembly was employed. Structures covered with accretions were treated as elastic bilayers, i.e. weakly coupled systems. The topology of the dispersion curves and asymptotic wave solutions were analysed and their significance for interface stress generation was discussed. Since many of the real world accretions are expected to be lossy, energy distribution and wave attenuation were looked at in order to specify the conditions under which waves may be ineffective in invoking delamination.

The thesis attempted to cover a broader perspective of unwanted build-ups. The influence of both the thickness and the stiffness (Young's modulus) of the accretion was assessed in a parametric study. The optimal wave modes for different build-ups were specified. The results were supported with the physical justification of the stress distribution in particular configurations based on the previous theoretical investigation.

The implications for practical application grounded in the free wave analysis provided only a qualitative insight. In order to broaden the perspective, the surface force excitation was introduced in the wave model in Chapter 3. The excitability based approach enabled analysing how the injected power is partitioned between the modes and how does it contribute to the interface shear stress generation. Based on the pin-force assumption, the approximate methodology for piezoelectric actuation was implemented and power requirements for sample structures are computed.

The adopted formulation had certain limitations from the viewpoint of the background application. The pin-force assumption limits the frequency range and the dimensions of the actuator as it assumes the interaction with the structure to be static. These restrictions cannot be met in power ultrasonics, where the intention is to induce high strain in the substrate and possibly operate near the resonance of the actuator. In order to circumvent these constraints, but also to enable modelling arbitrarily shaped waveguides, an alternative wave-based methodology (the semi-analytical finite element method) was implemented. The details of the formulation and the experimental validation for a force excitation were presented in Chapter 4. SAFE method is robust and can be applied to a wider range of waveguides since the cross-section can be arbitrary and material damping specified conveniently.

The aforementioned limitations of the common approximate models for piezoelectric excitation were overcome with the new methodology presented in Chapter 5. The approach was based on extending the SAFE formulation to include the piezoelectric coupling and invoking the inverse spatial Fourier transform to solve the distributed voltage excitation problem. This methodology enabled keeping the entire calculation in the wave domain but at the same time helped to overcome most of the limitations of the common approximate strategies which is particularly useful for applications where high power excitation is used (however nonlinear effects are not accounted for). The derivation of the piezoelectric semi-analytical element and the algorithm for calculating the wave response to a piezoelectric excitation are described in detail and experimentally validated on a beam-like waveguide with emulated anechoic terminations in Chapter 5.

Power transfer and conversion in waveguides excited with piezoelectric actuators is discussed in Chapter 6. The mechanical viewpoint was supplemented with the electrical perspective where the aspects of complex load driving and voltage wave reflection were included. The complete picture helped to understand the power requirements of a piezoelectric actuator and analyse how the electrical power is converted into mechanical wave power. The chapter was concluded with a parametric study which assessed the influence of the dimensions of the actuator on the power transduction.

Finally, in Chapter 7 the developed methodologies were applied to the problem of interface shear stress prediction in piezo-actuated waveguides with unwanted accretions. The stress recovery routine was presented and validated with a conventional finite elements package for a 2D and a 3D structure. The quasi-transfer functions that indicate the interface shear stress with reference to electrical power quantities were discussed. This enabled specifying the electrical power requirements for an illustrative waveguide covered with an ice layer. Furthermore, the final set of parametric analysis was performed assessing the influence of the properties of the accretion on the stress generation and

power transfer. The effect of the imperfect absorption at the boundaries was presented providing an outlook towards real world applications where some reflections exist even in a structure with highly absorptive boundaries. The final chapter was concluded with an experimental demonstration in which the patches made of plaster were successfully removed from a beam-like waveguide with emulated anechoic terminations with piezo-actuated structural waves. The concept of employing structural waves for delaminating surface accretions was proven to be feasible and effective.

8.2 Summary of findings

Interface shear stress generation in waveguides with unwanted accretions

The stiffness of accretions are often much lower than the stiffness of the structure. Therefore, waveguides with unwanted accretions were treated as elastic bilayers, i.e. weakly coupled systems. The typical characteristics of weakly coupled systems such as asymptotic solutions and mode veering were related to the problem of interface shear stress generation. It was shown that high stress is associated with build-up dominated waves as a consequence of the continuity condition at the interface. On the other hand these waves were associated with high wave attenuation if the accretion material is lossy. Therefore, the modal interface shear stress itself is not the optimal criterion for selecting wave modes for invoking delamination. Instead, one needs to consider both the interface shear stress and the associated wave attenuation. The parametric study that imposed a constraint on the analysed wave modes ensuring that no more than 60% of the energy propagates along the build-up was performed. It showed that for high stiffness accretion the flexural wave (A_0) is the most effective, whereas for low stiffness accretion the in-plane waves (S_0 and SH_0), which couple well with the build-up dominated modes at lower frequencies, are expected to provide better results.

Modelling the piezoelectric excitation including full actuator's dynamics

The newly developed methodology for modelling piezoelectric excitation in waveguides enables overcoming of common assumptions regarding the dynamics of the mutual actuator-structure interaction and the actuator itself and the bonding conditions. Thanks to the SAFE formulation the calculation is performed entirely in the wave domain so that the insight into wave composition of the response is retained. Moreover, the waveguide can have an arbitrary cross-section which was not achievable with the approaches known to date. With the aid of basic wave scattering relationships, an arbitrarily complex one-dimensional waveguide can be modelled using the presented approach. The

methodology was validated by an experiment on a beam-like waveguide with emulated anechoic terminations.

Power conversion analysis in piezo-actuated structural waveguides

The proposed wave model enables calculating the response to a high power excitation (assuming no nonlinear effects) with thick piezoelectric actuators. This facilitated the power conversion analysis. It was shown how the power provided by the excitation is partitioned among the propagating waves, and more generally how the electrical power is converted into the mechanical wave power. The power transfer is directly related to the complex and frequency dependent electrical impedance of the piezo-equipped structure and the electrical power transfer between the driving source and the amplifier. An actuator bonded to an anechoic waveguide usually shows high electrical impedance over a broad range of frequencies, the optimal transfer is observed at the cut-off frequencies of the higher-order waves. From a practical viewpoint, the ability to deliver particular power to the actuator is a major issue as impedance mismatch and hence voltage wave reflection occurs. Therefore, the required power capability of the driving source is identified as the most practical reference quantity when analysing power conversion. It is noted that the required power capability of the source is very close to the power rating of the actuator represented by apparent power. Finally, it was shown how the dimensions of the actuator affect the effectiveness of the power transduction (in the case of Lamb waves in a plate).

Application of the coupled-field wave model to interface shear stress prediction

The proposed coupled-field wave model was applied to the problem of interface shear stress prediction. The stress recovery routine was successfully validated with commercial finite elements package. The *quasi*-transfer functions relating stress to different power quantities (active power, apparent power, required capability of the source) were computed and presented. In particular, two structural configurations were used – a 1D cross-section referring to plane Lamb waves and a 2D cross-section referring to structural waves. In the light of the above the influence of the properties of the accreted layer was discussed. The model was shown to be a versatile tool for predicting interface shear stress and the electrical power consumption in the wave domain.

Experimental demonstration of accretion removal using structural waves

The concept of removing unwanted accretions using piezo-actuated structural waves was demonstrated experimentally. Patches made of a model material (plaster) were placed on a beam-like waveguide with emulated anechoic terminations. The attached piezoelectric actuator was excited near the first cut-off frequency, and the excited higher-order wave was successful in delaminating the patch. The experimental arrangement allowed recording the electrical power (active) consumption during the ultrasonic action. The experiment was supported with simulations and the numerical predictions were found to be in a good agreement (given the uncertainties in the configuration and the fact that the properties of plaster were assumed arbitrarily).

8.3 Future work

This thesis has investigated various physical aspects of piezo-actuated structural waveguides relevant to employing them for removal of unwanted accretions. The following suggestions indicate the future work directions which can be grouped into two sets:

- Modelling and concept
  - The numerical examples in this thesis were limited to flat structures. The methodology could be extended, in order to facilitate modelling waveguides with a curved cross-section (such as the leading edge profile or pipe wall).
  - The influence of the quality of the bond between the host structure and the accretion could be analysed. It is expected that weakly attached accretion would be difficult to remove as the achievable interface stress would be largely diminished.
  - Different types of actuators could be included in the study. This is expected not to require significant modelling work (at least for monolithic PZT), but only appropriate formulation and orientation of the matrices related to the piezoelectric material. It would also be advantageous to include other actuators (such as Macro Fiber Composite) in the model and validate it experimentally.
  - The wave-based formulation has the potential to be extended to a larger class of structures (e.g. two-dimensional wave propagation). This extension would contribute to modelling plate like structures, e.g. aircraft panels with accretions. It is also desired to extend the piezoelectric formulation so that it could model excitation of waves with PZT disk actuators.

  - The wave model could be optimised both from the formulation and the implementation viewpoint. Firstly, higher-order approximating polynomials on a non-uniform grid could be implemented (as in SFEM) which is expected to reduce the size of the matrices. Secondly, various properties of the system could be exploited to simplify the code and enhance the speed of computation. This task opens also a question on efficient algorithms for solving sparse quadratic eigenvalue problems, which could contribute to the optimisation considerably.
  - Various optimisation strategies such as a specific arrangement of the actuators or structural modifications could be investigated in order to reduce the power requirements.
  - In this thesis only the single frequency steady-state excitation was considered. The effect of transient excitation in time-domain using the developed model and inverse Fourier transform could be further examined, as in the light of the recent literature it might provide higher interface shear stress.

- Experiments

  - The experiment in the last chapter of this thesis has a demonstrative character. Due to the uncertainties and rough parameter estimation it cannot serve as a strictly quantitative argument. Dealing with these issues was not in the scope of this thesis, however it is crucial from the viewpoint of moving the concept towards a practical application. Therefore, the next step would be to conduct a more rigorous experimental campaign in which the properties and the dimensions of the accretion would be identified and kept fixed during a large number of experimental runs. The experiment would also include more materials, particularly different types of accretions.
  - The experiments could be also conducted on curved profiles such as the leading edge. The possibility of using Macro Fiber Composite actuators for invoking delamination could then be also assessed.
  - Emulating infinite waveguides sets the investigation in the worst-case scenario when the reflections do not enhance the generated interface shear stress. The experiments on a real-world riveted structures with highly absorptive boundaries would help to refine the power requirements.

Appendix A

Preliminary experiments for ultrasonically invoked delamination

A.1 Aim of the experiment

An informative assessment of the feasibility of a wave based method for invoking delamination is difficult since the effect of the ultrasonic action is binary: the accreted layer falls off or not. Therefore, in order to design and conduct a comprehensive experimental campaign a few questions and issues need to be answered, preferably empirically: (i) how much electrical power is needed to obtain a desired effect; (ii) what are the challenges of complex electrical load driving; (iii) what easy to handle material can be used in lab conditions to represent an unwanted build-up; (iv) what are the optimal parameters of the actuator. In order to address these issues a preliminary set of experiments was performed on a square plate with a PZT disk actuator similar to the one used in [21]. Although most of the theoretical work done up to date was focused on the effects associated with propagating waves, a finite plate was chosen for preliminary tests for a few reasons. Firstly, it facilitates achieving delamination since we benefit from multiple reflections of waves at a resonance. Moreover, it helps to address most of the aforementioned issues with a reference to similar experiments done in the past and presented in the literature.

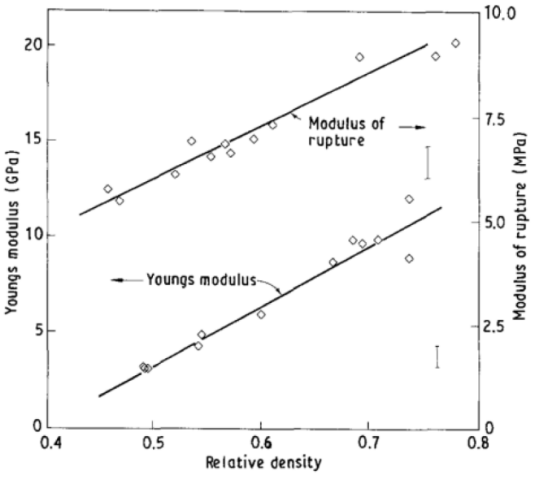

(a) Young's modulus of plaster [144].

Young's Modulus, GPa	from 2.5 to 8.3
Density, kg/m^3	from 600 to 900
Poisson ratio	0.351

(b) Mechanical properties of ice.

Figure A.1: The comparison of the fundamental mechanical properties of plaster and ice.

A.2 Procedure

A.2.1 Model material

In previously recalled references the experiments were performed on a plate with ice of which removal is one of the most significant possible applications of the concept. However, ice is not easy to work with in the laboratory conditions where it is required to conduct numerous sets of experiments with easily changeable configurations. In order to overcome the technical problems involved with ice, building plaster was used as a model material. Plaster is commonly used for similar reasons to simulate e.g. kidney stones, since it is easy to manufacture and reasonably controllable [145]. Its Young's modulus is in the range close to ice properties [144] (see Fig. A.1a) which are recalled for reference in Table A.1b.

A.2.1.1 Plaster preparation

Two types of plaster mixes were used in the experiments: one with 73% of dry plaster (mass content), and another with 62% of dry plaster (mass content). The procedure of preparing the mixes was repeated with attention to ensuring the same conditions. The aluminium plates prior to placing the plaster patches were carefully cleaned, roughened with a fine sandpaper and degreased. Patches were formed in the same locations (Fig. A.2a) for each plate and each iteration of the test and up to the same thickness within

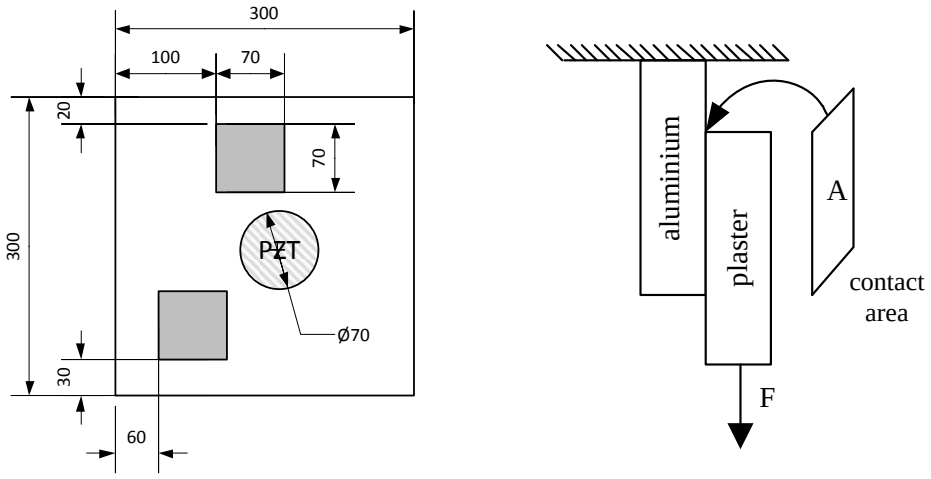

(a) (b)

Figure A.2: Plaster patches location and dimensions (a) and shear adhesion strength measurement (b).

the feasible accuracy ($\approx$ 4 mm). They were left for 24h to set before performing the experiments.

A.2.1.2 Static shear adhesion strength measurement

In order to evaluate the shear adhesion strength of plaster-aluminium bond, a simple lap shear test has been carried out. The aluminium plate's surface was prepared according to the procedure mentioned above. While forming the plaster patches, they were equipped with a metallic element enabling application of a load. The plate with plaster patches was fixed to a rigid frame vertically, so that the load could be realised as adding mass to a metal holder attached to a plaster patch (Fig. A.2b). After the patch had debonded upon a sufficient load the area of contact was measured. Knowing the breaking load F and the contact area A, the breaking shear stress τ was calculated as:

$$\tau = \frac{F}{A} \tag{A.1}$$

It has to be emphasised that although special attention was paid to ensure the same mixing procedure and surface condition for all samples, this test should not be taken as rigorous quantitative bond strength evaluation. The results are rather to be interpreted as an indication or an informed estimate within given uncertainties.

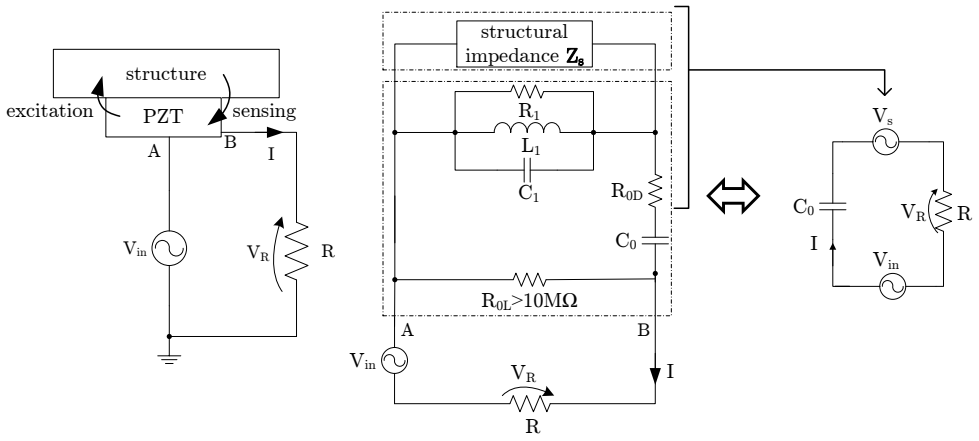

Figure A.3: Principle of impedance monitoring and loaded PZT transducer equivalent circuit.

A.2.2 Electrical impedance measurement

Electrical impedance (EMI is the common abbreviation since sometimes it is called an electromechanical impedance) measurement is widely used in structural health monitoring to capture the dynamic response of a system and assess its state[80]. Impedance can be easily captured using an impedance analyser. However this is a costly device and for many applications, simpler methods can be used. To evaluate electrical impedance, voltage and current waveforms have to be recorded. Then, they can be post-processed (FFT) using any capable device. The voltage can be measured directly at the amplifier, whereas the current is retrieved from a voltage drop across the known sensing resistor R (see Fig. A.3). The coupled PZT-structure impedance is denoted here by Z_{coupled}. From a viewpoint of a measuring circuit, the equivalent circuit from Fig. A.3 can be thought of as the complex impedance Z_{coupled} in series with the sensing resistor R. The current flowing through R is equal to:

$$I = \frac{V_R}{R} \tag{A.2}$$

Knowing the voltage sources and impedances we can write Ohm's law for the whole circuit as:

$$V_{\text{in}} + V_s = (Z_{\text{coupled}} + R)\frac{V_R}{R} \tag{A.3}$$

From (A.3) one can find the coupled impedance Z_{coupled}:

$$Z_{\text{coupled}} = R\left(\frac{V_{\text{in}} + V_s}{V_R} - 1\right) \tag{A.4}$$

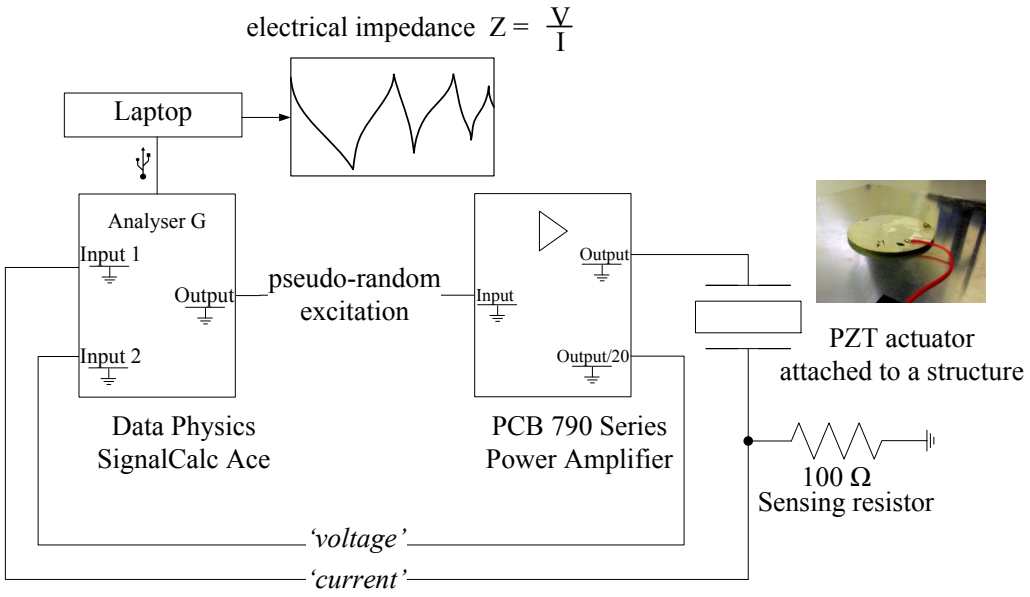

Figure A.4: Impedance measurement setup.

It is important to notice that voltage V_s is caused by V_{in} since the transducer is sensing vibrations excited by itself. Equation (A.4) shows that the information about structural response is embedded in the measured electrical impedance of a PZT [80].

Prior to forming any plaster patches on the plate and before each invoking delamination attempt the electrical impedance of the PZT actuator was recorded. The diagram of the measuring system is shown in Fig. A.4. A Data Physics Quattro Analyser was used to drive the actuator and to acquire and post-process the signals (Transfer Function module). A standard signal analyser used in structural dynamics is a cost-effective alternative for the costly impedance analyser. The voltage signal was captured directly at the power amplifier that provides an 'OUT/20' output. The current is measured indirectly as a voltage drop across a sensing resistor. The value of the resistor should be chosen carefully to compromise between a good signal-to-noise ratio (high resistance preferred) and a distortion of the measured impedance (low resistance preferred). For experiments described in this report the value for the sensing resistor was chosen to be 100 Ω.

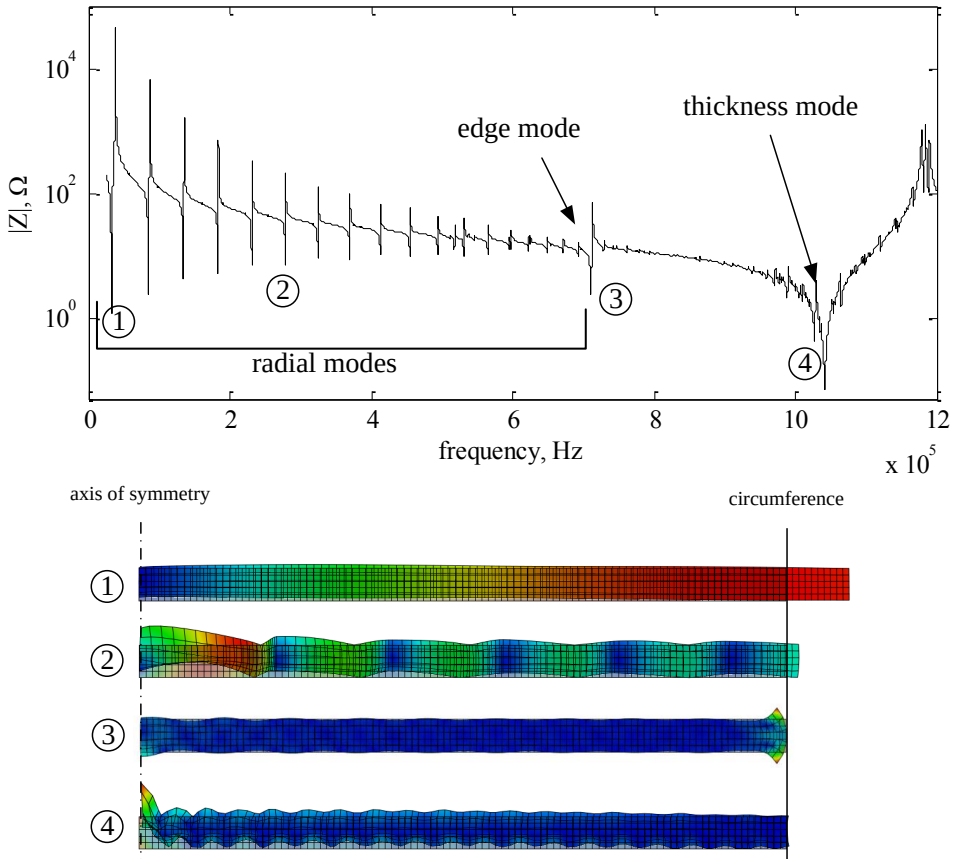

Figure A.5: Vibration modes of a PZT disk actuator.

A.2.3 Actuator

During the experiment the structure was excited using a PZT disk actuator. Disk actuators work in a so-called d_{31} mode experiencing high in-plane radial deformation and hence inducing large in-plane strain in a host plate. The impedance of the disk as used in the experiments together with a few mode shapes computed with an FE axisymmetric model in ABAQUS is shown in Fig. A.5. A series of radial, narrow resonance dips which are of greatest interest for this application comes first, then the edge mode, and the first thickness mode (wide dip). The fundamental radial mode (labelled with 1 in Fig. A.5) occurs at around 30 kHz.

The geometrical parameters of the actuator affect its dynamic behaviour as follows [79]:

- diameter (D): the first radial resonance frequency depends on D. Knowing the frequency constant (N_p) of the material provided by the manufacturer, the approximate radial resonance frequency can be calculated as $f_r = \frac{N_p}{D}$. Moreover, the

higher the D-to-thickness ratio, the larger the in-plane strain can be generated by the disk at a given electrical field.

- thickness (t) as mentioned above the D-t ratio influences the efficiency of exploiting the d_{31} effect of the piezoelectric material. However, the deformation depends on the electric field in the material. Therefore, for a fixed D, thicker actuator would require higher voltage to generate the same strain.

When the actuator is bonded to a plate, its impedance incorporates also the dynamic response of the structure. The modes originating from the actuator are dominant in the magnitude of the impedance but they get shifted in frequency due to coupling to an external dynamic stiffness. The modes originating from the structure are more clearly visible in the real part of the impedance. In order to get the maximum possible response the actuator will be excited at the strongest resonance.

A.2.4 Invoking delamination test

An experimental setup for the invoking delamination test is shown in Fig. A.6. The driving signal from the generator (set to be loaded with 50 Ω) was amplified by an RF amplifier from Electronics & Innovation (1020L). This amplifier is able to provide constantly up to 200 W power at frequencies from 10 kHz to 5 MHz. In addition to that the amplifier has a display on which the figures of forward and reflected powers are

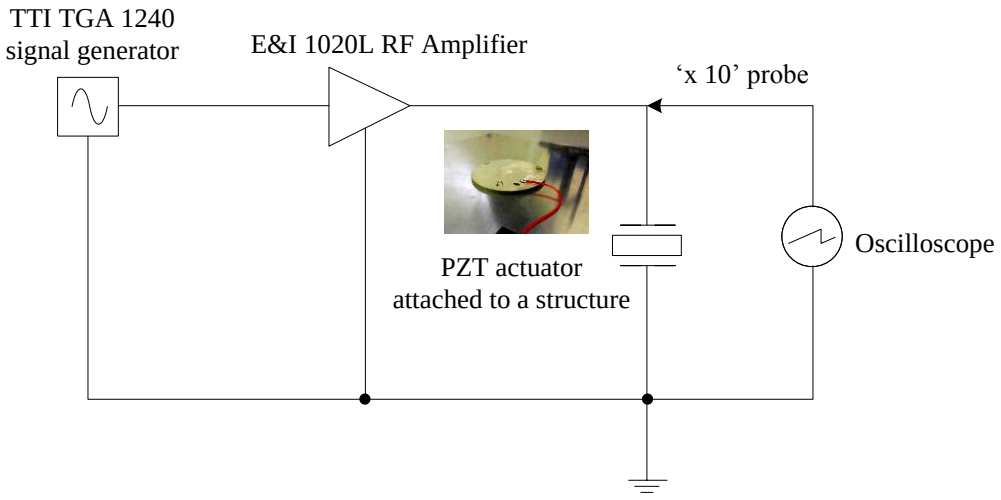

Figure A.6: Experimental setup for invoking delamination tests

No.	Outside diamater, mm	Thickness, mm	Material
1	69.85	1.75	PZT 403, Morgan Electro Ceramics
2	70	3	PZT 802, Morgan Electro Ceramics
3	70	3	PZT 802, Morgan Electro Ceramics

Table A.1: Actuators used in the experiment.

presented. These figures have been explained together with a common misconception in section 6.2.2. The voltage across the actuator was monitored using an oscilloscope during operation.

Initially, at low power input an excitation frequency was set as either read from the impedance graphs or selected after sweeping manually in a chosen range. The presence of the resonances was observed 'live' while frequency sweeping as a voltage drop on the oscilloscope or as lowering of the reflected power indication on the power amplifier display. Then, the power was increased (by increasing voltage on a signal generator within a specified range from 0 to 1 V_{rms}). For some cases the resonance was retuned at high power input, since the response of the structure seemed to have changed. This was repeated until the patch was debonded or no effect was observed at the highest power input available.

The test was conducted on three 1 mm thick aluminium plates with three disk actuators bonded using a conducting, silvered epoxy. The dimensions and material reference of the actuators used is presented in Table A.1.

A.3 Results and discussion

A.3.1 Static shear adhesion strength

Shear adhesion strength test results are shown in Fig. A.7. Two different plaster mixes were tested: samples 1-10 as in Fig. A.7 were made of 73% plaster mix, and samples 11-13 were made of 62.5% mix. For all cases the adhesion strength of plaster to aluminium is within the range between 0.142 and 0.366 MPa. No significant effect of changing the mixing ratio was observed. Moreover, it seems that the overall variability of the properties of patches due to mixing and forming process is higher than the supposed effect of increasing water content. Although high variability corresponds well to the real-type accretion scenarios, it is difficult to quantify using simple tests and makes the procedure more complicated. Conducting experiments with a much larger number of samples and more rigorous preparation and measuring conditions would possibly bring

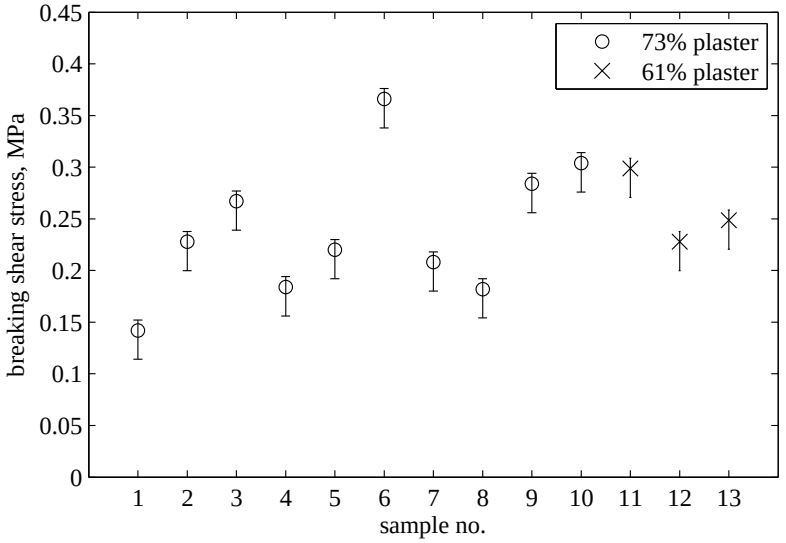

Figure A.7: Shear adhesion strength of the plaster-aluminium bond: experimental results.

more insightful observations. Nonetheless, the purpose of the presented experiment was to indicate a rough estimate of plaster's adhesion strength to aluminium and has been achieved. As mentioned above these results should be treated as a guideline rather than rigorous description of the material's behaviour.

A.3.2 Electrical impedance

Fig. A.8 shows the comparison between electrical impedances of plates with patches during different iterations of the experiment and for reference the impedance of the clean plate. It is clear from Fig. A.8 that plaster patches add significant damping to the structure as the resonance dips' heights are considerably decreased. This corresponds well to the reported ice behaviour the presence of which is usually associated with a drop of propagating wave amplitude or increased damping for steady-state vibrations. The location of the resonances along the frequency axis is significantly changed and many new local modes appear. It is expected that some of them are the localised vibration modes in the patches only. Therefore, it is somewhat awkward to identify the most promising frequency to use during the attempt to invoke delamination.

The impedances of plates with patches made of two different mixes are compared in Fig. A.9. It can be concluded that the difference in the water content as investigated here does not affect the dynamic response notably.

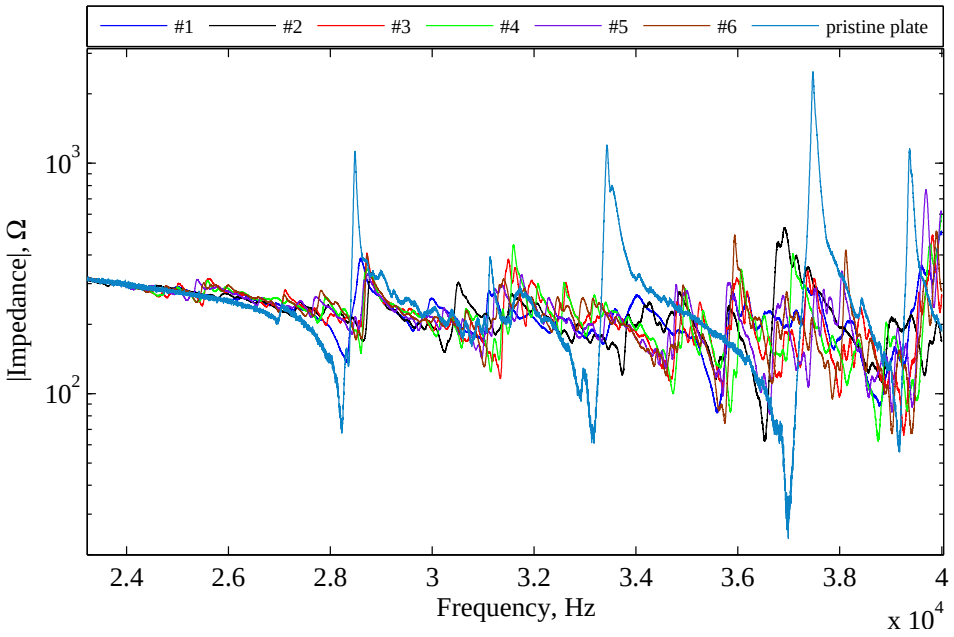

Figure A.8: Electrical impedance for different realisations of the experiment compared to the clean plate.

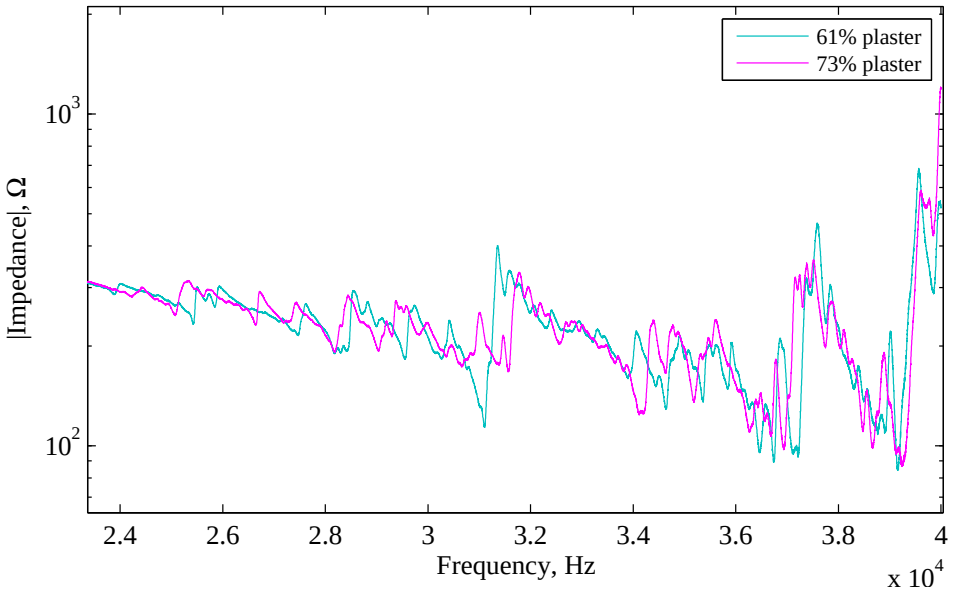

Figure A.9: Comparison of electrical impedances of plates with patches made of different plaster mixes.

A.3.3 Invoking delamination

As stated above, in this part of the experiment, the actuator was initially excited at the strongest resonance frequency as read from the impedance measurements presented in the previous section. However, while performing the test it was noticed that driving the

No.	f, kHz	$P_{\text{indicated}}$, W		$\lvert V_{\text{RMS}}\rvert$, V		P_R, W	Z, Ω	P_{capab}, VA
		FWD	RFD	FWD	RFD			
1	36.7	36	6	42.4	17.3	30	87.5-191.3j	81
2	36.7	91	14	67.5	26.5	77	87.5-191.3j	207
3	36.7	76	47	61.6	48.5	29	32.9-116.8j	126
4	36.7	79	53	62.8	51.5	26	65.8-131j	69
5	36.5	99	63	70.4	56.1	36	43-95.8j	112
6	36.5	113	25	75.2	35.4	88	43-95.8j	273
7	38.9	144	23	84.9	33.9	121	57.2-82.1j	286
8	38.9	114	48	75.5	49	66	57.2-82.1j	156
9	38	98	52	70	51	46	42.5-211j	249
10	38	123	33	78.4	40.6	90	42.5-211j	488
		amp display					measured prior	**inferred**

Table A.2: Summary of invoking delamination attempts.

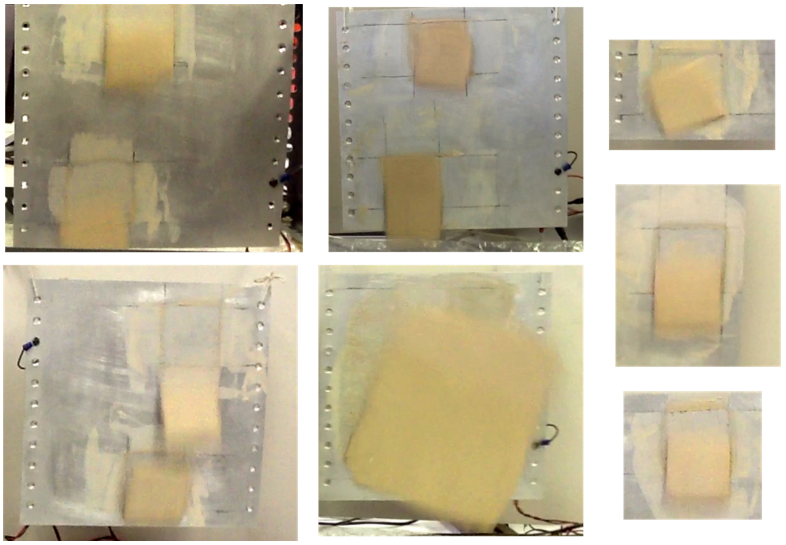

Figure A.10: Plaster patches debonding as captured by the camera (video frames).

actuator at the resonance chosen at first was usually not associated with an expected significant voltage drop and reduction of the reflected power figure shown on the amplifier's display. Therefore, the procedure was slightly amended. At low power level the deepest voltage drop was sought based on the waveform displayed on the oscilloscope. Finally, the actuator was driven with high power at this frequency until the patch was shed off or the power level was decided to be dangerous for the actuator.

A summary of the successful attempts to remove plaster patches from the aluminium host plate is presented in Table A.2 and some sample video snapshots demonstrating the debonding of the patches are gathered in Fig. A.10. For each iteration of the experiment the following figures are given in Table A.2: frequency, power indications as read from amplifier's display, corresponding voltage wave magnitudes as if the load is 50 Ω (see

Figure A.11: Cracked plaster patches.

Section 6.2.2 for details), active power absorbed by the load, the impedance as measured prior to the delamination test and inferred required power capability of the ultrasonic source (managing the impedance mismatch effect). The power figures are explained in detail in Section 6.2.2.

The horizontal line in Table A.2 separates the tests done on 73% plaster patches (1 to 6) and on 62% plaster patches (7 to 10). No clear conclusion on the effect of water content can be drawn from the data presented. However, it should be noted that the surface of the plate after debonding the patches of the wetter mix was uneven, rough and covered with plaster residuals.

For most cases internal cracks in plaster patches were noticed (see Fig. A.11) and a few patches detached from the host plate already in pieces. Additionally, after debonding surfaces of both the plate and patches were smooth and even except a few iterations - mainly those corresponding to patches made of a mix with increased water content.

Referring to the plaster adhesion strength measurements presented above, on average 61 W of active electrical power needs to be supplied to the actuator in order to remove patches adhered to the aluminium plate with a strength of 0.24 MPa (a mean of the results presented in Fig. A.7. Results shown here prove the concept of invoking delamination using ultrasonic excitation feasible and promising since the power requirement for a reasonably high interface stress is of an achievable order. Nonetheless, it has to be emphasized that the power figures from the last column in Table A.2 are estimates assuming that the structure's impedance at high power excitation is the same as the one measured before the test. In the light of the observations made during the experiment this assumption is probably wrong (which explains unexpectedly large values).

Similarly, it was observed that the impedance changed with increasing driving power. The resonances were shifting or floating around the frequency identified initially at low input power and further tuning at higher power input was needed. Two reasons for

Figure A.12: Actuators' degradation

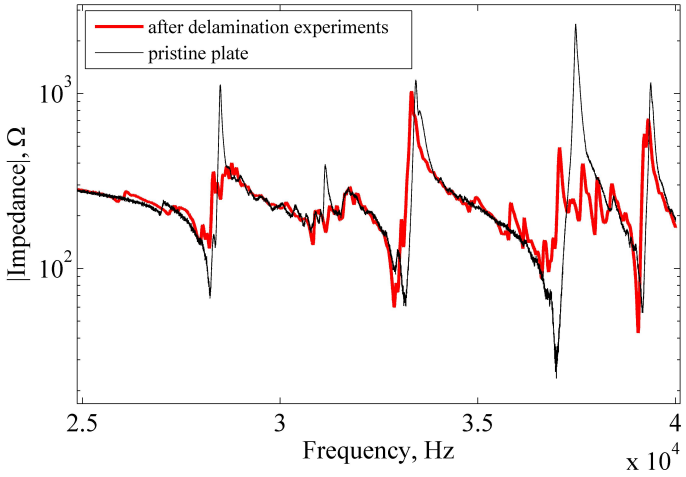

Figure A.13: Impedance evolution - comparing the actuator's impedance from before and after high power experiments.

such behaviour can be thought of. The first is that as a consequence of ultrasonic excitation some changes in the structural integrity occur. Although they are not visible with the naked eye, they contribute to changing the electromechanical behaviour of the coupled system and result in resonance shifts. Secondly, the non-linearity of piezoelectric material in the presence of the high electric field comes into play. From these two the latter requires further attention and needs to be quantified for this specific application in order to understand its effect and find ways to include them in the system design phase.

Comparing the figures from Table A.2 with Fig. A.8 leads to the conclusion that the ultrasonic action was effective at frequencies corresponding to the resonances of the clean plate. It implies that there is no need for tracking the resonance after the patches are formed. It is probably caused by the fact that their stiffness relative to the host structure

is small, but possibly also by gradually growing effect of power excitation which weakens the plaster-aluminium bond even at low power levels.

It has been noticed that for the thick actuators higher voltage needed to be applied in order to achieve the debonding effect. Since the diameter-to-thickness ratio was reduced, a higher electric field was required to induce similar deformation. Furthermore, as a result of increased thickness a higher voltage is also needed in order to keep the electric field at the same level as in the thin actuator case. Actuator's thickness has to be optimised with regard to these factors. It has also been reported in the literature that thick actuators are likely to debond themselves during the ultrasonic action due to the high inertia forces [21].

After a long excitation at high power level the actuator's cracking was observed (see Fig. A.12). In case of PZT disks this is the result of high radial tensile stresses within the piezoelectric material [24]. As reported by the manufacturer, the high signal compressive strength of both PZT 403 and PZT 802 materials is > 517 MPa, whereas the static tensile strength is 75.8 MPa [79]. A sinusoidal excitation causes a symmetric deformation so the tensile stress induced is of the same level as the compressive stress. However, the damage occurred at first in the thicker PZT disks. This can be attributed to the high influence of inertia forces in conjunction with an imperfect bonding not covering the whole actuator's surface (as observed after degradation). Therefore, in future special attention has to be paid so that the actuators are bonded well with a uniform layer of adhesive all over the electrode.

The impedance of the actuator after the delamination tests has changed compared to the pristine state (Fig. A.13). One of the reasons could be the growing material cracks which although invisible with the naked eye, can reveal themselves in the impedance curve. On the other hand, it is well known that piezoelectrics after high power excitation experience a distortion of its initial properties that is reversible with time. This phenomenon may put an undesired uncertainty in the whole system's behaviour and should be avoided. Therefore it is necessary to find the true reason for the impedance change and take an appropriate action to avoid temporary degradation of actuator's properties.

Above all, the test presented here proves the concept of wave based delamination invoking for ultrasonic steady-state vibration where the system benefits from multiple reflections of the induced waves from the edges of the plate. There is a need for a deeper insight into the interaction of the patch with a propagating wave which provides more physical understanding of the process of inducing debonding and reveal more clearly its limitations.

A.4 Conclusions

The concept of using the ultrasonic excitation to remove an unwanted accretion from a plate structure was investigated and proven feasible in the presented work. The physical basics of piezoelectric actuators dynamics were discussed together with comments on the important aspects of electrical power transfer and complex load driving. Furthermore, the principles of an electrical impedance measurement and its advantages were recalled. In the light of these foundations we designed and conducted a set of experiments using a model material simulating the real-type build-ups. An informed analysis of the key results was enforced with supplementary measurements of the static adhesion strength and the electrical impedance of the structure covered with undesired patches. The experimental observations include the discussion of problematic issues associated with high-power excitation.

Appendix B

Piece-wise wave-based formulation for a multi-component waveguide

In order to benefit from the full potential of wave based approach to structural dynamics with the emphasis on the piezoelectric semi-analytical finite elements presented in Chapter 5, a piece-wise wave formulation was developed. The core of the approach is to represent a one-dimensional waveguide as a series of wave elements that have constant properties over their lengths and express its steady-state vibrational or wave response in terms of waves travelling across the elements. The formulation allows for incompatibility of the adjacent elements, i.e. different dimensions and/or properties what results in reflection and scattering of the waves at the junctions (the meshes of the overlapping parts of the cross-sections need to be consistent, however). The excitation needs to be lumped at the boundaries of directly affected elements. The piece-wise character of the routine implies that the final solution is obtained by recursive reduction of the unknown variables on an element-by-element basis.

B.1 Assembly process workflow

The workflow of the approach is presented in Fig. B.1. The following stages are distinguished:

1. *Pre-processing.* This includes the definition of the materials and geometries of the cross-sections, separation into wave elements, assigning boundary and continuity conditions between the elements and defining excitation.

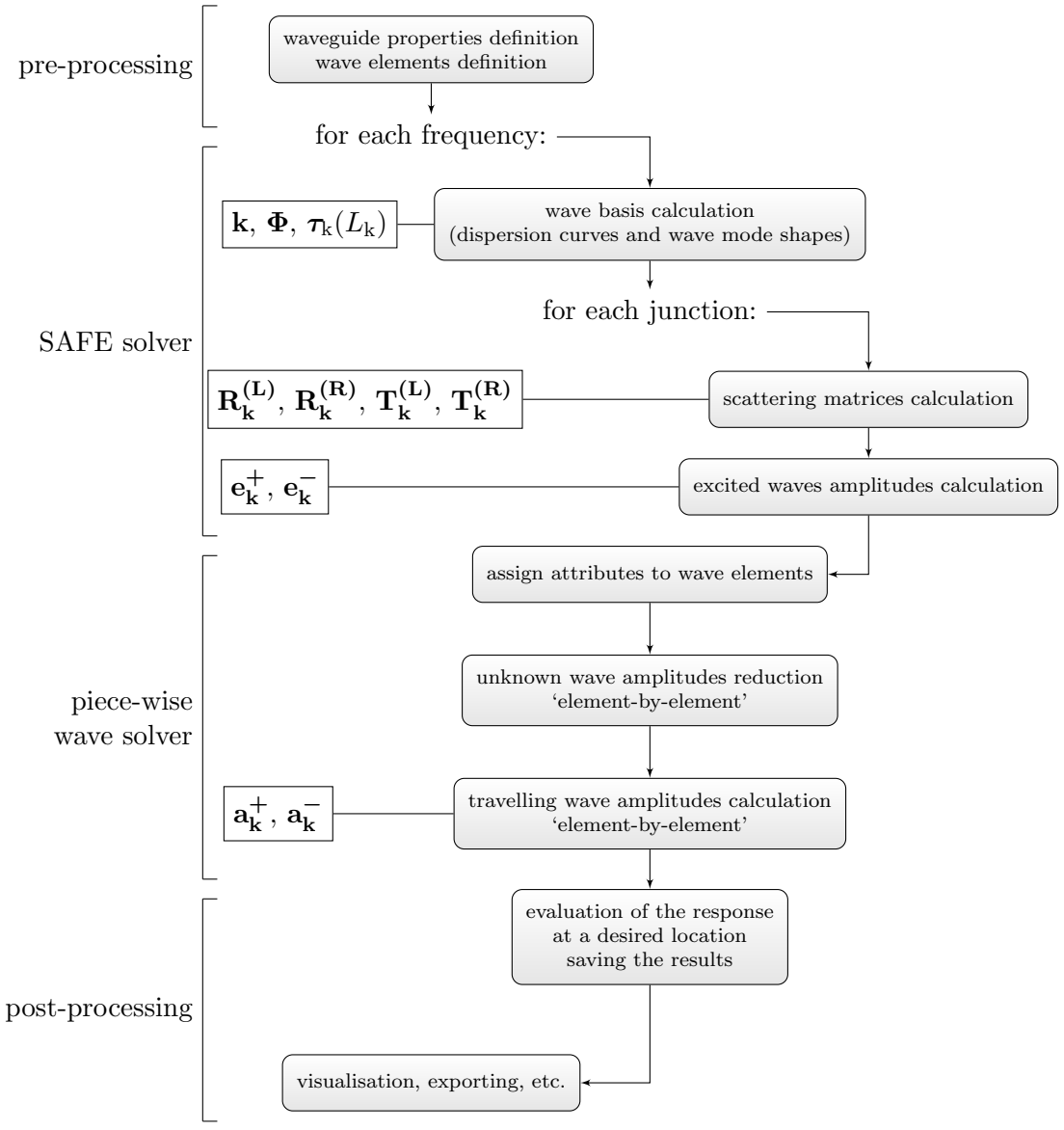

Figure B.1: Piece-wise routine workflow.

2. *SAFE solver.* For each frequency the wave basis (dispersion curves and wave mode shapes) for each type of wave element needs to be determined using SAFE method. Note that many wave elements in one model may share the wave basis even if their lengths vary. Following from the wave bases, reflection and scattering matrices and excited wave amplitudes are determined.

3. *Piece-wise structure definition.* Each wave element is assigned the attributes required for piece-wise calculation.

4. *Piece-wise solver.* Reduction of the unknown wave amplitudes on an element-by-element basis and then similarly travelling waves amplitudes calculation.

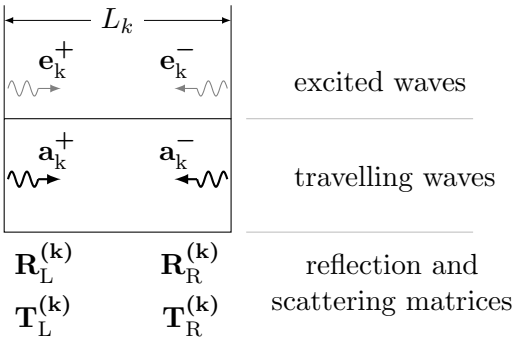

Figure B.2: Wave element and its attributes.

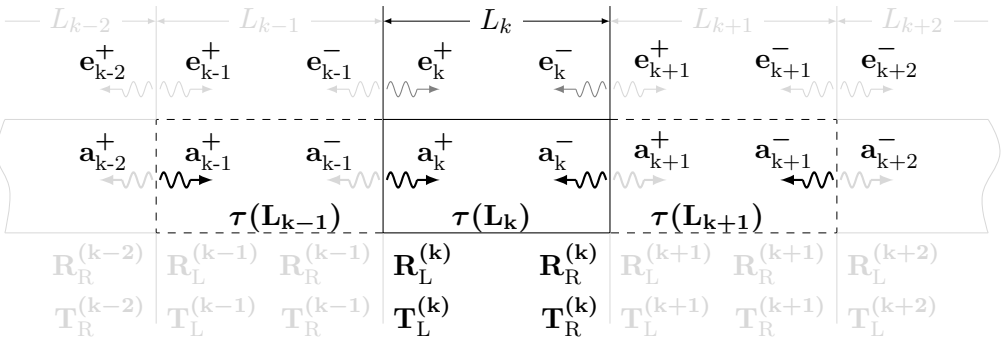

Figure B.3: Wave amplitudes and matrices required to fully describe the motion in a wave element.

5. *Post-processing.* Evaluation of the response at a desired location and plotting/saving the result.

A single wave element (Fig. B.2) has following attributes:

- dispersion curves and wave mode shapes
- cross-section dimensions and length along the waveguide
- excited wave amplitudes at the left and right borders of the element
- travelling wave amplitudes at the left and the right borders of the element
- reflection matrices at the borders of the element
- scattering matrices at the borders of an element describing how the wave incident upon the element are scattered after entering its domain

It is important to notice that in this formulation the origins of the positive- and negative-going waves are always at the left and the right borders of its 'parent' wave elements, respectively. This applies to both excited waves and travelling waves.

B.2 Element-by-element recursive solution

The waves required to fully describe wave motion in a wave element are shown in Fig. B.3. The labelling convention conforms with the one adopted in this thesis. Thereofre, $\mathbf{e}^{+,-}$ denotes excited waves, $\mathbf{T}$, $\mathbf{R}$, $\boldsymbol{\tau}$ are the scattering, reflection and propagation matrices and $\mathbf{a}^{+,-}$ are the travelling waves (i.e. superimposed including the reflections etc.). Positive travelling wave in an element can be expressed as a following superposition:

$$\begin{aligned}\mathbf{a}_k^+ &= \mathbf{e}_k^+ + \mathbf{R}_k^{\mathrm{L}}\boldsymbol{\tau}_k\mathbf{a}_k^- + \mathbf{T}_k^{\mathrm{L}}\boldsymbol{\tau}_{(k-1)}\mathbf{a}_{(k-1)}^+ \\ \mathbf{a}_k^- &= \mathbf{e}_k^- + \mathbf{R}_k^{\mathrm{R}}\boldsymbol{\tau}_k\mathbf{a}_k^+ + \mathbf{T}_k^{\mathrm{R}}\boldsymbol{\tau}_{(k+1)}\mathbf{a}_{(k+1)}^-\end{aligned} \tag{B.1}$$

The second equation can be substituted into the first yielding:

$$\begin{aligned}\mathbf{a}_k^+ &= \mathbf{e}_k^+ + \mathbf{R}_k^{\mathrm{L}}\boldsymbol{\tau}_k\left[\mathbf{e}_k^- + \mathbf{R}_k^{\mathrm{R}}\boldsymbol{\tau}_k\mathbf{a}_k^+ + \mathbf{T}_k^{\mathrm{R}}\boldsymbol{\tau}_{(k+1)}\mathbf{a}_{(k+1)}^-\right] + \mathbf{T}_k^{\mathrm{L}}\boldsymbol{\tau}_{(k-1)}\mathbf{a}_{(k-1)}^+ \\ &= \mathbf{e}_k^+ + \mathbf{R}_k^{\mathrm{L}}\boldsymbol{\tau}_k\mathbf{e}_k^- + \mathbf{R}_k^{\mathrm{L}}\boldsymbol{\tau}_k\mathbf{R}_k^{\mathrm{R}}\boldsymbol{\tau}_k\mathbf{a}_k^+ + \mathbf{R}_k^{\mathrm{L}}\boldsymbol{\tau}_k\mathbf{T}_k^{\mathrm{R}}\boldsymbol{\tau}_{(k+1)}\mathbf{a}_{(k+1)}^- + \mathbf{T}_k^{\mathrm{L}}\boldsymbol{\tau}_{(k-1)}\mathbf{a}_{(k-1)}^+\end{aligned} \tag{B.2}$$

From where the piece-wise expression for the positive travelling wave is obtained:

$$\mathbf{a}_k^+ = \left[\mathbf{I} - \mathbf{R}_k^{\mathrm{L}}\boldsymbol{\tau}_k\mathbf{R}_k^{\mathrm{R}}\boldsymbol{\tau}_k\right]^{-1}\left[\mathbf{e}_k^+ + \mathbf{R}_k^{\mathrm{L}}\boldsymbol{\tau}_k\mathbf{e}_k^- + \mathbf{T}_k^{\mathrm{L}}\boldsymbol{\tau}_{(k-1)}\mathbf{a}_{(k-1)}^+ + \mathbf{R}_k^{\mathrm{L}}\boldsymbol{\tau}_k\mathbf{T}_k^{\mathrm{R}}\boldsymbol{\tau}_{(k+1)}\mathbf{a}_{(k+1)}^-\right] \tag{B.3}$$

Eq. (B.3) describes how the positive travelling wave in the element depends on the excited wave amplitudes and travelling waves in adjacent elements. To simplify the notation the following are adopted:

$$\begin{aligned}\mathbf{A}_k^+ &= \left[\mathbf{I} - \mathbf{R}_k^{\mathrm{L}}\boldsymbol{\tau}_k\mathbf{R}_k^{\mathrm{R}}\boldsymbol{\tau}_k\right]^{-1} \\ \mathbf{B}_k^+ &= \mathbf{A}_k^+\mathbf{R}_k^{\mathrm{L}}\boldsymbol{\tau}_k \\ \mathbf{C}_k^+ &= \mathbf{A}_k^+\mathbf{T}_k^{\mathrm{L}}\boldsymbol{\tau}_{(k-1)} \\ \mathbf{D}_k^+ &= \mathbf{A}_k^+\mathbf{R}_k^{\mathrm{L}}\boldsymbol{\tau}_k\mathbf{T}_k^{\mathrm{R}}\boldsymbol{\tau}_{(k+1)}\end{aligned} \tag{B.4}$$

An analogous procedure can be performed for negative travelling wave, in which case the coefficient matrices change slightly:

$$\begin{aligned}\mathbf{B}_k^- &= \left[\mathbf{I} - \mathbf{R}_k^{\mathrm{R}}\boldsymbol{\tau}_k\mathbf{R}_k^{\mathrm{L}}\boldsymbol{\tau}_k\right]^{-1} \\ \mathbf{A}_k^- &= \mathbf{B}_k^-\mathbf{R}_k^{\mathrm{R}}\boldsymbol{\tau}_k \\ \mathbf{C}_k^- &= \mathbf{B}_k^-\mathbf{R}_k^{\mathrm{R}}\boldsymbol{\tau}_k\mathbf{T}_k^{\mathrm{L}}\boldsymbol{\tau}_{(k-1)} \\ \mathbf{D}_k^- &= \mathbf{B}_k^-\mathbf{T}_k^{\mathrm{R}}\boldsymbol{\tau}_{(k+1)}\end{aligned} \tag{B.5}$$

With the aid of Eqs. (B.4) and (B.5) a recursive expression for travelling waves in an element is written as:

$$\begin{aligned}\mathbf{a}_k^+ &= \mathbf{A}_k^+\mathbf{e}_k^+ + \mathbf{B}_k^+\mathbf{e}_k^- + \mathbf{C}_k^+\mathbf{a}_{(k-1)}^+ + \mathbf{D}_k^+\mathbf{a}_{(k+1)}^- \\ \mathbf{a}_k^- &= \mathbf{A}_k^-\mathbf{e}_k^+ + \mathbf{B}_k^-\mathbf{e}_k^- + \mathbf{C}_k^-\mathbf{a}_{(k-1)}^+ + \mathbf{D}_k^-\mathbf{a}_{(k+1)}^-\end{aligned} \tag{B.6}$$

The equations above relate the unknown travelling waves in an element to the travelling waves in adjacent elements and therefore can readily be used in the piece-wise solver. The piece-wise solution starts from the far-right (n^{th}) element for which the right incoming wave does not exist. Eq. (B.6) simplifies to:

$$\begin{aligned}\mathbf{a}_n^+ &= \mathbf{A}_n^+\mathbf{e}_n^+ + \mathbf{B}_n^+\mathbf{e}_n^- + \mathbf{C}_n^+\mathbf{a}_{(n-1)}^+ \\ \mathbf{a}_n^- &= \mathbf{A}_n^-\mathbf{e}_n^+ + \mathbf{B}_n^-\mathbf{e}_n^- + \mathbf{C}_n^-\mathbf{a}_{(n-1)}^+\end{aligned} \tag{B.7}$$

Moreover it is possible to relate $\mathbf{a}_n^-$ to $\mathbf{a}_n^+$ directly:

$$\mathbf{a}_n^- = \mathbf{e}_n^- + \mathbf{R}_n^{\mathrm{R}}\boldsymbol{\tau}_n\mathbf{a}_n^+ \tag{B.8}$$

Substituting Eq. (B.7) to Eq. (B.8) yields:

$$\mathbf{a}_n^- = \mathbf{R}_n^{\mathrm{R}}\boldsymbol{\tau}_n\mathbf{A}_n^+\mathbf{e}_n^+ + (\mathbf{R}_n^{\mathrm{R}}\boldsymbol{\tau}_n\mathbf{B}_n^+ + \mathbf{I})\mathbf{e}_n^- + \mathbf{R}_n^{\mathrm{R}}\boldsymbol{\tau}_n\mathbf{C}_n^+\mathbf{a}_{(n-1)}^+ = \mathbf{Z}_n^- + \mathbf{H}_n^-\mathbf{a}_{(n-1)}^+ \tag{B.9}$$

In the last step of Eq. (B.9) the two parts were distinguished: $\mathbf{Z}_\mathbf{n}^-$ that does not depend on the amplitudes of the waves in the adjacent sections, and $\mathbf{H}_\mathbf{n}^-$ that represents how $\mathbf{a}_{(\mathbf{n-1})}^+$ contributes to the positive travelling wave in the wave element considered.

The general wave element equation eq. (B.6) can be now written for the $(n-1)^{\text{th}}$ element:

$$\begin{aligned}\mathbf{a}_{(n-1)}^+ &= \mathbf{A}_{(n-1)}^+\mathbf{e}_{(n-1)}^+ + \mathbf{B}_{(n-1)}^+\mathbf{e}_{(n-1)}^- + \mathbf{C}_{(n-1)}^+\mathbf{a}_{(n-2)}^+ + \mathbf{D}_{(n-1)}^+\mathbf{a}_n^- \\ \mathbf{a}_{(n-1)}^- &= \mathbf{A}_{(n-1)}^-\mathbf{e}_{(n-1)}^+ + \mathbf{B}_{(n-1)}^-\mathbf{e}_{(n-1)}^- + \mathbf{C}_{(n-1)}^-\mathbf{a}_{(n-2)}^+ + \mathbf{D}_{(n-1)}^-\mathbf{a}_n^-\end{aligned} \tag{B.10}$$

Substituting Eq. (B.9) into Eq. (B.10) one gets:

$$\begin{aligned}
\mathbf{a}^{+}_{(n-1)} &= \mathbf{A}^{+}_{(n-1)}\mathbf{e}^{+}_{(n-1)} + \mathbf{B}^{+}_{(n-1)}\mathbf{e}^{-}_{(n-1)} + \mathbf{C}^{+}_{(n-1)}\mathbf{a}^{+}_{(n-2)} + \mathbf{D}^{+}_{(n-1)}\left(\mathbf{Z}^{-}_{n} + \mathbf{H}^{-}_{n}\mathbf{a}^{+}_{(n-1)}\right)\\
\mathbf{a}^{+}_{(n-1)} &= \mathbf{A}^{+}_{(n-1)}\mathbf{e}^{+}_{(n-1)} + \mathbf{B}^{+}_{(n-1)}\mathbf{e}^{-}_{(n-1)} + \mathbf{C}^{+}_{(n-1)}\mathbf{a}^{+}_{(n-2)} + \mathbf{D}^{+}_{(n-1)}\mathbf{Z}^{-}_{n} + \mathbf{D}^{+}_{(n-1)}\mathbf{H}^{-}_{n}\mathbf{a}^{+}_{(n-1)}\\
\mathbf{a}^{+}_{(n-1)} &= \left[\mathbf{I} - \mathbf{D}^{+}_{(n-1)}\mathbf{H}^{-}_{n}\right]^{-1}\left[\mathbf{A}^{+}_{(n-1)}\mathbf{e}^{+}_{(n-1)} + \mathbf{B}^{+}_{(n-1)}\mathbf{e}^{-}_{(n-1)} + \mathbf{C}_{(n-1)+}\mathbf{a}^{+}_{(n-2)} + \mathbf{D}^{+}_{(n-1)}\mathbf{Z}^{-}_{n}\right]\\
\mathbf{a}^{+}_{(n-1)} &= \left[\mathbf{I} - \mathbf{D}^{+}_{(n-1)}\mathbf{H}^{-}_{n}\right]^{-1}\left[\mathbf{A}^{+}_{(n-1)}\mathbf{e}^{+}_{(n-1)} + \mathbf{B}^{+}_{(n-1)}\mathbf{e}^{-}_{(n-1)} + \mathbf{D}_{(n-1)+}\mathbf{Z}^{-}_{n}\right] +\\
&\quad \left[\mathbf{I} - \mathbf{D}^{+}_{(n-1)}\mathbf{H}^{-}_{n}\right]^{-1}\mathbf{C}^{+}_{(n-1)}\mathbf{a}^{+}_{(n-2)}\\
\mathbf{a}^{+}_{(n-1)} &= \mathbf{Z}^{+}_{(n-1)} + \mathbf{H}^{+}_{(n-1)}\mathbf{a}^{+}_{(n-2)}
\end{aligned} \tag{B.11}$$

which provides an expression for the amplitude of the wave travelling in the wave element with respect to the positive travelling wave in the preceding section. Similarly, the recursive expression for the negative going wave can be established:

$$\begin{aligned}
\mathbf{a}^{-}_{(n-1)} &= \mathbf{A}^{-}_{(n-1)}\mathbf{e}^{+}_{(n-1)} + \mathbf{B}^{-}_{(n-1)}\mathbf{e}^{-}_{(n-1)} + \mathbf{C}^{-}_{(n-1)}\mathbf{a}^{+}_{(n-2)} + \mathbf{D}^{-}_{(n-1)}\mathbf{a}^{-}_{n}\\
&= \mathbf{A}^{-}_{(n-1)}\mathbf{e}^{+}_{(n-1)} + \mathbf{B}^{-}_{(n-1)}\mathbf{e}^{-}_{(n-1)} + \mathbf{C}^{-}_{(n-1)}\mathbf{a}^{+}_{(n-2)} + \mathbf{D}^{-}_{(n-1)}\left(\mathbf{Z}^{-}_{n} + \mathbf{H}^{-}_{n}\mathbf{a}^{+}_{(n-1)}\right)\\
&= \mathbf{A}^{-}_{(n-1)}\mathbf{e}^{+}_{(n-1)} + \mathbf{B}^{-}_{(n-1)}\mathbf{e}^{-}_{(n-1)} + \mathbf{C}^{-}_{(n-1)}\mathbf{a}^{+}_{(n-2)} +\\
&\quad \mathbf{D}^{-}_{(n-1)}\left[\mathbf{Z}^{-}_{n} + \mathbf{H}^{-}_{n}\left(\mathbf{Z}^{+}_{(n-1)} + \mathbf{H}^{+}_{(n-1)}\mathbf{a}^{+}_{(n-2)}\right)\right]\\
&= \mathbf{A}^{-}_{(n-1)}\mathbf{e}^{+}_{(n-1)} + \mathbf{B}^{-}_{(n-1)}\mathbf{e}^{-}_{(n-1)} +\\
&\quad \mathbf{D}^{-}_{(n-1)}\left(\mathbf{Z}^{-}_{n} + \mathbf{H}^{-}_{n}\mathbf{Z}^{+}_{(n-1)}\right) + \left(\mathbf{C}^{-}_{(n-1)} + \mathbf{D}^{-}_{(n-1)}\mathbf{H}^{-}_{n}\mathbf{H}^{+}_{(n-1)}\right)\mathbf{a}^{+}_{(n-2)}\\
&= \mathbf{Z}^{-}_{(n-1)} + \mathbf{H}^{-}_{(n-1)}\mathbf{a}^{+}_{(n-2)}
\end{aligned} \tag{B.12}$$

The above equations can be applied to all internal wave elements. For the 1$^{\text{th}}$ element, there is no incoming wave from the left side, hence the formulation is simplified to:

$$\begin{aligned}
\mathbf{a}^{+}_{1} &= \mathbf{A}^{+}_{1}\mathbf{e}^{+}_{1} + \mathbf{B}^{+}_{1}\mathbf{e}^{-}_{1} + \mathbf{D}^{+}_{1}\mathbf{a}^{-}_{2}\\
\mathbf{a}^{-}_{1} &= \mathbf{A}^{-}_{1}\mathbf{e}^{+}_{1} + \mathbf{B}^{-}_{1}\mathbf{e}^{-}_{1} + \mathbf{D}^{-}_{1}\mathbf{a}^{-}_{2}
\end{aligned} \tag{B.13}$$

Eq. (B.12) written for the 2$^{\text{nd}}$ element can be then substituted back into Eq. (B.13):

$$\begin{aligned}
\mathbf{a}^{+}_{1} &= \mathbf{A}^{+}_{1}\mathbf{e}^{+}_{1} + \mathbf{B}^{+}_{1}\mathbf{e}^{-}_{1} + \mathbf{D}^{+}_{1}\left[\mathbf{Z}^{-}_{2} + \mathbf{H}^{-}_{2}\mathbf{a}^{+}_{1}\right]\\
&= \mathbf{A}^{+}_{1}\mathbf{e}^{+}_{1} + \mathbf{B}^{+}_{1}\mathbf{e}^{-}_{1} + \mathbf{D}^{+}_{1}\mathbf{Z}^{-}_{2} + \mathbf{D}^{+}_{1}\mathbf{H}^{-}_{2}\mathbf{a}^{+}_{1}
\end{aligned} \tag{B.14}$$

From where one can solve for the positive travelling wave in the 1$^{\text{st}}$ element:

$$\mathbf{a}^{+}_{1} = \left[\mathbf{I} - \mathbf{D}^{+}_{1}\mathbf{H}^{-}_{2}\right]^{-1}\left[\mathbf{A}^{+}_{1}\mathbf{e}^{+}_{1} + \mathbf{B}^{+}_{1}\mathbf{e}^{-}_{1} + \mathbf{D}^{+}_{1}\mathbf{Z}^{-}_{2}\right] \tag{B.15}$$

After this solution is obtained travelling wave amplitudes in all wave elements are calculated on an element-by-element basis by substituting the left incoming travelling waves amplitudes into Eq. (B.12) and (B.11).

References

[1] Eskandarian M. *Ice shedding from overhead electrical lines by mechanical breaking.* PhD thesis, University of Quebec, September 2005.

[2] Palacios J.L. *Design, Fabrication and Testing of an Ultrasonic De-icing System for Helicopter Blades.* PhD thesis, Pennsylvania State University. Department of Aerospace Engineering, 2008.

[3] Gao H. and Rose J.L. Ice detection and classification on an aircraft wing with ultrasonic shear horizontal guided waves. *IEEE Transactions on Ultrasonics, Ferroelectrics, and Frequency Control*, 56(2):334–344, 2009.

[4] Rose J.L. A baseline and vision of ultrasonic guided wave inspection potential. *Journal of Pressure Vessel Technology*, 124(3):273–282, 2002.

[5] Rose J.L. Ultrasonic guided waves in structural health monitoring. *Key Engineering Materials*, 270-273:14–21, 2004.

[6] Su Z. and Ye L. *Identification of Damage Using Lamb Waves - From Fundamentals to Applications.* Lecture Notes in Applied and Computational Mechanics. Springer-Verlag, 2009.

[7] Loughborough D.L. and Hass E.G. Reduction of adhesion of ice to de-icer surfaces. *Journal of Aeronautical Sciences*, 13(3):126–134, 1946.

[8] Stallbrass J.R. and Price R.D. On the adhesion of ice to various materials. *Canadian Aeronautics and Space Journal*, pages 199–204, 1963.

[9] Chu M.C. and Scavuzzo R. J. Adhesive shear strength of impact ice. *AIAA Journal*, 29:1921–1926, 1991.

[10] Hassan M.F., Lim S.P., and Lee H.P. The variation of ice adhesion strength with substrate surface roughness. *Measurement Science & Technology*, 21, 2010.

[11] Raraty L.E. and Tabor D. The adhesion and strength properties of ice. *Proceedings of The Royal Society of London*, 245A:184–201, 1958.

[12] Gouni R. *A New Technique to Study Temperature Effects on Ice Adhesion Strength for Wind Turbine Materials.* PhD thesis, Case Western Reserve University, 2011.

[13] Adachi K., Saiki K., and Sato H. Supression of frosting on a metal surface using ultrasonic vibrations. *Proceedings of the IEEE Ultrasonics Symposium*, pages 759–762, 1998.

[14] Ramanathan S., Varadan V.V., and Varadan V.K. Deicing of helicopter blades using piezoelectric actuators. *Smart Structures and Materials 2000: Smart Electronics and MEMS. Proceedings of SPIE*, 3990:281–292, 2000.

[15] Ramanathan S. *An Investigation on the Deicing of Helicopter Blades Using Shear Horizontal Guided Waves.* PhD thesis, Pennsylvania State University. Department of Engineering Science and Mechanics, 2005.

[16] Seppings R.A. *Investigation of Ice Removal From Cooled Metal Surfaces.* PhD thesis, Imperial College, Mechanical Engineering Department, University of London, October 2005.

[17] Palacios J.L. and Smith E.C. Dynamic analysis and experimental testing of thin-walled structures. In *46th AIAA Structural Dynamics & Materials, AIAA-2009-2112, Austin, Texas*, pages 3862–3875, April 2005.

[18] Palacios J.L., Smith E.C., Gao H., and Rose J.L. Ultrasonic shear wave anti-icing system for helicopter rotor blades. In *62nd Annual Forum Proceedings - American Helicopter Society, Phoenix, Arizona*, pages 1492–1502, 2006.

[19] Palacios J.L. Ultrasonic shear and Lamb wave interface stress for helicopter rotor de-icing purposes. In *47th AIAA Structural Dynamics & Materials, Newport, Rhode Island*, 2006.

[20] Palacios J.L., Smith E.C., Zhu Y., and Rose J.L. Global ultrasonic shear wave anti-icing actuator for helicopter blades. In *American Helicopter Society 64th Annual Forum, Montreal, Canada*, 2007.

[21] Palacios J.L. and Smith E.C. Invetsigation of an ultrasonic ice protection system for helicopter rotor blades. In *American Helicopter Society 64th Annual Forum, Montreal, Canada*, 2008.

[22] Palacios J.L., Smith E.C., Rose J.L., and Royer R. Instantaneous de-icing of freezer ice via ultrasonic actuation. *AIAA Journal*, 49(6):1158–1167, 2011.

[23] Palacios J.L., Smith E.C., Rose J.L., and Royer R. Ultrasonic de-icing of wind-tunnel impact icing. *Journal of Aircraft*, 48(3):1020–1027, 2011.

[24] Overmeyer A., Palacios J.L., Smith E.C., and Royer R. Rotating testing of a low-power, non-thermal ultrasonic de-icing system for helicopter rotor blades. In *SAE 2011 International Conference on Aircraft and Engine Icing and Ground Deicing, Chicago, Illinois*, June 2011.

[25] Zhu Y. *Structural Tailoring and Actuation Studies for Low Power Ultrasonic De-icing of Aluminium and Composite Plates*. PhD thesis, Pennsylvania State University. Department of Engineering Science and Mechanics, 2010.

[26] DiPlacido N., Soltis J., Smith E.C., and Palacios J.L. Enhancement of ultrasonic de-icing via transient excitation. In *Proceedings of the 2nd Asian/Australian Rotorcraft Forum and The 4th International Basic Research Conference on Rotorcraft Technology*, Tianjin, China, September 2013.

[27] Li D. and Chen Z. Experimental study on instantaneously shedding frozen water droplets from cold vertical surface by ultrasonic vibration. *Experimental Thermal and Fluid Science*, 53:17–25, February 2014.

[28] Fahy F. and Gardonio P. *Sound and Structural Vibration. Radiation, Transmission and Response*. Academic Press, 2nd edition edition, 2006.

[29] Beltzer A.I. *Acoustics of Solids*. Springer-Verlag, 1988.

[30] Rose J.L. *Ultrasonic Waves in Solid Media*. Cambridge University Press, 1999.

[31] Harris J.G. *Linear Elastic Waves*. Cambridge Texts in Applied Mathematics. Cambridge University Press, 2001.

[32] Rayleigh L. On waves propagated along the plane surface of an elastic solid. *Proceedings of the London Mathematical Society*, s1-17(1):4–11, November 1885.

[33] Lamb H. On waves in an elastic plate. *Proceedings of the Royal Society of London. Series A*, 93(648):114–128, March 1917.

[34] Achenbach J.D. *Wave Propagation in Elastic Solids*. Applied Mathematics and Mechanics. North-Holland, Amsterdam, London, 1973.

[35] Graff K.F. *Wave Motion in Elastic Solids*. Dover, 1991.

[36] Cremer L. and Heckl M. *Structure-borne sound; structural vibrations and sound radiation at audio frequencies*. Springer-Verlag, 1973.

[37] Mace B.R. Wave reflection and transmission in beams. *Journal of Sound and Vibration*, 97(2):237–246, November 1984.

[38] Harland N.R., Mace B.R., and Jones R.W. Wave propagation, reflection and transmission in tunable fluid-filled beams. *Journal of Sound and Vibration*, 241 (5):735–754, April 2001.

[39] Waki Y. *On the application of finite element analysis to wave motion in one-dimensional waveguides*. PhD thesis, University of Southampton, 2007.

[40] Doyle J.F. *Wave propagation in structures: spectral analysis using fast discrete Fourier transforms*. Springer, New York, 1997.

[41] Lee U. *Spectral element method in structural dynamics*. J. Wiley & Sons Asia, Singapore; Hoboken, NJ, 2009.

[42] Patera A.T. A spectral element method for fluid dynamics: Laminar flow in a channel expansion. *Journal of Computational Physics*, 54(3):468–488, June 1984.

[43] Crighton D.G., Dowling A.P., Ffowcs Williams J.E., Heckl M.A., and Leppingtoon F.A. *Modern Methods in Analytical Acoustics*. Lecture Notes. Springer, 1992.

[44] Lee U. and Kim J. Dynamics of elastic-piezoelectric two-layer beams using spectral element method. *International journal of solids and structures*, 37(32):44034417, 2000.

[45] Park H.W., Kim E.J., Lim K.L., and Sohn H. Spectral element formulation for dynamic analysis of a coupled piezoelectric wafer and beam system. *Computers & Structures*, 88(9-10):567–580, May 2010.

[46] Solie L.P. and Auld B.A. Elastic waves in free anisotropic plates. *The Journal of the Acoustical Society of America*, 54(1):50–65, 1973.

[47] Thomson W.T. Transmission of elastic waves through a stratified solid. *Journal of Applied Physics*, 21:89–93, 1950.

[48] Haskell N.A. Dispersion of surface waves on multilayered media. *Bulletin of Seismological Society of America*, 43:17–34, 1953.

[49] Lowe M.J.S. *Plate Waves for the NDT of Diffusion Bonded Titanium*. PhD thesis, Imperial College of Science, Technology and Medicine. University of London, 1993.

[50] Lowe M.J.S. Matrix techniques for modeling ultrasonic waves in multilayered media. *IEEE Transactions on Ultrasonics, Ferroelectrics, and Frequency Control*, 42(4):525–542, 1995.

[51] Mace B.R., Duhamel D., Brennan M.J., and Hinke L. Finite element prediction of wave motion in structural waveguides. *The Journal of the Acoustical Society of America*, 117(5):2835–2843, April 2005.

[52] Duhamel D., Mace B.R., and Brennan M.J. Finite element analysis of the vibrations of waveguides and periodic structures. *Journal of Sound and Vibration*, 294 (1-2):205–220, June 2006.

[53] Waki Y., Mace B.R., and Brennan M.J. Free and forced vibrations of a tyre using a wave/finite element approach. *Journal of Sound and Vibration*, 323(3-5):737–756, June 2009.

[54] Renno J.M. and Mace B.R. On the forced response of waveguides using the wave and finite element method. *Journal of Sound and Vibration*, 329(26):5474–5488, December 2010.

[55] Renno J.M. and Mace B. R. Calculation of reflection and transmission coefficients of joints using a hybrid finite element/wave and finite element approach. *Journal of Sound and Vibration*, 332(9):2149–2164, April 2013.

[56] Waki Y., Mace B.R., and Brennan M.J. Numerical issues concerning the wave and finite element method for free and forced vibrations of waveguides. *Journal of Sound and Vibration*, 327(1-2):92–108, October 2009.

[57] Lagasse P. E. Higher-order finite-element analysis of topographic guides supporting elastic surface waves. *The Journal of the Acoustical Society of America*, 53(4): 1116–1122, 1973.

[58] Aalami B. Waves in prismatic guides of arbitrary cross section. *Journal of Applied Mechanics*, 40(4):1067–1072, December 1973.

[59] Finnveden S. Evaluation of modal density and group velocity by a finite element method. *Journal of Sound and Vibration*, 273(12):51–75, May 2004.

[60] Finnveden S. and Fraggstedt M. Waveguide finite elements for curved structures. *Journal of Sound and Vibration*, 312(45):644–671, May 2008.

[61] Nilsson C. M. and Finnveden S. Waves in thin-walled fluid-filled ducts with arbitrary cross-sections. *Journal of Sound and Vibration*, 310(12):58–76, February 2008.

[62] Loveday P.W. and Shatalov M.Y. Finite element computation of dispersion in piezoelectric waveguides. In *Proceedings of the SPIE, Volume 5757, pp. 432-440*, volume 5757, pages 432–440, 2005.

[63] Loveday P.W. Semi-analytical finite element analysis of elastic waveguides subjected to axial loads. *Ultrasonics*, 49(3):298–300, March 2009.

[64] Hayashi T., Song W., and Rose J.L. Guided wave dispersion curves for a bar with an arbitrary cross-section, a rod and rail example. *Ultrasonics*, 41(3):175–183, May 2003.

[65] Damljanovic V. and Weaver R.L. Forced response of a cylindrical waveguide with simulation of the wavenumber extraction problem. *The Journal of the Acoustical Society of America*, 115(4):1582, 2004.

[66] Bartoli I., Marzani A., Lanza di Scalea F., and Viola E. Modeling wave propagation in damped waveguides of arbitrary cross-section. *Journal of Sound and Vibration*, 295(3-5):685–707, August 2006.

[67] Predoi M.V., Castaings M., Hosten B., and Bacon C. Wave propagation along transversely periodic structures. *The Journal of the Acoustical Society of America*, 121(4):1935–1944, 2007.

[68] Le Crom B. and Castaings M. Shear horizontal guided wave modes to infer the shear stiffness of adhesive bond layers. *The Journal of the Acoustical Society of America*, 127(4):2220, 2010.

[69] Sheng X., Jones C.J.C., and Thompson D.J. Modelling ground vibration from railways using wavenumber finite- and boundary-element methods. *Proceedings of the Royal Society: Mathematical, Physical and Engineering Sciences*, 461(2059): 2043–2070, July 2005.

[70] Ryue J., Thompson D.J., White P.R., and Thompson D.R. Investigations of propagating wave types in railway tracks at high frequencies. *Journal of Sound and Vibration*, 315(1-2):157–175, August 2008.

[71] Gavric L. Computation of propagative waves in free rail using a finite element technique. *Journal of Sound and Vibration*, 185(3):531543, 1995.

[72] Gry L. Dynamic modelling of railway track based on wave propagation. *Journal of Sound and Vibration*, 195(3):477–505, August 1996.

[73] Finnveden S. Exact spectral finite element analysis of stationary vibrations in a rail way car structure. *Acta Acoustica*, 2, 1994.

[74] Finnveden S. Spectral finite element analysis of the vibration of straight fluid-filled pipes with flanges. *Journal of Sound and Vibration*, 199(1):125–154, January 1997.

[75] Orrenius U. and Finnveden S. Calculation of wave propagation in rib-stiffened plate structures. *Journal of Sound and Vibration*, 198(2):203–224, November 1996.

[76] Drozdz M.B. *Efficient Finite Element Modelling of Ultrasound Waves in Elastic Media*. PhD, Department of Mechanical Engineering, Imperial College, London, 2008.

[77] Moulin E., Assaad J., Delebarre C., and Osmont D. Modeling of lamb waves generated by integrated transducers in composite plates using a coupled finite elementnormal modes expansion method. *The Journal of the Acoustical Society of America*, 107(1):87–94, January 2000.

[78] Ostachowicz W., Kudela P., Krawczuk M., and Zak A. *Guided Waves in Structures for SHM: The Time-Domain Spectral Element Method*. John Wiley & Sons, Ltd, 2012.

[79] Morgan Electro Ceramics. *Piezoelectric Ceramics Brochure*. Morgan Electro Ceramics LTD, November 2007.

[80] Park G. and Inman D.J. Structural health monitoring using piezoelectric impedance measurements. *Proceedings of the Royal Society A: Mathematical, Physical and Engineering Sciences*, 365(1851):373–392, February 2007.

[81] Prokic M. *Piezoelectric transducers modelling and characterization*. MPInterconsulting, 2004.

[82] Rosiek M., Martowicz A., and Uhl T. Uncertainty and sensitivity analysis of electro-mechanical impedance based SHM system. *IOP Conference Series: Materials Science and Engineering*, 10(1):012207, 2010.

[83] Huang G., Song F., and Wang X. Quantitative modeling of coupled piezoelastodynamic behavior of piezoelectric actuators bonded to an elastic medium for structural health monitoring: A review. *Sensors*, 10(4):3681–3702, April 2010.

[84] Moll J., Golub M.V., Glushkov E., Glushkova N., and Fritzen C. Non-axisymmetric lamb wave excitation by piezoelectric wafer active sensors. *Sensors and Actuators A: Physical*, 174:173–180, February 2012.

[85] Crawley E.F. and De Luis J. Use of piezoelectric actuators as elements of intelligent structures. *AIAA Journal*, 25(10):1373–1385, October 1987.

[86] Chaudhry Z. and Rogers C.A. The pin-force model revisited. *Journal of Intelligent Material Systems and Structures*, 5(3):347–354, May 1994.

[87] Richard J.S. and Cudney H.H. Modeling multiple-layer piezoelectric actuators in active structural control. In *Proceedings of SPIE Smart Structures and Materials*, volume 1916, pages 231–243, 1993.

[88] Crawley E.F. and Lazarus K.B. Induced strain actuation of isotropic and anisotropic plates. *AIAA Journal*, 29(6):944–951, June 1991.

[89] Banks H.T. and Smith R.C. The modeling of piezoceramic patch interactions with shells, plates and beams. Technical report, DTIC Document, 1992.

[90] Batra R.C., Liang X.Q., and Yang J.S. The vibration of a simply supported rectangular elastic plate due to piezoelectric actuators. *International Journal of Solids and Structures*, 33(11):1597–1618, May 1996.

[91] Park I. and Lee U. Dynamic analysis of smart composite beams by using the frequency-domain spectral element method. *Journal of Mechanical Science and Technology*, 26(8):2511–2521, August 2012.

[92] Lee U., Kim D., and Park I. Dynamic modeling and analysis of the PZT-bonded composite timoshenko beams: Spectral element method. *Journal of Sound and Vibration*, 332(6):1585–1609, March 2013.

[93] Giurgiutiu V. *Structural health monitoring: with piezoelectric wafer active sensors*. Access Online via Elsevier, 2007.

[94] Yang J.S. Equations for thick elastic plates with partially electroded piezoelectric actuators and higher order electric fields. *Smart Materials and Structures*, 8(1): 73, February 1999.

[95] Lin X. and Yuan F.G. Diagnostic lamb waves in an integrated piezoelectric sensor/actuator plate: analytical and experimental studies. *Smart Materials and Structures*, 10(5):907, October 2001.

[96] Giurgiutiu V. Tuned lamb wave excitation and detection with piezoelectric wafer active sensors for structural health monitoring. *Journal of Intelligent Material Systems and Structures*, 16(4):291–305, April 2005.

[97] Lanza di Scalea F. and Salamone S. Temperature effects in ultrasonic lamb wave structural health monitoring systems. *The Journal of the Acoustical Society of America*, 124(1):161–174, July 2008.

[98] Yu L., Santoni-Bottai G., and Giurgiutiu V. Shear lag solution for tuning ultrasonic piezoelectric wafer active sensors with applications to lamb wave array imaging. *International Journal of Engineering Science*, 48(10):848–861, October 2010.

[99] Santoni-Bottai G. and Giurgiutiu V. Exact shear-lag solution for guided waves tuning with piezoelectric-wafer active sensors. *AIAA Journal*, 50(11):2285–2294, November 2012.

[100] Raghavan A. and Cesnik C. Finite-dimensional piezoelectric transducer modeling for guided wave based structural health monitoring. *Smart Materials and Structures*, 14(6):1448–1461, December 2005.

[101] Wang X.D. and Meguid S.A. On the electroelastic behaviour of a thin piezoelectric actuator attached to an infinite host structure. *International Journal of Solids and Structures*, 37(23):3231–3251, June 2000.

[102] Wang X.D. and Huang G.L. Wave propagation generated by piezoelectric actuators attached to elastic substrates. *Acta Mechanica*, 183(3-4):155–176, June 2006.

[103] Huang G.L. and Sun C.T. The dynamic behaviour of a piezoelectric actuator bonded to an anisotropic elastic medium. *International Journal of Solids and Structures*, 43(5):1291–1307, March 2006.

[104] Glushkov E., Glushkova N., Kvasha O., and Seemann W. Integral equation based modeling of the interaction between piezoelectric patch actuators and an elastic substrate. *Smart Materials and Structures*, 16(3):650–664, June 2007.

[105] Kim Y., Ha S., and Chang F. Time-domain spectral element method for built-in piezoelectric-actuator-induced lamb wave propagation analysis. *AIAA Journal*, 46 (3):591–600, March 2008.

[106] Ha S. and Chang F. Optimizing a spectral element for modeling PZT-induced lamb wave propagation in thin plates. *Smart Materials and Structures*, 19(1): 015015, January 2010.

[107] Packo P., Bielak T., Spencer A.B., Staszewski W.J., Uhl T., and Worden K. Lamb wave propagation modelling and simulation using parallel processing architecture and graphical cards. *Smart Materials and Structures*, 21(7):075001, July 2012.

[108] Pavlakovic B. and Lowe M.J.S. *Disperse User's Manual*. NDT Lab, Imperial College of London, London, 2003.

[109] Auld B.A. *Acoustic Fields in Elastic Solids, Vol. I, II*. Wiley-Interscience, 1973.

[110] Simonetti F. and Lowe M.J.S. On the meaning of lamb mode nonpropagating branches. *Journal of the Acoustical Society of America*, 118(1):186–192, 2005.

[111] Laperre J. and Thys W. Experimental and theoretical study of lamb wave dispersion in aluminum/polymer bilayers. *The Journal of the Acoustical Society of America*, 94(1):268–278, 1993.

[112] Simonetti F. Lamb wave propagation in elastic plates coated with viscoelastic materials. *The Journal of the Acoustical Society of America*, 115(5):2041–2053, 2004.

[113] Mace B.R. and Manconi E. Wave motion and dispersion phenomena: Veering, locking and strong coupling effects. *The Journal of the Acoustical Society of America*, 131(2):1015–1028, February 2012.

[114] Uberall H., Hosten B., Deschamps M., and Grard A. Repulsion of phasevelocity dispersion curves and the nature of plate vibrations. *The Journal of the Acoustical Society of America*, 96(2):908–917, August 1994.

[115] Prada C., Clorennec D., and Royer D. Local vibration of an elastic plate and zero-group velocity lamb modes. *The Journal of the Acoustical Society of America*, 124 (1):203–212, 2008.

[116] Wilcox P.D. Modeling the excitation of lamb and SH waves by point and line sources. *AIP Conference Proceedings*, 700(1):206–213, 2004.

[117] Wilcox P.D., Lowe M.J.S., and Cawley P. The excitation and detection of lamb waves with planar coil electromagnetic acoustic transducers. *Ultrasonics, Ferroelectrics and Frequency Control, IEEE Transactions on*, 52(12):2370 –2383, 2005.

[118] Velichko A. and Wilcox P.D. Modeling the excitation of guided waves in generally anisotropic multilayered media. *The Journal of the Acoustical Society of America*, 121(1):60–69, 2007.

[119] Treyssde F. and Laguerre L. Numerical and analytical calculation of modal excitability for elastic wave generation in lossy waveguides. *The Journal of the Acoustical Society of America*, 133(6):3827–3837, June 2013.

[120] IEEE Standards . IEEE standard on piezoelectricity. *ANSI/IEEE Std 176-1987*, 1988.

[121] Zhu M. and Leighton G. Dimensional reduction study of piezoelectric ceramics constitutive equations from 3-D to 2-D and 1-D. *IEEE transactions on ultrasonics, ferroelectrics, and frequency control*, 55(11):2377–2383, November 2008.

[122] Lin B., Giurgiutiu V., and Kamal A.M. The use of exact Lamb waves modes for modeling the power and energy transduction of structurally bonded piezoelectric wafer active sensors. In *SPIE Smart Structures and Materials+ Nondestructive Evaluation and Health Monitoring*, page 83450A83450A, 2012.

[123] Gao H. *Ultrasonic guided wave mechanics for composite material structural health monitoring*. PhD thesis, Pennsylvania State University, 2007.

[124] Petyt M. *Introduction to Finite Element Vibration Analysis*. Cambridge University Press, New York, 2nd edition edition, August 2010.

[125] Tisseur F. and Meerbergen K. The quadratic eigenvalue problem. *SIAM Review*, 43(2):235–286, January 2001.

[126] Treyssde F. Elastic waves in helical waveguides. *Wave Motion*, 45(4):457–470, March 2008.

[127] Morse P. and K. Ingard. *Theoretical Acoustics*. Princeton University Press, 1986.

[128] Nilsson C. M. and Finnveden S. Input power to waveguides calculated by a finite element method. *Journal of Sound and Vibration*, 305(45):641–658, September 2007.

[129] Skudrzyk E. *The Foundations of Acoustics - Basic Mathematics and Basic Acoustics*. Springer-Verlag, Wien - New York, 1st edition, 1971.

[130] Birgersson F., Ferguson N. S., and Finnveden S. Application of the spectral finite element method to turbulent boundary layer induced vibration of plates. *Journal of Sound and Vibration*, 259(4):873–891, January 2003.

[131] Gaudenzi P. *Smart Structures: Physical Behaviour, Mathematical Modelling and Applications*. John Wiley & Sons, October 2009.

[132] Gaudenzi P. and Bathe K. An iterative finite element procedure for the analysis of piezoelectric continua. *Journal of Intelligent Material Systems and Structures*, 6(2):266–273, March 1995.

[133] Allik H. and Hughes T.J.R. Finite element method for piezoelectric vibration. *International Journal for Numerical Methods in Engineering*, 2(2):151–157, 1970.

[134] Kocbach J. *Finite Element Modeling of Ultrasonic Piezoeelctric Transducers*. PhD, University of Bergen, 2000.

[135] Piefort V. *Finite element modelling of piezoelectric active structures*. PhD thesis, Universit Libre de Bruxelles, 2001.

[136] Boucher D., Lagier M., and Maerfeld C. Computation of the vibrational modes for piezoelectric array transducers using a mixed finite element-perturbation method. *Sonics and Ultrasonics, IEEE Transactions on*, 28(5):318–329, September 1981.

[137] White R. G. and Walker J. G. *Noise and vibration*. Ellis Horwood, 1982.

[138] Noliac Group. Piezo materials datasheet. www.noliac.com, ver1404.

[139] Mencik J. M. and Ichchou M. N. A substructuring technique for finite element wave propagation in multi-layered systems. *Computer Methods in Applied Mechanics and Engineering*, 197(68):505–523, January 2008.

[140] Mencik J. M. and Ichchou M. N. Multi-mode propagation and diffusion in structures through finite elements. *European Journal of Mechanics - A/Solids*, 24(5): 877–898, September 2005.

[141] Sortor J. *Driving a capacitive load*. Electronics & Innovation, 2005.

[142] Sholl R. A. Forward and reflected powers. what do they mean? Whitepaper SL-WHITE-270-01, Advanced Energy Industries, Inc., 1988.

[143] Lin B. and Giurgiutiu V. Power and energy transduction analysis of piezoelectric wafer-active sensors for structural health monitoring. *Structural Health Monitoring*, 11(1):109–121, July 2011.

[144] Vekinis G., Ashby M.F., and Beaumont P.W.R. Plaster of paris as a model material for brittle porous solids. *Journal of Materials Science*, 28(12):3221–3227, 1993.

[145] Heimbach D., Munver R., Zhong P., Jacobs J., Hesse A., Muller S.C., and Preminger G.M. Acoustic and mechanical properties of artificial stones in comparison to natural kidney stones. *The Journal of Urology*, 164(2):537–544, 2000.